TECHNICAL REPORT DOCUMENTATION PAGE

1. Report No.	2. Government Accession No.	3. Recipient's Catalog No.
FHWA/TX-94/1244-7		

4. Title and Subtitle	5. Report Date
FIELD TESTS AND ANALYSES OF CONCRETE PAVEMENT IN TEXARKANA AND LA PORTE, TEXAS	May 1994
	6. Performing Organization Code
7. Author(s)	8. Performing Organization Report No.
Tianxi Tang, Dan G. Zollinger, and B. Frank McCullough	Research Report 1244-7
9. Performing Organization Name and Address	10. Work Unit No. (TRAIS)
Texas Transportation Institute The Texas A&M University System College Station, Texas 77843-3135	11. Contract or Grant No. Study No. 0-1244
12. Sponsoring Agency Name and Address	13. Type of Report and Period Covered
Texas Department of Transportation Research and Technology Transfer Office P. O. Box 5080 Austin, Texas 78763-5080	Interim: September 1989-December 1992
	14. Sponsoring Agency Code

15. Supplementary Notes

Research performed in cooperation with the Texas Department of Transportation and the U.S. Department of Transportation, Federal Highway Administration

Research Study Title: Evaluation of the Performance of Texas Pavements Made with Different Coarse Aggregates

16. Abstract

This report summarizes the research results obtained from two field tests for Portland cement concrete pavements. One field test was carried out on test sections of jointed plain concrete pavement in Texarkana, Texas, and the other was carried out on test sections of continuously reinforced concrete pavement in La Porte, Texas. Laboratory tests and theoretical analysis were also performed to help in understanding and analyzing the field observation. A close-form solution is proposed for thermal stresses in a concrete slab when it is curled up. This solution is for the case where the temperature decrease in the concrete slab exceeds a limit so that a gap between the slab and foundation forms. This case was not addressed in the Westergaard solution. Fracture tests were applied to the concrete made with different coarse aggregates used for Texas pavements and have shown that fracture mechanics is a powerful tool to judge the quality of the pavement. With these efforts, a method based on fracture mechanics is proposed to determine the depth and spacing of the jointed plain concrete pavement. This method has successfully been applied to the test section in Texarkana.

17. Key Words	18. Distribution Statement
Aggregates, Concrete, Creep, Curing Methods, Fracture Mechanics, Joints, Mix Design, Portland Cement Concrete Pavements, Pulse Velocity, Sawcut,Shrinkage, Thermal Stress	No restrictions. This document is available to the public through NTIS: National Technical Information Service 5285 Port Royal Road Springfield, Virginia 22161

19. Security Classif. (of this report)	20. Security Classif. (of this page)	21. No. of Pages	22. Price
Unclassified	Unclassified	310	

FIELD TESTS AND ANALYSES OF CONCRETE PAVEMENT IN TEXARKANA AND LA PORTE, TEXAS

by

Tianxi Tang
Texas Transportation Institute

Dan G. Zollinger
Texas Transportation Institute

and

B. Frank McCullough
University of Texas at Austin

Research Report 1244-7
Research Study Number 0-1244
Study Title: Evaluation of the Performance of Texas Pavements Made with Different Coarse Aggregates

Sponsored by the
Texas Department of Transportation
In Cooperation with
U.S. Department of Transportation
Federal Highway Administration

May 1994

TEXAS TRANSPORTATION INSTITUTE
The Texas A&M University System
College Station, Texas 77845-3135

IMPLEMENTATION STATEMENT

The results from pavement test sections, one consisting of jointed plain concrete pavement, and the other, continuously reinforced concrete pavement, are summarized in this report. In these test sections, different concrete mix designs with different coarse aggregates (crushed limestone and river gravel) were used. Also, different methods were implemented to control locations of cracks, particularly those which occur early in the pavement life. These methods included: early-aged sawcutting, different curing methods, and use of different patterns of transverse reinforcement. Strengths, temperature, moisture, and pulse velocity of the pavement were monitored during the early ages of the pavement. Testing techniques used in these two test sections have been applied to other test sections performed afterwards under different conditions in this research project.

Material tests to determine the fracture toughness of concrete at an early age were conducted in the field as well as in the laboratory. Fracture toughness is an important material property for evaluating energy required to develop cracking in concrete. Analysis of pavement behavior based on fracture mechanics using the field test data is outlined in this report. It is shown that spacings and depths of sawcuts for pavement joints can be rationally determined with the analysis, indicating that fracture mechanics can be used to improve pavement design and construction procedures.

It is evident that interaction of temperature and moisture variations with constraint induces stresses in the pavement, especially at early ages. Changes in coarse aggregate selection can raise or lower the fracture toughness of a concrete material that will allow improved control of pavement cracking and of pavement performance. Implementation of techniques of this nature and others for controlling temperature and moisture (in light of the given pavement constraint conditions) should control cracking and other distresses in the pavement. Finally, these improvements can translate into direct cost savings to the Texas Department of Transportation and to the U.S. Department of Transportation (Federal Highway Administration).

DISCLAIMER

The contents of the report reflect the views of the authors, who are responsible for the facts and accuracy of the data presented herein. The contents do not necessarily reflect the official views or policies of the Federal Highway Administration or the Texas Department of Transportation. This report does not constitute a standard, specification, or regulation.

ACKNOWLEDGMENT

Research results included in this report arose from joint efforts between the Texas Transportation Institute and the University of Texas at Austin, Center for Transportation Research. We would like to thank the staff of the Texas Department of Transportation and the Federal Highway Administration for their support throughout this study.

TABLE OF CONTENTS

TABLE OF CONTENTS (Continued)

TABLE OF CONTENTS (Continued)

LIST OF FIGURES

LIST OF FIGURES (Continued)

LIST OF FIGURES (Continued)

LIST OF FIGURES (Continued)

LIST OF FIGURES (Continued)

LIST OF FIGURES (Continued)

LIST OF FIGURES (Continued)

LIST OF FIGURES (Continued)

LIST OF FIGURES (Continued)

LIST OF TABLES

LIST OF TABLES (Continued)

LIST OF TABLES (Continued)

SUMMARY

This report summarizes the research results obtained from two field tests on pavement test sections under Research Project 1244 "Evaluation of the Performance of Texas Pavements Made with Different Coarse Aggregates." One of the field tests was a study of *jointed plain concrete pavement*, for which pavement test sections were constructed on FM 559 in Texarkana, Texas. They were paved from October 14 to November 8, 1991. The other field test was carried out on *continuously reinforced concrete pavement*. Its pavement test sections were located on SH 225 in La Porte, Texas, and paved on November 11, 1991. When the two field tests were being performed, some laboratory tests and theoretical analysis were also completed. These efforts have successfully helped in understanding and analyzing the field observation. Results of these efforts are included in this report.

The report consists of five chapters. Chapters 1 and 2 pertain to the details of the Texarkana and La Porte field tests, respectively. Original test data are included in these two chapters. Because of climatic stresses, cracks occur in the concrete pavement at early ages, and these cracks can develop and form severe distresses later on. To control these early cracks, it is necessary to understand the mechanism of induction of the climatic stresses and the strength of the concrete pavement at its early ages.

Chapter 3 presents a closed-form solution for thermal stress (curling stress) analysis of a concrete slab when it is curled up. This solution is proposed for the case where the temperature decrease in the concrete slab exceeds a limit so that a gap between the slab and foundation forms. This case was not addressed in the Westergaard solution. The solution can also be applied for shrinkage-caused stress (warping stress).

Fracture tests of concrete used in Texas pavements made with different coarse aggregates are reported in Chapter 4. Since failure of concrete typically involves stable growth of large cracking zones and formation of large fractures, only a failure criterion which takes into account crack propagation can precisely predict the strength of a concrete structure. Experienced design engineers know that it is not proper to directly apply the strength value obtained from small specimens in the laboratory to the structure. This so-

called size effect of the concrete structure has been well interpreted by the nonlinear fracture models of concrete. As well as in the laboratory, tests were conducted at the Texarkana and La Porte areas. These tests are believed to be the first applications of nonlinear fracture models of concrete to the field. The fracture parameters of concrete obtained from the tests have provided very significant evaluations of the coarse aggregates used in Texas pavements. The fracture parameters are material constants from which the strength for the concrete pavement of any shape and size can be predicted. The test procedure and the theory that the tests were based on are included in Chapter 4.

By comparing the climatic stresses in and the fracture strength of the jointed plain concrete pavement, Chapter 5 proposes a method based on fracture mechanics to determine sawcut spacing and depth. The test section in the Texarkana area is analyzed with this method, demonstrating that this method is successful and reliable. Less expensive, the early-age sawcutting has tremendous promise for crack control. Contents of Chapter 5 were presented at the 72nd Annual Meeting of the Transportation Research Board. A paper based on Capter 5 has been accepted for publication in the Transportation Research Record.

CHAPTER 1: FIELD TEST IN TEXARKANA

1.1. INTRODUCTION

The test sections on FM 559 in Texarkana, Texas, were paved from October 14 to November 8, 1991. They were opened to traffic on July 17, 1992. These test sections are jointed plain concrete pavement placed 13 inches (33 cm) thick which consist of five different concrete mix designs. Of these mix designs, three used siliceous river gravel as the coarse aggregate, one used crushed limestone as the coarse aggregate, and a blend of siliceous river gravel and crushed limestone coarse aggregates were used in another mix design. Figs. 1.1 to 1.8 give the layout of the pavement test sections of these mix designs, which are noted as Mix Designs 1 through 5 in the figures. Details of these mix designs will be given in the following section of this report. The paving direction was identical to the traffic direction, which was basically northbound. Different curing methods were used to control the drying process of the concrete. Joints of the pavement were cut by two different sawcut methods: the more conventional method which requires the use of water to cool the saw blade during cutting operations, and a light and portable concrete saw used to cut the concrete "dry" at an early age. Several different types of data were collected after placement of the concrete pavement. Surveys for cracks at sawed joint locations were conducted at different intervals on October 16, November 10 and 26, and December 19 in 1991; and January 8, February 20, June 4, and July 13 in 1992. The information obtained during these crack surveys is noted in Figs. 1.1 to 1.8 and is analyzed in Section 1.10 "Crack Survey - Observation of Formation of Joints by Sawcutting." One of the purposes of this field investigation was to detect factors that affect the formation of joints and behavior of the jointed concrete pavement in light of different coarse aggregate characteristics. A discussion of the scope of this experimental pavement section follows.

1.2. MIX DESIGNS AND CURING METHODS

The five mix designs used in the test sections used different aggregates, as shown in Table 1.1.

Table 1.1. Aggregates Used in Different Mix Designs.

Mix Design	Coarse Aggregate	Intermediate Aggregate	Fine Aggregate
1 Control Mix	1½" (38 mm) SRG (100%) Item 360.1 (3)	None	Little River Sand (100%) Item 360.1 (4)
2	1½" (38 mm) L.S. (50%) ¾" SRG (50%) Item 360.1 (3)	Buckshot	Little River Sand (35%) Crushed Sand (65%) Item 360.1 (4)
3	1½" (38 mm) SRG (100%) Item 360.1 (3)	Same as above	Same as above
4	¾" (19 mm) SRG (100%) Item 421.2	Same as above	Same as above
5	1½" (38 mm) L.S. (100%) Item 360.1 (3)	Same as above	same as above

Note: SRG - siliceous river gravel
LS - crushed limestone

Mix Design 1 is the control mix design for the experimental sections. In the other four mix designs, buckshot was added as an intermediate aggregate to improve gradation of aggregates. With no intermediate aggregate, "gaps" are formed among coarse aggregate grains. The volume of these "gaps" is so small that it cannot be occupied by the coarse aggregate, and it must be provided by mortar. With intermediate aggregate, medium particles fill in these "gaps" and decrease the amount of mortar needed. As a result, the volume of voids in the concrete is decreased by adding intermediate aggregate. This effect of the intermediate aggregate will be shown by the

cored specimens of this experimental pavement. (See Section 1.9 "Analysis of Specimens Cored from the Pavement.")

Mix Design 5 used crushed limestone as the coarse aggregate. Mix Design 2 used a blend of siliceous river gravel and crushed limestone as the coarse aggregate. Previous investigations have shown that pavement of river-gravel concrete tends to crack more likely in the early ages than crushed-limestone concrete. Mix Designs 3 and 5 were proposed to compare effects of river gravel and crushed limestone on joint formation. Mix Design 2 was proposed to observe how a hybrid of crushed limestone and river gravel change properties of concrete. One of the main objectives was to prove that adding small coarse river gravel in the concrete, which is designed to use crushed limestone as the coarse aggregate, helps joint formation. It will be shown that this objective has been achieved in this field experiment. (See Section 1.10 "Crack Survey - Observation of Formation of Joints by Sawcutting" of this report.) Different from Mix Design 3, Mix Design 4 used smaller siliceous river gravel as the coarse aggregate. These two mix designs were planned to understand size effects of coarse aggregates. It will be shown later in Section 1.6 "Measurement of Fracture Toughness in the Field" that smaller coarse aggregates caused the pavement to become more brittle at early ages. In all these mix designs, the design water/cement ratio was 0.39 and the design slump was 1.5 inches (38 mm). The proportioning, aggregate gradation, and other material characteristics of each mix design are listed in Section 1.13, an appendix of this chapter.

Twenty 6 x 6 x 20-inches (152 x 152 x 508 mm) beam specimens were tested to certify each mix design by the contractor (Two States Construction Company, Inc.) at a concrete age of seven days. Table 1.2 lists the average flexural strength, and its standard deviation of each mix design based on these tests.

Compression tests were performed for each mix design at concrete ages of 3, 5, 7, 14 and 28 days. Fig. 1.9 shows the increase in the compressive strength with the concrete age. Obviously, the specimen of Mix Design 5 (with crushed limestone as the coarse aggregate) had higher tensile and compressive strengths at these ages than Mix Designs 1, 3 and 4 (all with siliceous river gravel as the coarse aggregate) at these

concrete ages. Mix Design 2 was different from Mix Design 5 by the replacement of 50% of 1.5-inch (38 mm) limestone by 0.75-inch (19 mm) siliceous river gravel (Table 1.1). Although the compressive strength of Mix Design 2 was higher (Fig. 1.9) than that of Mix 5, it did not show a higher tensile strength at the age of 7 days (Table 1.2). Mix Designs 3 and 4 used the same fine aggregate and the same intermediate aggregate, but the coarse aggregate in Mix 3 was nominally 1.5 inches (38 mm) while Mix Design 4 was nominally 0.75 inch (19 mm). As a result, Mix 3 had higher compressive and tensile strengths than Mix 4. On the other side, though Mix Design 1 had a larger coarse aggregate than Mix Design 4, these two mix designs had similar tensile and compressive strengths at the age of 7 days. It may be interesting to note that the compressive strength of Mix 4 was higher than that of Mix 1 at the age of 5 days, but lower after the age was older than 7 days.

Table 1.2. Average Flexural Strength at the Age of Seven Days.

Mix Design	Average Flexural Strength	Standard Deviation
1	662 psi (4.56 MPa)	34 psi (0.23 MPa)
2	805 psi (5.55 MPa)	50 psi (0.34 MPa)
3	693 psi (4.78 MPa)	27 psi (0.19 MPa)
4	662 psi (4.56 MPa)	26 psi (0.18 MPa)
5	841 psi (5.80 MPa)	46 psi (0.32 MPa)

The pavement shown in Fig. 1.1 is the test section paved on October 14, 1991 with the concrete of Mix Design 3. Fig. 1.2 shows another segment of paving completed in one day, which was paved with Mix Design 1 on October 16, 1991. Three segments paved on October 18, October 26, and November 6, 1991, all used Mix Design 5 as shown in Figs. 1.3 to 1.6 respectively. The test section of Mix Design 2 was paved on November 8, 1991, and its layout is shown in Fig. 1.7. The six test

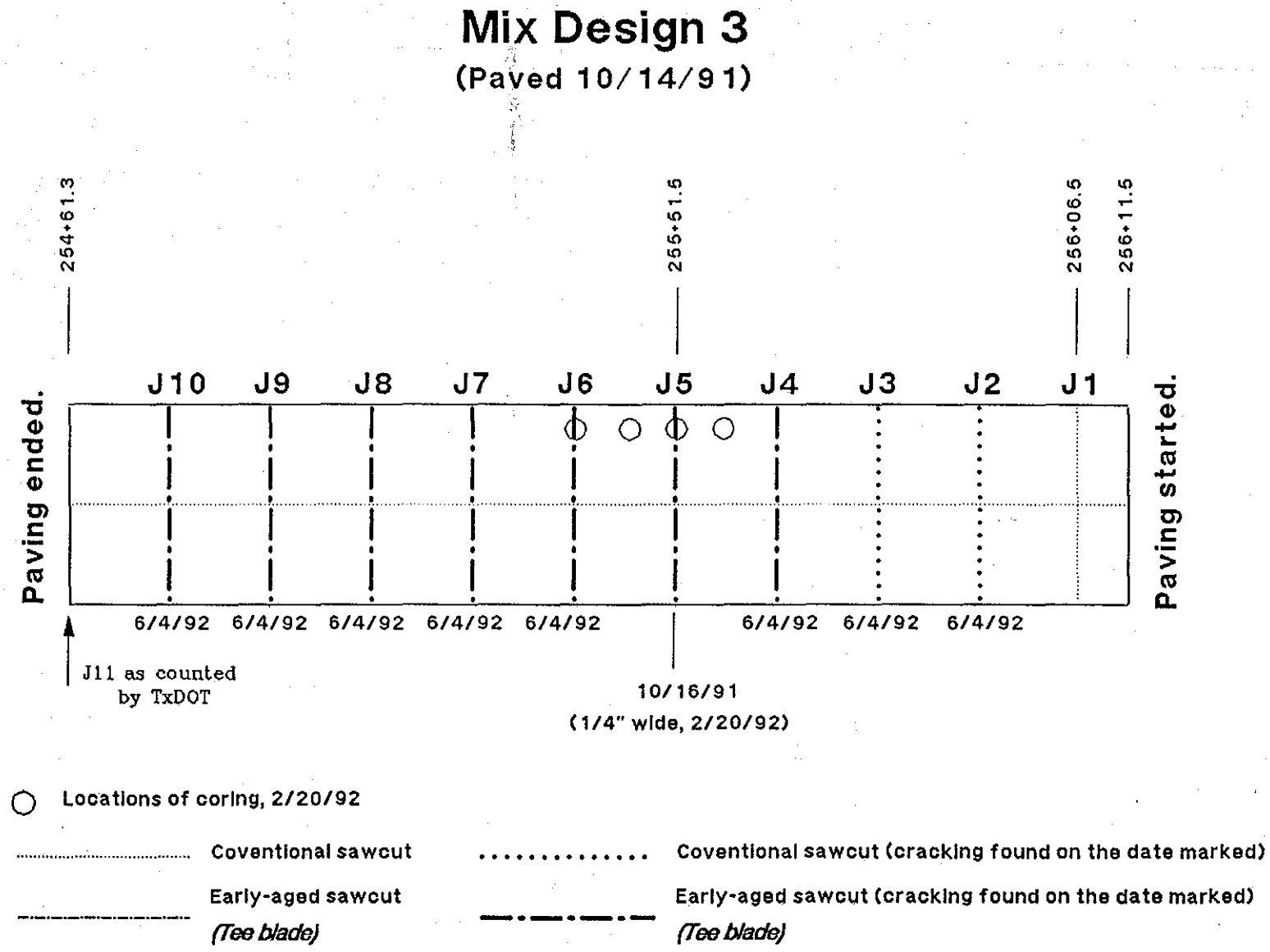

Fig. 1.1. Layout of the Test Sections (Part 1).

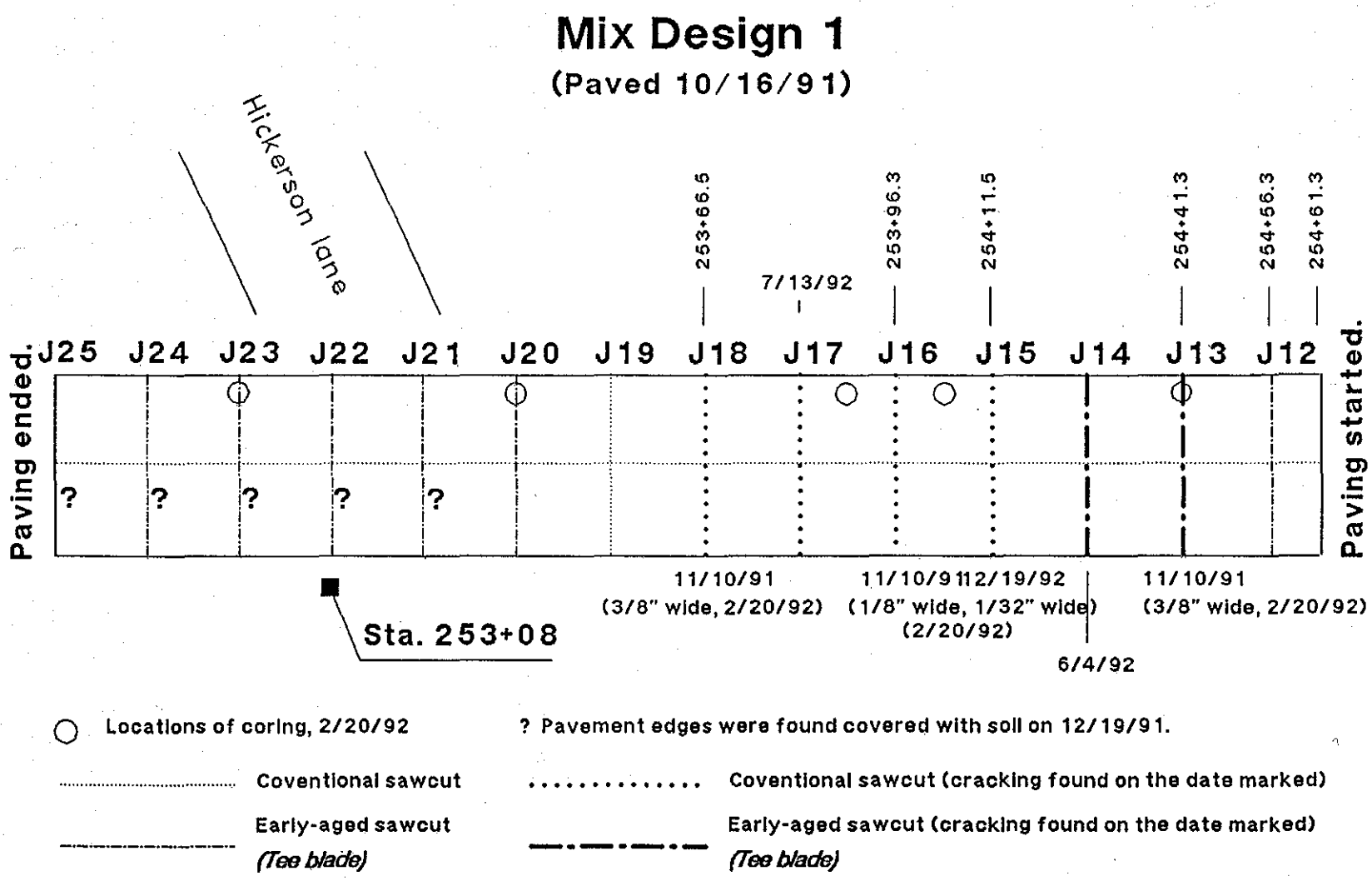

Fig. 1.2. Layout of the Test Sections (Part 2).

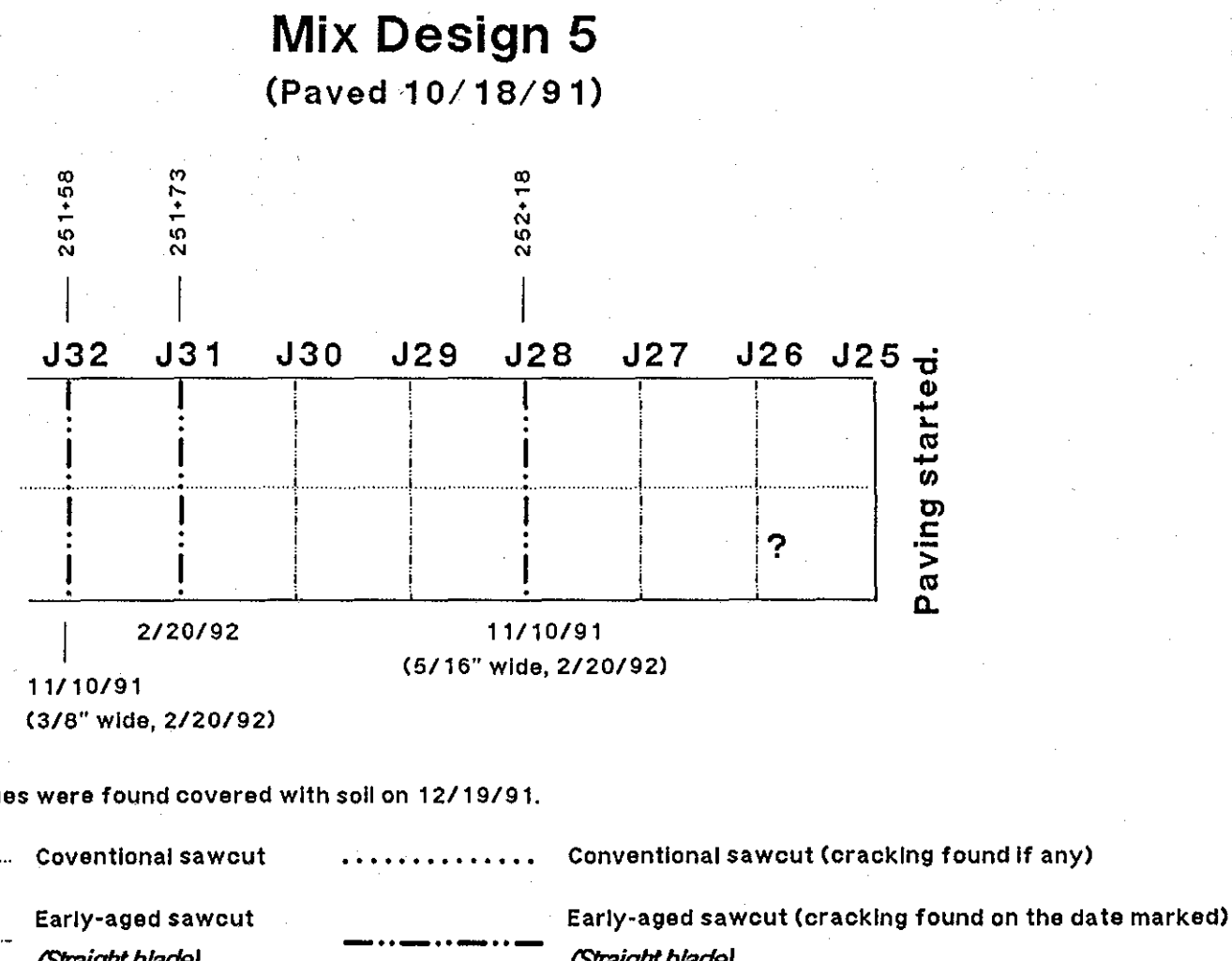

Fig. 1.3. Layout of the Test Sections (Part 3).

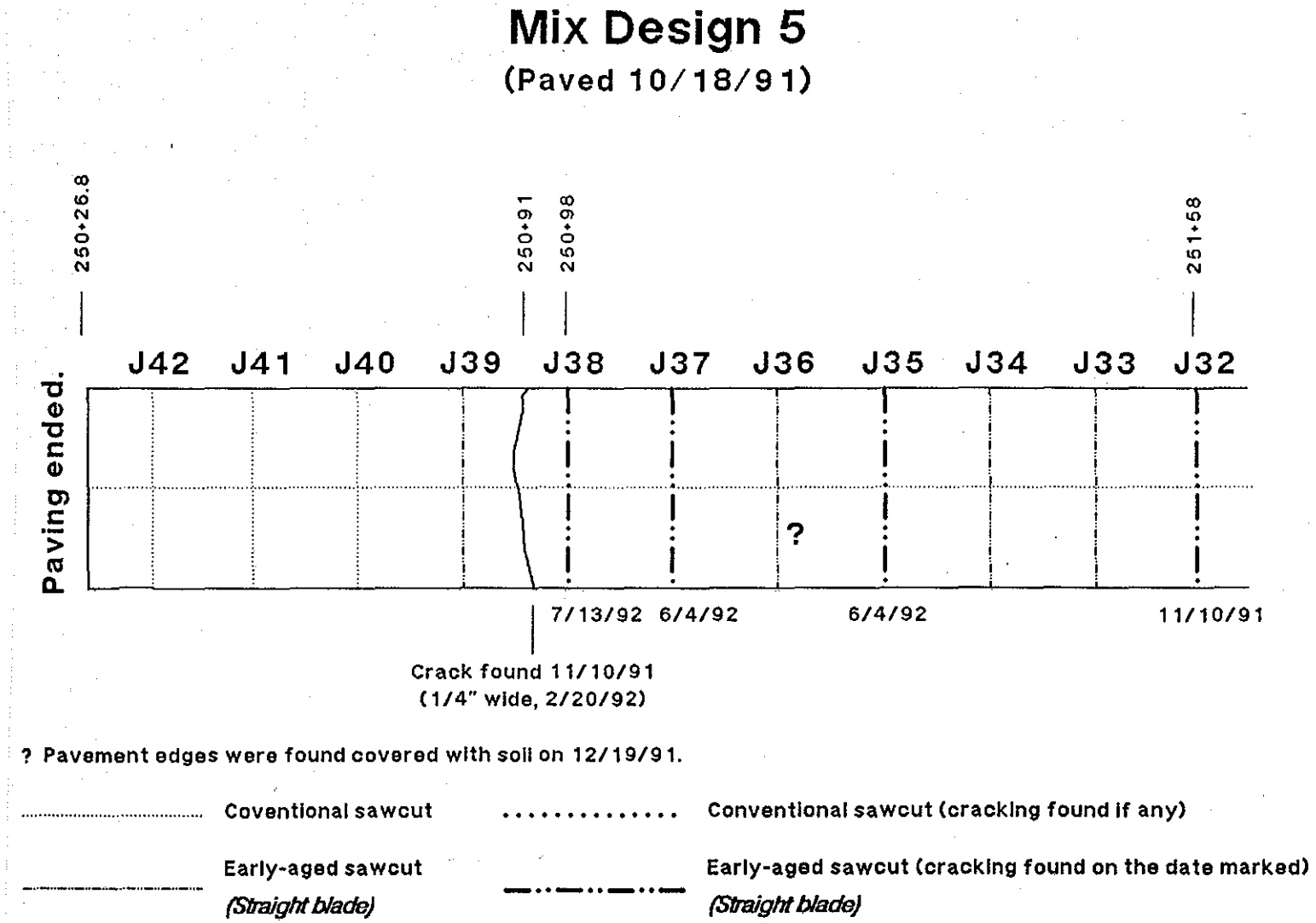

Fig. 1.4. Layout of the Test Sections (Part 4).

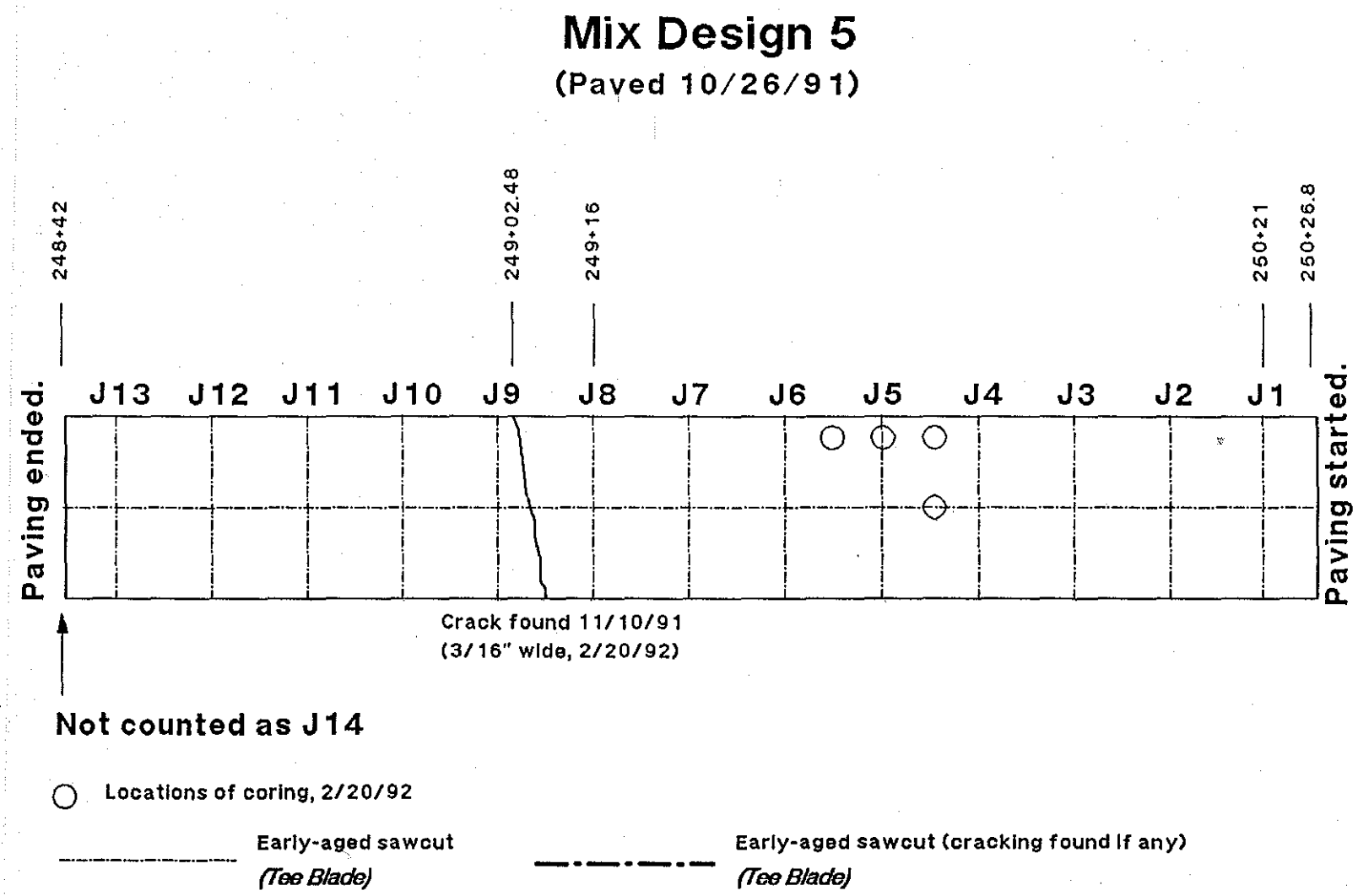

Fig. 1.5. Layout of the Test Sections (Part 5).

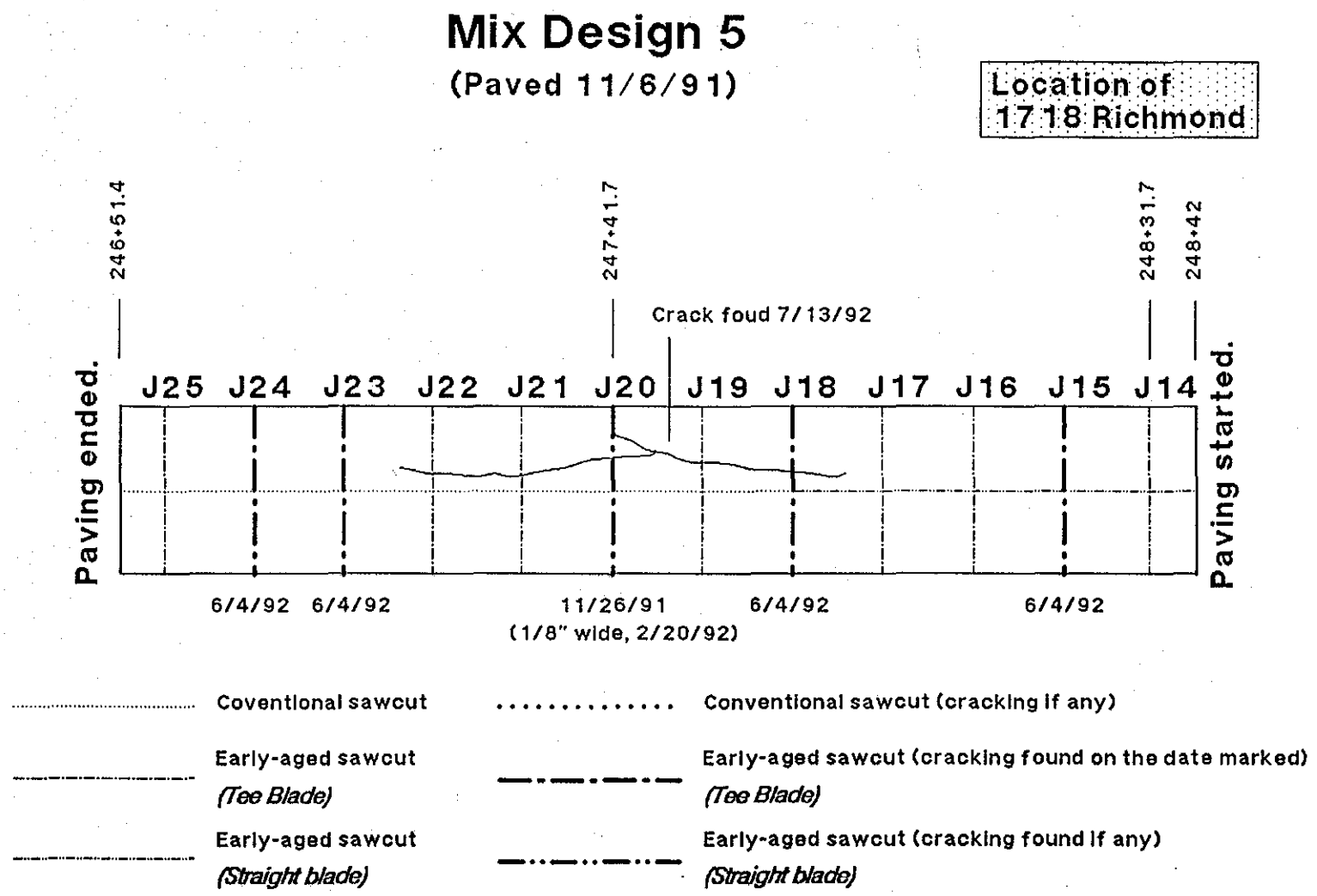

Fig. 1.6. Layout of the Test Sections (Part 6).

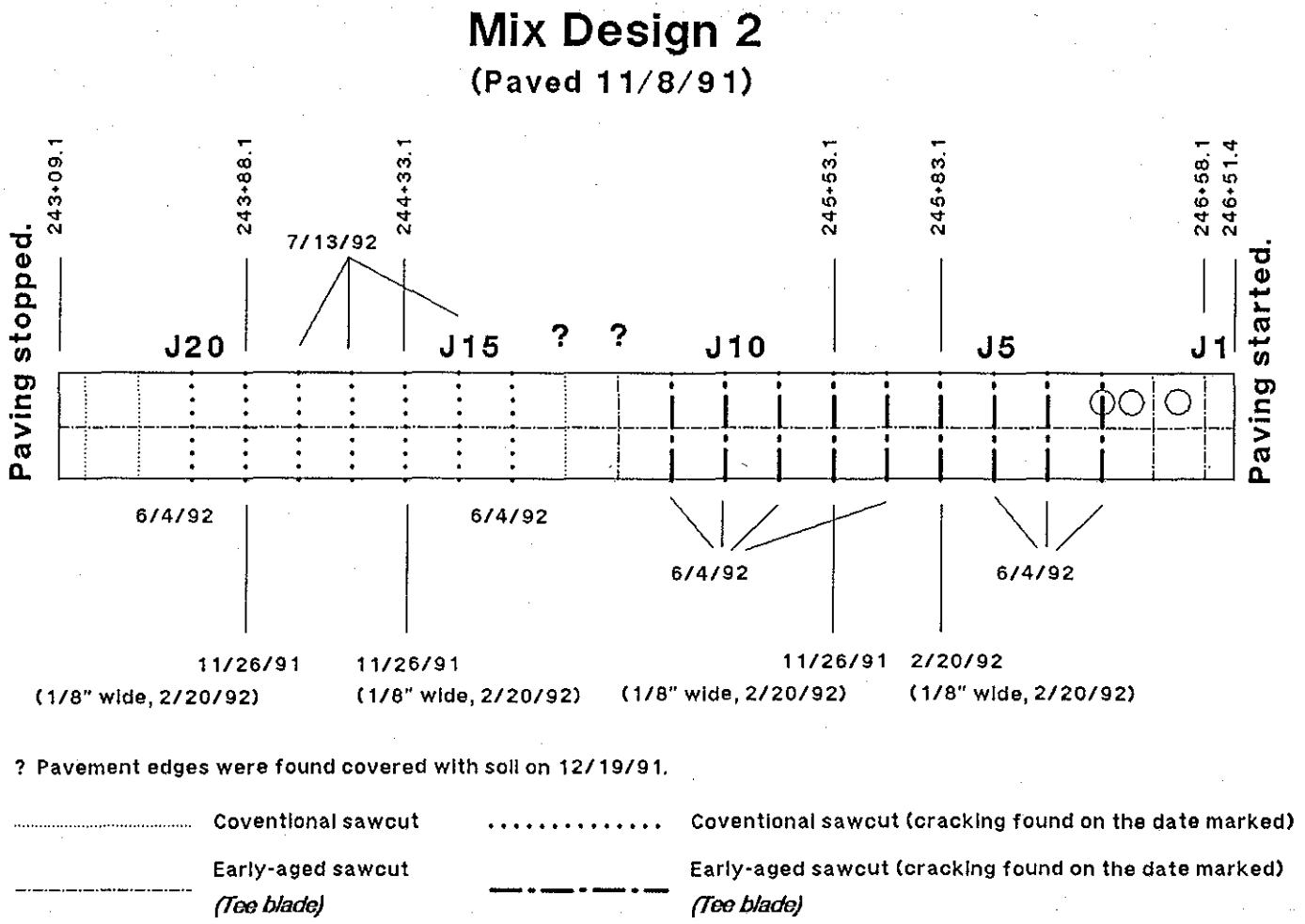

Fig. 1.7. Layout of the Test Sections (Part 7).

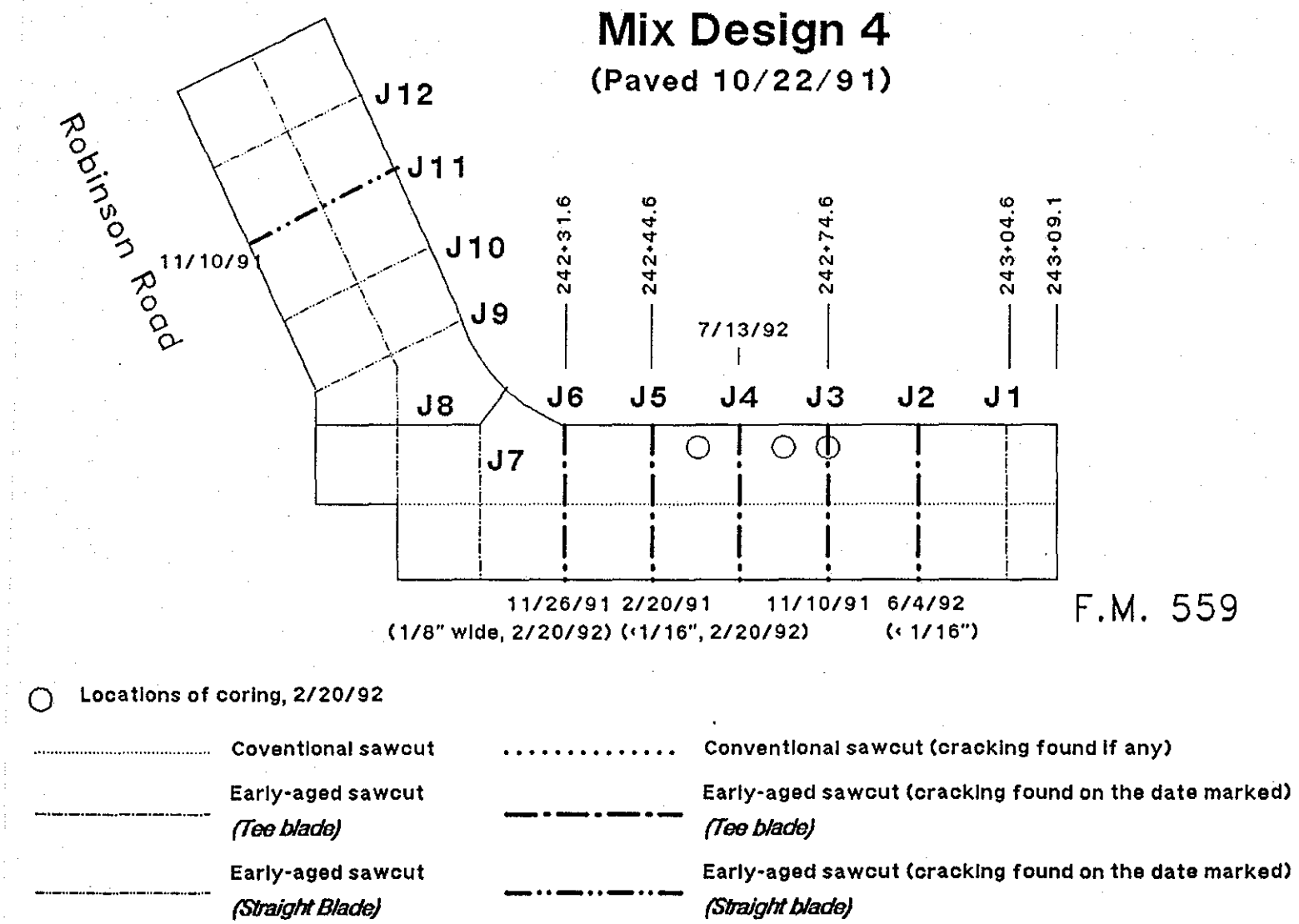

Fig. 1.8. Layout of the Test Sections (Part 8).

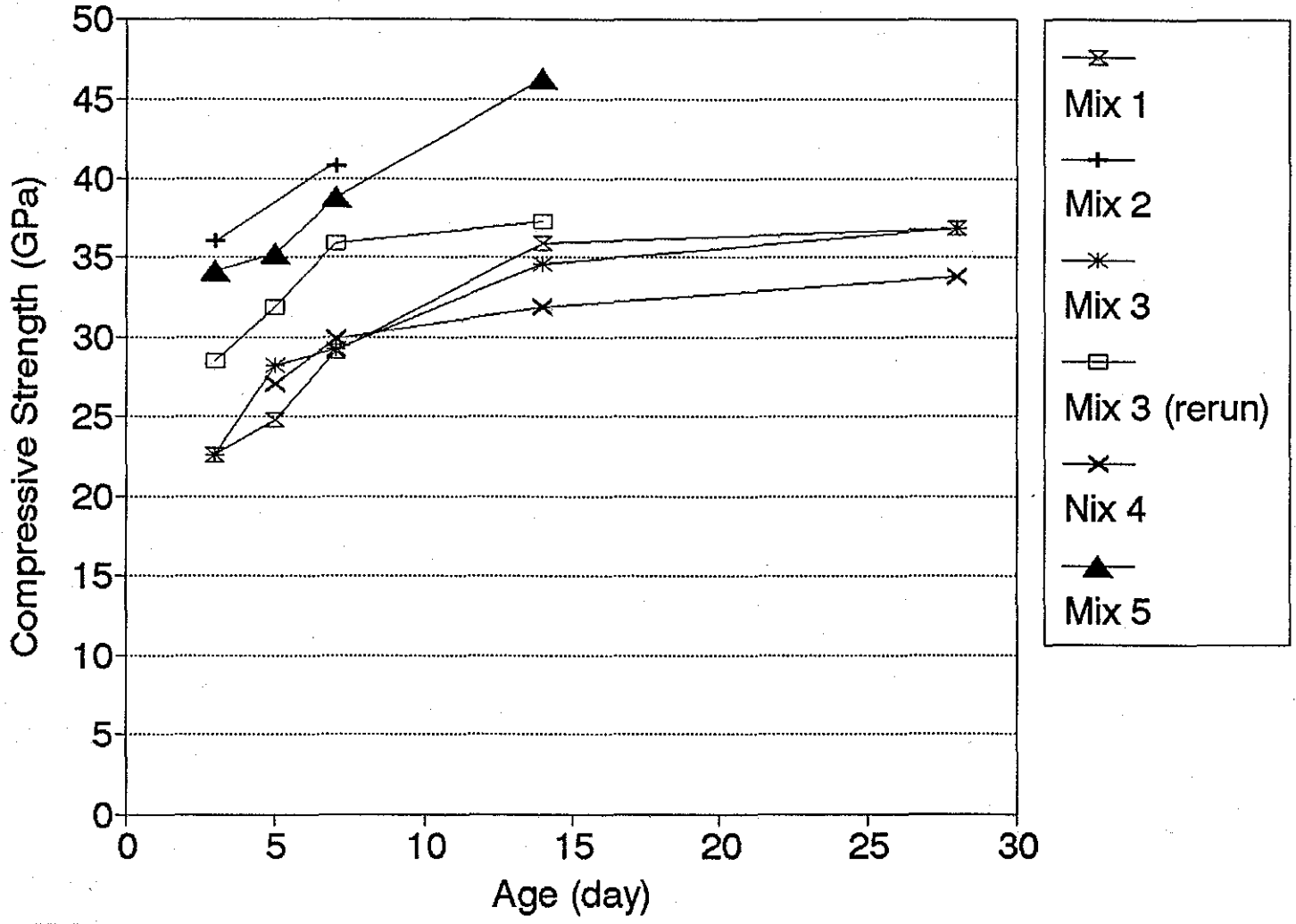

Fig. 1.9. Compressive Strengths of Concrete.

section segments mentioned were all paved from south to north. Another test section (Fig. 1.8) was paved from south to north and then turned to northeast. This section used Mix Design 4 and was paved on October 22, 1991, using a vibrating screen. It was noted by the contractor that the concrete was very easy to place using this mix design as were all the mix designs using the intermediate aggregate. This was evidenced further by the lack of "honey combing" in core samples obtained several months after the concrete was placed.

Four different curing methods were employed in this experimental section. These curing methods are as follows:

(i) Membrane curing compound, Item 360.2 (13), which is called the standard curing method;

(ii) Membrane curing compound, Item 360.2 (13), using Procrete - a proprietary product;

(iii) Cotton mat curing, Item 360.2 (15), plus membrane curing, Item 360.2 (13), called "Cotton Mat";

(iv) Polyethylene film curing, Item 360.2 (12), plus membrane curing, Item 360.2 (13), called "Polyethylene" for brevity.

1.3. JOINT SAWCUTTING

As described previously, two sawcut techniques were used for longitudinal and transverse joints: conventional sawcutting and early-aged sawcutting. The early-aged sawcut technique uses a light and portable sawcut machine that allows the pavement to be cut earlier than by using the conventional sawcut technique, differing from the conventional sawcut method, which uses water to cool the blade during cutting operations.

The spacing of the transverse joints in this experimental pavement was 15 feet (4.57 m). The notch cut by the early-aged sawcut method was approximately 1 inch (25 mm) deep. The conventional method was used to cut the pavement D/4 which was approximately 3 inches (76.2 mm) deep. The sawcut methods used at each joint are noted in the layout of each test section (Figs. 1.1 to 1.8). Two different types of

diamond blades were used with the early-aged cutting method. One was T-shaped while the other was a straight blade.

Early-aged sawcut operations generally started 4.5 to 5.5 hours after placement of the concrete. When the weather was cold and humid, dry sawcut was delayed until the pavement was solid enough to walk on. In some instances, this delay was extensive. For example, in the test section where Mix Design 3 was used, the paving started at 9:00 a.m., and it was not sawcut until midnight. No apparent ravelling happened along the notches sawcut by the early-aged sawcut technique.

1.4. WEATHER INFORMATION

Weather information was obtained from the weather station at the Texarkana airport, located in Texarkana, Arkansas. The highest and lowest temperatures from October 13 to November 11, 1991 are shown in Fig. 1.10. Daily average temperatures during this period are given in Fig. 1.11. A portable weather station, Campbell Scientific 012, was placed near the test sections and obtained ambient temperature and relative humidity from November 7 to 10. Fig. 1.12 shows these data.

1.5 MEASUREMENT OF COMPRESSIVE STRENGTHS OF CONCRETE SPECIMENS PREPARED IN THE FIELD

Cylindrical specimens and beam specimens were prepared and cured in the field while each mix design was placed. The cylindrical specimens were 6-inch (152 mm) in diameter and 12-inch (305 mm) in height. Data from the compression tests are shown in Table 1.3.

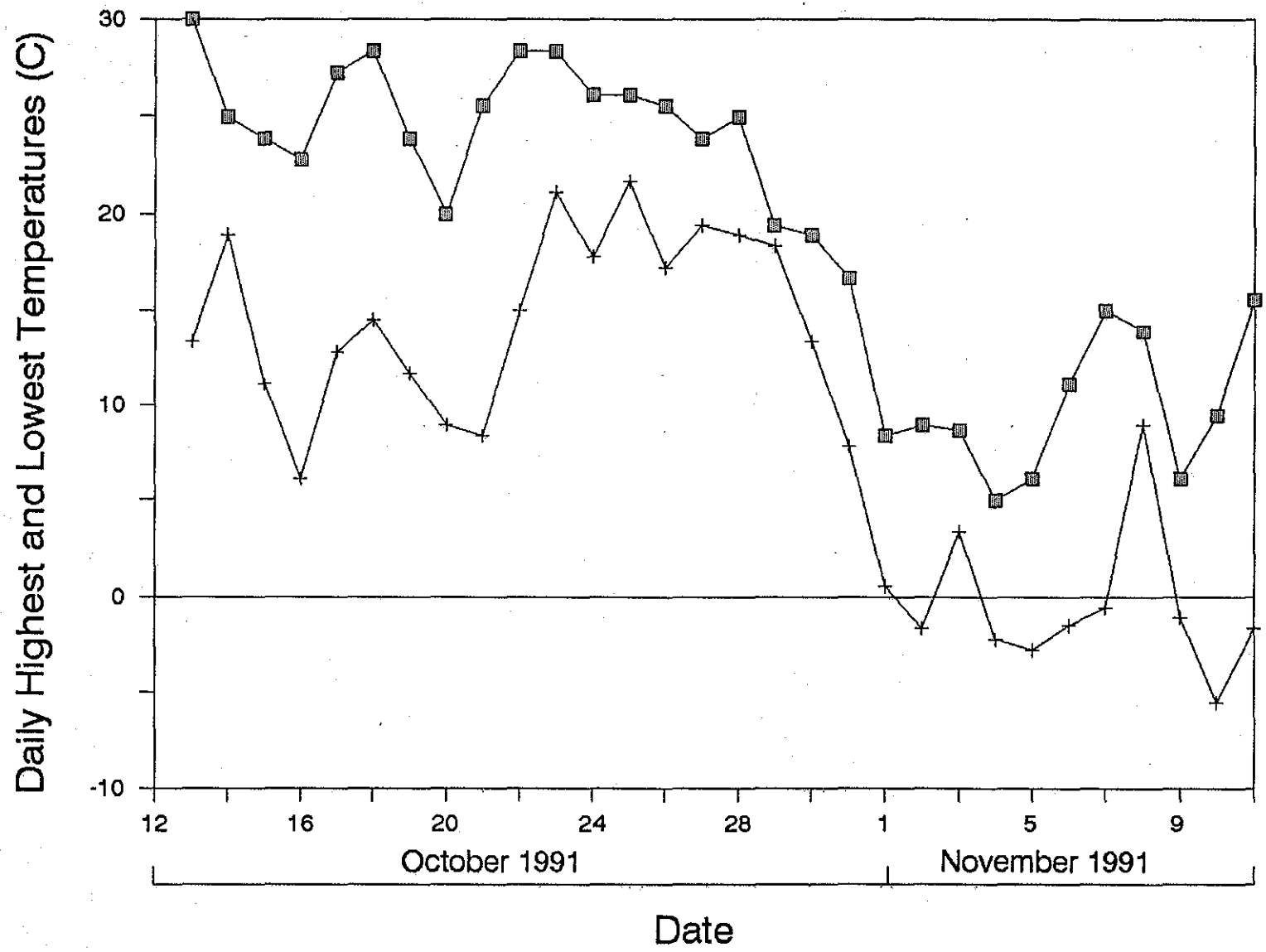

Fig. 1.10. Daily Highest and Lowest Temperatures.

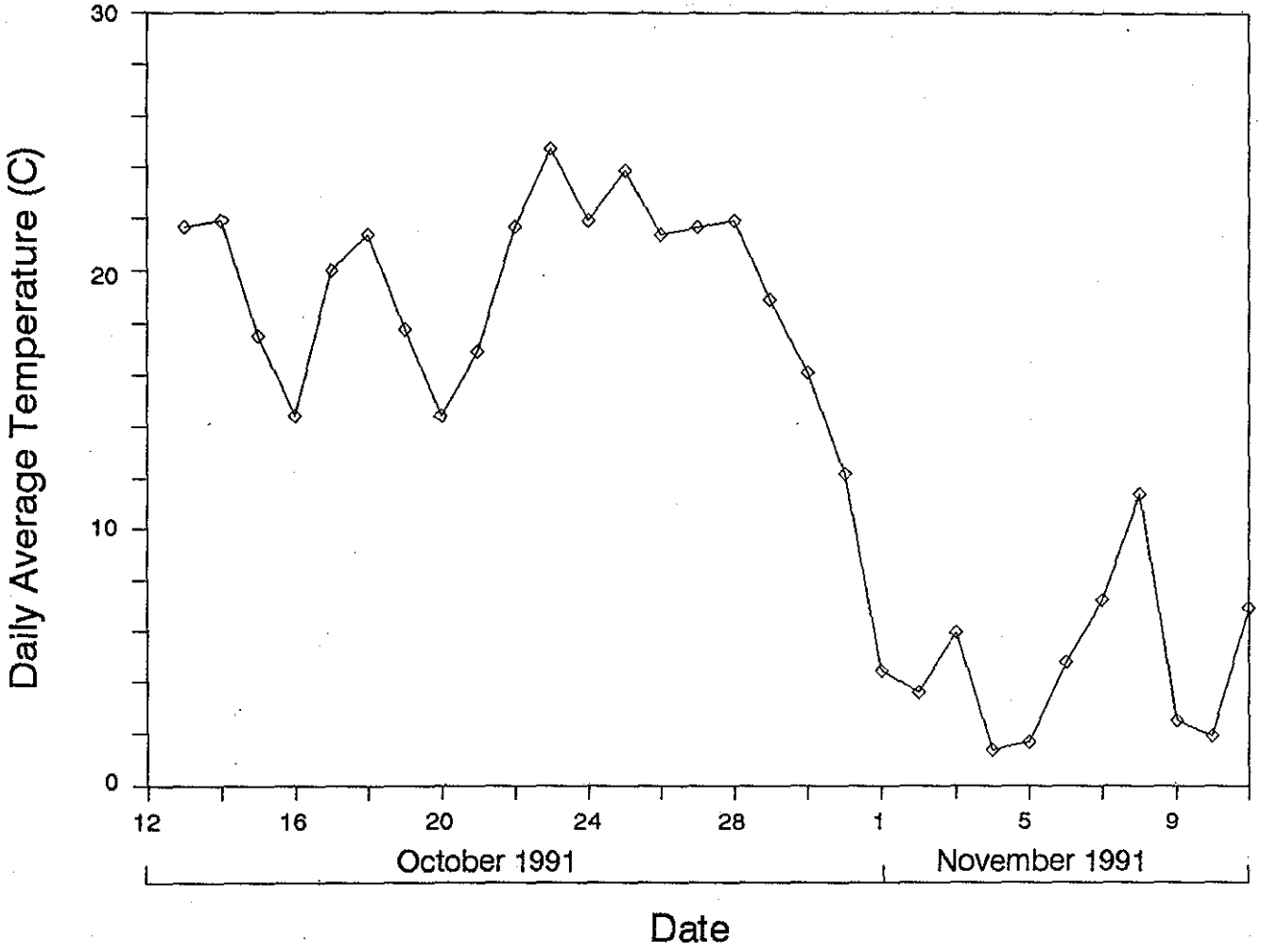

Fig. 1.11. Daily Average Temperatures.

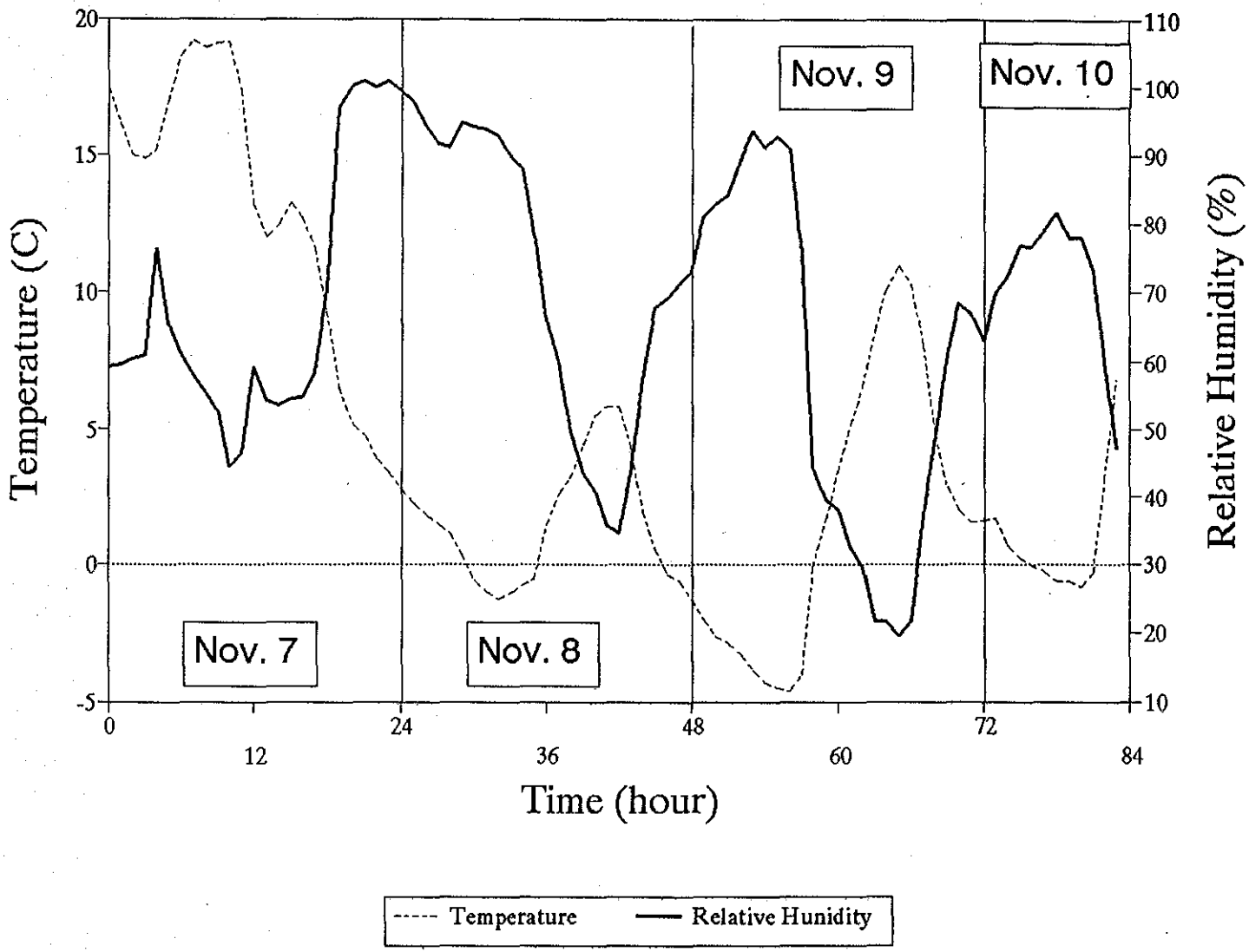

Fig. 1.12. Temperature and Relative Humidity Records by the Weather Station.

Table 1.3. Compressive Strengths of Concrete Specimens Prepared in the Test Sections.

Mix Design	Specimen Preparation Date	Average Compressive Strength	Age of Concrete Specimens
1	October 16, 1991	4,970 psi (34.3 MPa)	56 days
3	October 14, 1991	5,480 psi (37.8 MPa)	58 days
4	October 22, 1991	1,680 psi (11.6 MPa)*	1 day
		2,620 psi (18.1 MPa)	2 days
		5,600 psi (38.6 MPa)	50 days
5	October 26, 1991	1,190 psi (8.21 MPa)*	1 day
		5,780 psi (39.9 MPa)	46 days

Note: Data noted with * are the average of three tests performed by Southwestern Laboratory, Texarkana, Texas. Other data are the average of three tests performed at Texas Transportation Institute.

1.6. MEASUREMENT OF FRACTURE TOUGHNESS IN THE FIELD

Four beam specimens of different sizes were prepared in the field for each of Mix Designs 3, 4 and 5. These specimens were of the same shape (Fig. 1.13). The support span of the beam specimens was 2.5 times the depth of the specimens. The depths of the specimens were 4.5 inches (114 mm), 6 inches (152 mm), 9 inches (229 mm) and 12 inches (305 mm), respectively. A notch was cut before testing where the length of the notch was a quarter of the beam depth and the width of the notch was about 1/8 inch (3.2 mm). Three-point bending tests were performed on the specimens 24 hours after preparation of the specimens as illustrated in Fig. 1.13. Two fracture parameters were calculated from the peak loads of the four tests based on the size effect law, a nonlinear fracture model for concrete. For the theory and details of the test method,

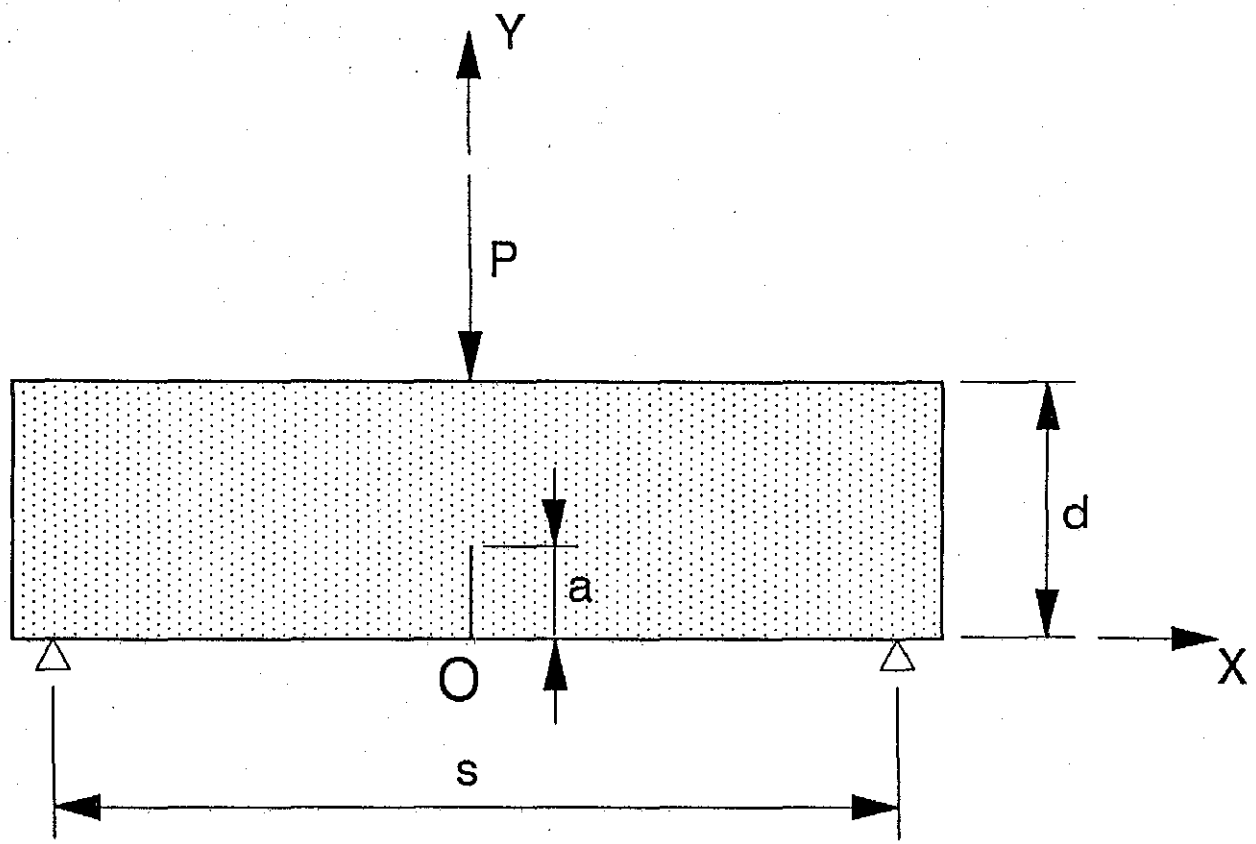

Fig. 1.13. Geometry of the Beam Specimen.

see Chapter 4. Table 1.4 shows the two fracture parameters: K_{If} - the critical stress intensity factor for an infinite specimen, and c_f - the effective critical crack increase for an infinite specimen. They are both material parameters.

Table 1.4. Two Fracture Parameters at 1-Day Age Measured in the Field.

Mix Design	Concrete Age (day)	K_{If}	c_f
3	1	717 psi$\sqrt{}$in (0.788 MPa$\sqrt{}$m)	1.98 in. (50.3 mm)
4	1	687 psi$\sqrt{}$in (0.755 MPa$\sqrt{}$m)	0.56 in. (14.2 mm)
5	1	827 psi$\sqrt{}$in (0.909 MPa$\sqrt{}$m)	1.31 in. (33.3 mm)

Mix Design 4, using smaller coarse aggregate than Mix Design 3, had Lower K_{If} and c_f value than Mix Design 3. Mix Design 5, which used crushed limestone as the coarse aggregate, had a higher K_{If} value at the one-day age than the other two mix designs in Table 1.4, which both used siliceous river gravel as the coarse aggregate. Fig. 1.14 gives comparisons of K_{If} values for the three mix designs.

The two fracture parameters are material parameters. In other words, they are independent of the specimens. Although the loading condition of the concrete pavement is more complicated than three-point bending, these two parameters obtained from bending beams also apply to the pavement. As long as stresses caused by temperature variation and concrete drying shrinkage were known in the pavement, another index "brittleness number" (see Chapter 4) could be calculated. In the experimental section, pavements of different mix designs were of the same size and the same geometry. Assuming that the same thermal and shrinkage-caused stress distribution is produced in different pavements, the brittleness number of the pavement is inversely proportional to c_f. If the brittleness number of Mix 5 pavement is given $ß_5$ at the one-day age, then $ß_3 = 0.66\ ß_5$ and $ß_4 = 2.33\ ß_5$, where $ß_3$ and $ß_4$ are the brittleness numbers of the pavements of Mix 3 and Mix 5, respectively, at the one-day age. Fig. 1.15 compares these brittleness numbers. The relative brittleness number in the figure is the ratio of

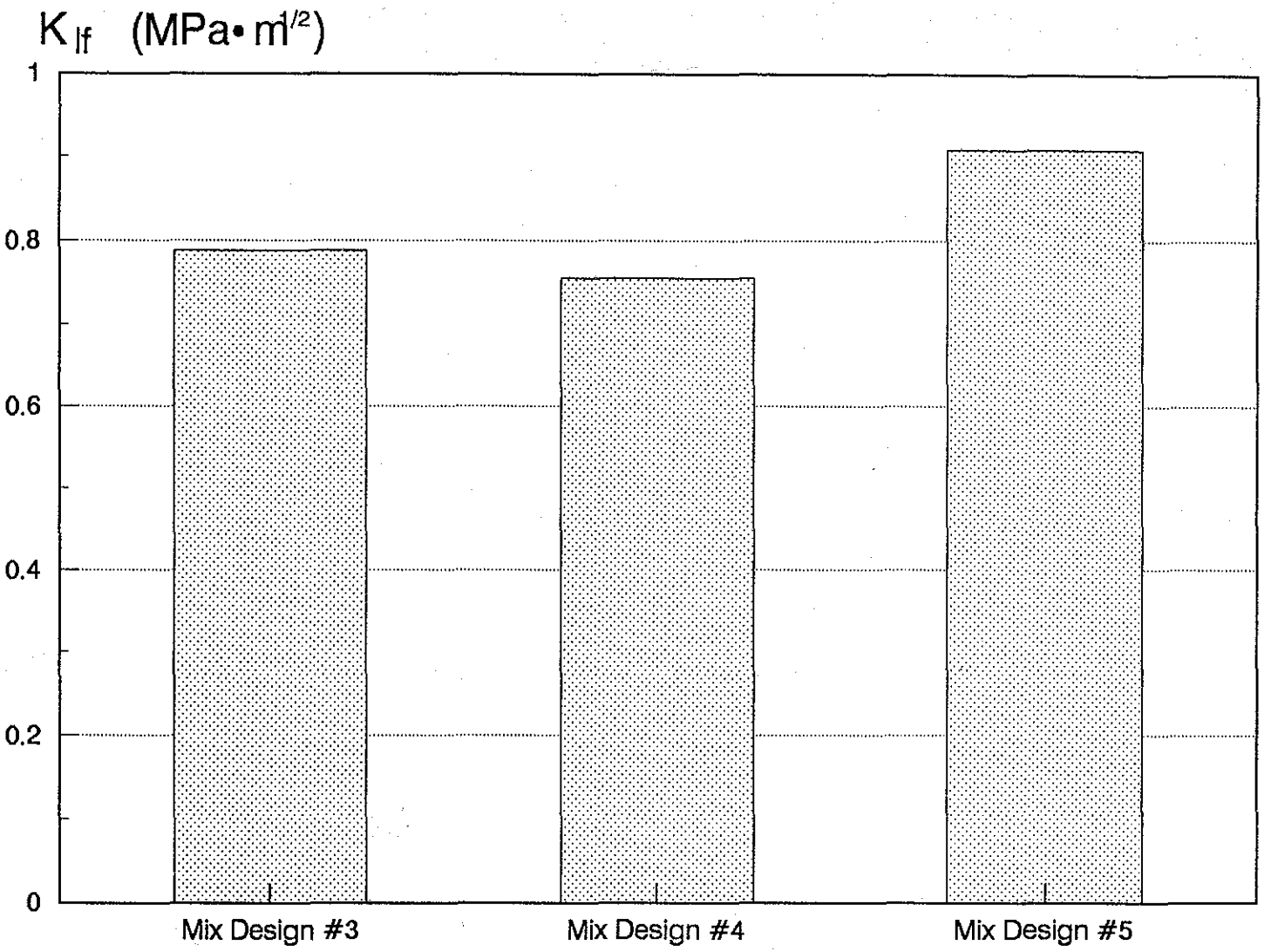

Fig. 1.14. Fracture Toughness of Concrete Measured at One-Day Age.

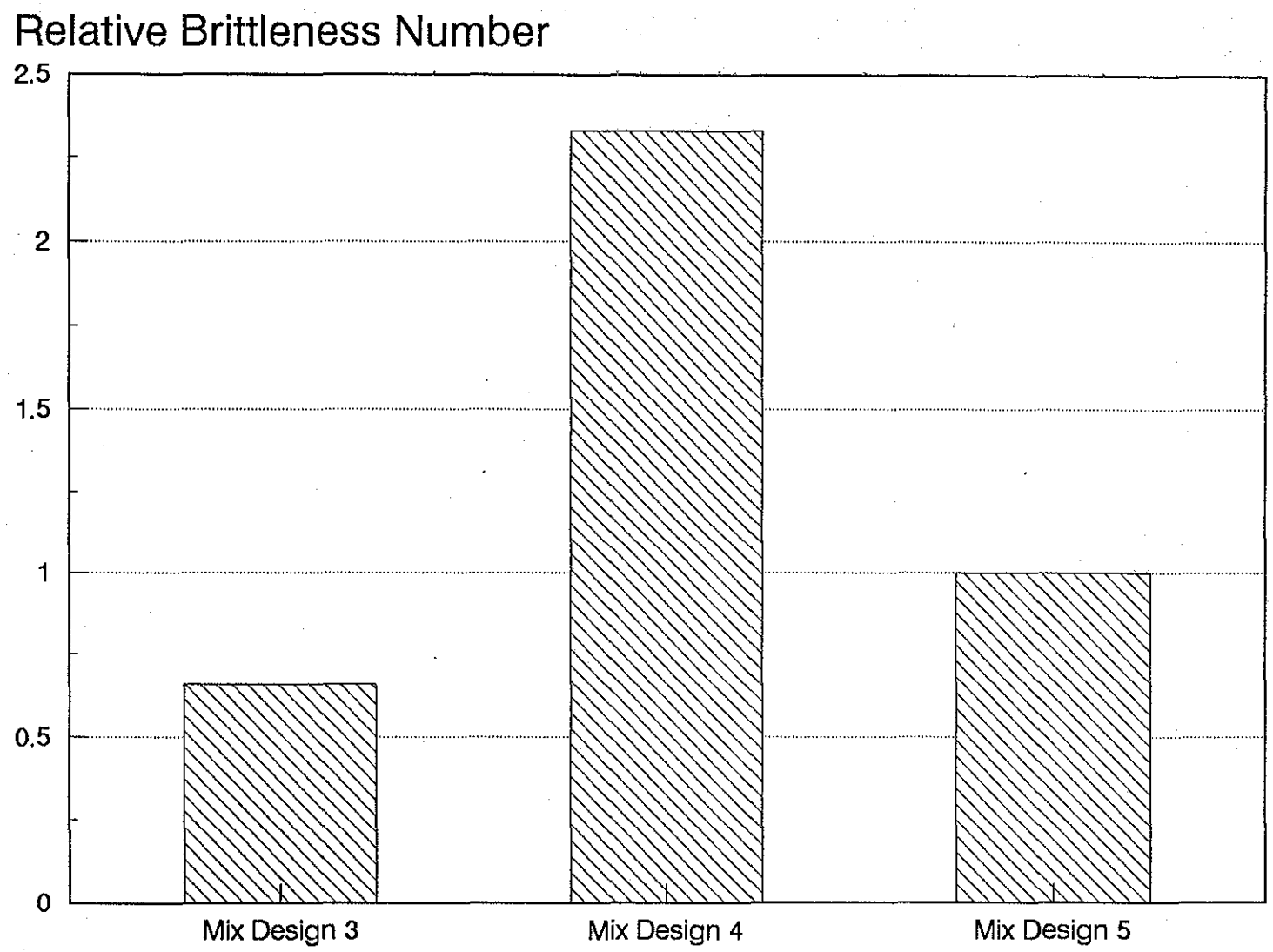

Fig. 1.15. Brittleness Number for Pavements of Different Mix Designs at One-Day Age.

the brittleness number of the specific pavement to the brittleness number of the pavement of Mix 5. It will be seen later in this report that the larger the brittleness number at the one-edge age, the more sawcuts cracked at early ages. (The percentage of cracked sawcuts is shown in Fig. 1.26 of Section 1.9.)

1.7. MEASUREMENT OF PAVEMENT TEMPERATURE AND RELATIVE HUMIDITY

Temperature and relative humidity are two important variables in their effect on concrete. Changes in either of these conditions can induce stresses in the pavement as well as affect the rate of the strength gain of the concrete. The influence of these parameters is very apparent during the early ages of the concrete. Both temperature and relative humidity in the test sections were measured with three different digital systems. One system, a product of Vaisala, measures both temperature and humidity in the concrete, where the sensor works on a capacitance basis. It monitors the change in capacitance of a thin polymer film as it absorbs water vapor. Another sensor, manufactured by General Eastern, measures the change in electric resistance of a bulk polymer sensor with the moisture that the sensor absorbs. The third digital system used was a product of Omega.

To apply these instruments, a PVC tube was inserted in the pavement surface. The sealed tube was placed while the concrete was fresh so that the concrete exposed inside the tube was protected from the outside atmosphere (Fig. 1.16). When the temperature and relative humidity were measured, the probe of the measuring system was inserted in the PVC tube with a rubber "O" ring to seal the small space between the sensor unit and the wall of the PVC tube. After the measurement, the probe was removed from the PVC tube, and a PVC cap was screwed on the top end of the tube to prevent air exchange between the space inside the tube and the atmosphere.

For comparison of different curing methods, temperature and relative humidity data for the test section using Mix Design 3, which was placed on October 14, 1991 are shown in Figs. 1.17 and 1.18. Data were collected at different times as shown in the

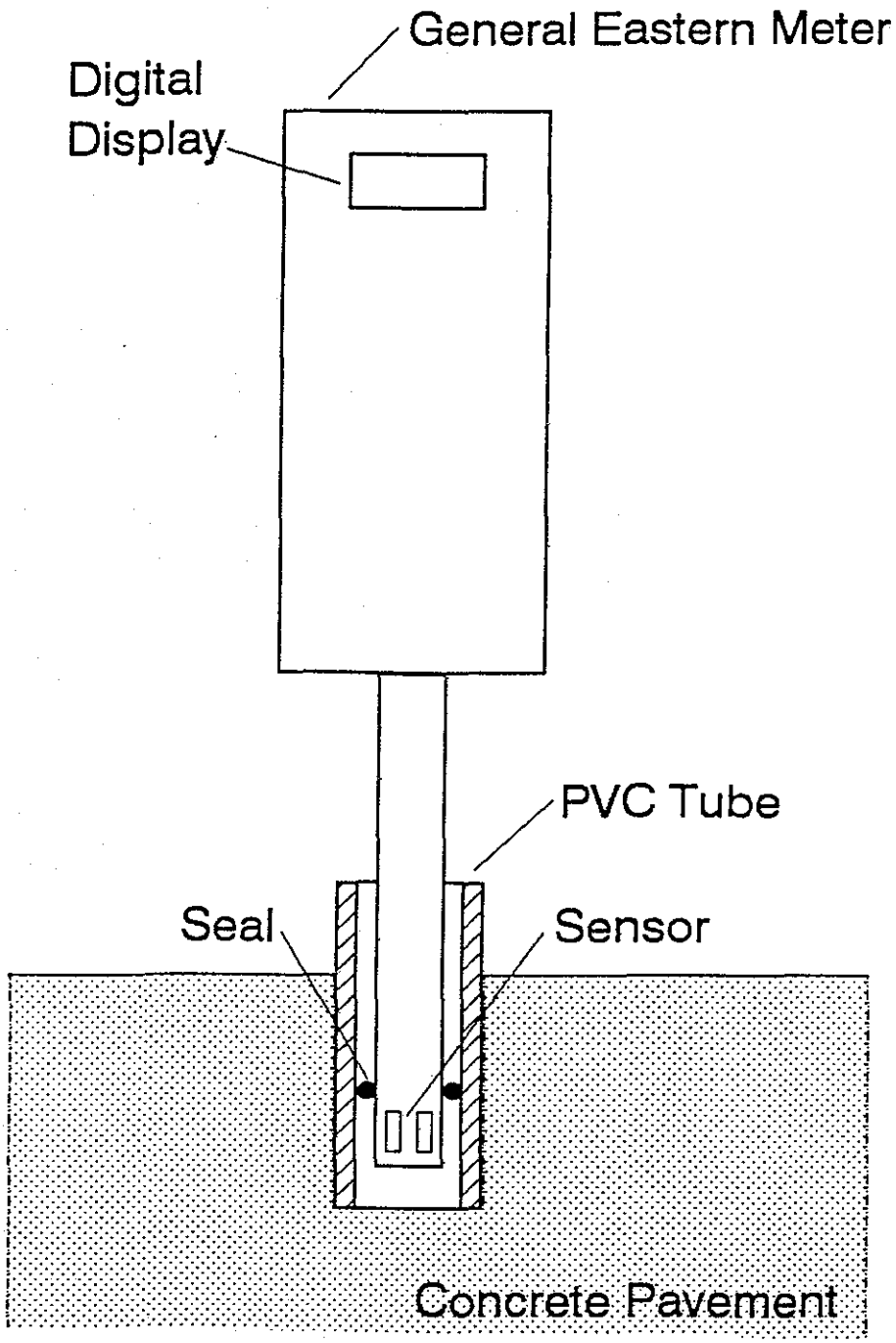

Fig. 1.16. Sketch of the Setup for Relative Humidity Measurement in Concrete.

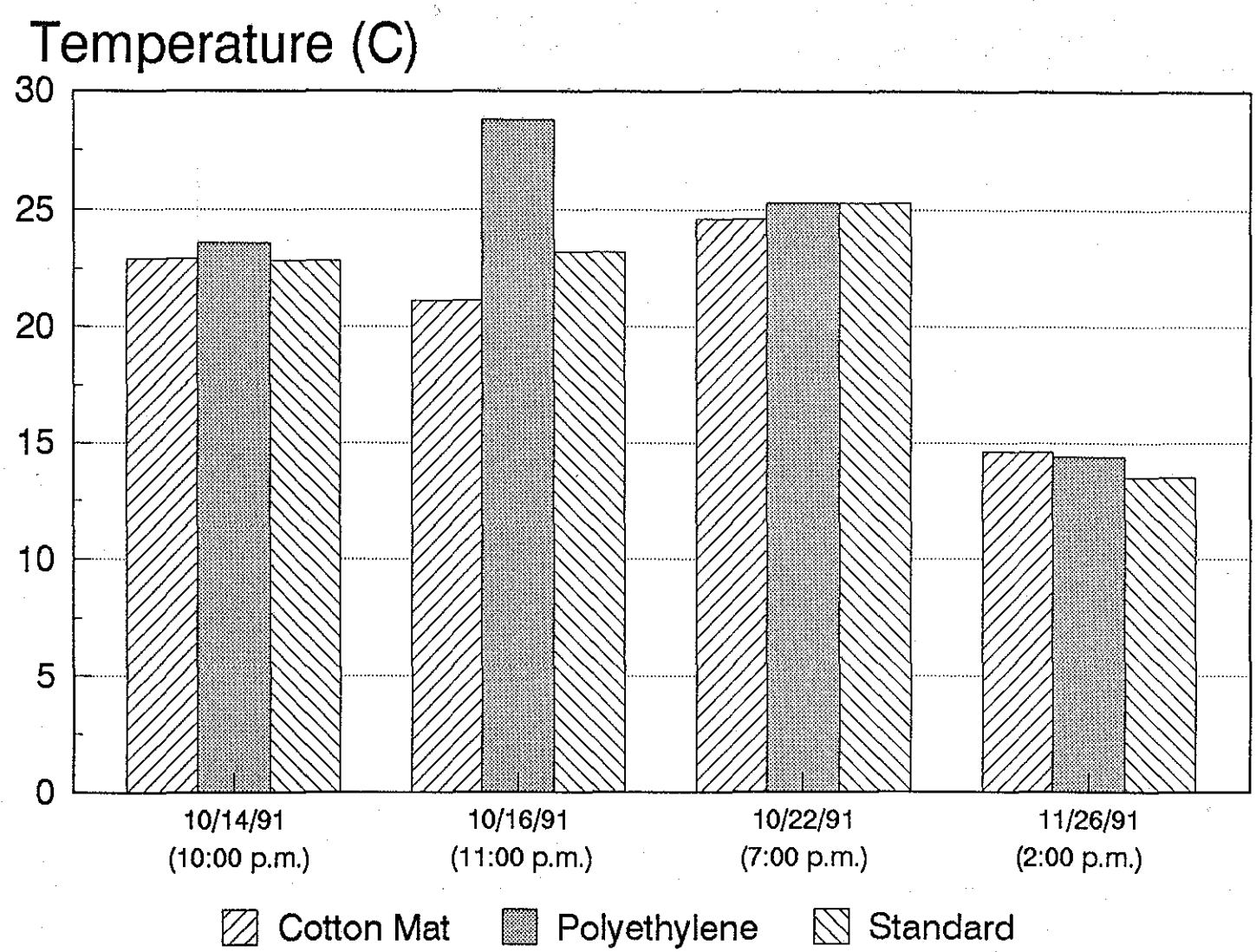

Fig. 1.17. Temperatures in Concrete (Mix Design 3, Paved on October 14, 1991).

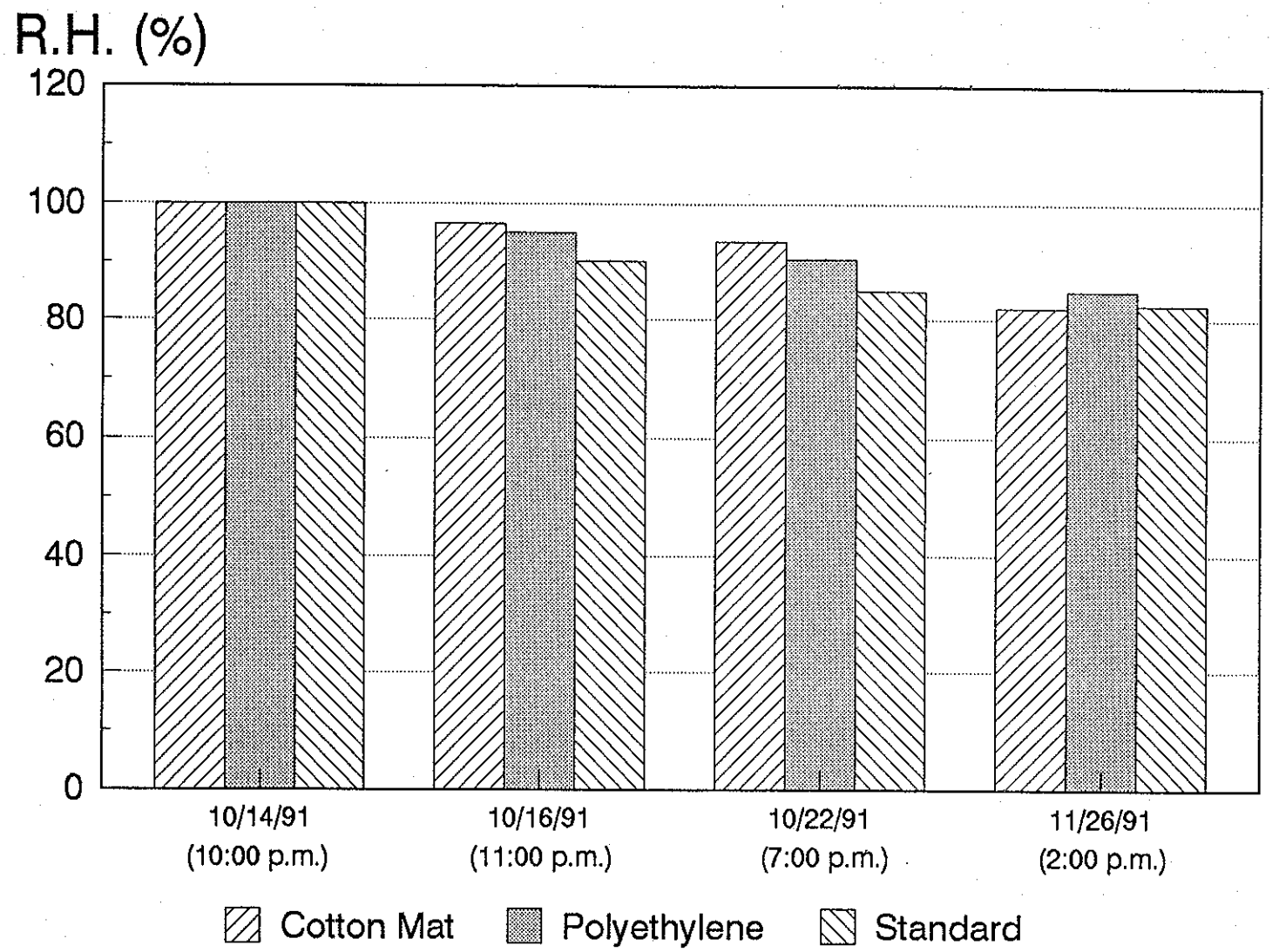

Fig. 1.18. Relative Humidity in Concrete (Mix Design 3, Paved on October 14, 1991).

figures. It is speculated that the pavement covered by the cotton mat obstructed solar radiation and resulted in a lower pavement temperature as compared with the pavement cured with the standard method. The pavement section covered with polyethylene film was subjected to a "greenhouse" effect, which made the temperature in the pavement higher than in the pavement cured with the standard curing method. On the other hand, the relative humidity in the pavement cured with the cotton mat method and the polyethylene method was higher than in the pavement cured by the standard curing method. This was because the cotton mat and the polyethylene film isolated the pavement top surface from the atmosphere and kept the moisture in the pavement from evaporating. The differences between the temperatures and relative humidities in the pavements cured with the three different methods decreased after approximately 30 days. The cotton mat and polyethylene film remained in place on the pavements for seven days after pavement construction. The differences in temperature and relative humidity caused by different curing methods in the test section of Mix Design 2, placed on November 8, 1991 (Figs. 1.19 and 1.20), showed similar trends observed in the test section of Mix Design 3.

In the test section of Mix Design 4, a different trend in temperature is observed in Fig. 1.21. In the first two days, the temperature in the pavement covered by cotton mat was the highest of all the curing test sections. On the third day, temperatures in the pavement sections covered by cotton mat and polyethylene film were lower than pavement sections cured with the standard method. This may have been caused by an increase in the ambient temperature which occurred from October 22 to 25 (Fig. 1.10). In the previous two cases (Mix Designs 2 and 3), ambient temperatures tended to decrease from those which occurred during the paving with these mixes. The pavement cured with the standard method may have absorbed more solar radiation thereby affecting the temperatures in the pavement. There was no apparent difference in the relative humidity with respect to the curing method (Fig. 1.22). However, by the third day, the relative humidity in the test sections covered by either cotton mat or polyethylene film was higher than the relative humidity in the test sections with the standard curing method. As far as the proprietary-product method, higher pavement

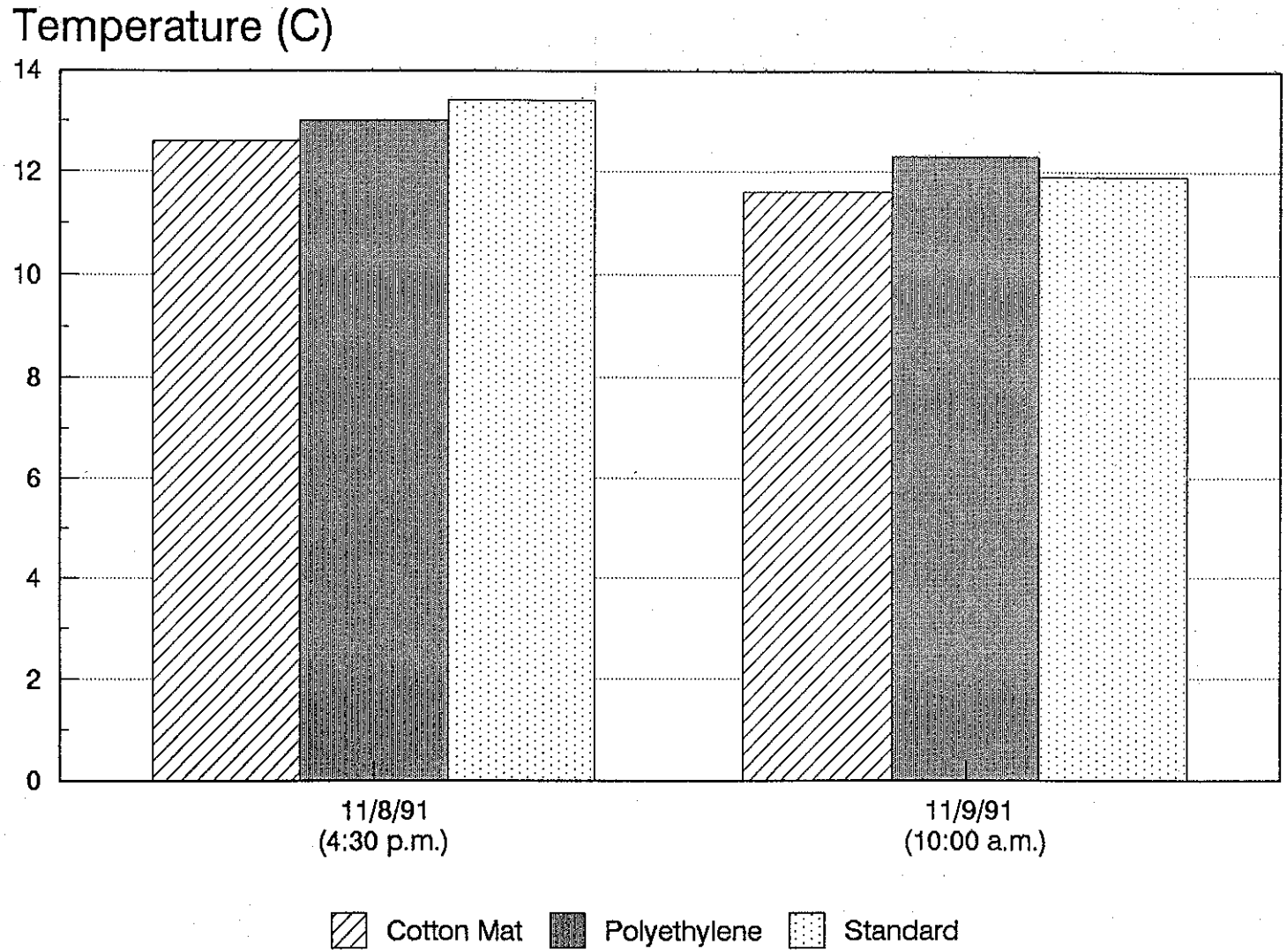

Fig. 1.19. Temperatures in Concrete (Mix Design 2, Paved on November 8, 1991).

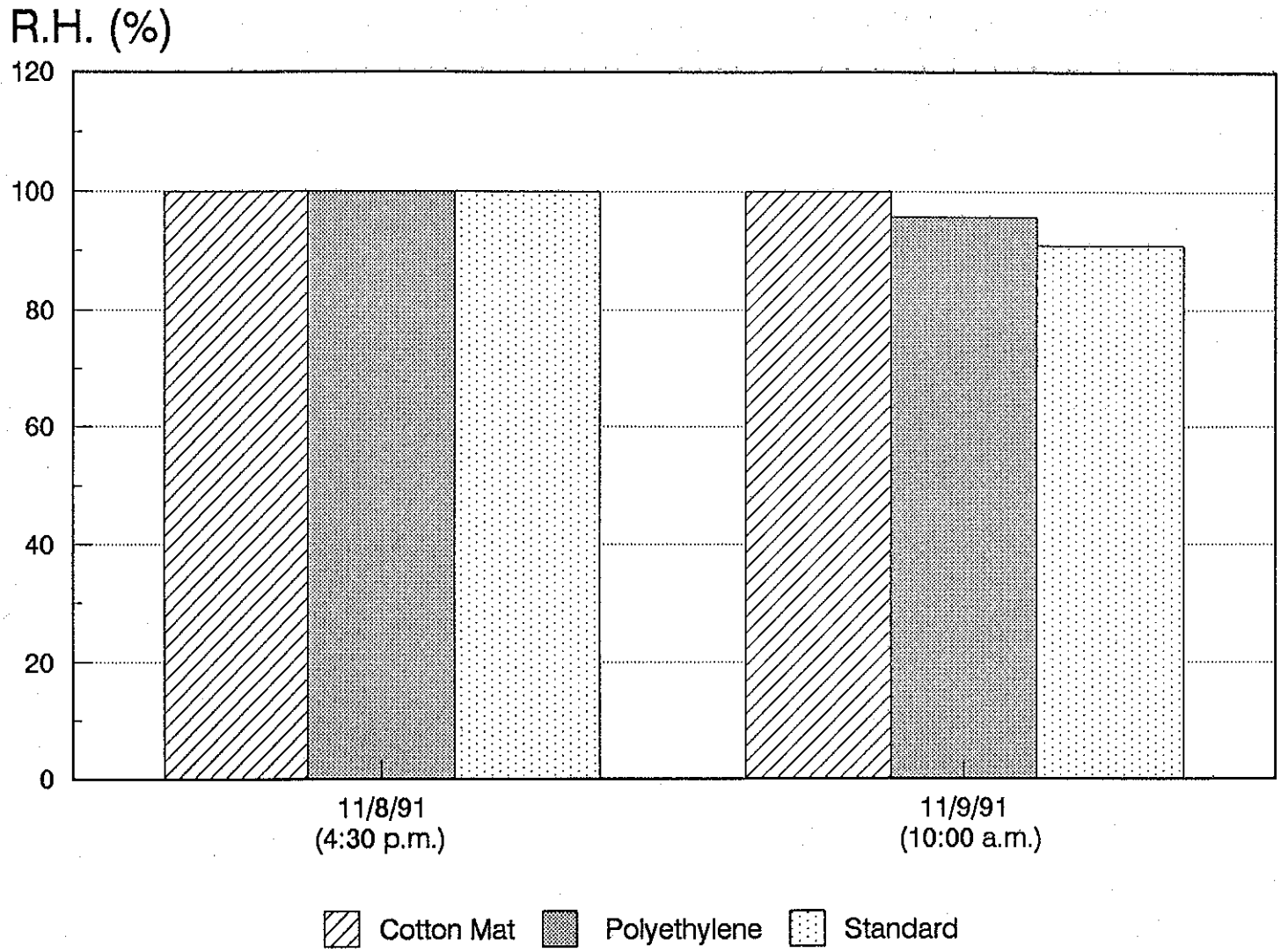

Fig. 1.20. Relative Humidity in Concrete (Mix Design 2, Paved on November 8, 1991).

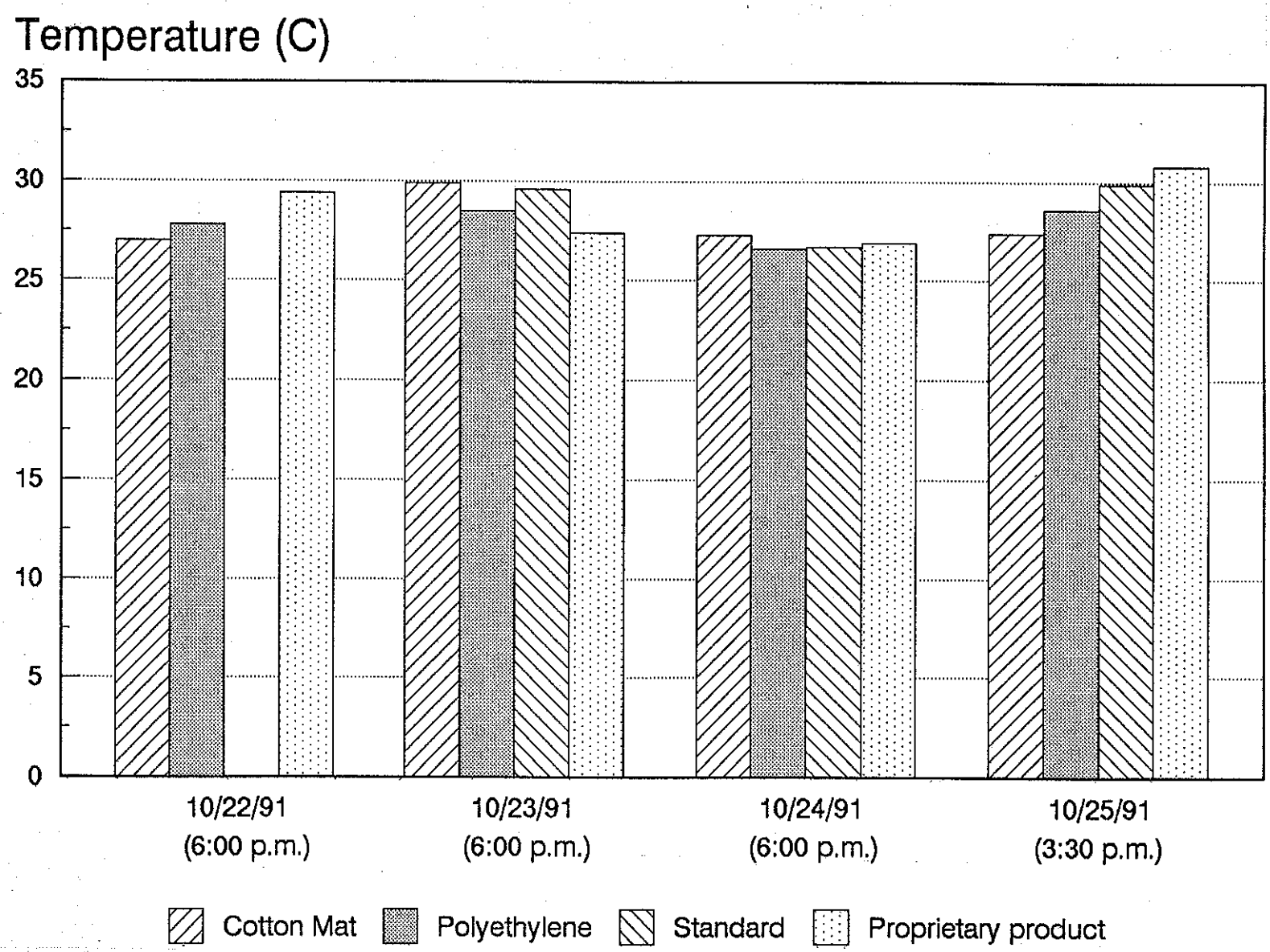

Fig. 1.21. Temperatures in Concrete (Mix Design 4, Paved on October 22, 1991).

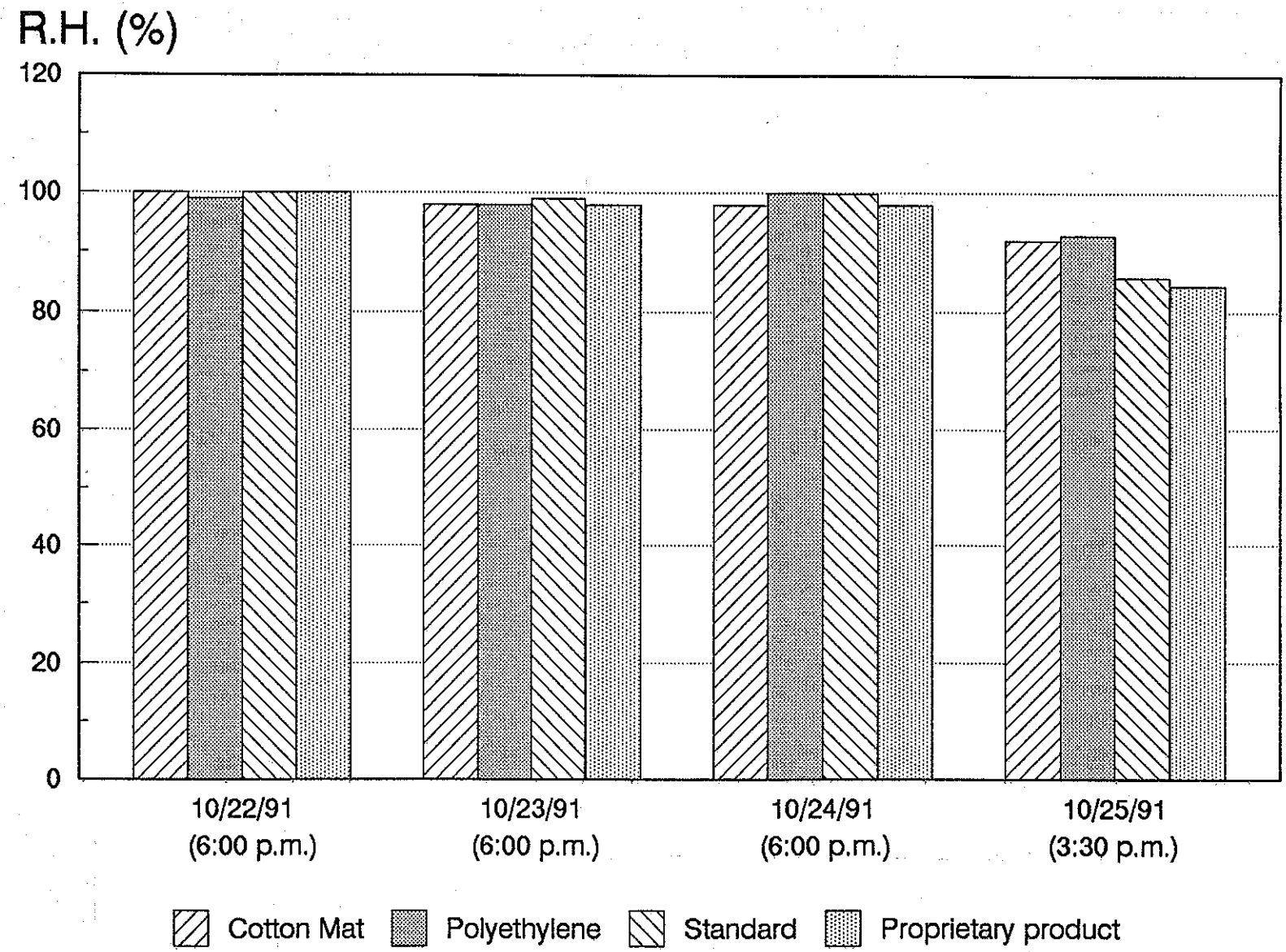

Fig. 1.22. Relative Humidity in Concrete (Mix Design 4, Paved on October 22, 1991).

temperature and lower relative humidity occurred on the third day than those in the pavement sections cured with the standard method.

The test section consisting of Mix Design 5 was placed on October 26, 1991, after which construction delays occurred due to rainfall which continued through November 6. Another test section of Mix Design 5 was placed on November 6, 1991. The test section of Mix Design 1 was placed on October 16, 1991.

1.8. MEASUREMENT OF PULSE VELOCITY OF PAVEMENT

The basic idea behind the pulse velocity method is: Given the velocity of a longitudinal wave through a medium and the density and Poisson's ratio of the medium, then the dynamic modulus of elasticity of the medium can be computed. Furthermore, knowing the modulus of elasticity, other mechanical properties can be estimated from empirical correlation with the dynamic modulus of elasticity.

Pulse velocity measurements in test sections of Mix Designs 2, 3, 4 and 5 were performed. Previous research had indicated that temperature and moisture conditions of the concrete had insignificant effects on the pulse velocity readings.

The V-Meter, a portable ultrasonic testing unit, was provided by the Federal Highway Administration (FHWA) and used in the test sections to measure the pulse velocity. The V-Meter uses transducers, each for transmitting and receiving the ultrasonic pulse. The pulse travel time is displayed in three numerical digits ranging from 0.1 to 999 micro-seconds. In the test sections, the two transducers were placed on the pavement top surface, 12 inches (305 mm) apart from each other. Grease was used to improve the contact between the transducer end surface and the pavement surface. The pulse velocity was simply obtained by dividing the distance between the two transducers, 12 inches (305 mm), by the recorded pulse traveling time, and then multiplied by a factor 1.05. The factor 1.05 was a compensation for the pulse travelling distance since the pulse path was not along a straight line (Fig. 1.23). This technique was also applied in the field test in La Porte (Section 2.6).

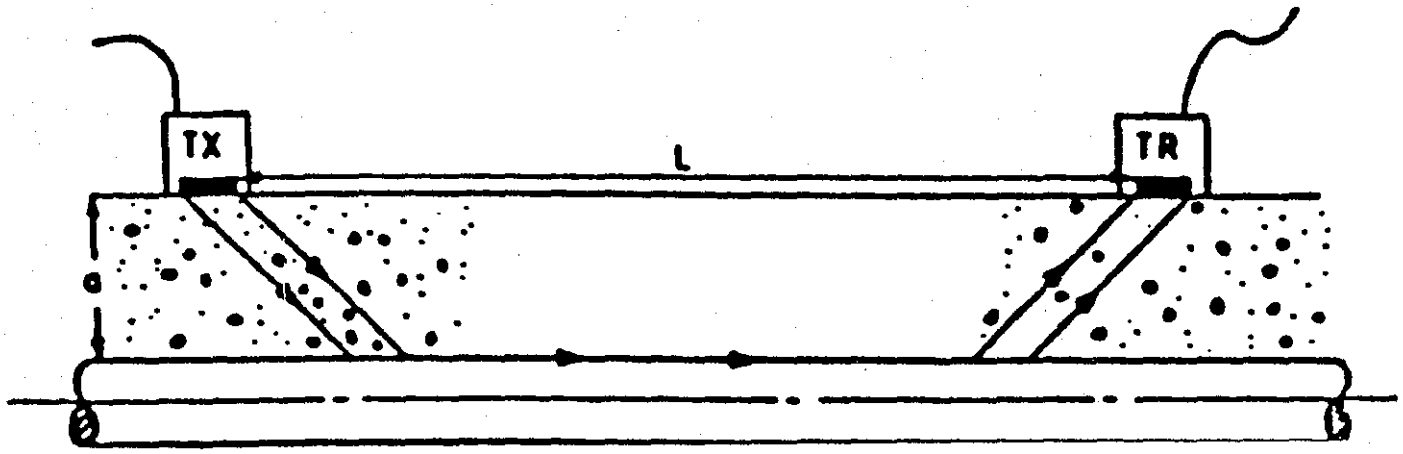

Fig. 1.23. Pulse Traveling Path in the Pulse Velocity Measurement.

Measurements show that the pulse velocity increased rapidly in the first days after concrete was paved. For example, Fig. 1.24 shows changes in the pulse velocity in the test section of Mix Design 5 paved on October 26, 1991. The origin of the time scale in the figure is the time of pouring for the part where measurements were performed, that is, 10:00 a.m., October 26. It is apparent that the pulse velocity increased even more in the first several hours than at later ages, which reflects the fact that the strength of concrete increases at a greater rate in the early ages. The pulse velocity was correlated with early-aged sawcutting operations. These values ranged from 4.38×10^4 inches/sec or 3650 feet/sec (1110 m/sec) in the concrete cured with the polyethylene method, and 5.5×10^4 inches/sec or 4580 feet/sec (1400 m/sec) in the concrete cured with the proprietary product. No apparent ravelling occurred along the dry sawcuts.

1.9. ANALYSIS OF SPECIMENS CORED FROM THE PAVEMENT

Specimens of four inches (102 mm) in diameter were cored from pavement of different mix design test sections on February 20, 1992. The coring locations are all noted in Figs. 1.1 to 1.8. These specimens were observed and tested for the following engineering properties and features: (a) Honeycombing, (b) Compressive Strength, (c) Elastic Modulus, and (d) Split Tensile Strength.

To explain honeycombing, an index has been developed called as "level of honeycombing." Level of honeycombing is defined in terms of size and spacing of air pockets in concrete. The smallest air pocket considered is an elongation of 1/8 inch (3.2 mm). The different severity levels of honeycombing, which are somewhat subjective in natures are given in Table 1.5.

Measuring elongation and spacing of air pockets can be done by linear traversing, but specifying the common spacing is difficult as air pockets are scattered randomly in the concrete body. In most of the cored specimens, the maximum elongation of air pockets is 1/2 inch (12.7 mm). For these specimens, severity of honeycombing can be described in terms of spacing of the air pockets as follows:

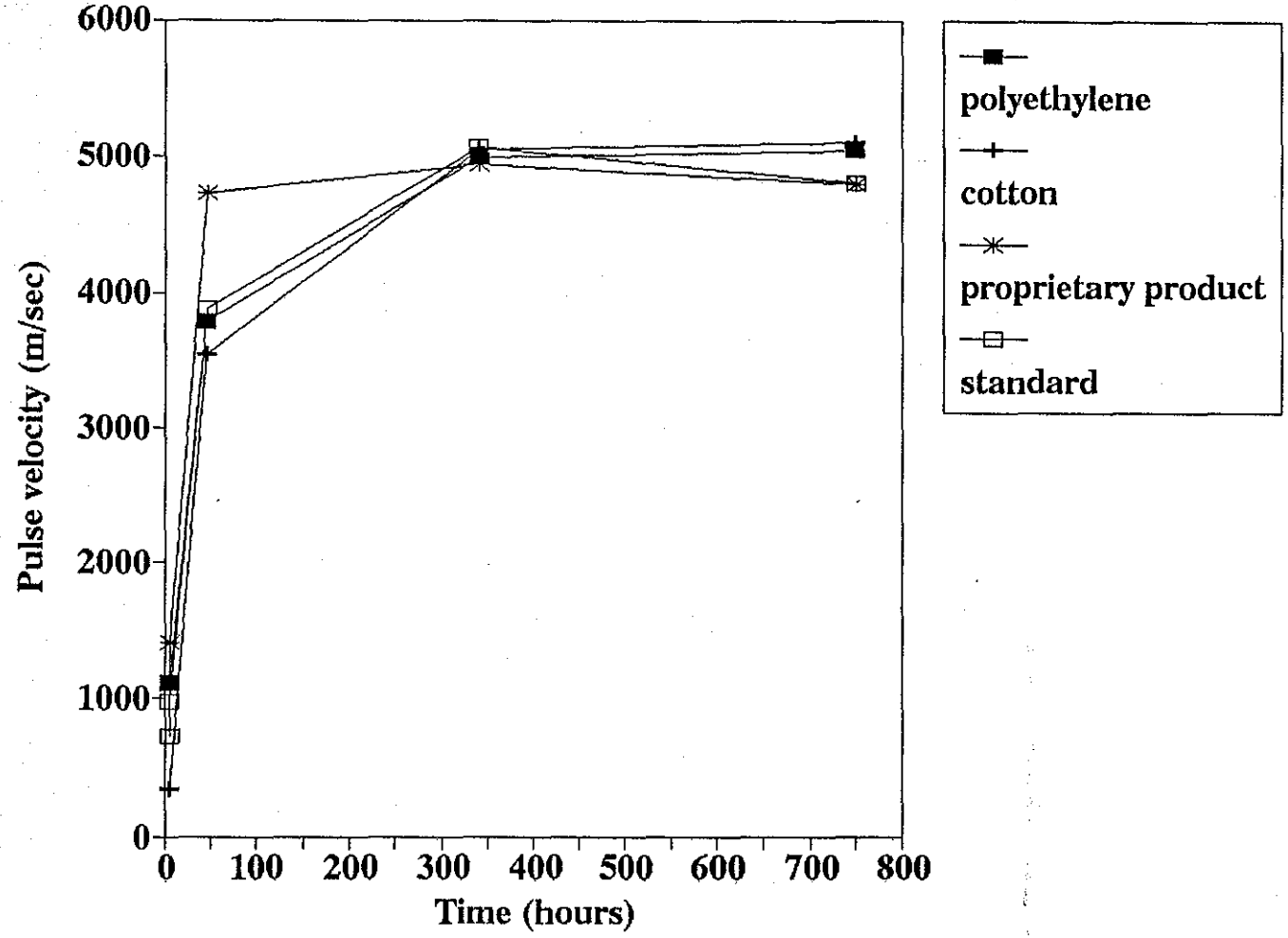

Fig. 1.24. Pulse Velocities in the Test Section of Mix Design 5 (Paved on October 26, 1991).

Table 1.5. Criteria for Level of Honeycombing.

Level of Honeycombing	Severity
A	low (small air pockets)
B	moderate (small air pockets)
C	high (small air pockets)
D	very high (small air pockets)
I	very high (large air pockets)

Level of Honeycombing A - indicates presence of air pockets with a spacing of 2 inches (50.8 mm) or more which is consistently distributed.

Level of Honeycombing B - indicates presence of air pockets with a spacing of 1/2 - 1 inch (12.7 - 25.4 mm) which is sparsely distributed.

Level of Honeycombing C - indicates presence of air pockets with a spacing of 1/2 inch (12.7 mm) which is less densely distributed than level D.

Level of Honeycombing D - indicates presence of air pockets very closely distributed with a consistent spacing as small as 1/4 inch (6.4 mm).

In the cored specimens of Mix Design 1, elongation of air pockets is very large. The maximum elongation is near 1 inch (25.4 mm), and spacing is as large as 1 - 2 inches (25.4 - 50.8 mm). It may be because of lack of intermediate aggregates. A description of this honeycombing case is provided below:

Level of Honeycombing I - indicates presence of large air pockets up to 1 inch (25 mm) long, with a spacing of 1 - 2 inches (25.4 - 50.8 mm), which is sparsely distributed. In terms of percentage of air pockets over the lateral surface of the cored specimen, severity of Level 1 may be equivalent to Level C or Level D.

Level of honeycombing of cored specimens taken from each mix design is listed in Table 1.6.

One cored specimen of each mix design was tested for the compression strength on July 2, 1992. The 13-inch (330 mm) long core was cut at both ends with a diamond saw to make the specimen 12 inches (305 mm) long. The specimen was capped before

testing. The compressive strength of each tested specimen is tabulated in Table 1.7. Note that the diameter of the specimen was 4 inches (102 mm) rather than six inches (152 mm). If specimens had been 6 inches (152 mm) in diameter, strength values obtained from the tests may have been different from the values shown in the table. Young's moduli, shown in Table 1.7, are estimated values with the formula $E = 57{,}000\ (f'_c)^{1/2}$, where E is Young's modulus in psi, and f'_c is the compressive strength in psi.

Table 1.6. Level of Honeycombing of Cored Specimen of Each Mix Design.

Design No.	Level of Honeycombing	Severity and Remarks
1	I	Very High
2	C	High
3	D	Very High
4	B	Medium
5	A	Low

Table 1.7. Compressive Strength of Cored Specimen.

Mix Design	Paving Date (Age)	Coring Location	Compressive Strength	Young's Modulus
1	10-16-91 (26 days)	on J23 (Fig. 1.2)	6030 psi (41.6 MPa)	4430 ksi (30.5 GPa)
2	11-8-91 (237 days)	between J1 and J2 (Fig. 1.7)	5540 psi (38.2 MPa)	4240 ksi (29.2 GPa)
3	10-14-91 (262 days)	between J4 and J5 (Fig. 1.1)	6490 psi (44.7 MPa)	4590 ksi (31.6 GPa)
4	10-22-91 (254 days)	between J4 and J5 (Fig. 1.8)	5310 psi (36.6 MPa)	4150 ksi (28.6 GPa)
5	10-26-91 (250 days)	between J4 and J5 (Fig. 1.5)	6080 psi (41.9 MPa)	4440 psi (30.6 GPa)

Although Mix 2 showed higher compressive strengths than the other mixes at ages of three days and five days in the lab tests (Fig. 1.9), the cored specimen of Mix 2 had a lower compressive strength than Mixes 1, 3 and 5 due to the level of honeycombing that was evident in this mix.

For Mixes 1, 2, 3, and 5, split tension tests were performed on July 8, 1992. The cored specimens were cut with a diamond saw into three or four 3-inch (76 mm) thick cylindrical specimens. The split tensile strengths of these specimens are shown in Table 1.8.

Table 1.8. Split Tensile Strength of Cored Specimen.

Mix	Paving Date	Coring Location	Location of Split Tension Specimen from Top Surface of Pavement	Split Tensile Strength
1	10-16-91	between J16 and J17	0-3" (0-76.2 mm)	595 psi (4.10 MPa)
			3-6" (76.2-152 mm)	613 psi (4.23 MPa)
			6-9" (152-229 mm)	681 psi (4.70 MPa)
			9-12" (229-305 mm)	725 psi (5.00 MPa)
2	10-22-91	on J3	1.5-4.5" (38-114 mm)	613 psi (4.23 MPa)
			4.5-7.5" (114-191 mm)	706 psi (4.87 MPa)
			7.5-10.5" (191-267 mm)	722 psi (4.98 MPa)
3	10-14-91	on J6	1.5-4.5" (38-114 mm)	738 psi (5.09 MPa)
			4.5-7.5" (114-191 mm)	780 psi (5.38 MPa)
			7.5-10.5" (191-267 mm)	840 psi (5.79 MPa)
5	10-26-91	between J5 and J6	0-3" (0-76.2 mm)	645 psi (4.45 MPa)
			3-6" (76.2-152 mm)	730 psi (5.03 MPa)
			6-9" (152-229 mm)	803 psi (5.54 MPa)

Data shown in Table 1.8 indicate that the tensile strength of concrete increases with the depth in the pavement. These data are plotted in Fig. 1.25. The distance of

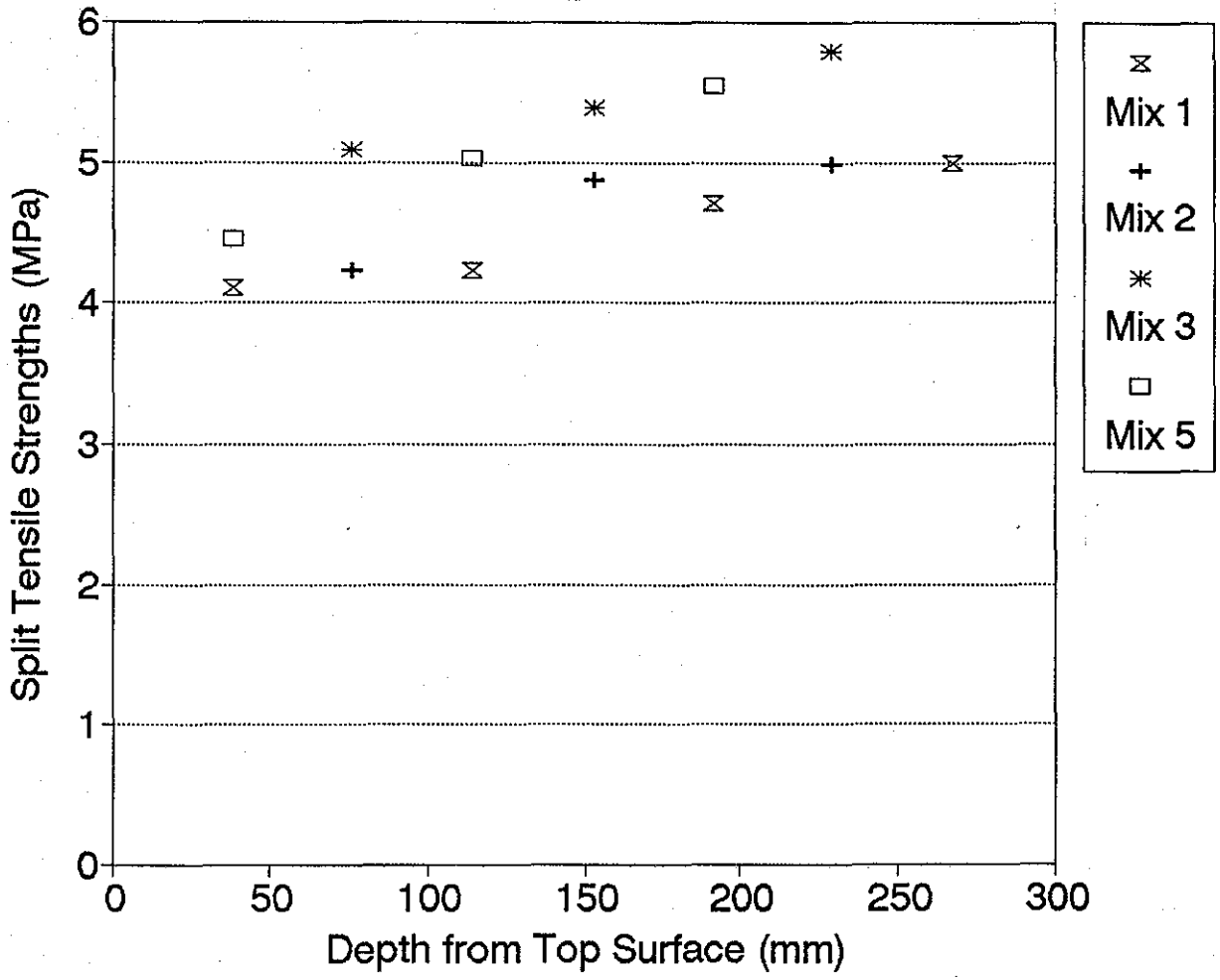

Fig. 1.25. Split (Indirect) Tensile Strengths of Cored Specimens at Different Depths in Concrete Pavement.

the midpoint of the split tension specimen from the top surface of the pavement is taken as the depth of the specimen, which is noted as the horizontal coordinate in Fig. 1.25.

1.10. CRACK SURVEY - OBSERVATION OF FORMATION OF JOINTS BY SAWCUTTING

All the sections were surveyed on October 16, November 10 and 26, and December 19 in 1991, and January 8, February 20, June 4, and July 13 in 1992 to observe the formation of joints, which were transversely sawcut after paving. All these surveys were conducted before the sections were open to traffic on July 17, 1992. Every observed crack that occurred from the sawcut tip and developed downward has been noted in the layout of the sections shown in Figs. 1.1 to 1.8. The date shown near a crack (or a formed joint) is the date the crack was first observed. Construction joints were constructed with dowel bars at the energy bulkhead, where paving terminated.

Cracks at the sawcut locations are desired and are considered to be controlled cracks. Two transverse uncontrolled cracks were observed during the survey of November 10, 1991. Although these two uncontrolled cracks occurred in sections that were constructed of Mix Design 5 (in which crushed limestone was used as the coarse aggregate), both cracks initiated from the corner of drainage blackouts where stress concentration existed. If the joint labeled number 38 (Fig. 1.4) had been cut at the station 250 + 91 instead of the station 250 + 98 or the blockout had been designed so that its corner were located at the station 250 + 98 instead of the station 250 + 91, the uncontrolled transverse crack may not have occurred. Also, the uncontrolled transverse crack shown in Fig. 1.5 may have been avoided if Joint 9 had been designed at the station 249 + 02.48. Therefore, it is recommended that joint layouts be reversed on future projects in light of the above observations.

A longitudinal uncontrolled crack was inspected in the survey of July 13, 1992 (Fig. 1.6). It is located in the section of Mix Design 5 paved on November 6, 1991. Parallel to the crack is a longitudinal sawcut made with the conventional sawcut technique. It has not been determined what caused this crack; however, late cutting has been the cause of problems similar to this in the past.

The development of the transverse cracking at the sawed joint locations is described in Fig. 1.26 in terms of the percentage of sawcuts which cracked. Some portions of the pavement edges were backfilled and were unobservable since November 19, 1991 (Figs. 1.2, 1.3, 1.4 and 1.7). Consequently, these joints are not included in the percentages shown in Fig. 1.26. Of all the sawcuts adjacent to a construction joint, only Joint 10 in Fig. 1.1 has developed a crack. This particular joint is 15 feet (4.6 m) (designed transverse joint spacing away) from the construction joint, (Joint 11) while all other sawcuts adjacent to construction joints are less than this. The shorter the distance from a planned joint to the end of paving, the less the restraint provided to induce stresses at the joint location. It is suggested that, with certain limits, construction joints may replace planned sawcut joints. Due to the lack of restraint, those sawcuts less than 15 feet (4.6 m) from the construction joint were also not included in the percentages shown in Fig. 1.26. Joints 7 to 12 in a section of Mix Design 4 (Fig. 1.8) were not included in the analysis either because the area around these joints was paved in December 1991, and a cracking observation has been impossible since then.

As seen in Fig. 1.26, in sections of concrete using river gravel as the coarse aggregate (Mix Designs 1, 3 and 4), transverse joints (controlled cracks) showed a greater likelihood of formation than the concrete using crushed limestone as the coarse aggregate (Mix Design 5). It is also noted that including river gravel in a blend with limestone significantly affects the potential for crack development at the joint location. The potential for crack development can be evaluated quantitatively with the brittleness number of the pavement at the early ages of concrete as discussed previously shown (Fig. 1.15). Of all the mix designs where only river gravel was used as the coarse aggregate (Mix Designs 1, 3 and 4), improved aggregate gradation in Mix Designs 3 and 4 made cracking more probable than the control mix, Mix Design 1. In the section of Mix Design 5 paved on October 26, 1991, only one uncontrolled transverse crack has been observed. Perhaps the weather conditions during and after paving played a role in suppressing the development of stresses in pavement. A period of abnormal weather began on October 27 in Texarkana when it rained for ten days. Paving did not begin again until November 6. The rain may have reduced temperature change, blocked

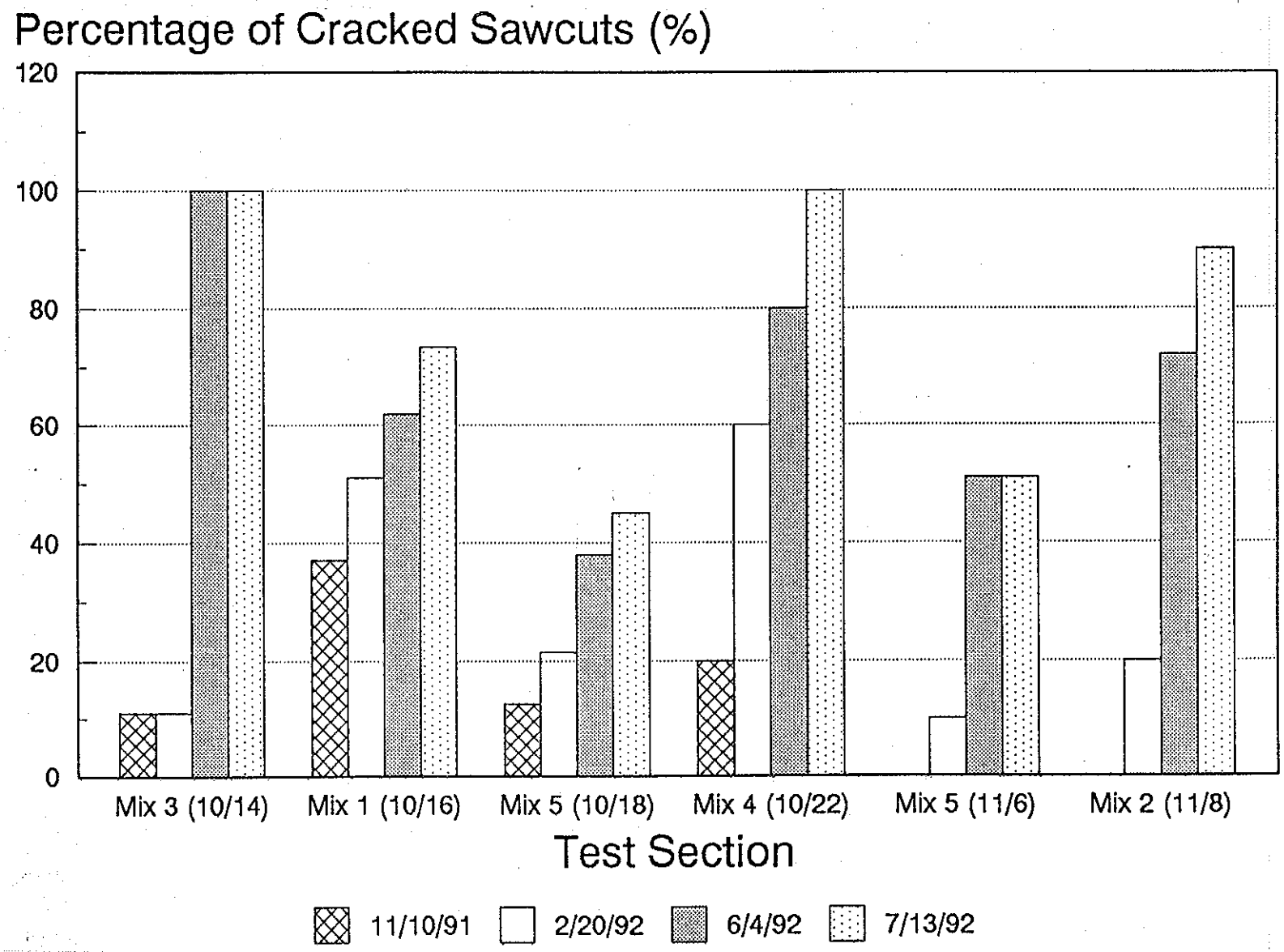

Fig. 1.26. Percentage of Cracked Sawcuts Observed on Different Dates.

drying of concrete, and slowed down the hydration of concrete. As a result, small stresses were induced.

It is interesting to note that the first cracking occurred approximately in the middle of a one-day placement. The typical examples can be seen in the section of Mix Design 3, paved on October 14, 1991 (Fig. 1.1), and the section of Mix Design 5, paved on November 6, 1991 (Fig. 1.6). It is understood that, in the middle of a pour, stresses caused by curling and friction are larger than elsewhere. Cracks did not grow simultaneously at every sawcut in the same section but appeared to develop gradually on a random basis. The cracks which formed early opened widely, such as those cracks observed in 1991. These widely-opened cracks may have lessened the restraint of the pavement for stress development, not to mention the diminished load transfer efficiency at the widened joints. Joint openings should be monitored as additional cracking at other joints progresses to determine future distributions of the openings.

Percentage of cracked sawcuts on three different dates, February 20, June 4 and July 13, 1992, is shown in Figs. 1.27 to 1.29 as a function of sawcut type and mix design. Transverse sawcuts in the sections of Mix Design 4, paved on October 22, 1991 (Fig. 1.8), and of Mix Design 5, paved on November 6, 1991 (Fig. 1.6), were made with the early-aged technique. Therefore, data shown in Fig. 1.26 for these two sections are based on the early-aged sawcuts. (These data are not included in Figs. 1.27 to 1.29.) As of February 20, 1992, in two of the four sections referred to in Fig. 1.27 (Mixes 3 and 5), all of the observed cracks occurred at the early-aged sawcuts while in the other sections, Mix 1 and Mix 2, there were more cracks at the conventional sawcuts than at the early-aged sawcuts. As of June 4, 1992, in each of the four sections, there were more cracks at the early-aged sawcut than at the conventional sawcuts. More than a month later, on July 13, 1992, a greater number of conventionally made sawcuts had induced cracking than the early-aged sawcuts in sections in Mix Designs 1 and 2. Except for the section of Mix Design 5, percentages of cracked early-aged sawcuts and percentages of cracked conventional sawcuts showed no significant difference in performance as of July 13, 1992. The early-aged sawcut technique did not require a supply of water for blade cooling and probably will result

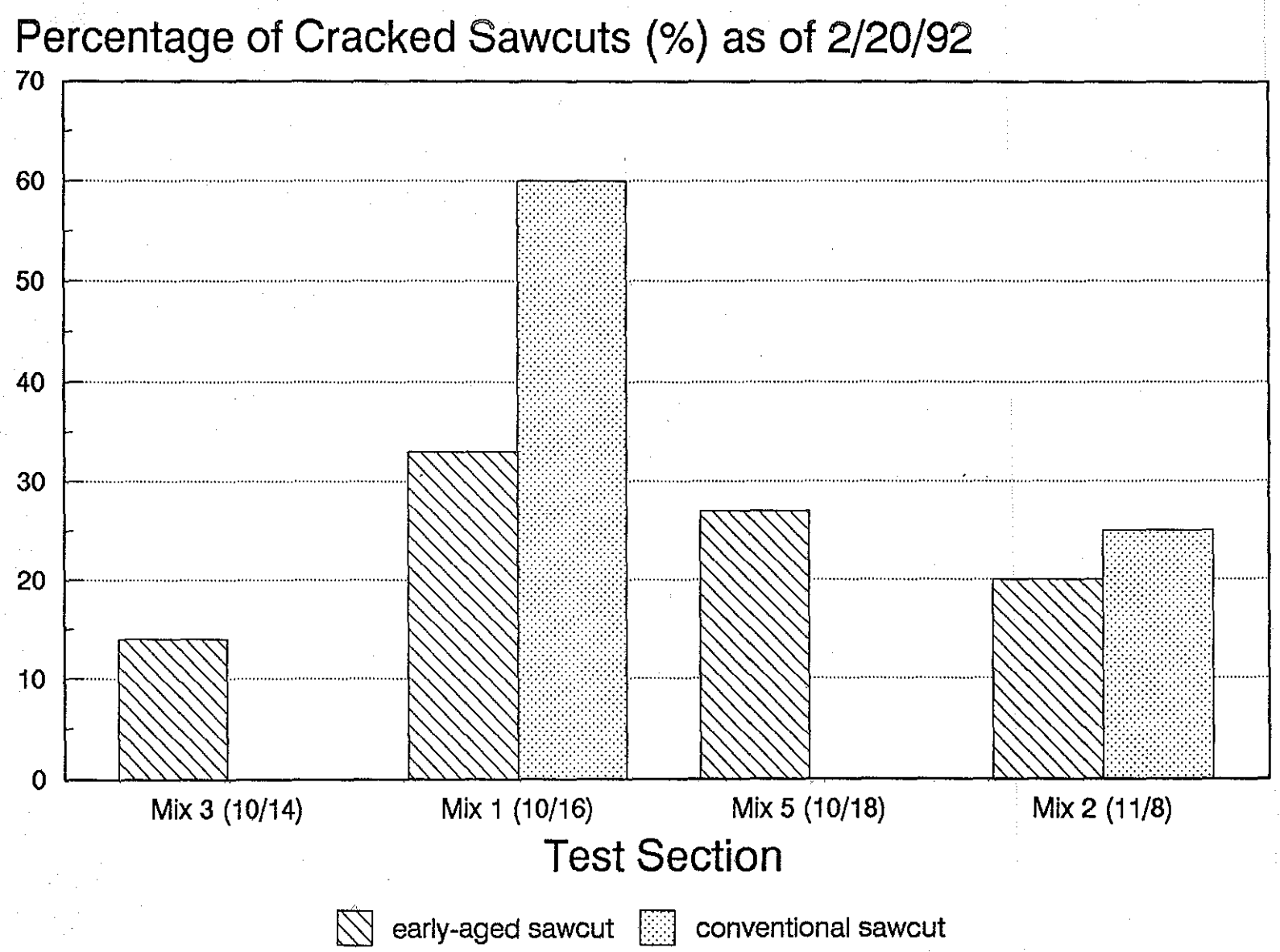

Fig. 1.27. Percentage of Cracked Sawcuts Observed on February 20, 1992.

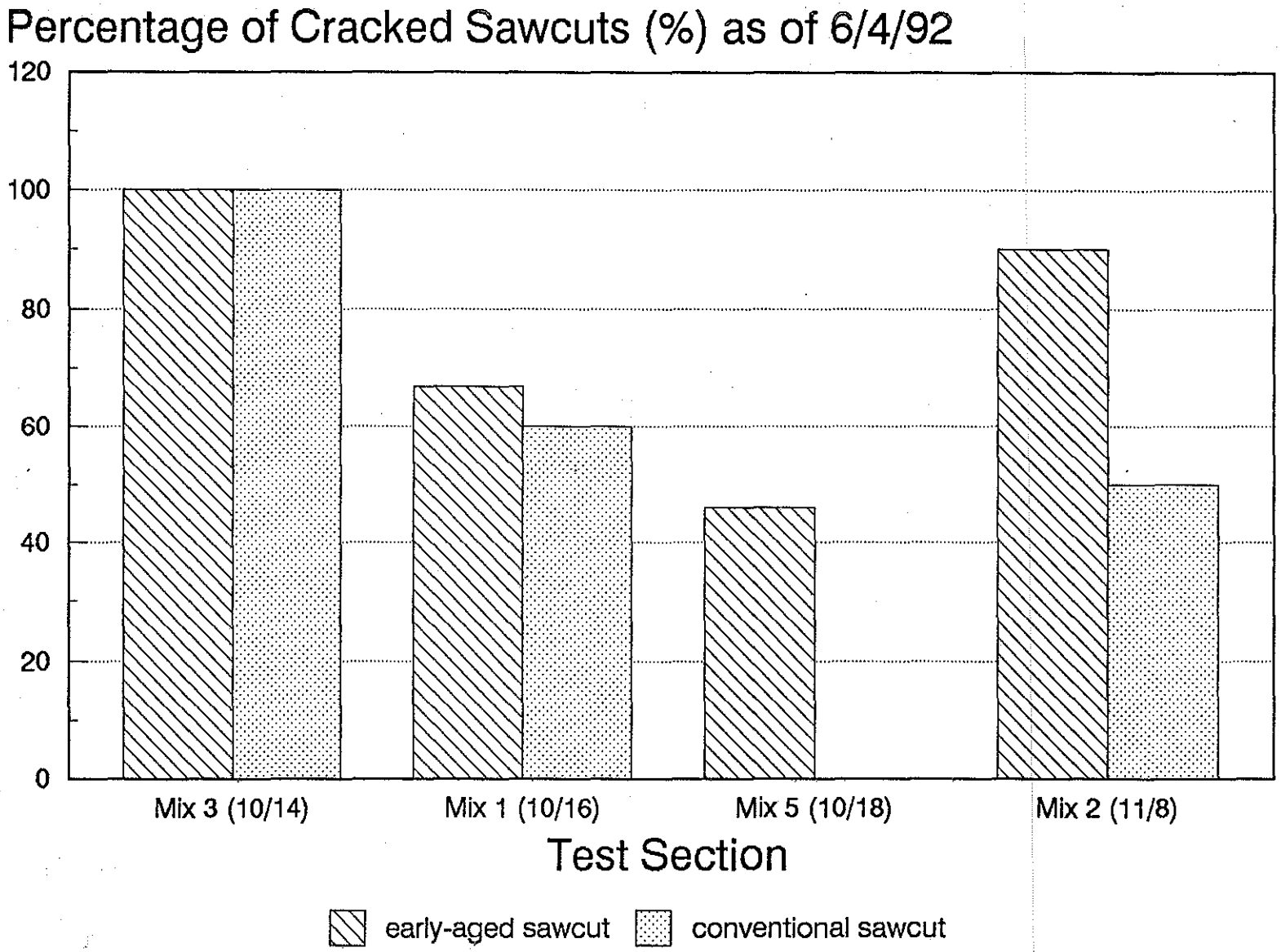

Fig. 1.28. Percentage of Cracked Sawcuts Observed on June 4, 1992.

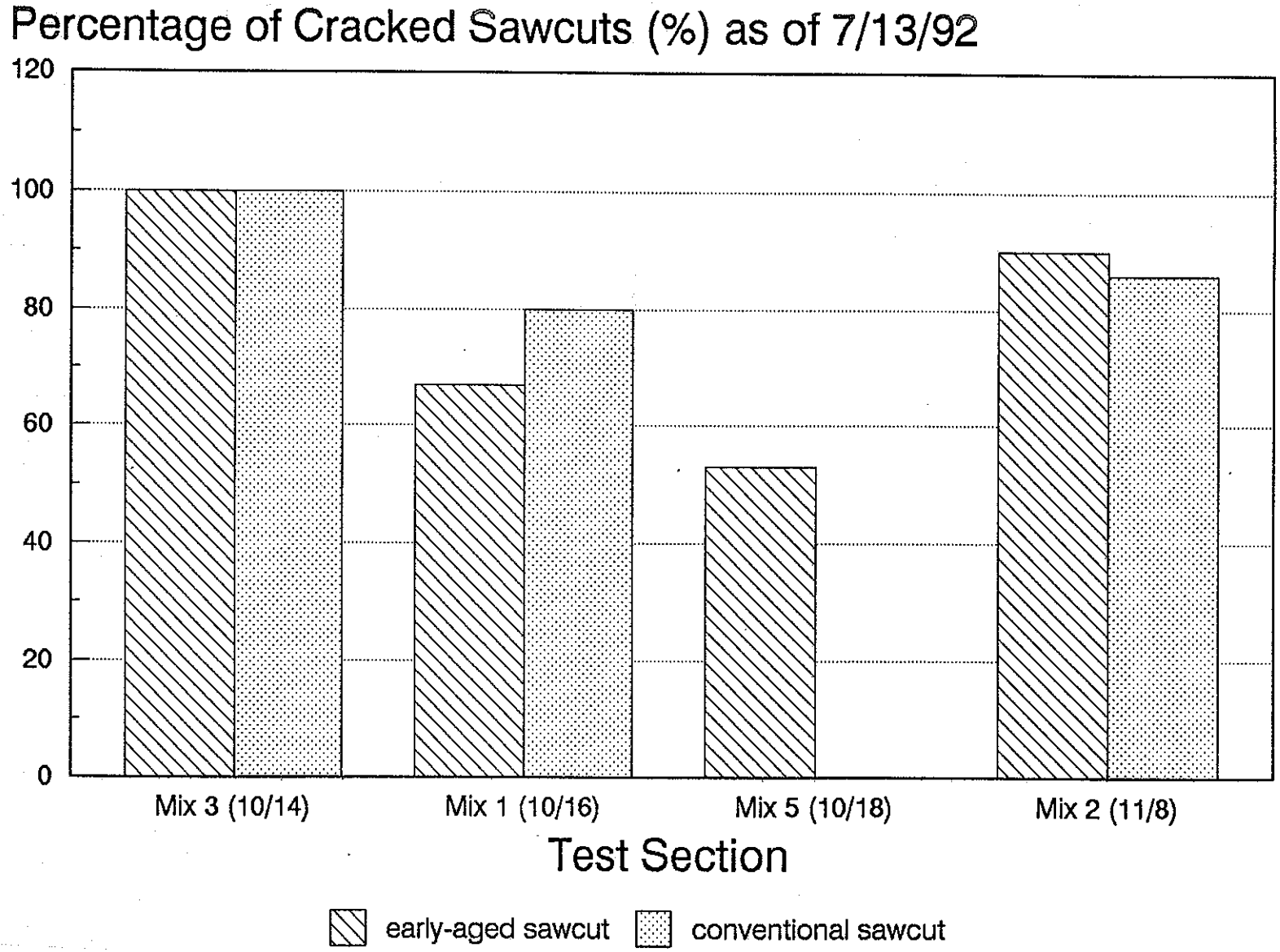

Fig. 1.29. Percentage of Cracked Sawcuts Observed on July 13, 1992.

in lower blade costs per foot. This method also provided a great deal of convenience in pavement construction. This technique can be recommended for joint sawcutting in jointed concrete pavement from the standpoint of performance noted in this project. It should also be noted that the weather conditions under which most of these test sections were placed were some of the most-stringent conditions as far as crack control is concerned. Improved curing techniques may enhance the performance of the early-aged sawcuts, but all things considered, this early-aged method did very well in controlling cracking in the pavement system.

1.11. FWD TEST MEASUREMENT OF LOAD TRANSFER EFFICIENCY AND EFFECTIVE MODULUS AT THE JOINTS

FWD (falling weight deflectometer) testing was conducted on several sawcut joints, construction joints and cracks on the morning of February 20, 1992. Locations of these joints and cracks are listed in the first column of Table 1.9. The testing equipment is a trailer-mounted FWD weighing approximately 1,500 pounds (6,670 N). The impulse force is created by dropping masses. The load, measured by a transducer, is transmitted to the pavement through a load plate having a radius of 5.9055 inches (150 mm). Deflections are measured by using velocity transducers mounted on a bar that is lowered simultaneously with the load plate to the pavement surface. The loading plate and deflection sensors layout is on 12-inch (304.8 mm) centers. Eight sensors are mounted on the bar. One of the sensors measures the deflection at the load, noted as D_0. Six sensors are on one side of the load at 12 inches (304.8 mm), 24 inches (609.6 mm), 36 inches (914.4 mm), 48 inches (1219 mm), 60 inches (1524 mm) and 72 inches (1829 mm) away from the load position. Deflection measured by these sensors is designated as D_1, D_2, D_3, D_4, D_5 and D_6, respectively. Another sensor is on the other side of the load, 12 inches (304.8 mm) away from load. It measures the deflection noted as D_{-1}.

The results of the FWD field measurements are described in terms of the load plate deflection (D_0), the load transfer efficiency (LTE), and the effective stiffness (E_c) at the joint. The LTE is equal to the change in deflection on the unloaded side of the

Table 1.9. Results of FWD Tests.

Station	Mix Design Number	Date of Paving	Type of Joint or Crack	Downstream LTE (%)	Upstream LTE (%)	Upstream Effective Stiffness
255+51.55	3	10-14-91	early-aged sawcut	88.89	No data	No data
254+61.3	3-5		construction joint	82.06	81.28	1154 ksi (7.957 GPa)
254+41.3	1	10-16-91	early-aged sawcut	81.06	78.18	568 ksi (3.916 GPa)
254+11.5	1	10-16-91	conventional sawcut	78.31	79.36	967 ksi (6.667 GPa)
253+96.3	1	10-16-91	conventional sawcut	80.20	78.00	571 ksi (3.937 GPa)
253+66.5	1	10-16-91	conventional sawcut	81.96	79.58	559 ksi (3.854 GPa)
252+18.0	5	10-18-91	early-aged sawcut	87.80	79.62	504 ksi (3.475 GPa)
251+73.0	5	10-18-91	early-aged sawcut	78.99	85.64	1845 ksi (12.72 GPa)
251+58.0	5	10-18-91	early-aged sawcut	84.16	80.34	776 ksi (5.351 GPa)
250+91.0	5	10-18-91	crack	67.15	82.58	974 ksi (6.716 GPa)
250+26.8	5		construction joint	81.05	79.64	770 ksi (5.309 GPa)
249+2.48	5	10-26-91	crack	84.69	81.09	819 ksi (5.647 GPa)
248+42.0	5		construction joint	79.39	82.91	1151 ksi (7.936 GPa)
247+41.7	5	11-6-91	early-aged sawcut	80.79	77.68	2694 ksi (18.58 GPa)
246+51.4	5-2		construction joint	87.11	78.14	998 ksi (6.881 GPa)
245+83.1	2	11-8-91	early-aged sawcut	85.97	89.28	1475 ksi (10.17 GPa)
245+53.1	2	11-8-91	early-aged sawcut	85.86	88.08	1788 ksi (12.33 GPa)
244+33.1	2	11-8-91	conventional sawcut	89.74	85.56	1433 ksi (9.881 GPa)
243+88.1	2	11-8-91	conventional sawcut	87.65	85.55	1252 ksi (8.633 GPa)
243+9.1	2-4		construction joint	87.17	87.35	1475 ksi (10.17 GPa)
242+74.6	4	10-23-91	early-aged sawcut	99.73	86.52	1384 ksi (9.543 GPa)
242+4.41	4	10-23-91	early-aged sawcut	92.92	87.44	1738 ksi (11.98 GPa)
241+31.6	4	10-23-91	early-aged sawcut	88.10	94.67	4208 ksi (29.01 GPa)

joint divided by the change in deflection on the loaded side of the joint. The effective stiffness E_c is determined from the Westergaard solution for slab-on-grade deflections at an interior load position. The simplified form of the Westergaard solution rearranged to solve for the modulus of subgrade reaction K (assuming Poisson's ratio $\mu = 0.15$ for concrete) is:

$$K = \frac{P}{8\, D_0 \ell_k^2} \left[1 - \left(\frac{a}{\ell_K}\right)^2 (0.217 - 0.367 \log\frac{a}{\ell_K}) \right] \tag{1.1}$$

where P is the applied load, a is the radius of the FWD load plate (150 mm), and ℓ_k is the radius of relative stiffness of the slab based on the area basin. It leads to

$$E_c = K(\ell_k)^4\ (11.73)/h^3 \tag{1.2}$$

where h is the pavement thickness and ℓ_k can be determined from the deflection basin area through the Westergaard solution or the computer program ILLISLAB.

The deflection basin area is defined as (Fig. 1.30).

$$\text{Area} = \frac{6}{D_0\,[D_0 + 2(D_1 + D_2) + D_3]} \tag{1.3}$$

The FWD was equipped with seven channels for deflection recording. Deflections D_{-1}, D_0, D_1, D_2, D_4, D_5, and D_6 were recorded in the FWD tests on the test sections. Since D_3 was not recorded, D_3 in Eq. (1.3) was replaced by $\frac{1}{2}(D_2 + D_4)$ in calculating the basin area.

In all the tests, the sensor for D_{-1} was on the downstream side of the joint or crack while the sensors for D_1 through D_6 were on the upstream side. Therefore, when the load acted on the upstream side of the joint or crack, the downstream LTE value was obtained as $LTD = D_1/D_0$. When the load was acted on the downstream side of the joint or crack, the upstream LTE was obtained as $LTD = D_{-1}/D_0$. The deflection basin area was determined when the load was placed on the upstream side of the joint or

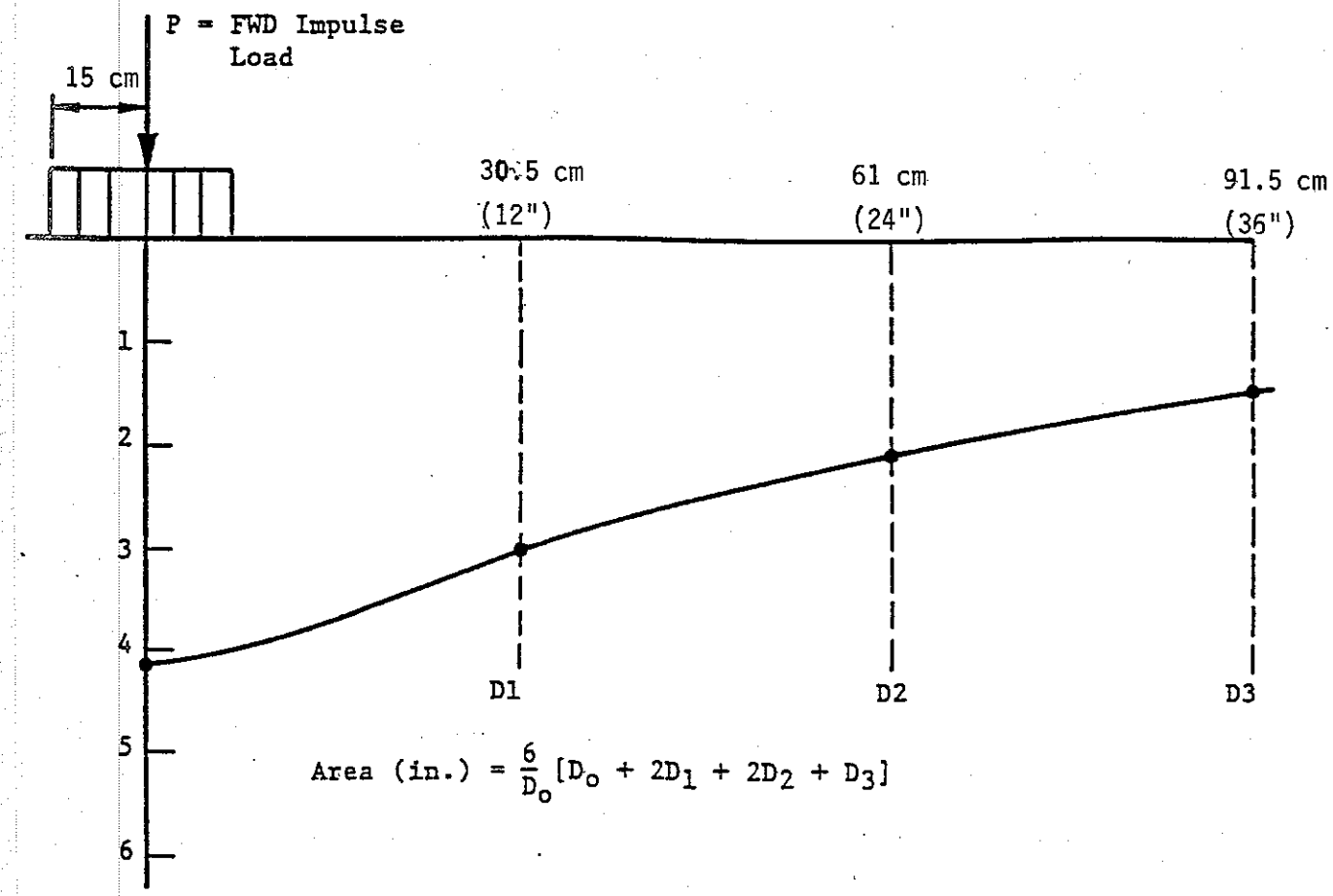

Fig. 1.30. Basin Area Measurement from FWD Test.

crack and then E_c was calculated with Eqs. (1.1) to (1.3). The E_c obtained represents an upstream datum of the effective stiffness.

All the LTE and effective stiffness values obtained from the FWD test are shown in Table 1.9. Fig. 1.31 shows the average LTE value as a function of the joint type or crack. Joints induced by the early-aged sawcut technique showed the highest average LTE values. Construction joints and cracks showed comparatively low LTE values. Average effective stiffness values for each type of joint and crack are displayed in Fig. 1.32, where the early-aged sawcut technique is shown to have caused higher effective modulus along the joint than the conventional sawcut technique. The differences in the average LTE and the average effective stiffness at the conventional sawcut and at the early-aged sawcut may be related to the average crack spacing. Since some portion of the pavement edges had been backfilled and were unobservable, the average crack spacing of those sections on February 20, 1992, was hardly calculated. However, only edges of two sawcuts in the section paved on November 8, 1991, were not backfilled (Fig. 1.7). Also in this section, about half the sawcuts were formed by the conventional sawcut technique and the rest were formed by the early-aged sawcut technique. Therefore, study of this section provides comparison of the effect of sawcut method on the average crack spacing. On February 20, 1992, two conventional sawcuts and two early-aged sawcuts had been cracked. FWD tests were performed at all four sawcuts. The average crack spacing of the conventional sawcuts on this date was 72.25 ft (22.02 m). The average crack spacing of the early-aged sawcuts on this date was 62.08 ft (18.92 m). On July 13, 1992, the average crack spacing of the conventional sawcuts was 26.75 ft (8.153 m) while the average crack spacing of the early aged sawcuts was 18.83 ft (5.739 m). Those cracks observed after February 20, 1992, may have been initiated inside the pavement before this date. Those existing but unobservable cracks also affected the measurements of the effective stiffness and LTE. Figs. 1.33 and 1.34 give average LTE and effective stiffness values versus type of mix design of concrete, respectively. Except for the control mix, Mix Design 1, the concrete using river gravel as the coarse aggregate (Mix Designs 3 and 4) caused higher LTE values than the concrete using crushed limestone as the coarse aggregate. No data for the effective

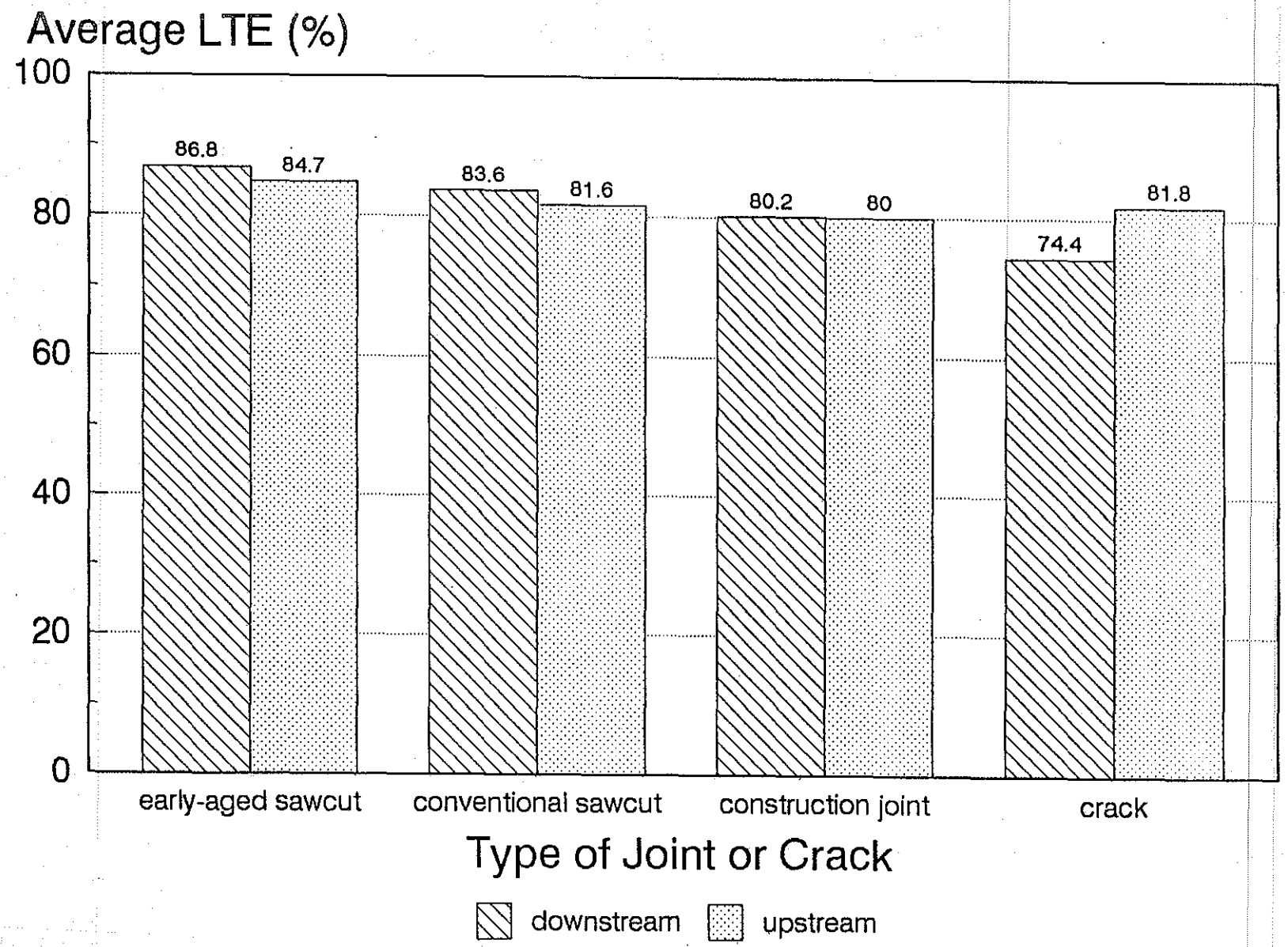

Fig. 1.31. Average Load Transfer Efficiency at Joints and Cracks.

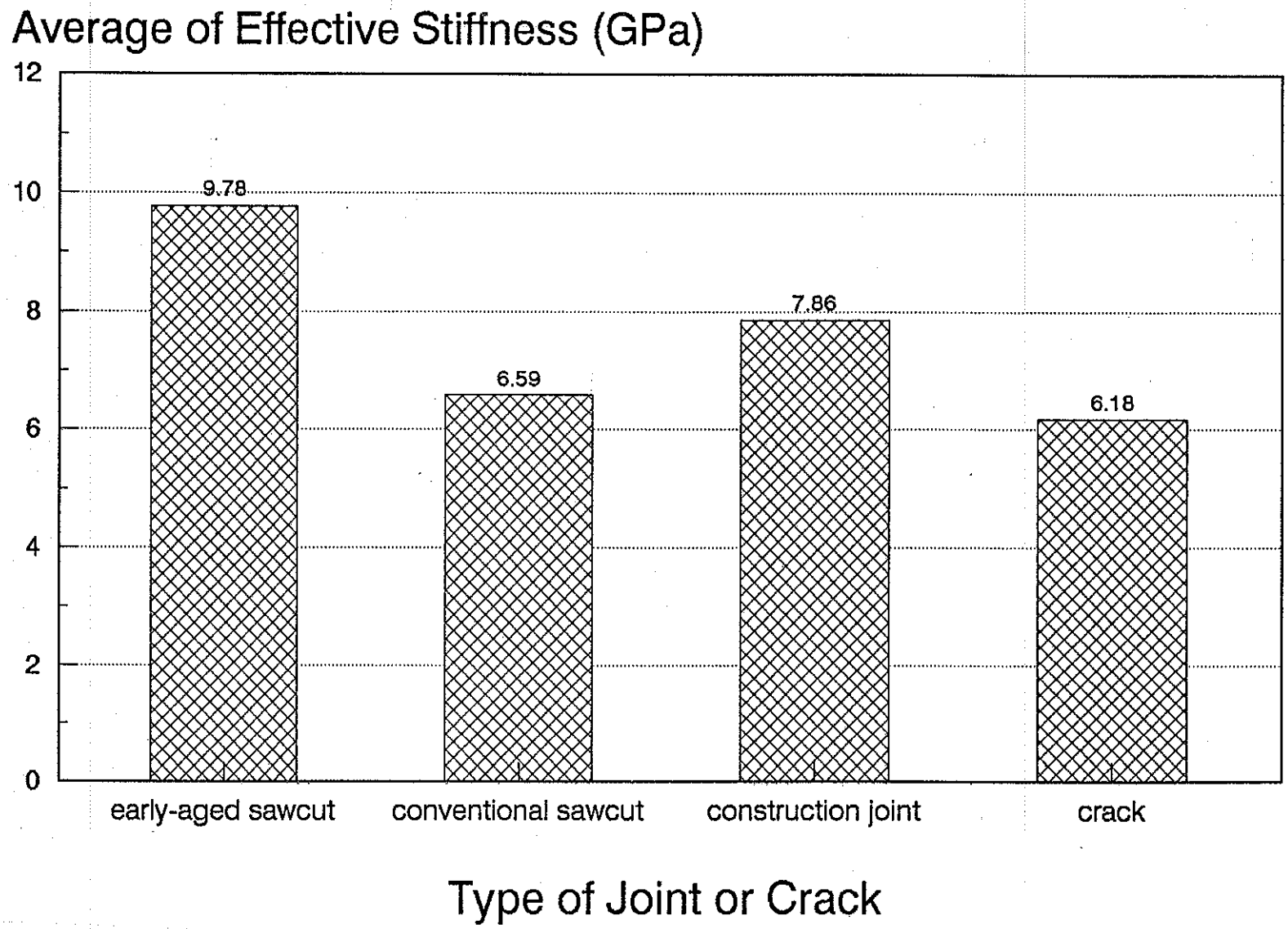

Fig. 1.32. Average Effective Stiffness at Joints and Cracks.

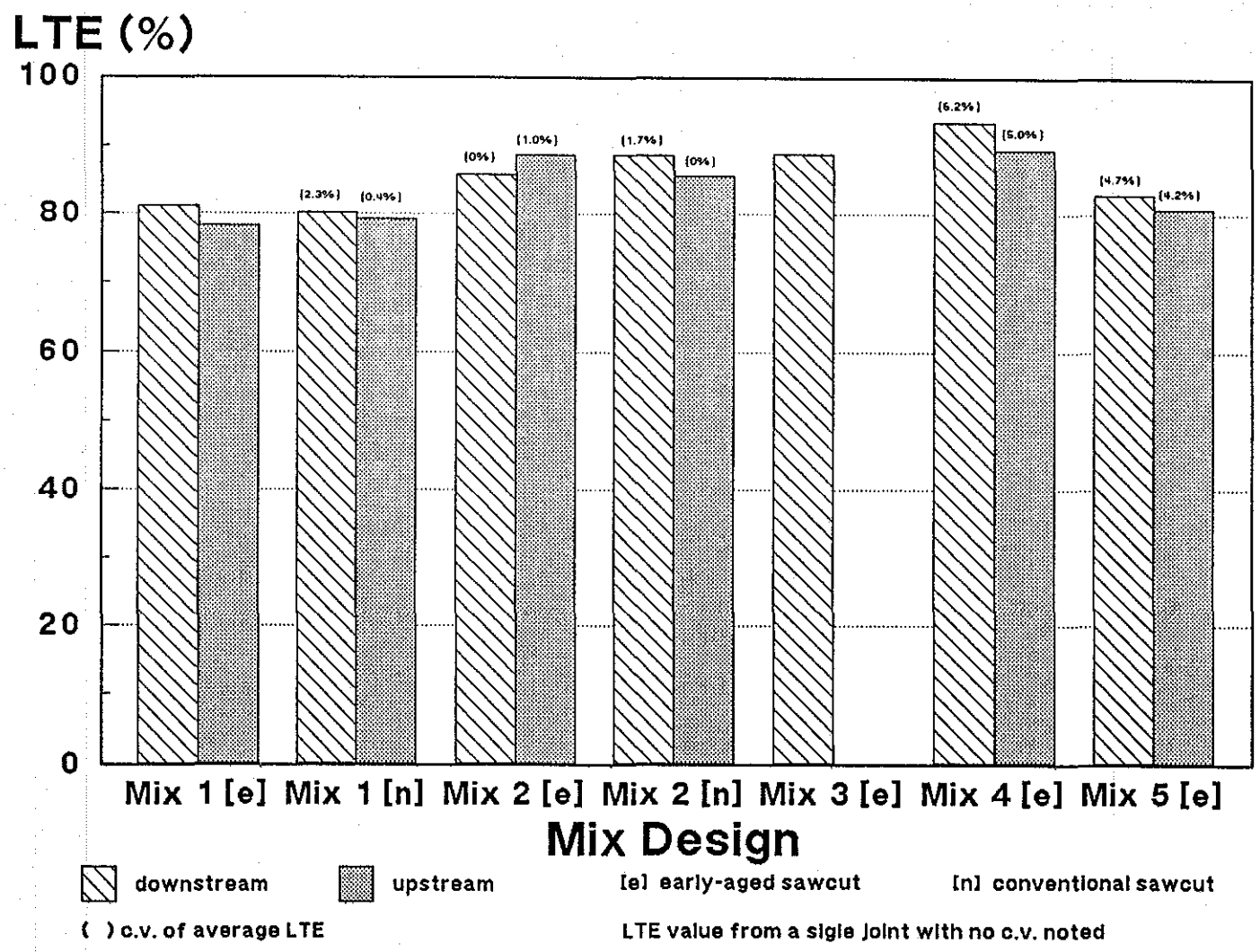

Fig. 1.33. Average Load Transfer Efficiency at Joints Formed by Early-Aged and Conventional Sawcut Techniques.

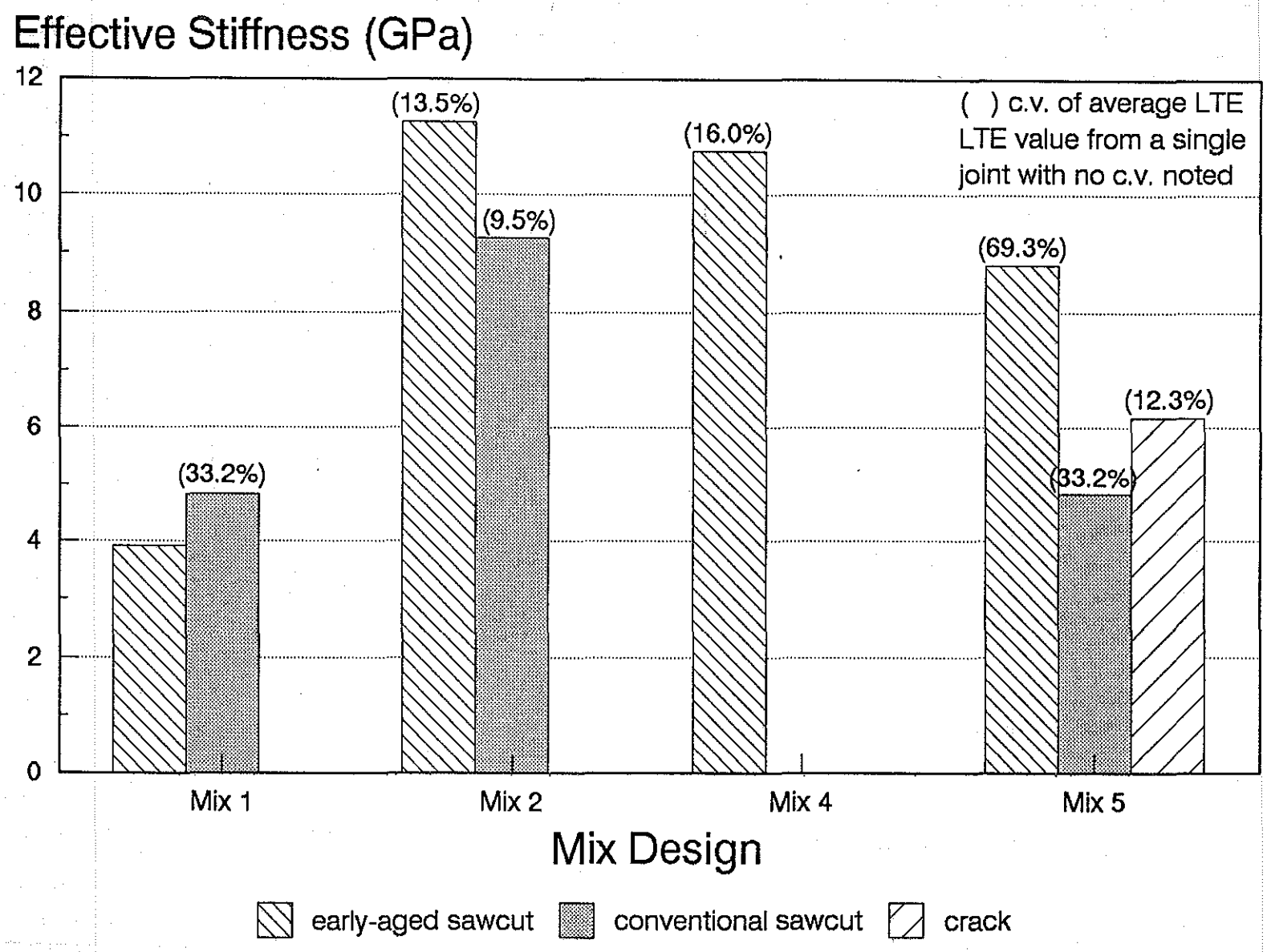

Fig. 1.34. Average Effective Stiffness at Joints Formed by Early-Aged and Conventional Sawcut Techniques.

stiffness along joints in the test section of Mix Design 3 were acquired. However, it is shown that Mix Design 4 provided higher effective stiffness values than Mix Design 5. Mix Design 2, replacing part of crushed limestone by 0.75 inch (19 mm) river gravel, provided even higher LTE and effective stiffness than Mix Design 5. These differences for sections of different mix design may also be explained by the average crack spacing. The average crack spacings of the early-aged sawcut sections of Mix Designs 2, 4 and 5

The advantage of river gravel for the joint load transfer can be attributed to its fracture behavior in concrete. Limestone is softer and may break during fracturing of the concrete. In contrast, river gravel is very hard. The fracture toughness of river gravel is higher than that of mortar as well as the interface between river gravel and mortar. When concrete using river gravel as the coarse aggregate fractures, the fracture surface goes around the river gravel aggregates. Therefore, in the pavement of river gravel concrete, the joint surface, formed by fracturing from the sawcut, is tortuous. Hard river gravel aggregates protrude from both sides of the joint and interlock one another. More gravel interlocking provides better performance of joint in transferring load across the joint are listed in Table 1.10 for comparison.

Table 1.10. Average Crack Spacings of the Early-Aged Sawcut Part.

Mix	Paving Date	Average Crack Spacing	
		February 20, 1992	July 13, 1992
2	November 8, 1991	62 ft (19 m)	19 ft (5.8 m)
4	October 22, 1991	36 ft (11 m)	18 ft (5.5 m)
5	November 6, 1991	95 ft (29 m)	32 ft (10 m)

1.12. CONCLUSIONS AND RECOMMENDATIONS

1. A jointed concrete pavement test section was placed in Texarkana, Texas, for experimental studies in concrete placement, joint formation, and crack control. Five

different mix designs of concrete (using different coarse aggregates: crushed limestone, river gravel, or blends of both) and different curing methods were applied to different sections of the pavement to compare their influences on performance of the pavement. Two sawcut techniques, the conventional and the early-aged, were used for formation of the joint. Temperature and relative humidity in these sections were monitored. Cracks were surveyed eight times during the period of nine months after paving. It was found that differences made by different mix designs, curing methods and sawcut techniques were obvious, which made it clear that such field tests are useful in helping to understand the effects of coarse aggregates, curing methods and sawcut techniques.

2. Early cracking at the sawcut tip occurred more frequently in sections of river-gravel concrete (Mix Designs 1, 3 and 4) than in sections of crushed-limestone concrete (Mix Design 5). It also occurred more frequently in the concrete that consisted of a blend of crushed limestone and river gravel as the coarse aggregate (Mix Design 2) than concrete that used only pure crushed limestone purely as the aggregate (Mix Design 5). Concrete of the control mix design that used 1.5-inch (38 mm) river gravel as the coarse aggregate (Mix Design 1) was improved by adding buckshot as the intermediate aggregate. The improved mix design (Mix Design 3) was better than the control mix design in formation of controlled cracks. Another mix design (Mix Design 4) that used 0.75-inch (19 mm) river gravel as the coarse aggregate and buckshot as the intermediate aggregate also showed better performance in formation of control cracks than the control mix design.

3. Lab tests showed that concrete of crushed limestone had higher flexural and compressive strengths than concrete of river gravel. This may explain why cracks were more likely to grow in river-gravel concrete. Also, smaller aggregates may have lowered the strength of the concrete and increased the tendency to crack. However, strength cannot explain why Mix Design 3 performed better in formation of controlled cracks than Mix Design 1. From both lab specimen and cored specimen tests, Mix Design 3 had higher compressive and tensile strengths than Mix Design 1. As observed in crack surveys, some cracks occurred within one or two days after paving while formation of some other cracks took a period as long as 9 months. For the cracks that

formed at the early ages of concrete, an analysis is included in Chapter 5. For those delayed cracks, further study is needed. In the delayed fracture process, effects of creep and fatigue may be important aspects.

4. There were two uncontrolled transverse cracks in the whole test section pavement. Both of them were initiated from a blockout corner where stress concentration existed. It is suggested that such stress-concentration causing sharp corners should be avoided in design or a joint (sawcut) should be located to connect to any sharp corner to control cracking. A random longitudinal crack was observed alongside a part of the longitudinal sawcut, which was formed with the conventional sawcut technique, although the cause is not clear yet.

5. The early-aged sawcut technique has the capability to be applied to pavement earlier than the conventional sawcut technique so that controlled cracks were formed earlier. With the early-aged sawcut method, the depth of cut was 1 inch (25 mm), much less than D/4 to D/3 as used for the conventional sawcutting of joints. In addition, the early-aged method did not require a supply of water for cooling saw blades. These advantages of the early-aged sawcut technique provided great convenience in construction. In this study, minimal raveling occurred along with the early-aged sawcutting operations. Data showed that the operations can be arranged when the pulse velocity reaches the order of 3600 - 4600 feet/sec (1110 - 1400 m/sec).

6. FWD tests were conducted at some of the joints where cracking had occurred at the sawcut tip and developed through the pavement bottom surface, as well as at the construction joints and the two uncontrolled transverse cracks. The tests were conducted in order to obtain the load transfer efficiency and effective stiffness at these locations. Sawcutting formed joints were found to have higher load transfer efficiencies and higher effective stiffness than construction joints and uncontrolled cracks on the average. The early-aged sawcutting provided higher load transfer efficiency and higher effective stiffness than the conventional sawcutting. One apparent reason is that the early-aged sawcut was 2 inches (51 mm) shallower than the conventional sawcut so that a 2-inch longer zig-zag fracture surface existed at the joint by the early-aged sawcutting providing more aggregate interlocking. A wide crack opening may have occurred at the

joint by the conventional sawcutting. However, it is not yet clear since the crack opening was not measured with an instrument any better than a common ruler. Although the crushed-limestone concrete had higher compressive and tensile strengths than the river gravel concrete, the crushed-limestone concrete did not provide higher load transfer efficiency. It may be due to different behaviors of limestone and river gravel in concrete fracturing. River gravel does not break when concrete fractures, so it provides better aggregate interlocking. With intermediate aggregate in concrete, aggregate interlocking would be improved, and therefore, load transfer performance at the joint would be improved.

7. The strength of concrete in the pavement not only depends on the mix design, but also on construction operation. From tests on specimens prepared in the laboratory, compressive and flexural tension strengths of concrete of Mix Design 2 were comparatively high while the split tension strengths of the cored specimen of Mix Design 2 were comparatively low. The most serious air pockets were observed in the cored specimen of Mix Design 2.

8. Split tension tests on specimens from the same core but at different depths in the pavement showed that the tensile strength increased with depth. This indicates that concrete is not homogeneous through the pavement depth. Inhomogeneity in concrete properties along the pavement depth would be a significant factor in stress analysis in the pavement. Further experimental investigation of this phenomenon is needed.

9. In comparison with the membrane curing method (using standard white pigments or Procrete), cotton mat and polyethylene film both slowed down the drying process in pavement concrete. When the daily average ambient temperature dropped from the day of the paving, the wet cotton mat may have helped cool the pavement, and therefore, maintained the mat covered pavement at a lower temperature than the membrane cured pavement. The polyethylene film covering the pavement formed a "greenhouse" effect over the pavement, which made the temperature in the pavement higher than in the pavement cured with the membrane method. When there was sun and the daily average ambient temperature increased after the day of paving, pavement with neither cotton mat nor polyethylene film covering absorbed more solar radiation,

and therefore, temperature was higher than that in pavement covered with cotton mat or polyethylene film.

1.13. APPENDIX: MIX DESIGN USED IN THE TEST SECTIONS

The 5 mix designs with mix analysis, aggregates gradation, all-components gradation and material distribution by sieve are given in this appendix. Terms used in analysis are defined as follows.

Q - The plus 3/8-inch (9.5 mm) sieve particles are the high *quality*, insert filler sizes.

I - The minus 3/8-inch (9.5 mm), plus No. 8 (2.36 mm) sieve particles are the *intermediate* particles that fill major voids and aid in mix mobility, or, if elongated and sharp, interference particles that contribute to mix harshness.

W - The minus No. 8 (2.36 mm) sieve particles give the mixture *workability*.

Coarseness - It is defined as Q/(Q+I).

Workability-Adjusted - The amount of fine aggregate needed is influenced by the amount of cementitious materials. As cement content is varied, the sand content should be adjusted. One 94-lb (42.6 kg) US bag of cement is equal to approximately 2.5 percent of the combined aggregate. Workability = Workability-Adjusted when the cement factor is 6 bags. If the cement factor is higher than 6 bags, Workability-Adjusted will be higher than Workability and vice versa.

The mix designs were made by following the Construction Bulletin issued by the Texas Department of Transportation.

Mix Design 1 and Analysis

Mix 1 is the control design using Gifford Hill Spec. 360 coarse aggregate and natural river sand from the Little River Plant. Data for the mix design are listed in Tables 1.11 to 1.15 which are followed by a design summary. Data are also shown in Figs. 1.35 to 1.37.

Note - This coarse aggregate also overlaps the Grade 3 gradation.

Table 1.11. Mix Design 1 (1 cubic yard, or 0.765 m^3, of concrete).

Material (All solid materials saturated surface-dry)	Weight or Volume	Yield ft^3 (m^3)
ASHGROVE CEMENT TYPE 1	379 lb (172 kg)	1.93 (0.0547)
GIFFORD-HILL TYPE "C" FLY ASH	142 lb (64.4 kg)	0.83 (0.0235)
G-H L. RIVER CONC. SAND	1187 lb (538 kg)	7.26 (0.0283)
G-H L. RIVER 360 (GRD 3)	1980 lb (898 kg)	12.35 (2.54)
WATER, GAL-US	24.6 gal-US (93 l)	3.29 (0.0932)
TOTAL AIR	5.0 $\pm$ 1.0%	1.35 (0.0382)
MONEX 434	26.0 oz-US (0.737 kg)	
SOLAIRE	5.2 oz-US (0.15 kg)	
WATER/CEMENT RATIO	0.39	
SLUMP	1.50 in (38 mm)	
CONCRETE DENSITY	144.2 lb/ft^3 (2310 kg/m^3)	
TOTAL YIELD		27.00 (0.765)

Table 1.12. Mix Analysis of Mix Design 1.

MIX VOLUME (ft^3)	27.00 (0.765 m^3)
COARSENESS (Q/(Q+I))	31.3
WORKABILITY	30.2
W - ADJUST	29.0
PERCENT MORTAR	49.2
TOTAL FINENESS MODULUS	5.56

Note - Fig. 1.35 shows the Workability vs. the Coarseness.

Table 1.13. Materials Characteristics for Mix Design 1.

	SRG	SAND
SPECIFIC GRAVITY	2.57	2.62
% PASSING 3/8" (9.5 mm) SIEVE	9.9	100.0
% PASSING # 8 SIEVE	0.1	81.8
FINENESS OF AGGREGATE	7.22	2.75
PERCENT OF AGGREGATE	63.0	37.0
MINERAL ADMIXTURE,	SPECIFIC GRAVITY	2.75

Table 1.14. Full Gradation Analysis of Mix Design 1.

SIEVE	SRG	SAND	PASTE	TOTAL	AGGR
1 1/2" (38 mm)	100.0			100.0	100.0
1" (25 mm)	90.1			95.5	93.8
3/4" (19 mm)	68.0			85.4	79.8
1/2" (12.7 mm)	31.2			68.5	56.7
3/8" (9.5 mm)	9.9	100.0		58.8	43.3
# 4	0.5	98.5		54.1	36.8
# 8	0.1	81.3		49.3	30.2
# 16	-	70.2		46.3	26.0
# 30	-	57.6		42.9	21.8
# 50	-	16.6		31.8	6.1
# 100	-	0.9		27.6	0.3
# 200	-	0.1	100.0	27.4	0.0
# 325	-	-	95.5	26.2	-
Liquid	-	-	62.8	17.2	-

Note - Fig. 1.36 shows the Gradation Analysis.

Table 1.15. Materials Distribution of Mix Design 1.

SIEVE	SRG	SAND	PASTE	TOTAL	AGGR
1 1/2" (38 mm)	100.0			0.0	-
1" (25 mm)	90.1			4.5	6.2
3/4" (19 mm)	68.0			10.1	13.9
1/2" (12.7 mm)	31.2			16.8	23.2
3/8" (9.5 mm)	9.9	100.0		9.7	13.4
# 4	0.5	98.5		4.7	6.5
# 8	0.1	81.3		4.8	6.6
# 16	-	70.2		3.0	4.2
# 30	-	57.6		3.4	4.7
# 50	-	16.6		11.0	15.2
# 100	-	0.9		4.2	5.8
# 200	-	0.1	100.0	0.2	0.3
# 325	-	-	95.5	1.3	0.0
Liquid	-	-	62.8	9.0	-

Note - Fig. 1.37 shows the Materials Distribution of Sieve.

DESIGN SUMMARY FOR MIX 1

DESIGN COMPRESSIVE STRENGTH:	4550 PSI (31.4 MPa)
EQUIVALENT FLEXURAL STRENGTH:	700 PSI (4.83 MPa)

MAXIMUM AGGREGATE SIZE	AGGREGATE SHAPE
1 1/2 IN (38 mm)	NATURAL GRAVEL

TOTAL AIR: 5.00% +/-1.00	SLUMP: 1.50 IN (38 mm)

WATER METHOD:	MANUAL ENTRY
AMOUNT:	24.6 GAL-US (93 liters)

CEMENT METHOD:		MANUAL ENTRY
AMOUNT:	541	[379] LB (172 kg)
W/C :	4.3	[4.4] GAL/SK (16.7 liters)

MINERAL ADDITIVE METHOD:		REPLACEMENT BY VOLUME
ADDITIVE 1:	142	[142] LB (64.4 kg)

SEVERE EXPOSURE CONDITIONS
NO SEVERE EXPOSURE

COARSE AGGREGATE METHOD:		W-ADJUST WORKABILITY FACTOR	
ACI bbo	-	PERCENT STONE	63.0
W-ADJUST	29.0	PERCENT MORTAR	49.3
TOTAL FM	5.56	NRMCA FM	-

	AMOUNT	FINENESS MODULUS
SRG	1980 LB (898 kg)	7.22

FINE AGGREGATE METHOD:	PRODUCE A SPECIFIC VOLUME
SAND	FINENESS MODULUS
AMOUNT	
1187 LB (538 kg)	2.75

MIX VOLUME: 27.00 CU FT (0.765 m^3)

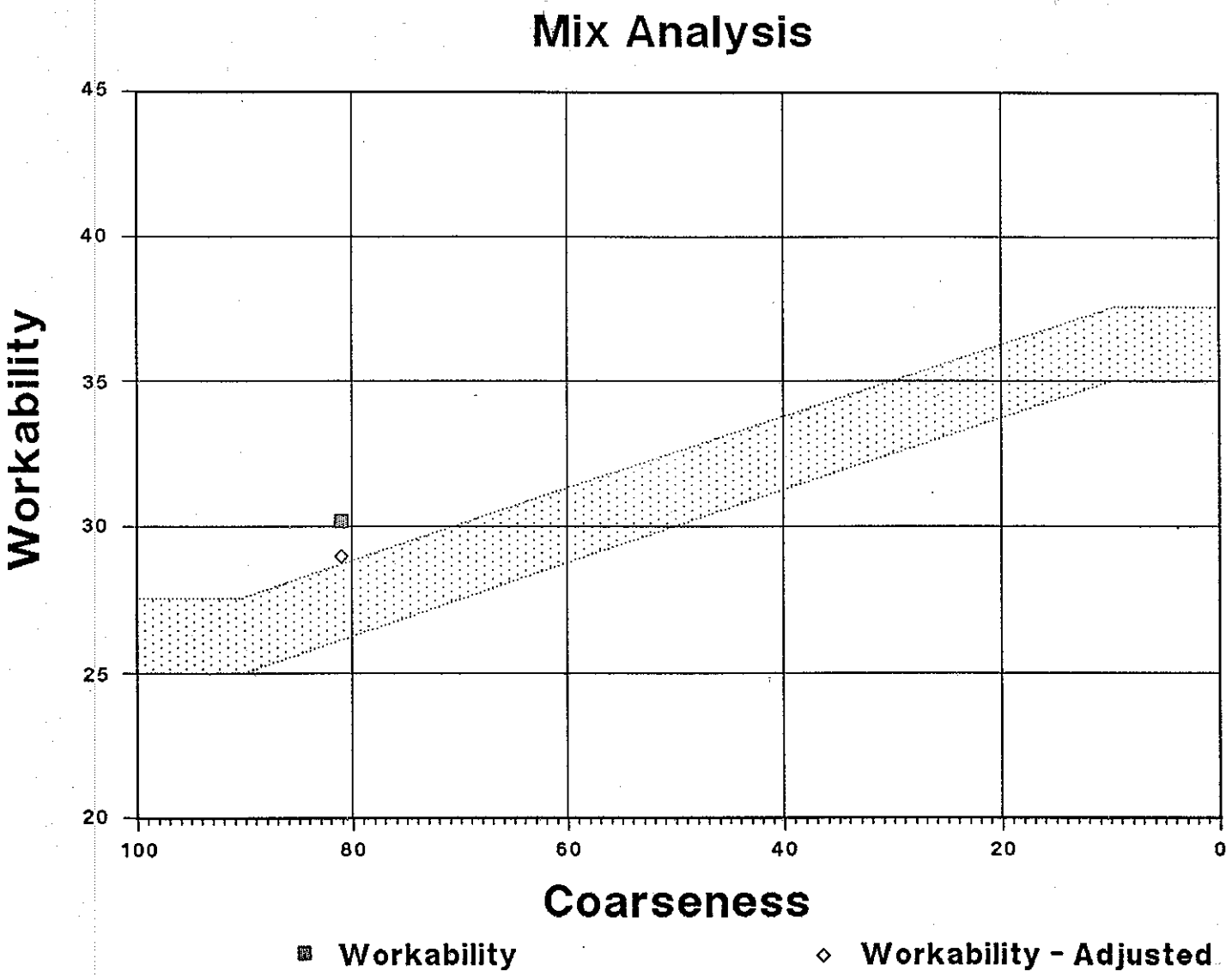

Fig. 1.35. Workbility versus Coarseness of Mix Design 1.

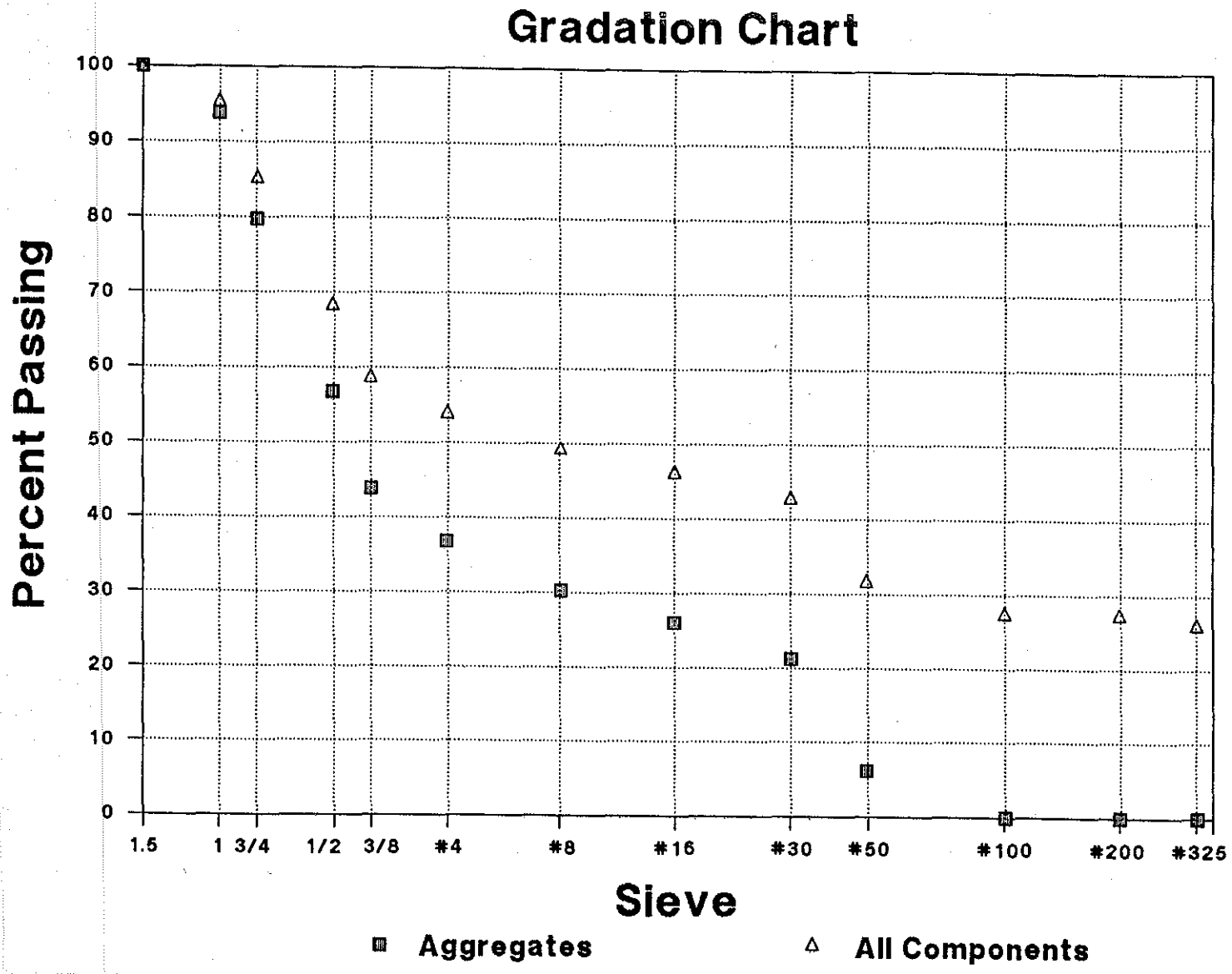

Fig. 1.36. Full Gradation of Mix Design 1.

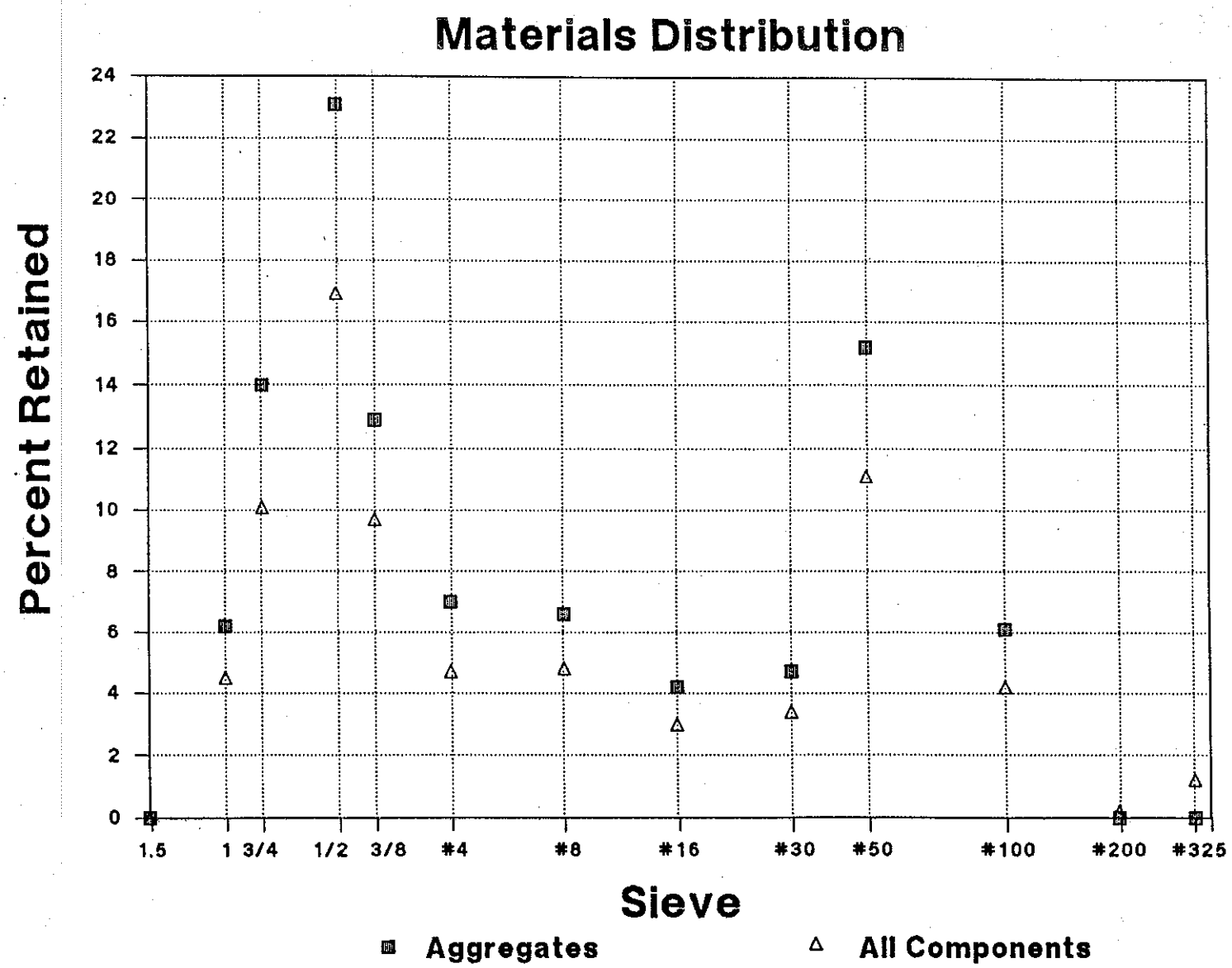

Fig. 1.37. Materials Distribution of Mix Design 1.

Mix Design 2 and Analysis

Mix 2 is a design using a 50/50% blend of 1 1/2-inch (38 mm) crushed Limestone and 3/4-inch (19 mm) SRG from the Gifford Hill Delight Plant; Gifford Hill Buckshot from the Hoot Plant; 65% Gifford Hill crushed sand; and 35% concrete sand from Little River. Data for the mix design are listed in Tables 1.16 to 1.20, followed by a design summary. Data are also shown in Figs. 1.38 to 1.40.

Table 1.16. Mix Design 2 (1 cubic yard, or 0.765m^3, of concrete).

Material (All solid materials saturated surface-dry)	Weight or Volume	Yield ft^3 (m^3)
ASHGROVE CEMENT TYPE 1	379 lb (172 kg)	1.93 (0.0546)
GIFFORD-HILL TYPE "C" FLY ASH	142 lb (64.4 kg)	0.83 (0.0235)
G-H HOOT PLANT/BUCKSHOT, LB	379 lb (172 kg)	2.35 (0.0666)
G-H LITTLE RIVER/CRUSHED SAND	740 lb (336 kg)	4.58 (0.130)
G-H LITTLE CONCRETE SAND	403 lb (183 kg)	2.46 (0.0697)
G-H 1 1/2" (38 mm) CRUSHED LIMESTONE	857 lb (389 kg)	5.11 (0.145)
G-H DELIGHT PLANT 3/4" (19 mm) SRG	826 lb (375 kg)	5.11 (0.145)
WATER	24.6 gal-US (93 l)	3.29 (0.0932)
TOTAL AIR	5.0 $\pm$ %	1.35 (0.0382)
MONEX 434	26.0 oz-US (0.737 kg)	
SOLAIRE	5.2 oz-US (0.15 kg)	
WATER/CEMENT RATIO	0.39	
SLUMP	1.50 in (38 mm)	
CONCRETE UNIT WEIGHT	145.6 (lb/ft^3) (2330 kg/m^3)	
TOTAL YIELD		27.00 (0.765)

Table 1.17. Mix Analysis of Mix Design 2.

MIX VOLUME	27.00 ft^3 (0.765 m^3)
COARSENESS (Q/(Q+I))	55.8
WORKABILITY	32.7
W-ADJUST	31.5
PERCENT MORTAR	51.1
TOTAL FINENESS MODULUS	5.21

Note - Fig. 1.38 shows the Workability vs. the Coarseness.

Table 1.18. Material Characteristics for Mix Design 2.

	LIMESTONE	SRG	BUCKSHOT	CRUSHED SAND	CONCRETE SAND
DENSITY SPECIFIC GRAVITY	2.69	2.59	2.59	2.59	2.59
% PASSING 3/8" (9.5 mm) SIEVE	17.7	38.0	100.0	100.0	100.0
% PASSING # 8 SIEVE	0.6	1.0	13.1	87.6	81.3
FINENESS MODULUS	7.32	6.60	4.86	2.82	2.75
PERCENT OF AGGREGATE	26.1	26.1	12.0	28.4	12.4
MINERAL ADMIXTURE, SPECIFIC GRAVITY 2.75					

Table 1.19. Full Gradation Analysis of Mix Design 2.

SIEVE	LIMESTONE	SRG	BUCKSHOT	CRUSHED SAND	CONCRETE SAND	PASTE	TOTAL	AGGR
1 1/2" (38 mm)	100.0						100.0	100
1" (25 mm)	75.9	100.0					95.4	93.6
3/4" (19 mm)	47.6	96.0					89.3	85.0
1/2" (12.7 mm)	31.2	59.0					79.2	71.0
3/8" (9.5 mm)	17.7	38.0	100.0	100.0	100.0		72.7	62.0
# 4	2.1	5.0	85.8	99.5	98.5		62.1	47.4
# 8	0.6	1.0	13.1	87.6	81.3		51.1	32.4
# 16	-	-	6.8	60.5	70.2		44.6	23.6
# 30	-	-	5.5	38.6	57.6		39.7	16.8
# 50	-	-	2.1	22.6	16.6		32.9	7.6
# 100	-	-	0.4	9.6	0.9		29.1	2.4
# 200	-	-	0.1	3.3	0.1	100.0	28.0	0.5
# 325	-	-	-	-	-	95.5	26.2	0
Liquid	-	-	-	-	-	62.8	17.2	0

Note - Fig. 1.39 shows the Workability vs. the Coarseness.

Table 1.20. Materials Distribution of Mix Design 2.

SIEVE	LIMESTONE	SRG	BUCKSHOT	CRUSHED SAND	CONCRETE SAND	PASTE	TOTAL	AGGR
1 1/2" (38 mm)	100.0						0.0	0
1" (25 mm)	75.9	100.0					4.6	6.4
3/4' (19 mm)	47.6	96.0					6.1	8.6
1/2" (12.7 mm)	31.2	59.0					10.1	13.9
3/8" (9.5 mm)	17.7	38.0	100.0	100.0	100.0		6.5	9.0
# 4	2.1	5.0	85.8	99.6	98.5		10.6	14.6
# 8	0.6	1.0	13.1	87.6	81.3		11.0	15.0
# 16	-	-	6.8	60.5	70.2		6.5	8.8
# 30	-	-	5.5	38.6	57.6		5.0	6.7
# 50	-	-	2.1	22.6	16.6		6.8	9.3
# 100	-	-	0.4	9.6	0.9		3.8	5.2
# 200	-	-	0.1	3.3	0.1	100.0	1.2	1.8
# 325	-	-	-	-	-	95.5	1.8	0.6
Liquid	-	-	-	-	-	62.8	9.0	0

Note - Fig. 1.40 shows the Materials Distribution by Sieve.

DESIGN SUMMARY FOR MIX 2

DESIGN COMPRESSIVE STRENGTH:	550 PSI (31.4 MPa)
EQUIVALENT FLEXURAL STRENGTH:	700 PSI (4.83 MPa)

MAXIMUM AGGREGATE SIZE	AGGREGATE SHAPE
1 1/2 IN (38 mm)	NATURAL GRAVEL

TOTAL AIR: 5.00% +/-1.00	SLUMP: 1.50 IN (38 mm)

WATER METHOD:	MANUAL ENTRY
AMOUNT:	24.6 GAL-US (93 liters)

CEMENT METHOD:		MANUAL ENTRY
AMOUNT:	541	[379] LB (172 kg)
W/C :	4.3	[4.4] GAL/SK

MINERAL ADDITIVE METHOD:		REPLACEMENT BY VOLUME
ADDITIVE 1:	142	[142] LB (64.4 kg)

SEVERE EXPOSURE CONDITIONS
NO SEVERE EXPOSURE

COARSE AGGREGATE METHOD:		W-ADJUST WORKABILITY FACTOR	
ACI bbo	-	PERCENT STONE	52.1
W-ADJUST	31.5	PERCENT MORTAR	51.1
TOTAL FM	5.21	NRMCA FM	-

	AMOUNT	FINENESS MODULUS
LIMESTONE	857 LB (389 kg)	7.32
SRG	826 LB (375 kg)	6.60

FINE AGGREGATE METHOD:		PRODUCE A SPECIFIC VOLUME
	AMOUNT	FINENESS MODULUS
BUCKSHOT	379 LB (172 kg)	4.86
CRUSHED SAND	740 LB (336 kg)	2.82
CONCRETE SAND	403 LB (183 kg)	2.75

MIX VOLUME:	27.00 CU FT (0.765 m^3)

DESIGN SUMMARY FOR MIX 3

DESIGN COMPRESSIVE STRENGTH:	4550 PSI (31.4 MPa)
EQUIVALENT FLEXURAL STRENGTH:	700 PSI (4.83 MPa)

MAXIMUM AGGREGATE SIZE	AGGREGATE SHAPE
1 1/2 IN (38 mm)	NATURAL GRAVEL

TOTAL AIR: 5.00% +/-1.00	SLUMP: 1.50 IN (38 mm)
WATER METHOD:	MANUAL ENTRY
AMOUNT:	24.6 GAL-US (93 liters)
CEMENT METHOD:	MANUAL ENTRY
AMOUNT: 541	[379] LB (172 kg)
W/C : 4.3	[4.4] GAL/SK (16.7 liters/sk)
MINERAL ADDITIVE METHOD:	REPLACEMENT BY VOLUME
ADDITIVE 1: 142	[142] LB

SEVERE EXPOSURE CONDITIONS
NO SEVERE EXPOSURE

COARSE AGGREGATE METHOD:		W-ADJUST WORKABILITY FACTOR	
ACI bbo	-	PERCENT STONE	64.3
W-ADJUST	31.0	PERCENT MORTAR	50.7
TOTAL FM	5.28	NRMCA FM	-

	AMOUNT	FINENESS MODULUS
SRG	1618 LB (734 kg)	7.11
BUCKSHOT	408 LB (185 kg)	4.86

FINE AGGREGATE METHOD:	PRODUCE A SPECIFIC VOLUME	
	AMOUNT	FINENESS MODULUS
CRUSHED SAND	735 LB (333 kg)	2.81
CONCRETE SAND	400 LB (181 kg)	2.75

MIX VOLUME: 27.00 CU FT (0.765 m^3)

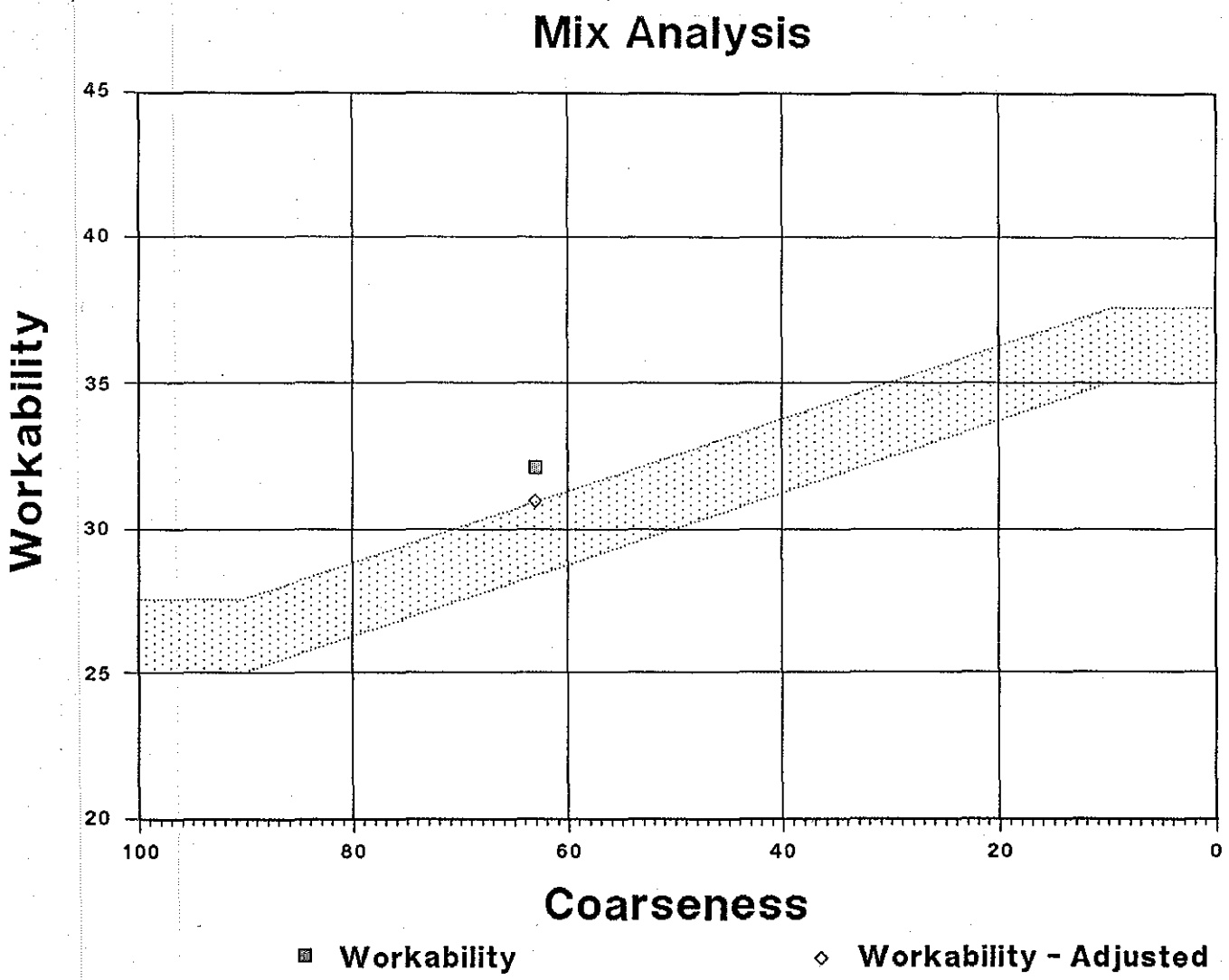

Fig. 1.41. Workbility versus Coarseness of Mix Design 3.

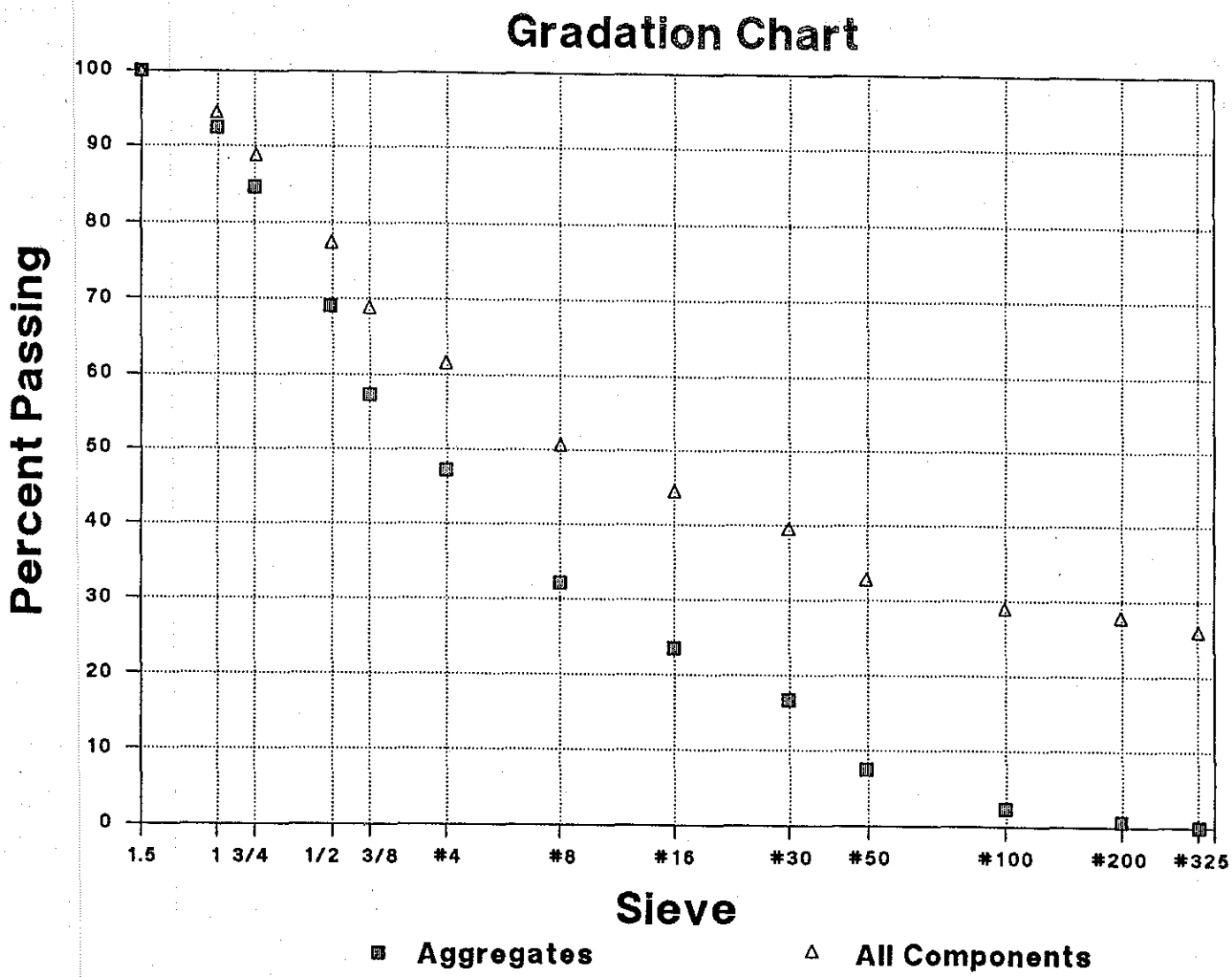

Fig. 1.42. Full Gradation of Mix Design 3.

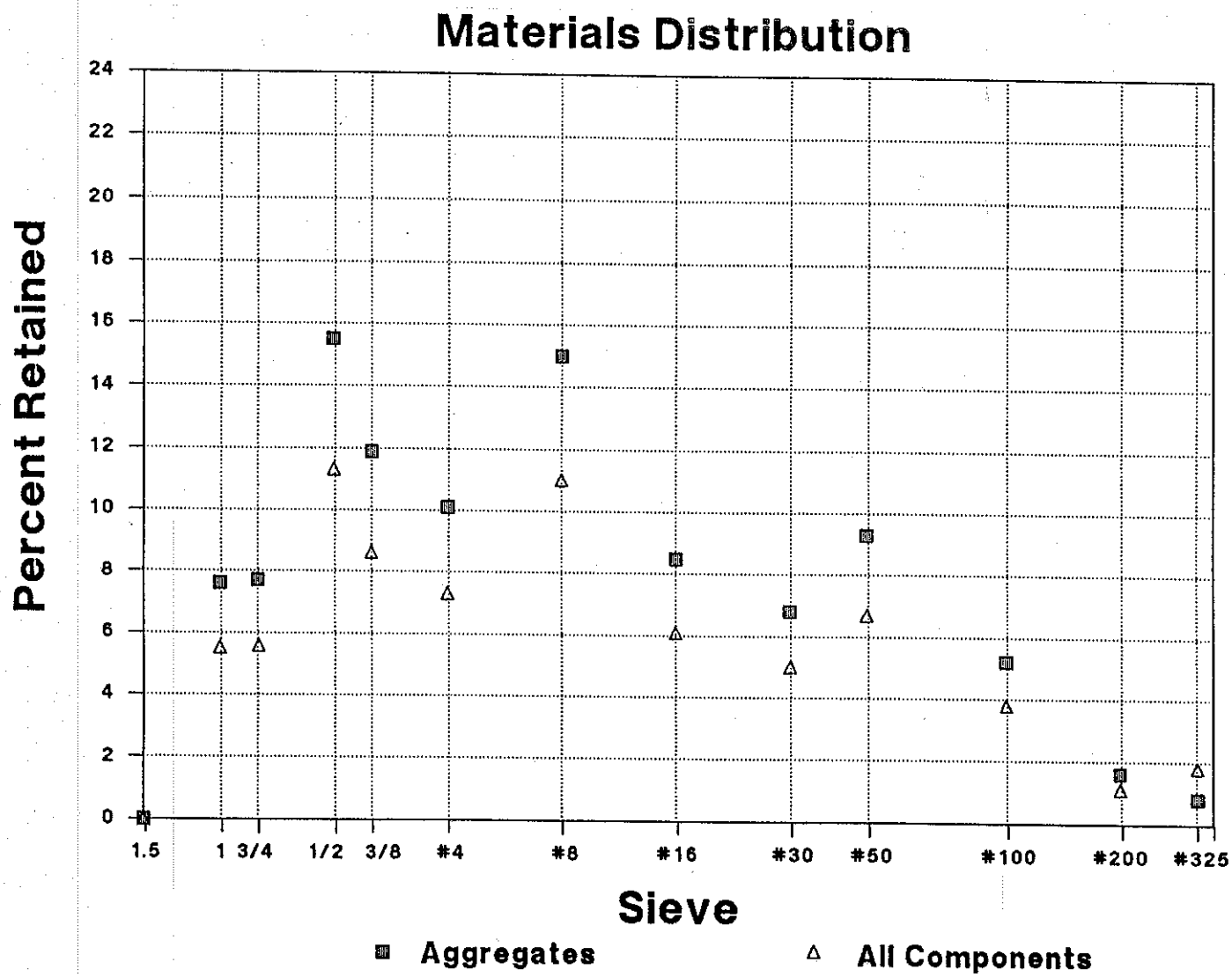

Fig. 1.43. Materials Distribution of Mix Design 3.

Mix Design 4 and Analysis

Mix 4 is a design using Gifford Hill Grade 5 coarse aggregate from the Delight Plant and buckshot from the Hoot Plant with 65% crushed sand and 35% concrete sand from Gifford Hill's Little River Plant. Data for the mix design are listed in Tables 1.26 to 1.30, followed by a design summary. Data are also shown in Figs. 1.44 to 1.46.

Table 1.26. Mix Design 4 (one cubic yard, or 0.765 m^3, of concrete).

Material (All solid materials saturated, surface dry)	Weight or Volume	Yield ft^3 (m^3)
ASHGROVE CEMENT TYPE 1	379 lb (172 kg)	1.93 (0.0547)
GIFFORD-HILL TYPE "C" FLY ASH	142 lb (64.4 kg)	0.83 (0.0235)
G-H BUCKSHOT SAND	402 lb (182 kg)	2.49 (0.0705)
G-H L.R. CRUSHED SAND	780 lb (354 kg)	4.88 (0.1382)
G-H L.R. CONC. SAND	418 lb (190 kg)	2.64 (0.0748)
G-H 3/4" (19 mm) DELIGHT PLANT	1560 lb (708 kg)	9.65 (0.273)
WATER	24.6 oz-US (93 l)	3.29 (0.0932)
TOTAL AIR	5.0 $\pm$ 1.0%	1.35 (0.0382)
MONEX 434	26.0 oz-US (0.737 kg)	
SOLAIRE	5.2 oz-US (0.15 kg)	
WATER/CEMENT RATIO	0.39	
SLUMP	1.50 in (38 mm)	
CONCRETE UNIT WEIGHT	144.4 lb/ft^3 (2313 kg/m^3)	
TOTAL YIELD		27.00 (0.765)

Table 1.27. Mix Analysis of Mix Design 4.

MIX VOLUME	27.00 ft^3 (0.765 m^3)
COARSENESS (Q/(Q+I))	46.7
WORKABILITY	34.7
W-ADJUST	33.5
PERCENT MORTAR	52.5
TOTAL FINENESS MODULUS	4.93

Note - Fig. 1.44 shows the Workability vs. the Coarseness.

Table 1.28. Materials Characteristics for Mix Design 4.

	SRG	BUCKSHOT	CRUSHED SAND	CONCRETE SAND
SPECIFIC GRAVITY	2.59	2.59	2.59	2.62
% PASSING 3/8" (9.5 mm) SIEVE	38.0	100.0	100.0	100.0
% PASSING # 8 SIEVE	1.0	13.1	87.6	81.3
FINENESS MODULUS	6.60	4.86	2.82	2.75
PERCENT OF AGGREGATE	49.2	12.7	24.6	12.5
MINERAL ADMIXTURE, SPECIFIC GRAVITY 2.75				

Table 1.29. Full Gradation Analysis of Mix Design 4.

SIEVE	SRG	BUCKSHOT	CRUSHED SAND	CONCRETE SAND	PASTE	TOTAL	AGGR
1 1/2" (38 mm)	100.0					100.0	100.0
1" (25 mm)	96.0					100.0	100.0
3/4" (19 mm)	59.0					98.6	98.0
1/2" (12.7 mm)	38.0					85.3	79.8
3/8" (9.5 mm)	5.0	100.0	100.0	100.0		77.8	69.5
# 4	1.0	85.8	99.6	98.5		64.5	51.1
# 8	-	13.1	87.6	81.3		52.5	34.7
# 16	-	6.8	60.5	70.2		45.7	25.2
# 30	-	5.5	38.6	57.6		40.4	18.0
# 50	-	2.1	22.6	16.6		33.2	8.1
# 100	-	0.4	9.6	0.9		29.2	2.5
# 200	-	0.1	3.3	0.1	100.0	28.0	0.8
# 325	-	-	-	-	95.5	26.2	-
Liquid	-	-	-	-	62.8	17.2	-

Note - Fig. 1.45 shows the Gradation Analysis.

Table 1.30. Materials Distribution of Mix Design 4.

SIEVE	SRG	BUCKSHOT	CRUSHED SAND	CONCRETE SAND	PASTE	TOTAL	AGGR
1 1/2" (38 mm)	-					0.0	0.0
1" (25 mm)	100.0					-	-
3/4" (19 mm)	96.0					1.4	2.0
1/2" (12.7 mm)	59.0					13.2	18.2
3/8" (9.5 mm)	38.0	100.0	100.0	100.0		7.5	10.3
# 4	5.0	85.8	99.6	98.5		13.3	18.4
# 8	1.0	13.1	87.6	81.3		12.0	16.5
# 16	-	6.8	60.5	70.2		6.9	9.5
# 30	-	5.5	38.6	57.6		5.3	7.3
# 50	-	2.1	22.6	16.6		7.2	9.9
# 100	-	0.4	9.6	0.9		4.0	5.5
# 200	-	0.1	3.3	0.1	100.0	1.2	1.7
# 325	-	-	-	-	95.5	1.8	0.8
Liquid	-	-	-	-	62.8	9.0	-

Note - Fig. 1.46 shows the Materials Distribution by Sieve.

DESIGN SUMMARY FOR MIX 4

DESIGN COMPRESSIVE STRENGTH:	4550 PSI (31.4 MPa)
EQUIVALENT FLEXURAL STRENGTH:	700 PSI (4.83 MPa)

MAXIMUM AGGREGATE SIZE	AGGREGATE SHAPE
3/4 IN (19 mm)	NATURAL GRAVEL

TOTAL AIR: 5.00% +/-1.00	SLUMP: 1.50 (38 mm)

WATER METHOD:	MANUAL ENTRY
AMOUNT:	24.6 GAL-US (93 l)

CEMENT METHOD:		MANUAL ENTRY
AMOUNT:	541	[379] LB (172 kg)
W/C :	4.3	[4.4] GAL/SK (16.7 liters/sk)

MINERAL ADDITIVE METHOD:		REPLACEMENT BY VOLUME
ADDITIVE 1:	142	[142] LB (64.4 kg)

SEVERE EXPOSURE CONDITIONS
NO SEVERE EXPOSURE

COARSE AGGREGATE METHOD:		W-ADJUST WORKABILITY FACTOR	
ACI bbo	-	PERCENT STONE	49.2
W-ADJUST	33.5	PERCENT MORTAR	52.5
TOTAL FM	4.93	NRMCA FM	-

	AMOUNT	FINENESS MODULUS
SRG	1560 LB (708 kg)	6.60

FINE AGGREGATE METHOD:		PRODUCE A SPECIFIC VOLUME
	AMOUNT	FINENESS MODULUS
BUCKSHOT	402 LB (182 kg)	4.86
CRUSHED SAND	780 LB (35.4 kg)	3.82
CONCRETE SAND	431 LB (196 kg)	2.75

MIX VOLUME: 27.00 CU FT (0.765 m^3)

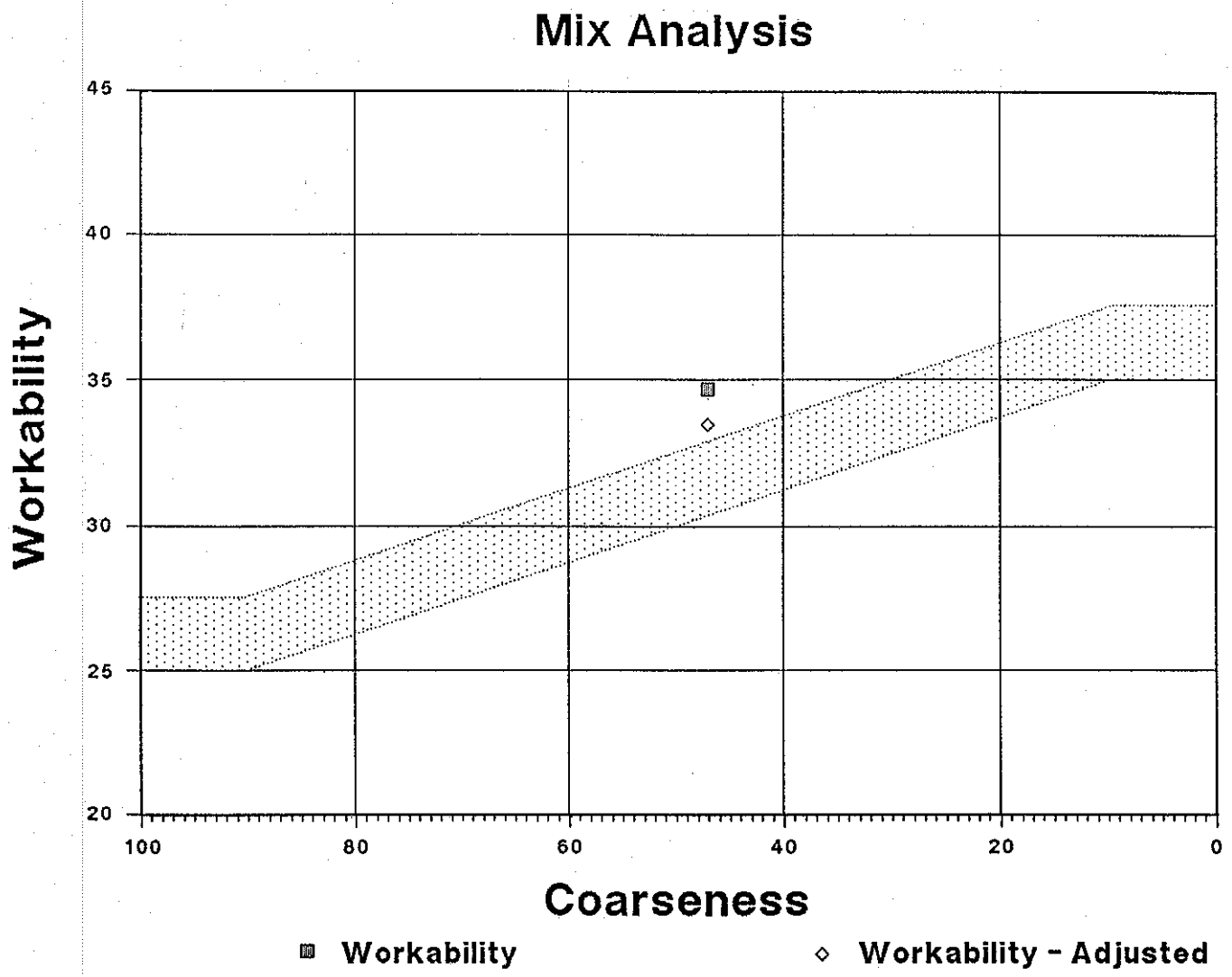

Fig. 1.44. Workbility versus Coarseness of Mix Design 4.

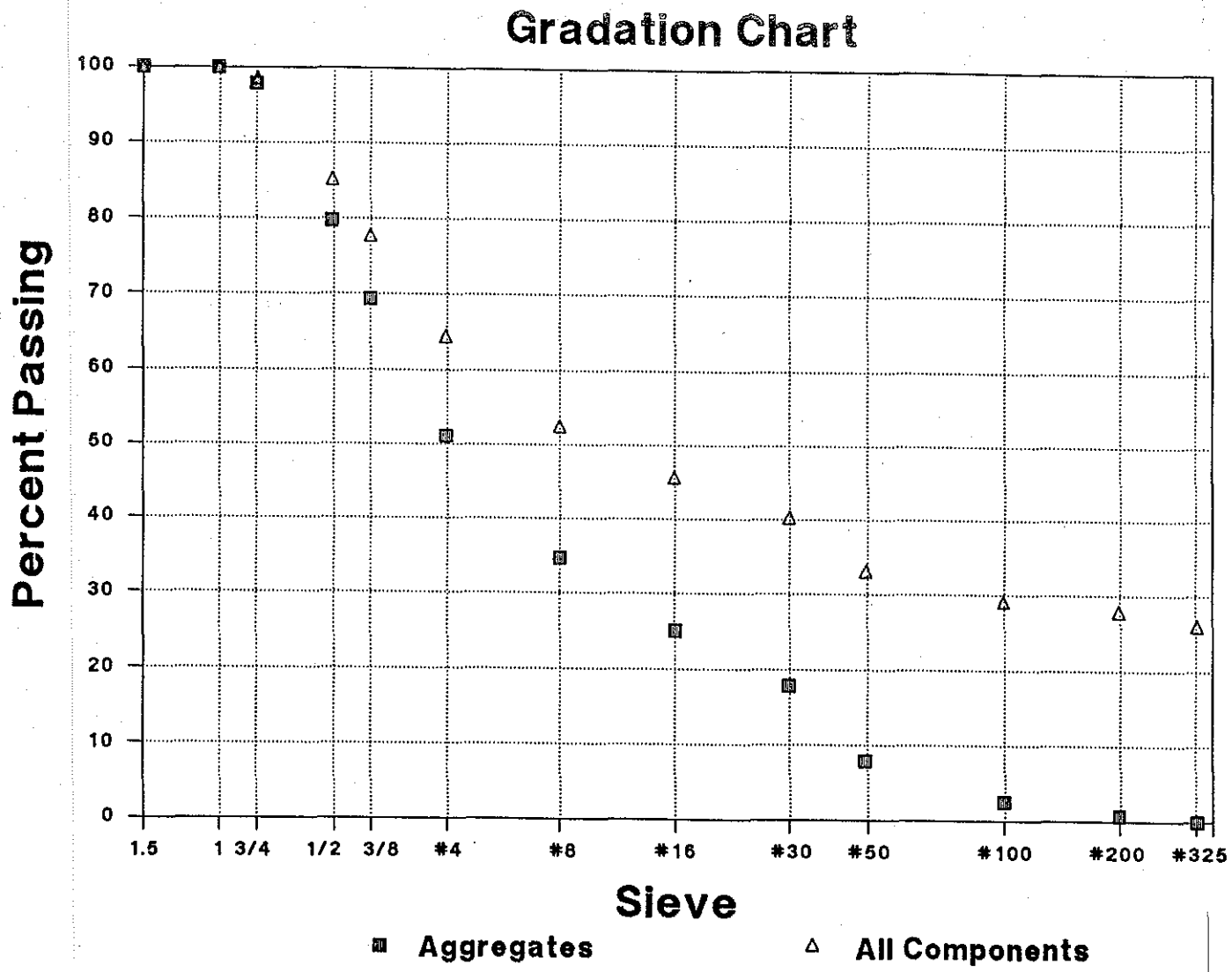

Fig. 1.45. Full Gradation of Mix Design 4.

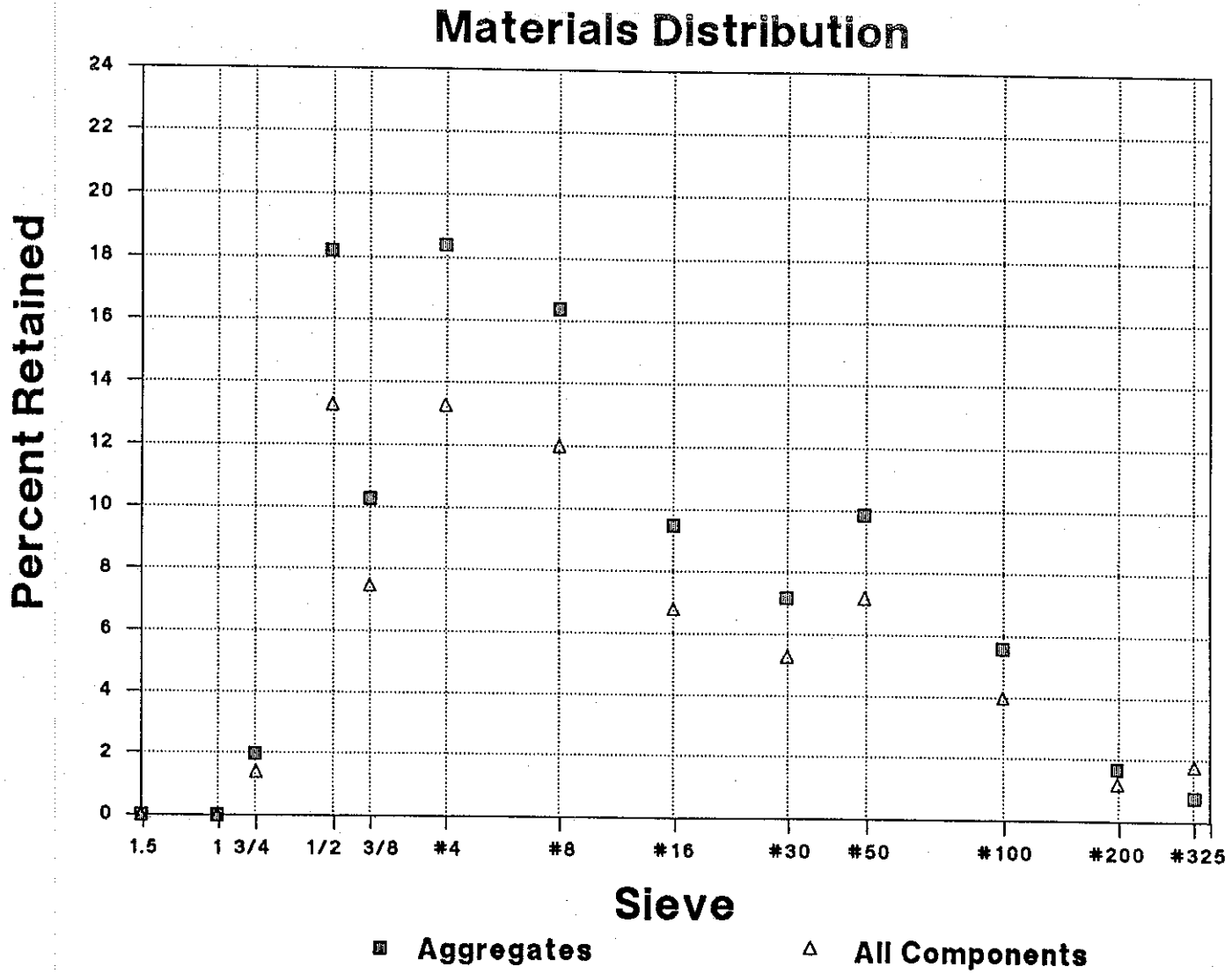

Fig. 1.46. Materials Distribution of Mix Design 4.

Mix Design 5 and Analysis

Mix 5 is a design using Gifford Hill limestone aggregate from Bridgeport with buckshot and a 65% crushed sand with 35% natural sand from the Little River Plant. Data for the mix design are listed in Tables 1.31 to 1.35, followed by a design summary. Data are also shown in Figs. 1.47 to 1.49.

Table 1.31. Mix Design 5 (1 cubic yard, or 0.765 m^3, of concrete).

Material (All solid materials saturated, surface dry)	Weight or Volume	Yield ft^3 (m^3)
ASHGROVE CEMENT TYPE 1	379 lb (172 kg)	1.93 (0.0547)
GIFFORD-HILL TYPE "C"	142 lb (64.4 kg)	0.83 (0.0235)
G-H BUCKSHOT	381 lb (173 kg)	2.36 (0.0668)
G-H CRUSHED SAND	742 lb (337 kg)	4.50 (0.127)
G-H NATURAL SAND	405 lb (184 kg)	2.48 (0.0702)
G-H CRUSHED LIMESTONE	1711 lb (776 kg)	10.10 (0.286)
WATER	24.5 oz-US (92.7 l)	3.29 (0.0932)
TOTAL AIR	5.0 $\pm$ 1.0%	1.35 (0.0382)
MONEX 434	26.0 oz-US (0.737 kg)	
SOLAIRE	5.2 (oz-US)	
WATER/CEMENT RATIO	0.39	
SLUMP	1.50 in (38 mm)	
CONCRETE DENSITY	146.8 lb/ft^3 (2353 kg/m^3)	
TOTAL YIELD		27.00 (0.765)

Table 1.32. Mix Analysis of Mix Design 5.

MIX VOLUME	27.00 ft^3 (0.765 m^3)
COARSENESS (Q/(Q+I))	63.5
WORKABILITY	32.7
W-ADJUST	31.5
PERCENT MORTAR	51.1
TOTAL FINENESS MODULUS	5.39

Note - Fig. 1.47 shows the Workability vs. the Coarseness.

Table 1.33. Materials Characteristics for Mix Design 5.

	STONE	BUCKSHOT	CRUSHED SAND	CONCRETE SAND
DENSITY SPECIFIC GRAVITY	2.69	2.59	2.59	2.62
% PASSING 3/8" (9.5 mm) SIEVE	17.7	100.0	100.0	100.0
% PASSING # 8 SIEVE	0.6	13.1	87.6	81.3
FINENESS MODULUS	7.32	4.86	2.32	2.75
PERCENT OF AGGREGATE	51.9	12.0	23.4	19.6
MINERAL ADMIXTURE DENSITY SPECIFIC GRAVITY 2.75				

Table 1.34. Full Gradation Analysis of Mix Design 5.

SIEVE	LIMESTONE	BUCKSHOT	CRUSHED SAND	CONCRETE SAND	PASTE	TOTAL	AGGR
1 1/2" (38 mm)	100.0					100.0	100.0
1" (25 mm)	75.9					90.0	87.5
3/4" (19 mm)	47.6					80.2	72.3
1/2" (12.7 mm)	31.2					74.0	64.3
3/8" (9.5 mm)	17.7	100.0	100.0	100.0		68.9	57.2
# 4	2.1	85.8	99.6	98.5		61.6	47.2
# 8	0.6	13.1	87.6	81.3		51.1	32.7
# 16	-	6.8	60.5	70.2		44.7	23.8
# 30	-	5.5	38.6	57.6		39.7	17.0
# 50	-	2.1	22.6	16.6		32.9	7.6
# 100	-	0.4	9.6	0.8		29.1	2.4
# 200	-	0.1	3.3	0.1	100.0	27.9	0.8
# 325	-	-	-	-	95.5	26.1	-
Liquid	-	-	-	-	62.7	17.1	-

Note - Fig. 1.48 shows the Gradation Analysis.

Table 1.35. Materials Distribution of Mix Design 5.

SIEVE	LIMESTONE	BUCKSHOT	CRUSHED SAND	CONCRETE SAND	PASTE	TOTAL	AGGR
1 1/2" (38 mm)	100.0					0.0	-
1" (25 mm)	75.9					9.1	12.5
3/4" (19 mm)	47.6					10.7	14.7
1/2" (12.7 mm)	31.2					6.2	8.5
3/8" (9.5 mm)	17.7	100.0	100.0	100.0		5.1	7.0
# 4	2.1	85.8	99.6	98.5		7.3	10.1
# 8	0.6	13.1	87.6	81.3		10.5	14.5
# 16	-	6.8	60.5	70.2		6.4	8.8
# 30	-	5.5	38.6	57.6		5.0	6.9
# 50	-	2.1	22.6	16.6		6.8	9.3
# 100	-	0.4	9.6	0.8		8.8	5.2
# 200	-	0.1	3.3	0.1	100.0	1.2	1.6
# 325	-	-	-	-	95.5	1.8	0.8
Liquid	-	-	-	-	62.8	9.0	-

Note - Fig. 1.49 shows the Materials Distribution by Sieve.

DESIGN SUMMARY FOR MIX 5

DESIGN COMPRESSIVE STRENGTH:	4550 PSI (31.4 MPa)
EQUIVALENT FLEXURAL STRENGTH:	700 PSI (4.83 MPa)

MAXIMUM AGGREGATE SIZE	AGGREGATE SHAPE
1 1/2 IN (38 mm)	NATURAL GRAVEL

TOTAL AIR: 5.00% +/-1.00	SLUMP: 1.50 IN (38 mm)

WATER METHOD:	MANUAL ENTRY
AMOUNT:	24.5 GAL-US (92.7 liters)

CEMENT METHOD:		MANUAL ENTRY
AMOUNT:	541	[379] LB (172 kg)
W/C :	4.3	[4.4] GAL/SK (16.7 liters/sk)

MINERAL ADDITIVE METHOD:		REPLACEMENT BY VOLUME
ADDITIVE 1:	142	[142] LB (64.4 kg)

SEVERE EXPOSURE CONDITIONS
NO SEVERE EXPOSURE

COARSE AGGREGATE METHOD:		W-ADJUST WORKABILITY FACTOR	
ACI bbo	-	PERCENT STONE	51.9
W-ADJUST	31.5	PERCENT MORTAR	51.1
TOTAL FM	5.39	NRMCA FM	-

	AMOUNT	FINENESS MODULUS
LIMESTONE	1711 LB (776 kg)	7.32

FINE AGGREGATE METHOD:		PRODUCE A SPECIFIC VOLUME
	AMOUNT	FINENESS MODULUS
BUCKSHOT	381 LB (173 kg)	4.86
CRUSHED SAND	742 LB (337 kg)	2.82
CONCRETE SAND	405 LB (184 kg)	2.75

MIX VOLUME: 27.00 CU FT (0.765 m^3)

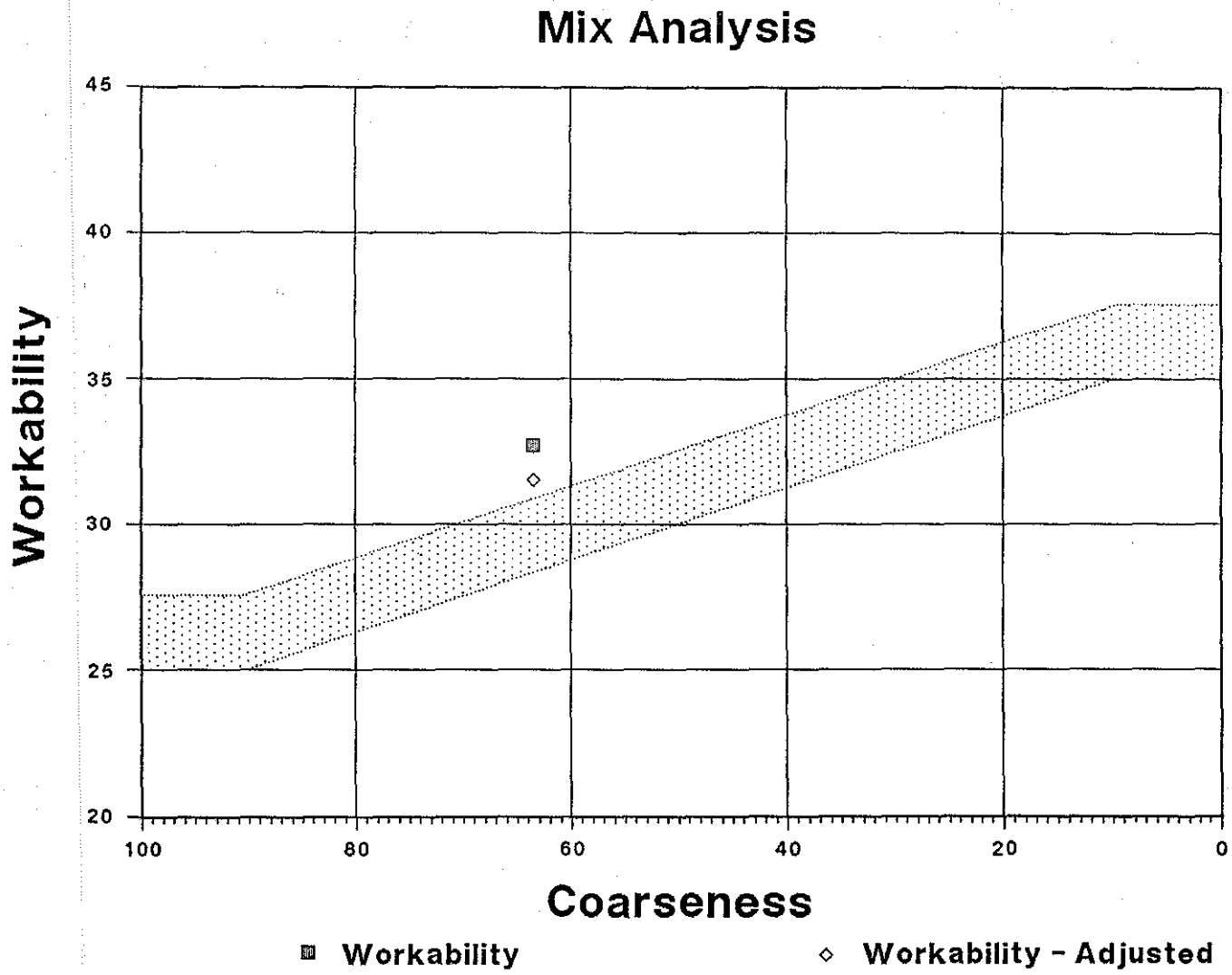

Fig. 1.47. Workbility versus Coarseness of Mix Design 5.

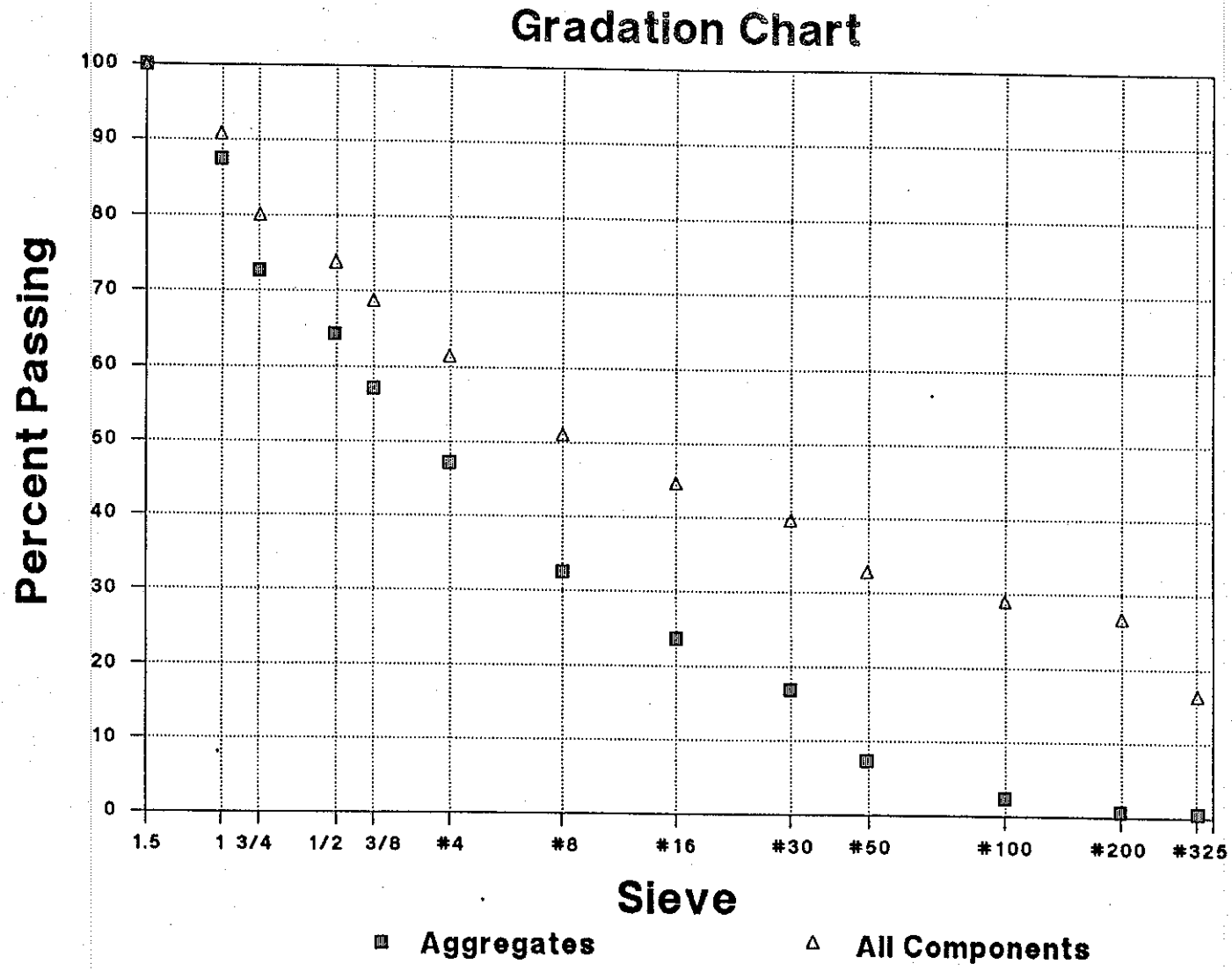

Fig. 1.48. Full Gradation of Mix Design 5.

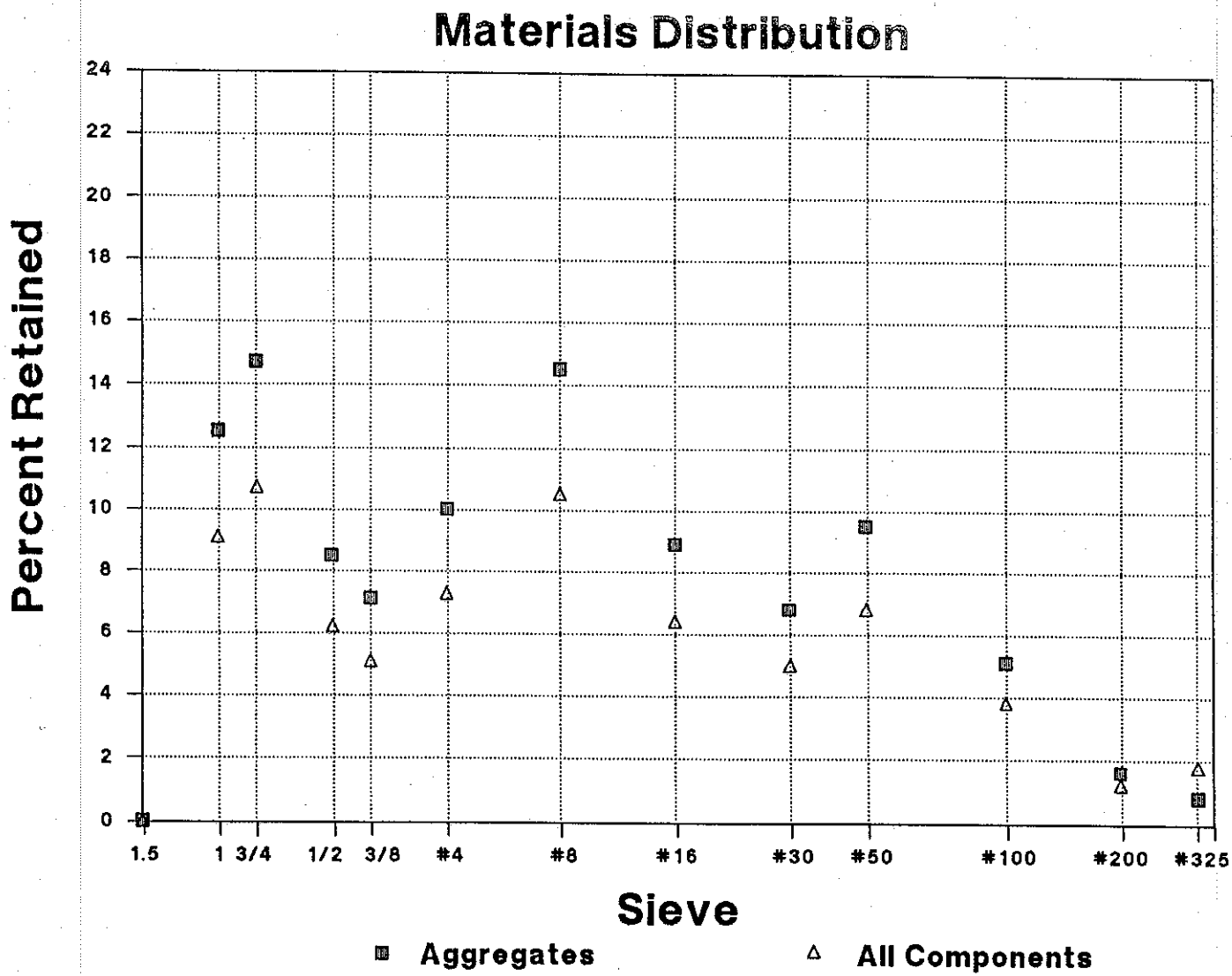

Fig. 1.49. Materials Distribution of Mix Design 5.

CHAPTER 2: FIELD TEST IN LA PORTE

2.1. INTRODUCTION

The test sections on SH 225 in La Porte, Texas, were paved on November 11, 1991 and opened to traffic on December 12, 1991. These test sections are new CRC pavement placed 13 inches (330 mm) thick with two layers of steel reinforcement. The total length of the test pavement was 2550 feet (777 m) (Fig. 2.1) and was sub-divided into nine test sub-sections (with a buffer section at each end). Each sub-section was 250 feet (76 m) long, 12 feet (3.66 m) wide and each buffer section, 150 feet (45.7 m) long. Paving started at the west end of the test pavement at 8:00 a.m. and ended at the east end of the test pavement at 8:30 p.m. The paving direction was identical with the traffic direction. Although the concrete mix design was the same for each sub-section pavement of the test, different orientations of the transverse steel reinforcing, different curing methods and different cracking control methods were applied. The purpose of the field investigation was to detect the factors that affect the cracking behavior of the CRC pavement. Many different variables were measured and cracks were surveyed at pavement ages ranging from 3 days to 125 days.

2.2. STEEL REINFORCEMENT AND CURING METHODS

The concrete used for the pavement contained river gravel as the coarse aggregate. The pavement section had two layers of reinforced steel with #5 steel as the longitudinal rebars and #6 steel as the transverse rebars. The top layer of transverse rebars was placed at the mid-depth of the pavement; and the bottom layer of transverse rebars was 2.5 inches (63.5 mm) above the surface of the subgrade (Fig. 2.2). In all the sub-sections except Sub-Section 2, the transverse rebars were perpendicular to the longitudinal reinforcement, and the interval between adjacent longitudinal rebars was 8 inches (203 mm) while adjacent transverse rebars were placed 3 feet (0.91 m) on center. Accordingly, the percentage of the longitudinal steel was 0.6%. The transverse reinforcement was placed in an alternating pattern between the top and bottom layers of longitudinal steel as shown in Fig. 2.2.

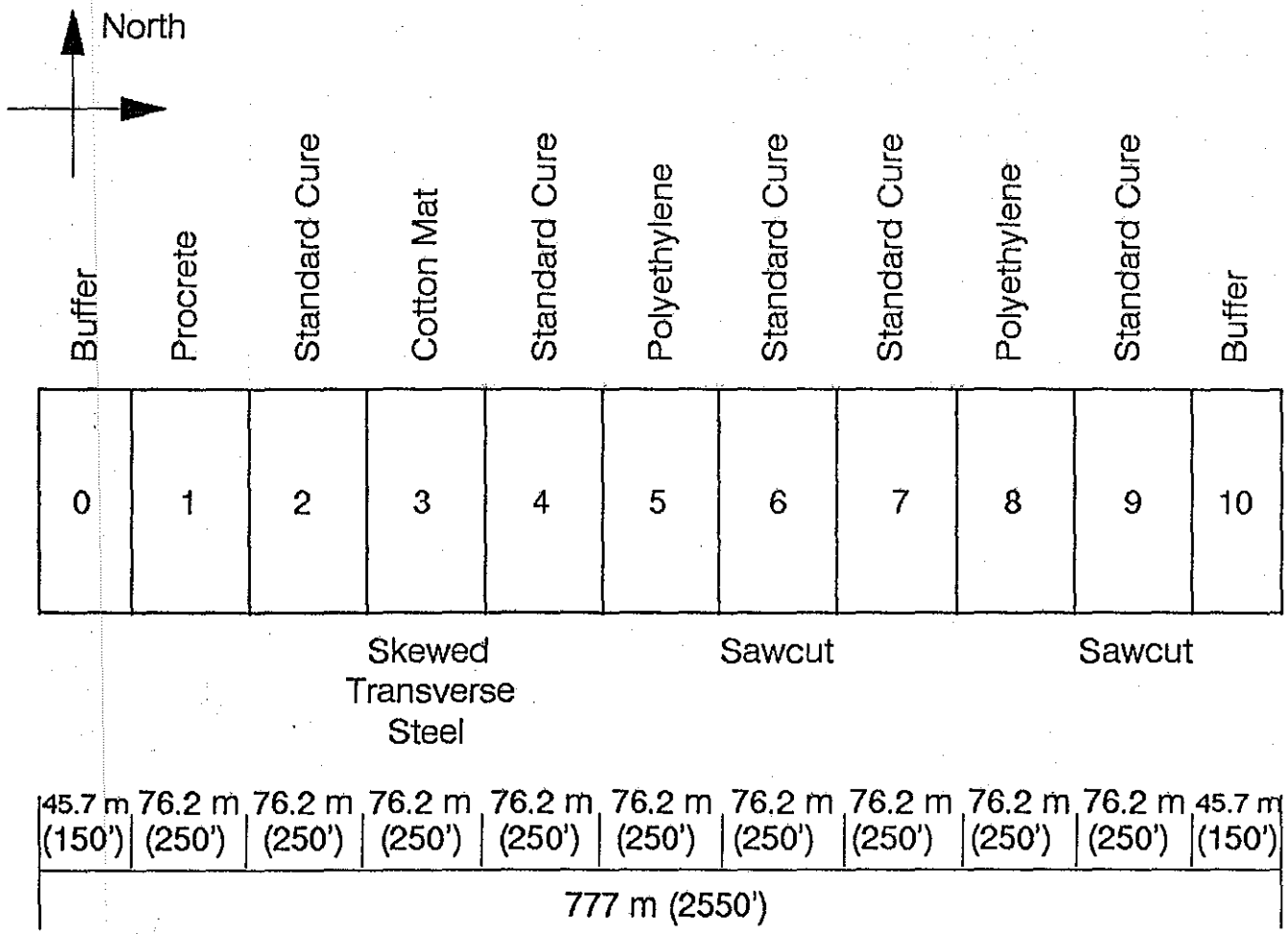

Fig. 2.1. Layout of the Test Sections in La Porte, Texas.

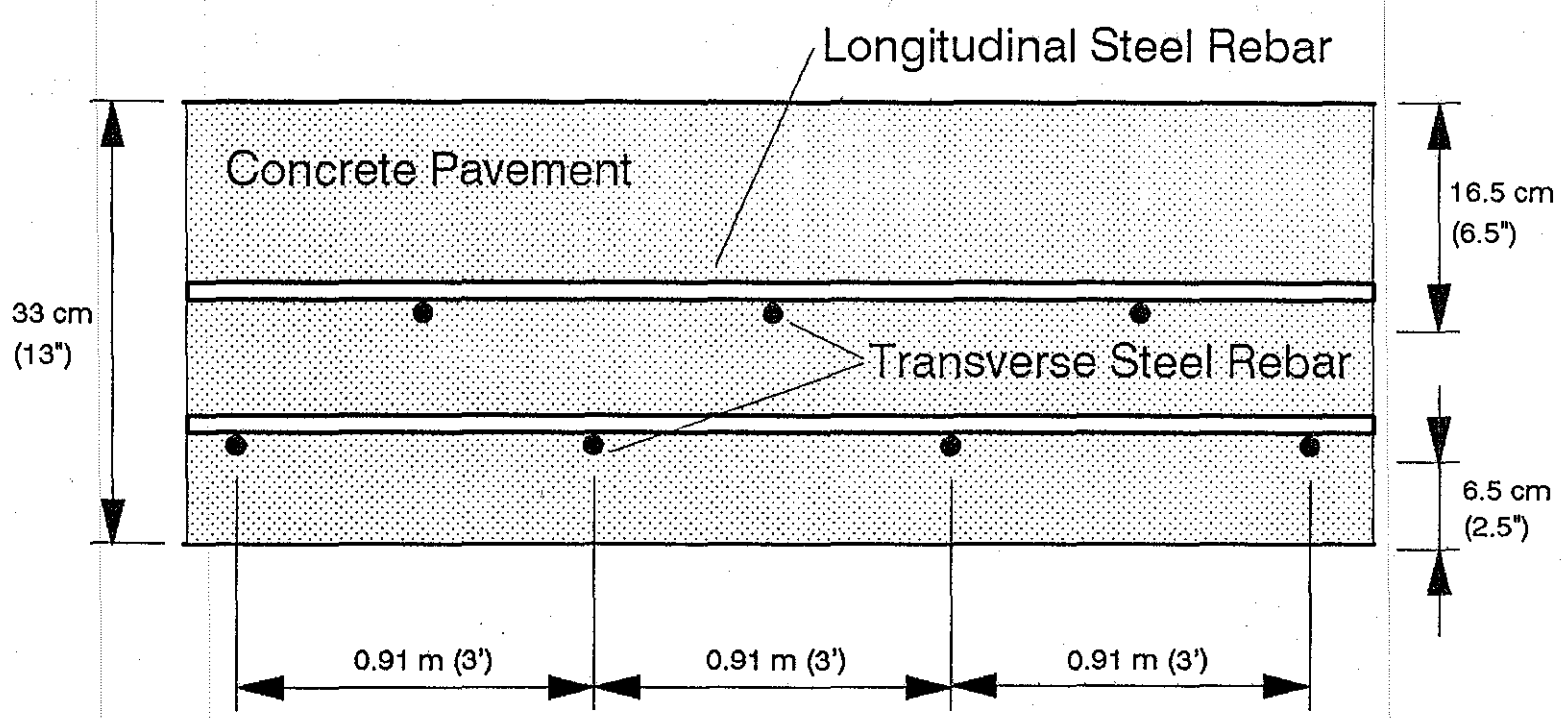

This sketch is not in proportion to the actual size.

Fig. 2.2. Steel Rebars in the Pavement of the Test Sections.

Transverse steel rebars were skewed in Sub-Section 2 to form an angle of 60° with the pavement edge. These rebars were also placed 3 (0.91 m) feet on center. Four different curing methods were employed. The curing method applied to each section is indicated in Fig. 2.1. These curing methods are as follows:

(i) Membrane curing compound, Item 360.2 (13), is referred to as the standard curing method and noted as "Standard Cure";

(ii) Membrane curing compound, Item 360.2 (13), using Procrete - a proprietary product, is noted as "Procrete";

(iii) Cotton mat curing, Item 360.2 (15), plus membrane curing, Item 360.2 (13), noted as "Cotton Mat"; and

(iv) Polyethylene film curing, Item 360.2 (12), plus membrane curing, Item 360.2 (13), noted as "Polyethylene."

The buffer sections were cured with the standard curing methods.

2.3. Sawcut for Crack Control

The longitudinal joint in the test sections was cut by using early-aged sawcutting techniques. This technique is different from conventional sawcut methods which use external sources of water to cool the blade during cutting operations. This method allows the concrete to be sawcut at an early age with minimal or no raveling which is typically much earlier than what is possible using conventional sawcut methods. The notch placed by the early-aged method was approximately 1 inch (25.4 mm) in depth.

The early-aged technique was used to place transverse sawcuts at specified intervals in Sub-Sections 6 and 9. A series of transverse sawcuts 175 feet (53.3 m) in length was placed in Sub-Section 6. Within the series, the spacing of the transverse sawcuts was 3 feet for a length of 57 feet, and in the remaining portion, the spacing of the transverse sawcuts was 5 feet (4.5 m). The transverse sawcut operations started at 9:00 p.m. on Nov. 11, or about seven hours after placement of the concrete in Sub-Section 6. Four sawcut machines were used simultaneously in order to meet the pavement cutting schedule. Sawcutting operations, Sub-Section 6, ended at 9:00 a.m., November 12. No apparent ravelling of the sawcut joints was evident. Twenty-five feet of Sub- Section 9 was sawcut transversely.

2.4. Weather Information

A portable weather station was placed near the test sections during and after placement of the concrete, recording the ambient temperature and relative humidity at the time of paving. Fig. 2.3 shows hourly temperature data acquired once an hour from November 11 to November 16, 1991. The origin of the time scale in the figure indicates 0:00 a.m., November 11. The relative humidity data represent instantly recorded data while the temperature data represent an average over an hour. As seen in the figure, the daily average temperature rose over the three-day period as did the daily average relative humidity.

2.5. Measurement of Pavement Temperature and Relative Humidity

Temperature and relative humidity are two important variables for concrete. Changes in either of these conditions can induce stresses in the pavement as well as affect the rate of the strength gain of the concrete. The influence of the parameters is very apparent during the early ages of the concrete. Both temperature and relative humidity in the test sub-sections were measured with two different digital systems. One was a product of Vaisala, in which the sensor is a capacitor. It monitors the change in capacitance of a thin polymer film as it absorbs water vapor. The other, manufactured by General Eastern, measures the change in electric resistance of a bulk polymer sensor with the moisture the sensor absorbs.

To implement these instruments, a PVC tube was inserted in the pavement from the pavement top surface. The lateral wall of the tube was tightly fitted into the pavement concrete and the concrete was exposed to the sensor though the opening end of the tube (Fig. 2.4). When the temperature and relative humidity were measured, the probe of the measuring system was inserted in the PVC tube with a rubber seal fastened around it to form a small closed space between the sensor unit and the concrete. After the measurement, the probe was removed and a PVC cap was placed on the top end of the tube to prevent air exchange between the space inside the tube and the atmosphere.

For each sub-section, 1 and 1/2 inch (25 or 13 mm) deep holes were formed in the pavement surface where the probe was inserted. Therefore, the temperature and relative humidity measurements were for the concrete close to the pavement top surface. Where

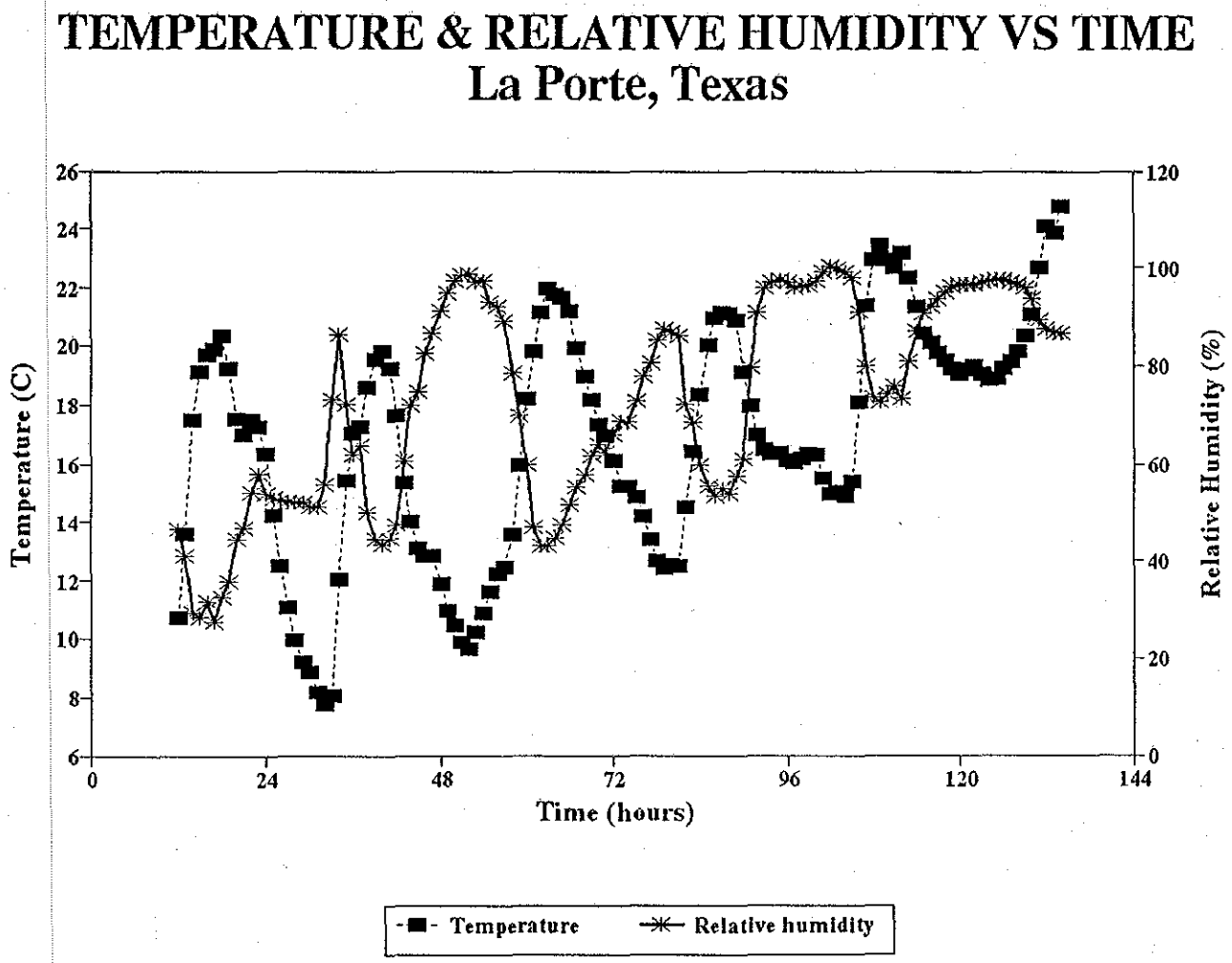

Fig. 2.3. Ambient Temperature and Relative Humidity Records.

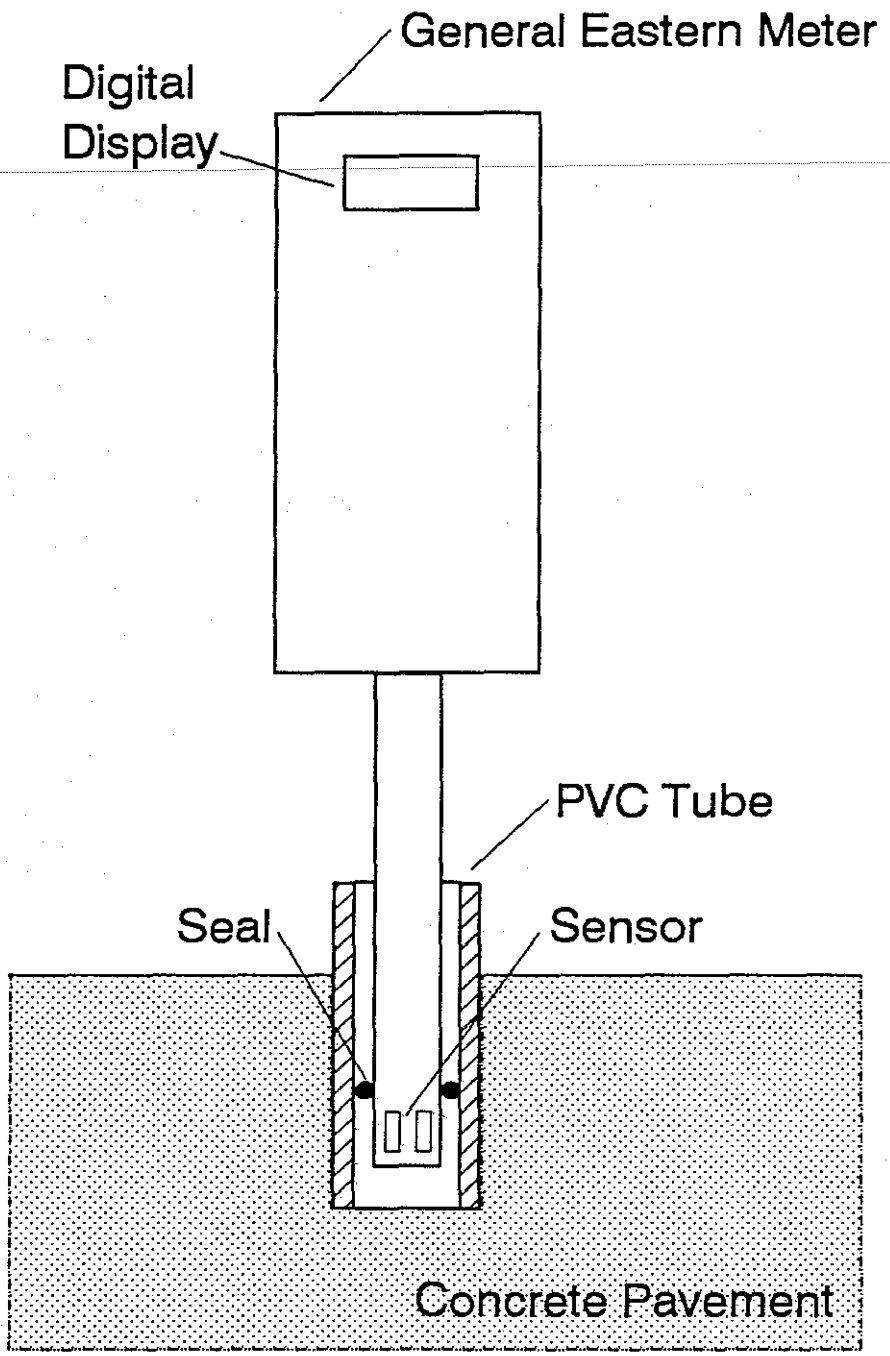

Fig. 2.4. A Set-Up for Measurement of Temperature and Relative Humidity in the Pavement.

these measurements were made automatically by a portable data recording system, the data were downloaded from the data logger system for analysis. In this way, continuous recording was achieved. Three channels in the data logger (with one probe per channel) were used to record the temperature and relative humidity at three different depths in the pavement: 1 inch (25.4 mm), 2 inches (50.8 mm) and 4 inches (101.6 mm). For security reasons, the logger system had to be dismantled during off hours, which meant that data during these periods of time were not recorded. The digital records and the graphs are included in Appendix I. As shown in the graphs, a period of time is necessary to achieve a stable record of the relative humidity. The readings over 100% were caused by saturation of the sensor element and should be considered showing 100% relative humidity in the closed space. Two of the three channels had good calibration for temperature measurement. The other one must be calibrated such that the reading can be interpreted properly.

Changes in the temperature and relative humidity in each test section measured are shown in Figs. 2.5 to 2.13, one figure for each section. The starting time of paving for each section is shown in the caption of the figure.

For comparison of different curing methods, temperature and relative humidity data for Sub-Sections 1, 3, 5 and 6 are shown in Figs. 2.14 and 2.15. The curing method used in each of these sections is indicated in the figures. It is speculated that the cotton mat kept the pavement from solar radiation, and, as a result the temperature in Sub-Section 3 was lower than in other sections (Fig. 2.14). The polyethylene film covering the pavement (Sub-Section 5) caused a "greenhouse" effect, which made the temperature in Sub-Section 5 higher than that in sub-sections which used other curing methods. However, change in temperature of pavement was caused by complicated environmental conditions as well as properties of concrete mix. Further observations are necessary before a conclusion may be reached. On the other hand, the relative humidity in Sub-Section 5 was the highest (Fig. 2.15), since the polyethylene film isolated the pavement top surface from the atmosphere and kept the moisture in the pavement from evaporating. Between the two membrane curing methods, the standard method (Item 360) caused a lower temperature and higher relative humidity in the pavement than the proprietary product.

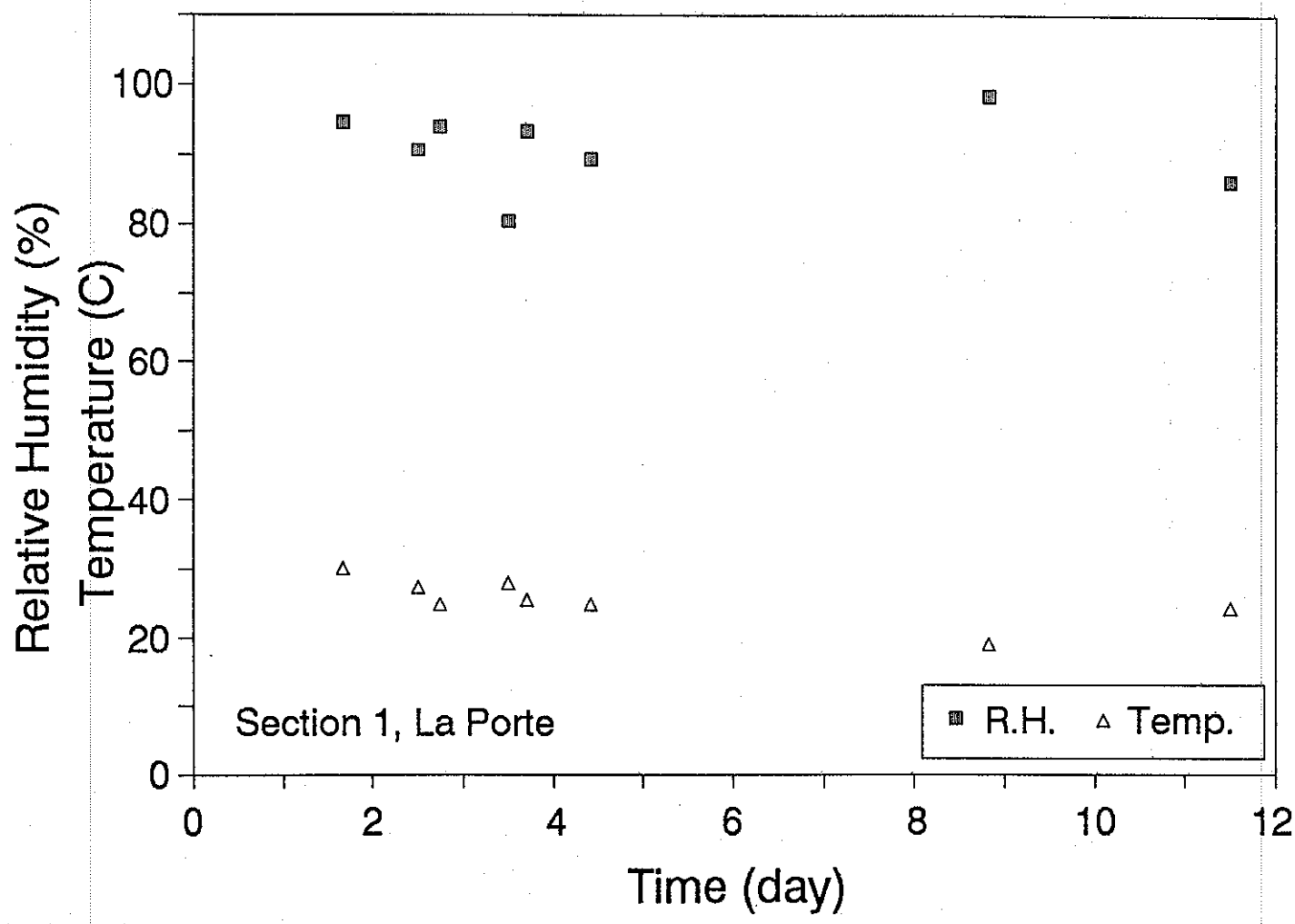

Fig. 2.5. Temperature and Relative Humidity Records for Section 1.

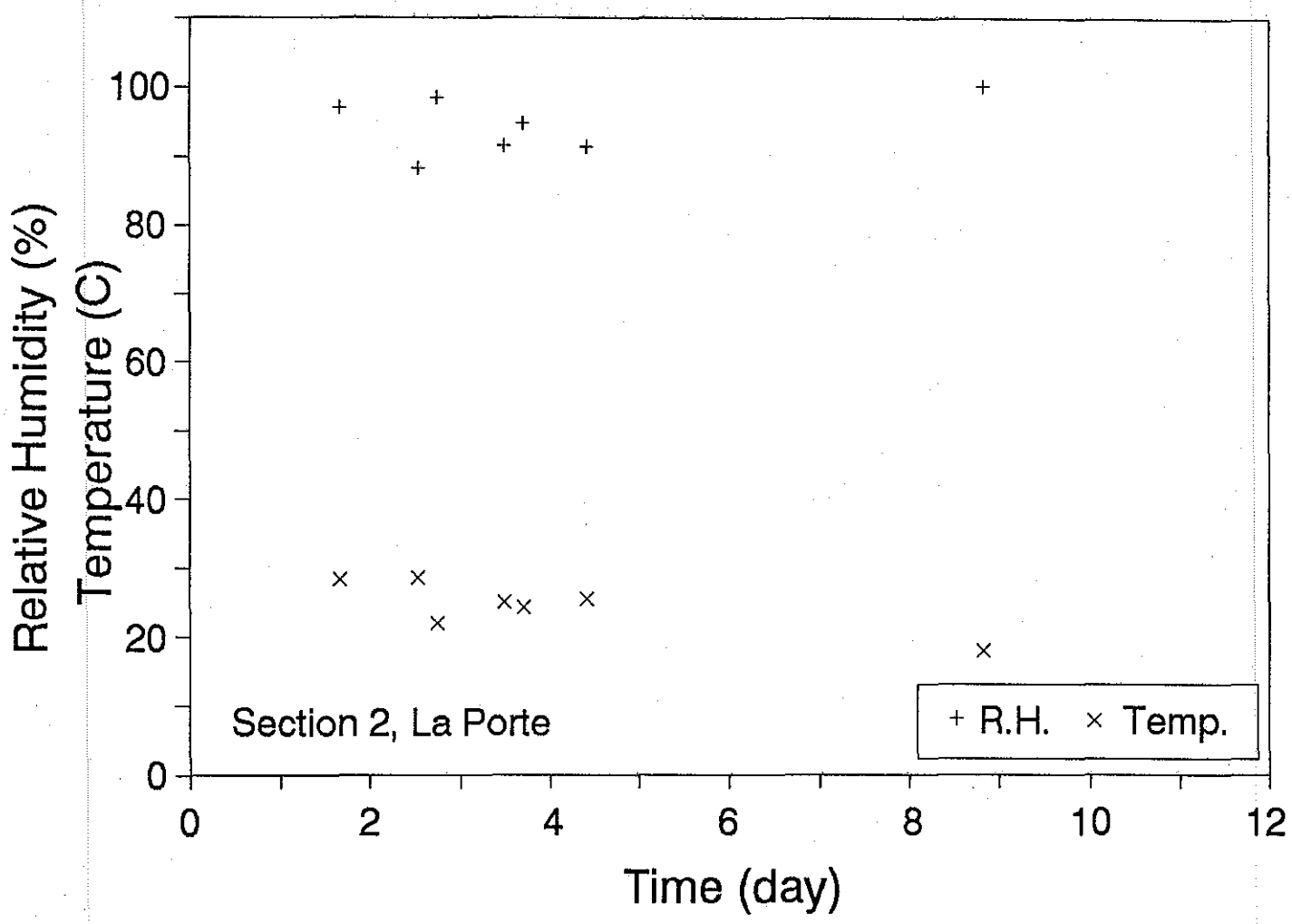

Fig. 2.6. Temperature and Relative Humidity Records for Section 2.

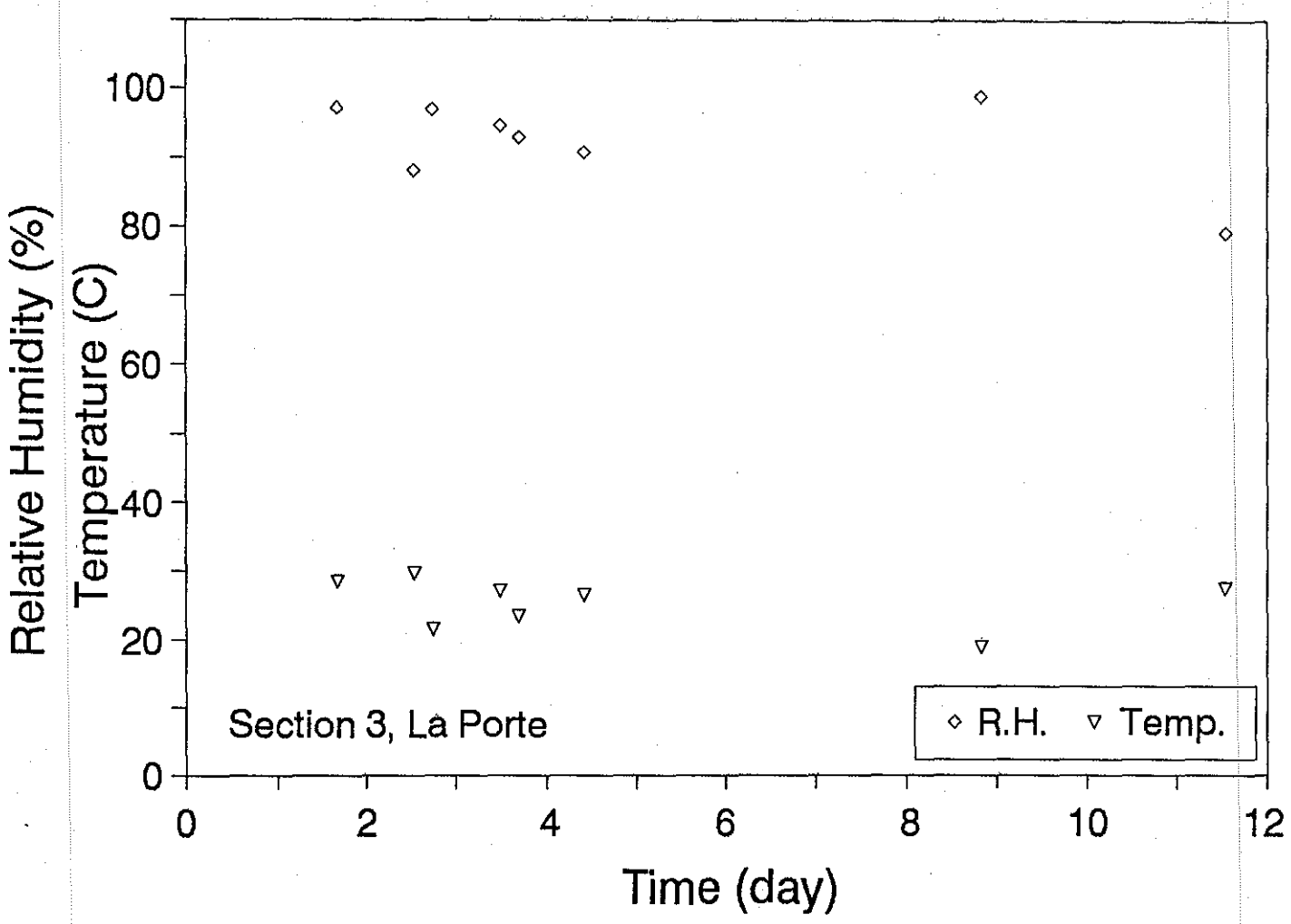

Fig. 2.7. Temperature and Relative Humidity Records for Section 3.

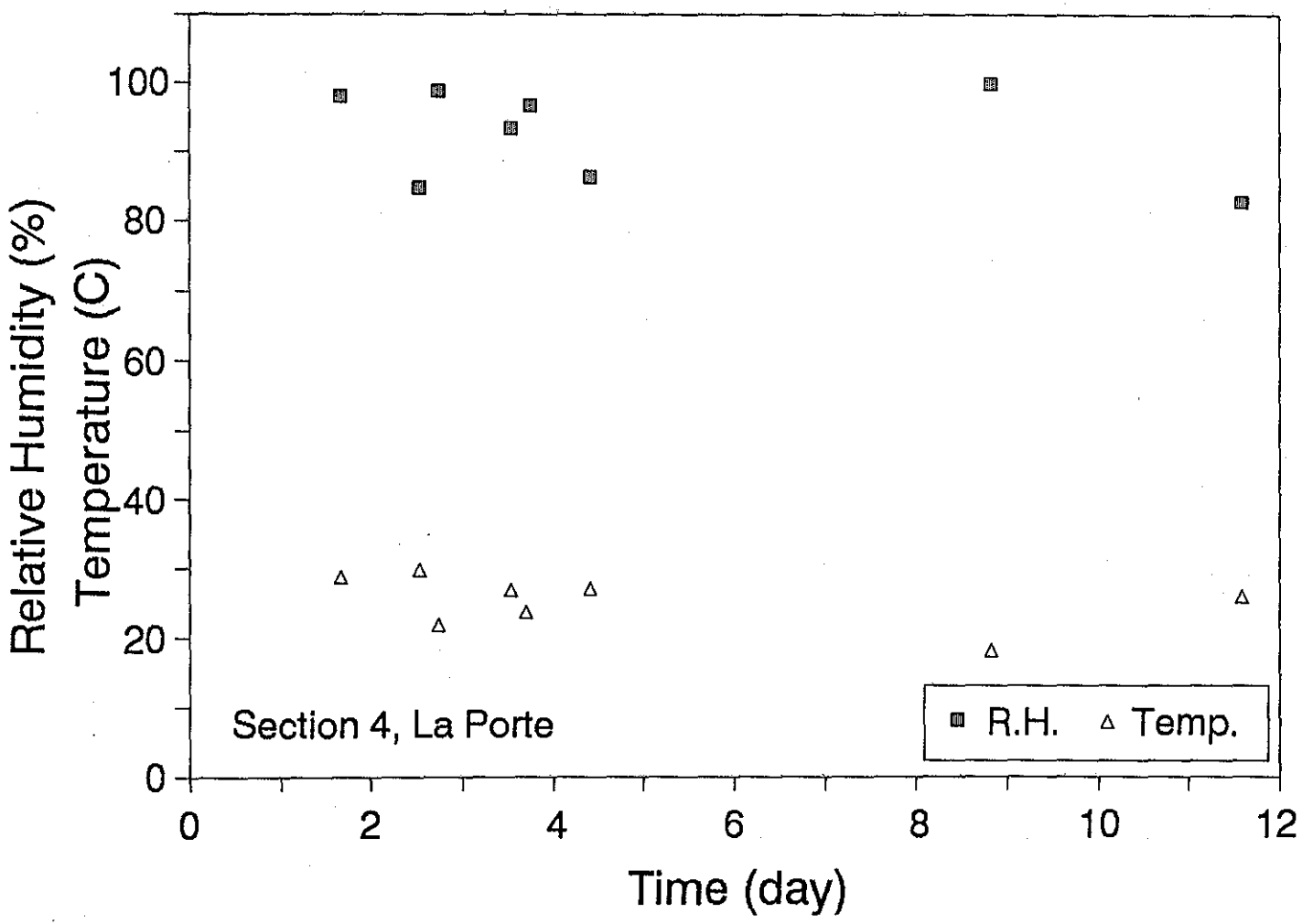

Fig. 2.8. Temperature and Relative Humidity Records for Section 4.

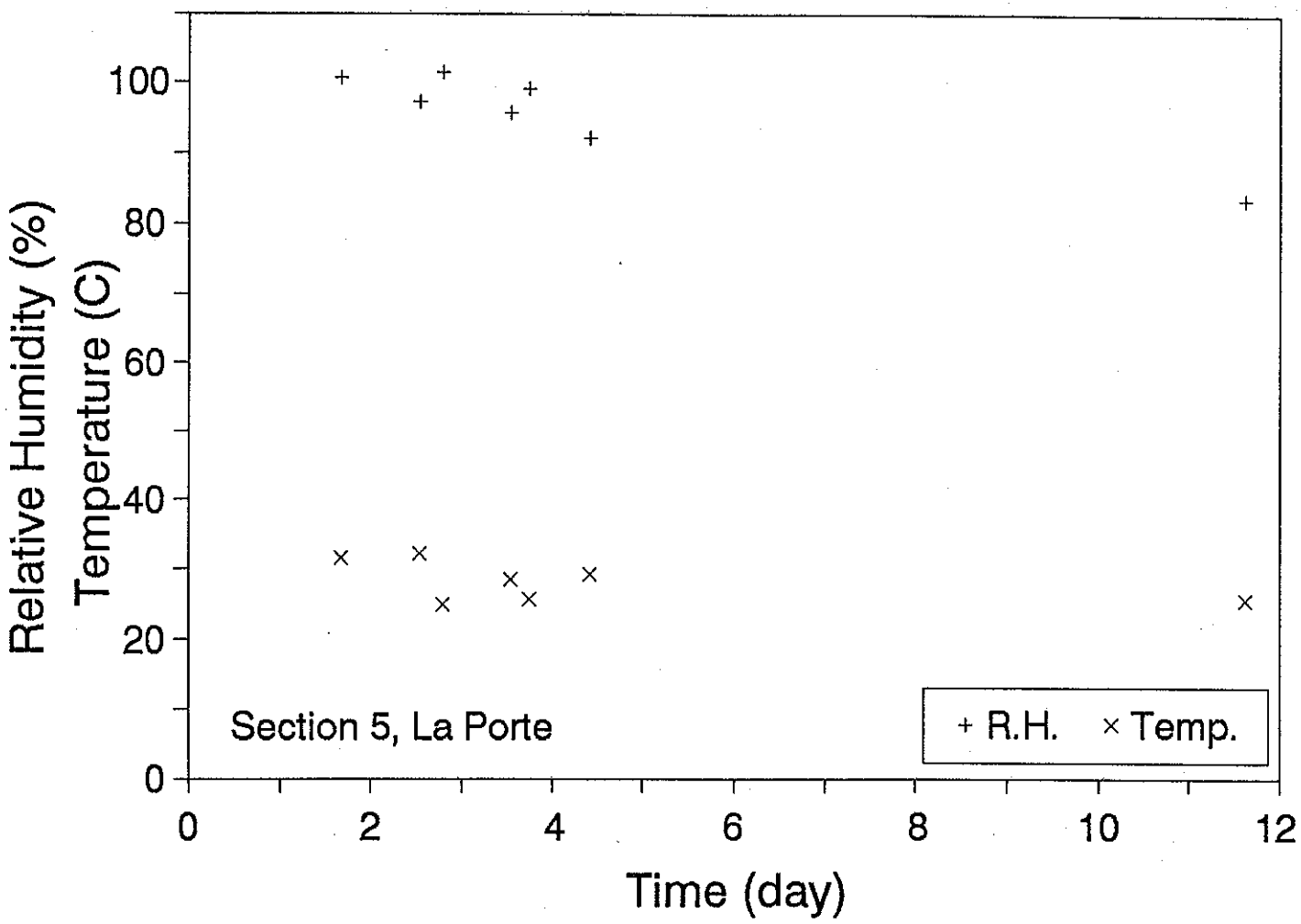

Fig. 2.9. Temperature and Relative Humidity Records for Section 5.

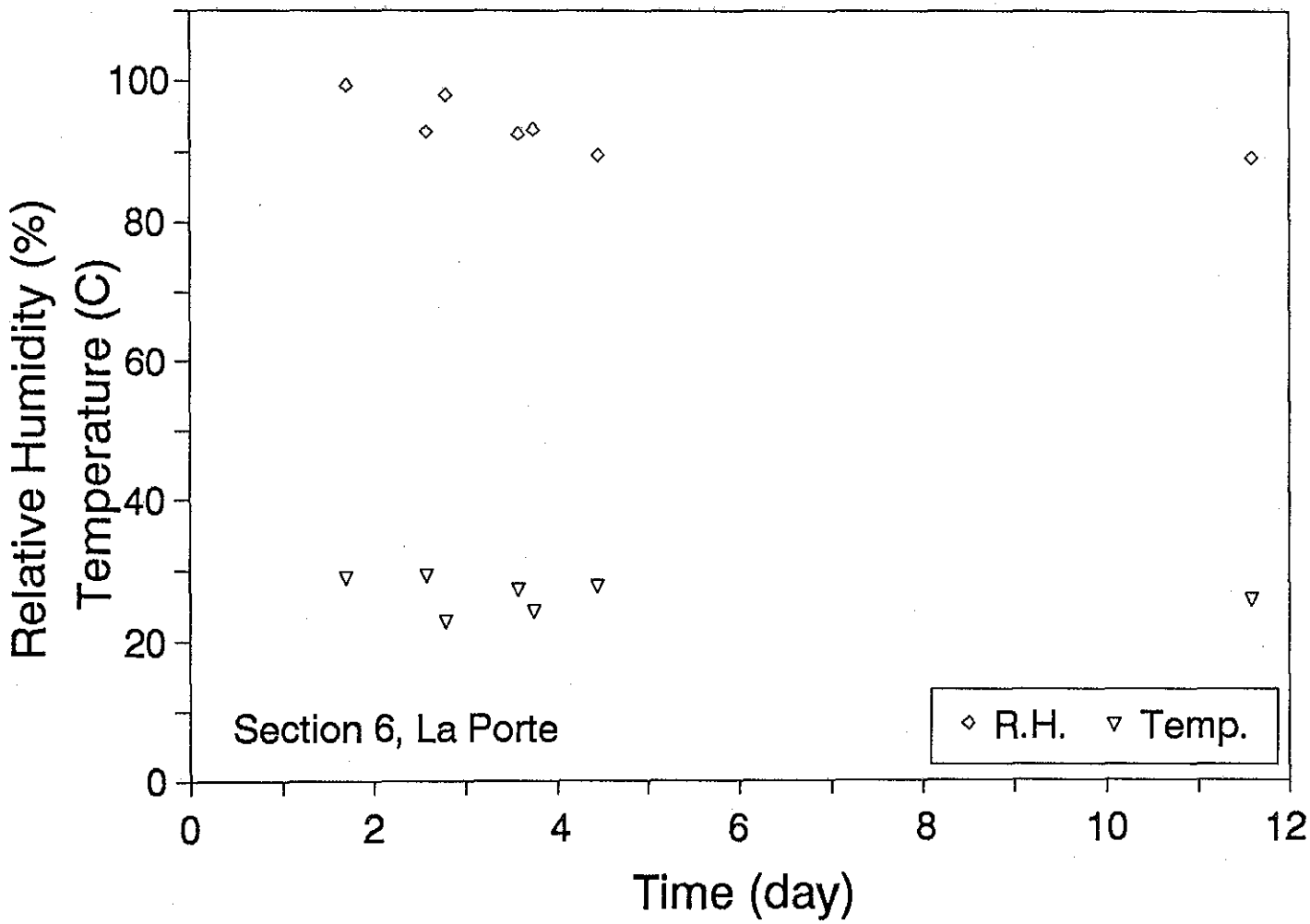

Fig. 2.10. Temperature and Relative Humidity Records for Section 6.

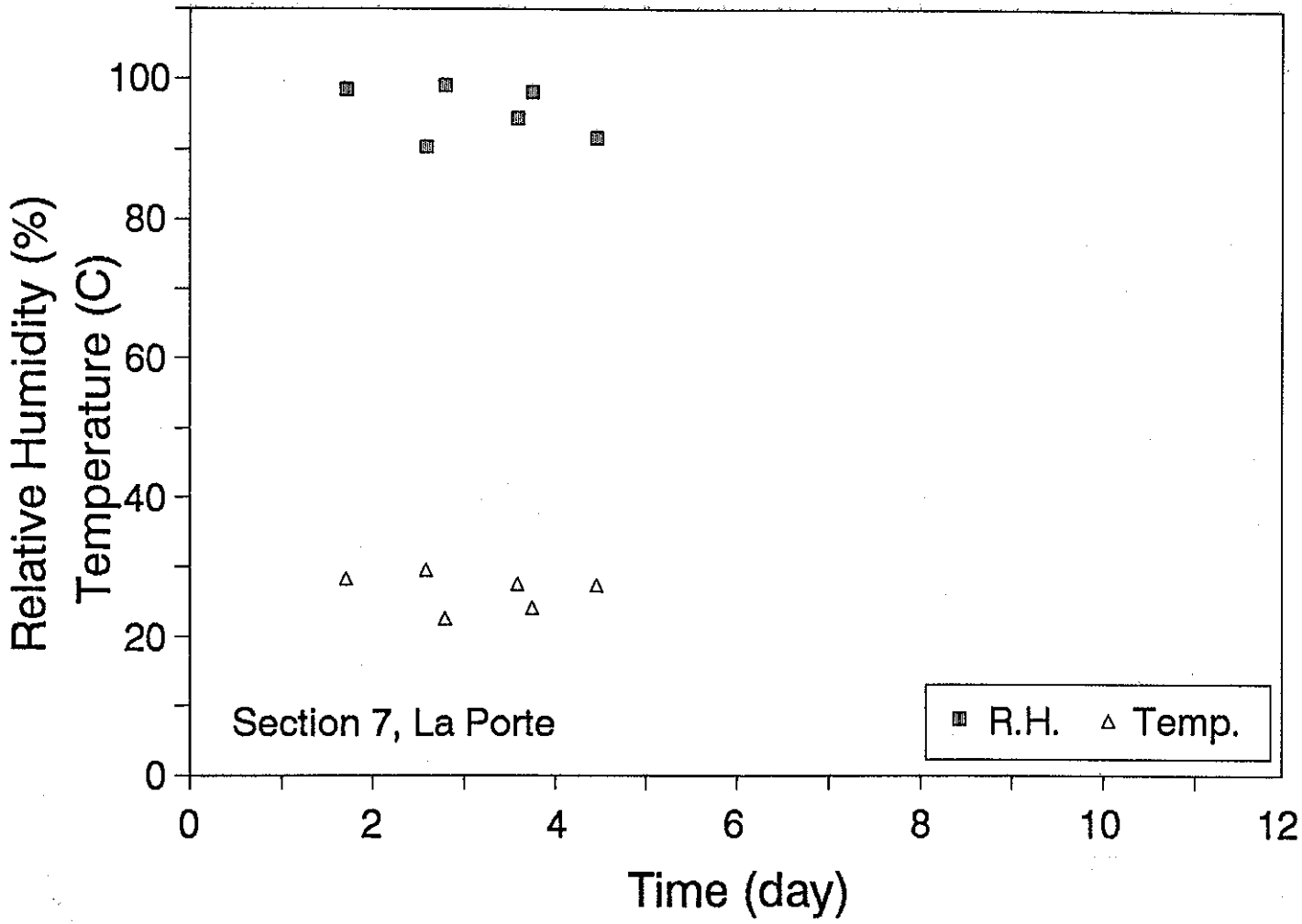

Fig. 2.11. Temperature and Relative Humidity Records for Section 7.

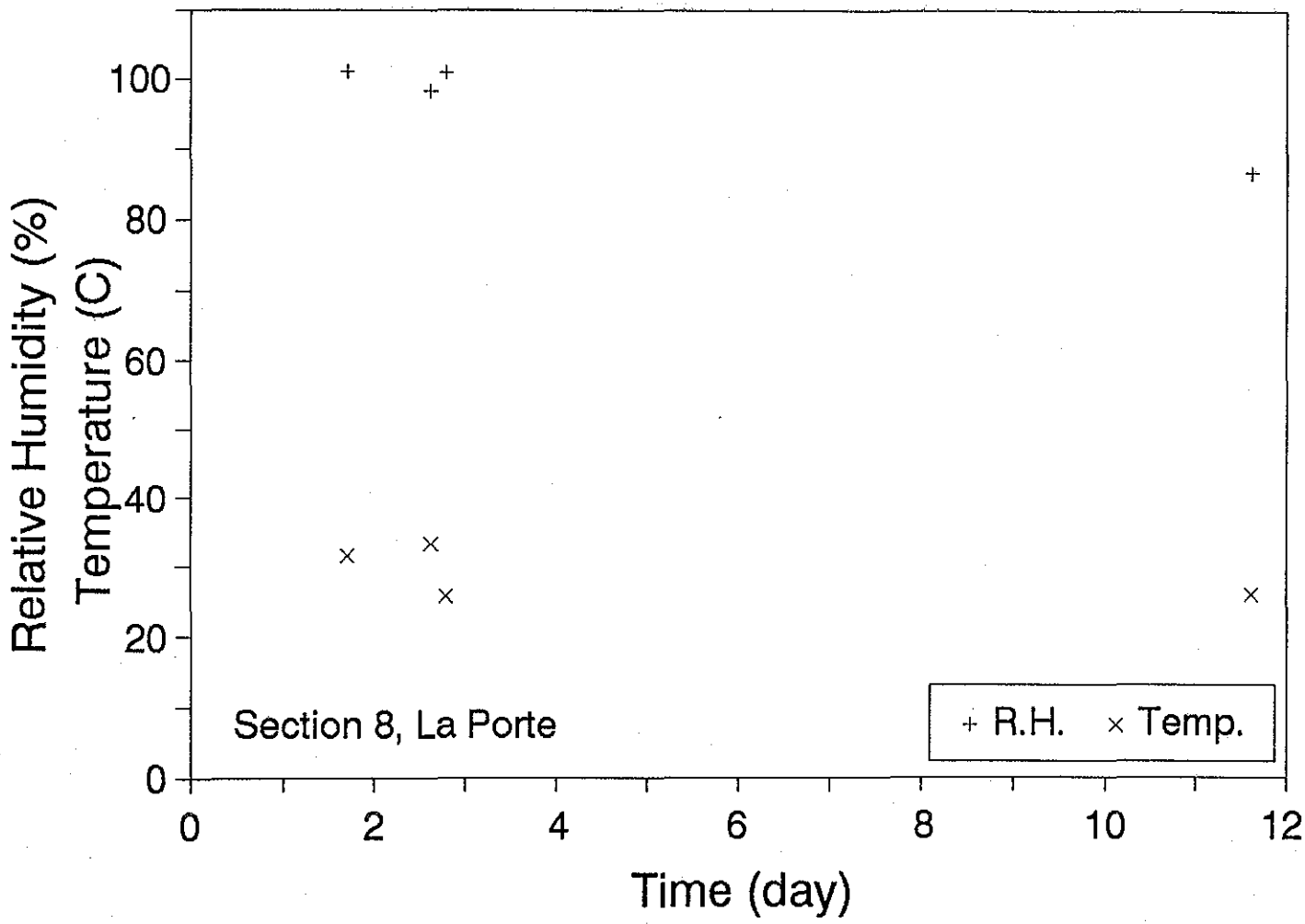

Fig. 2.12. Temperature and Relative Humidity Records for Section 8.

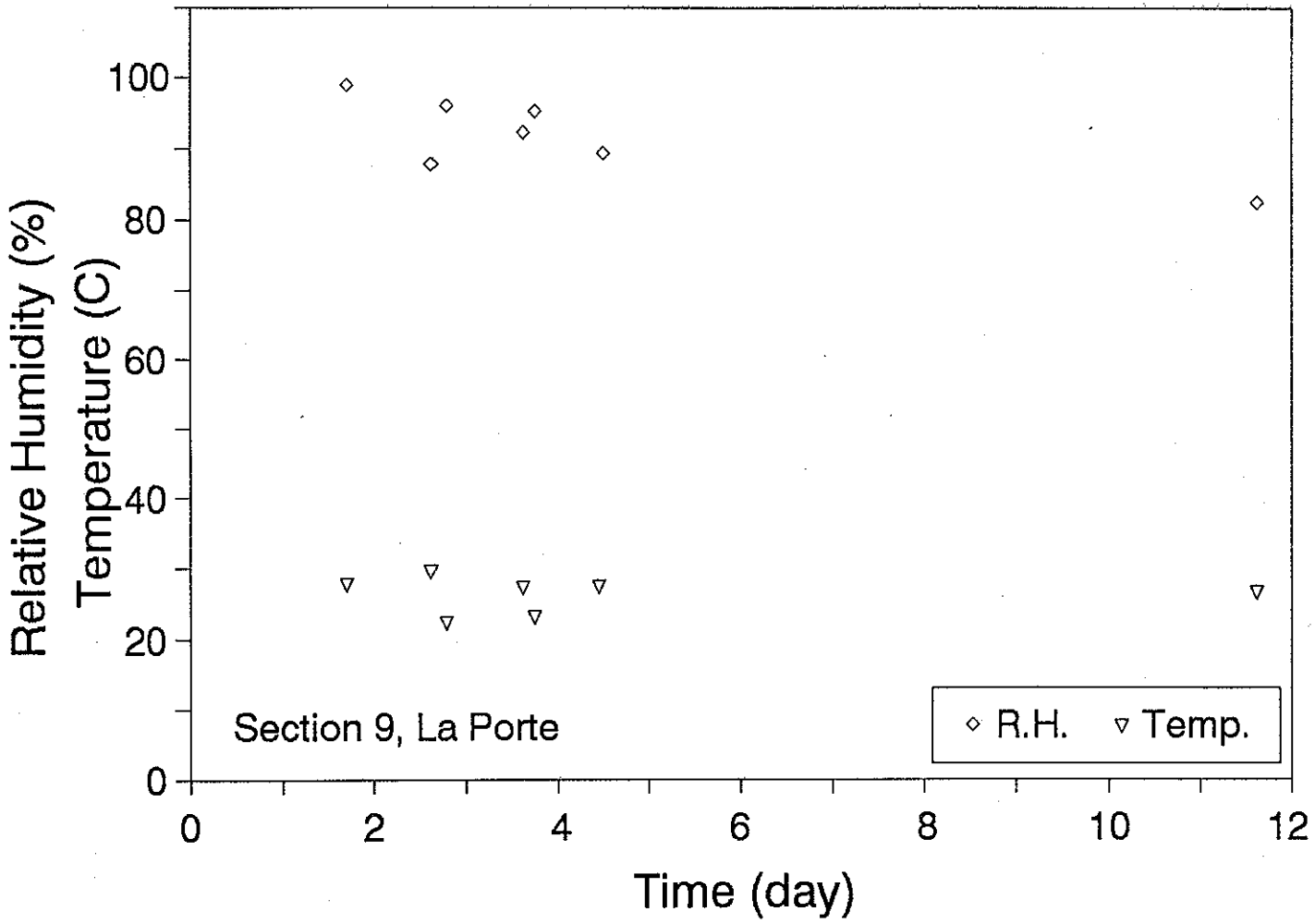

Fig. 2.13. Temperature and Relative Humidity Records for Section 9.

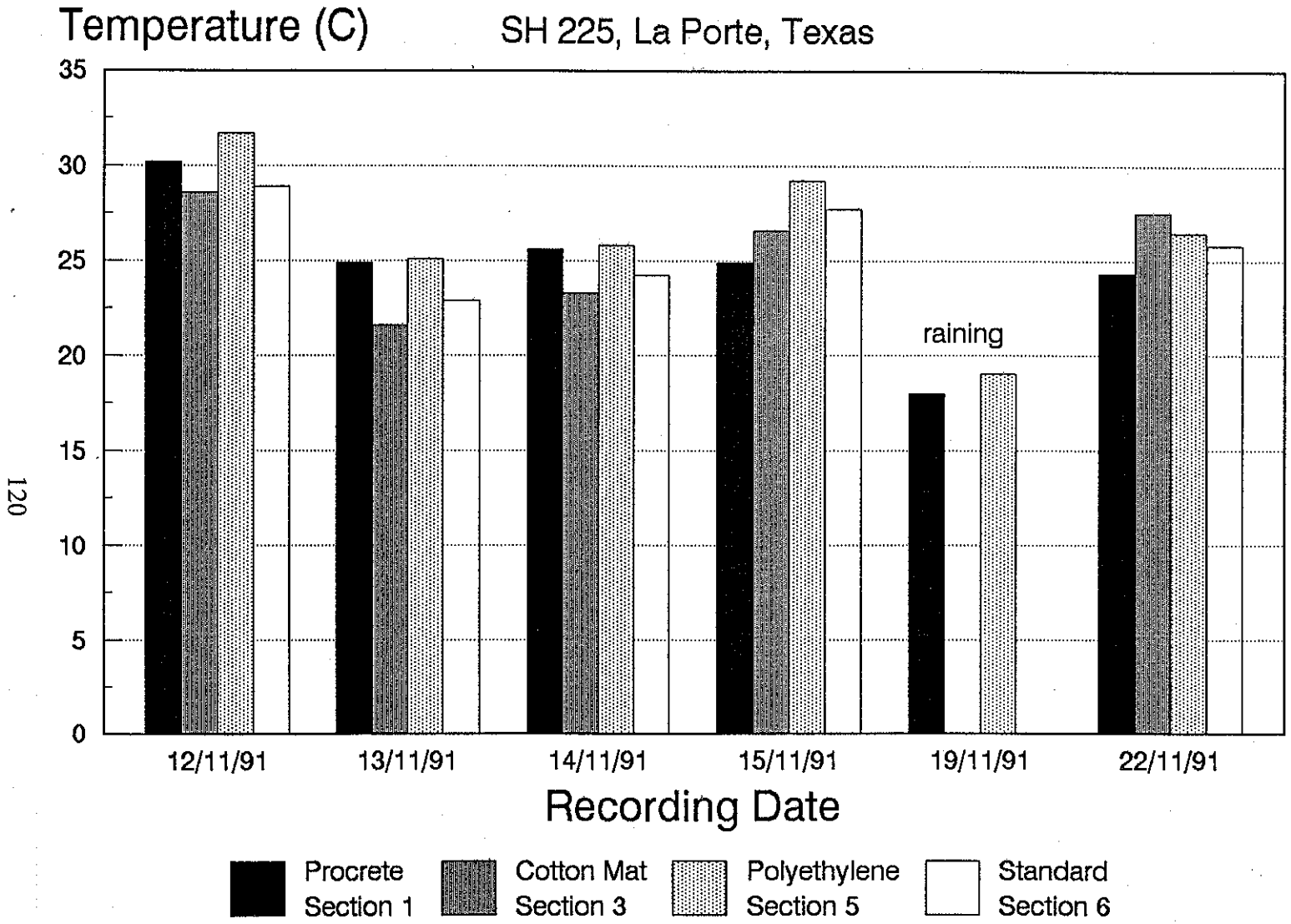

Fig. 2.14. Temperature Change in Sections Cured with Different Methods.

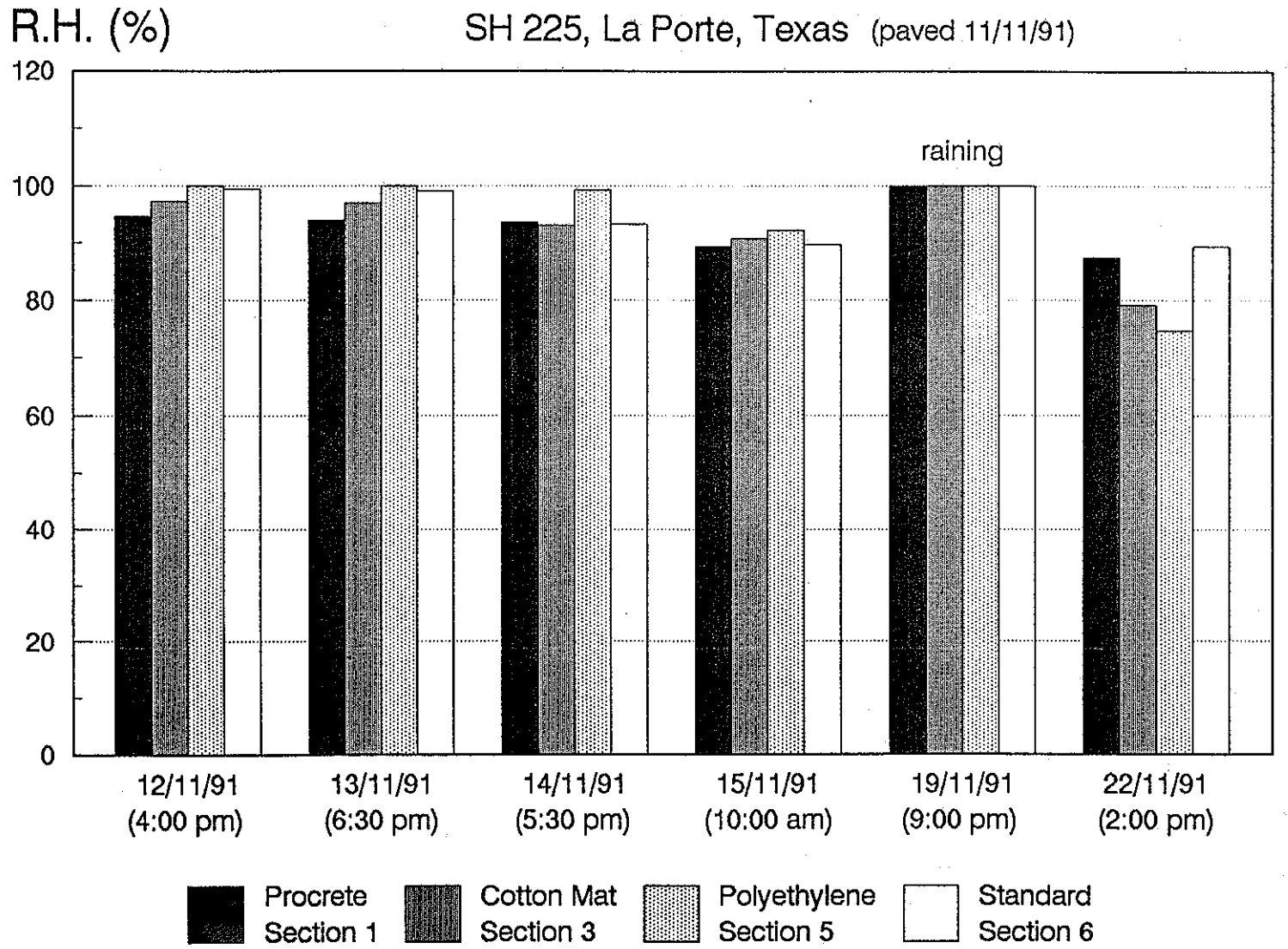

Fig. 2.15. Relative Humidity Change in Sections Cured with Different Methods.

2.6. Measurement of Pulse Velocity of Pavement

The basic principle upon which the pulse velocity method is founded proposes that if the velocity of a pulse of longitudinal waves through a medium can be determined, and if the density and the Poisson's ratio of the medium is known, then the dynamic modulus of elasticity of the medium can be computed. Furthermore, knowing the dynamic modulus of elasticity, other mechanical properties can be estimated from empirical correlation with it.

Pulse velocity measurements in each section were made in conjunction with temperature and relative humidity readings, because previous research indicated that temperature and moisture conditions of the concrete had insignificant effects on the pulse velocity. Accordingly, the pulse velocity could be considered an independent parameter to estimate the concrete strength. It was also of interest to examine the possibility of determining the proper time of sawcutting based on pulse velocity readings.

The V-Meter, a portable ultrasonic testing unit, was borrowed from the Federal Highway Administration (FHWA) in Washington, D.C. and used in every test sub-section to measure the pulse velocity. The V-Meter uses two transducers, one each for transmitting and receiving the ultrasonic pulse. The pulse travel time is displayed in three numerical digits ranging from 0.1 to 999 microseconds. In the sub-sections, the two transducers were placed on the pavement top surface, 12 inches (304.8 mm) apart from each other. Grease was used to improve the contact between the transducer end surface and the pavement surface. The measured ultrasonic velocities for each test section are shown in Figs. 2.16 to 2.18. For digital data, see Appendix II.

Since there was reinforcing steel in the pavement, a question may exist if the effect of the rebar on the pulse traveling time is negligible. Analysis results indicate that the effect of the rebar can be ignored when the rebar is embedded deeper than half the distance between the transducers, which is the case of the measurements performed in the sub-sections. For further discussion, see Appendix III. Therefore, the pulse velocity was simply obtained by dividing the distance between the two transducers, 12 inches (304.8 mm), by the recorded pulse traveling time, and then multiplied by a factor 1.05. The factor 1.05 was a

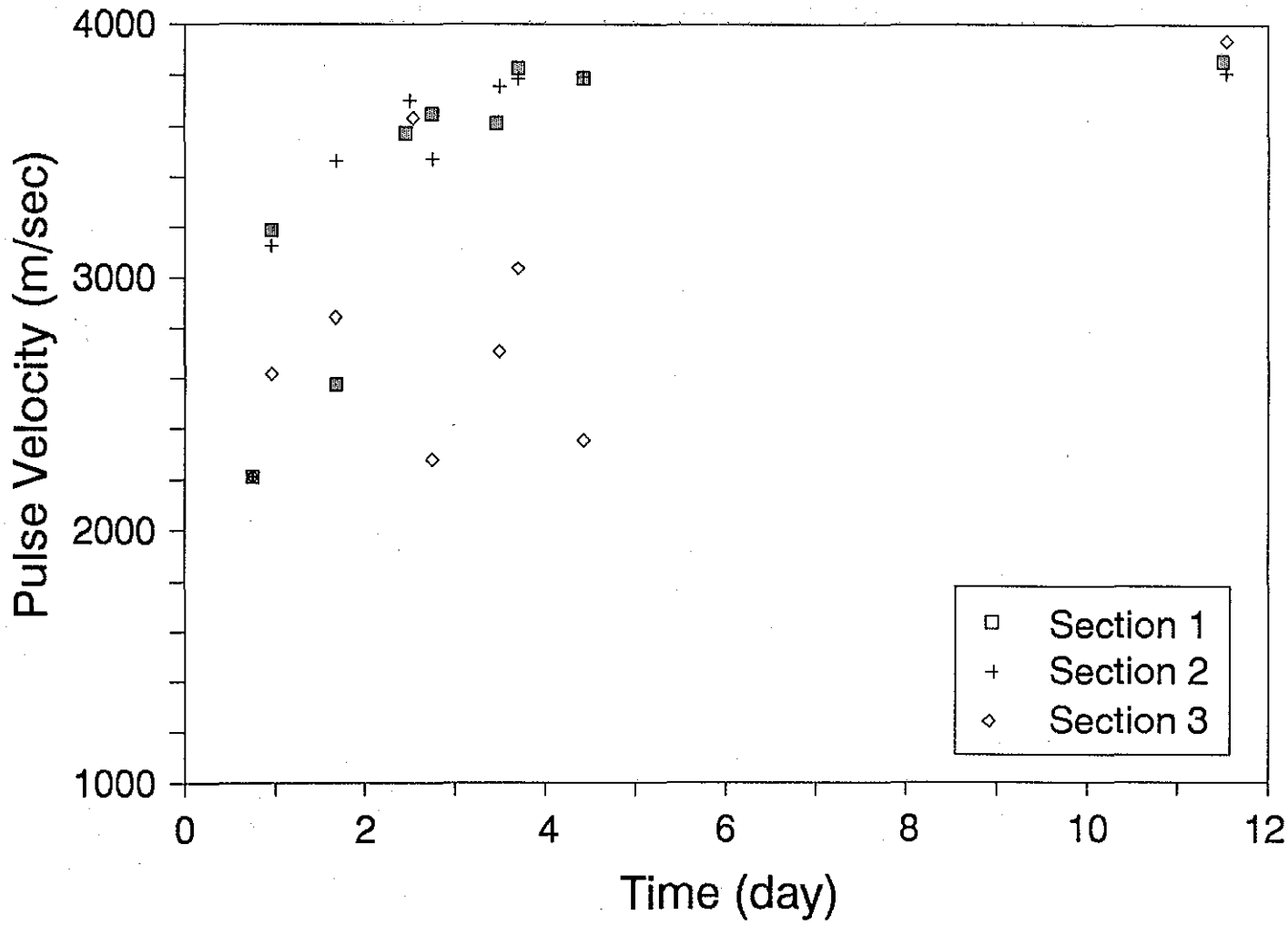

Fig. 2.16. The Pulse Velocity in Sections 1 to 3.

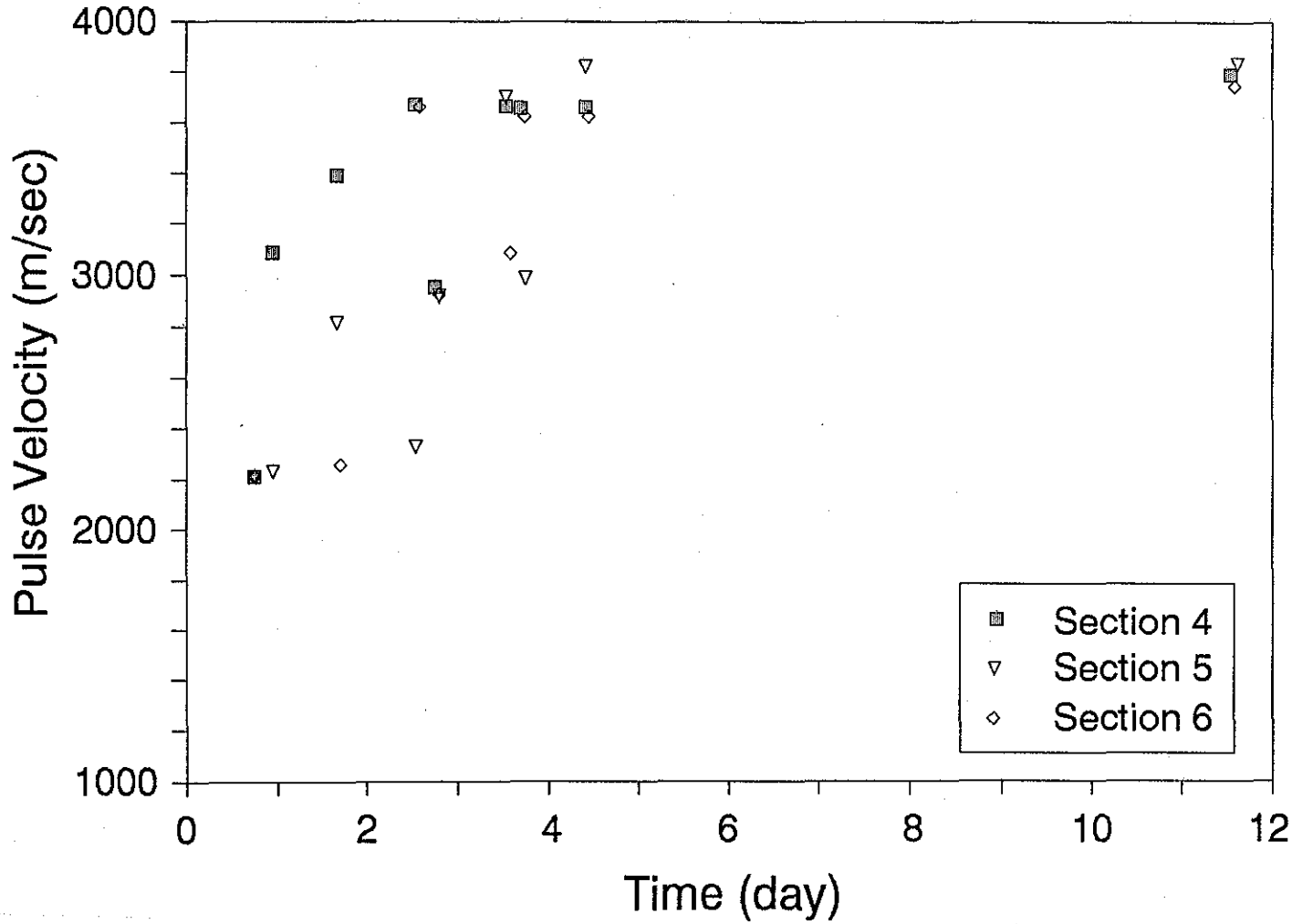

Fig. 2.17. The Pulse Velocity in Sections 4 to 6.

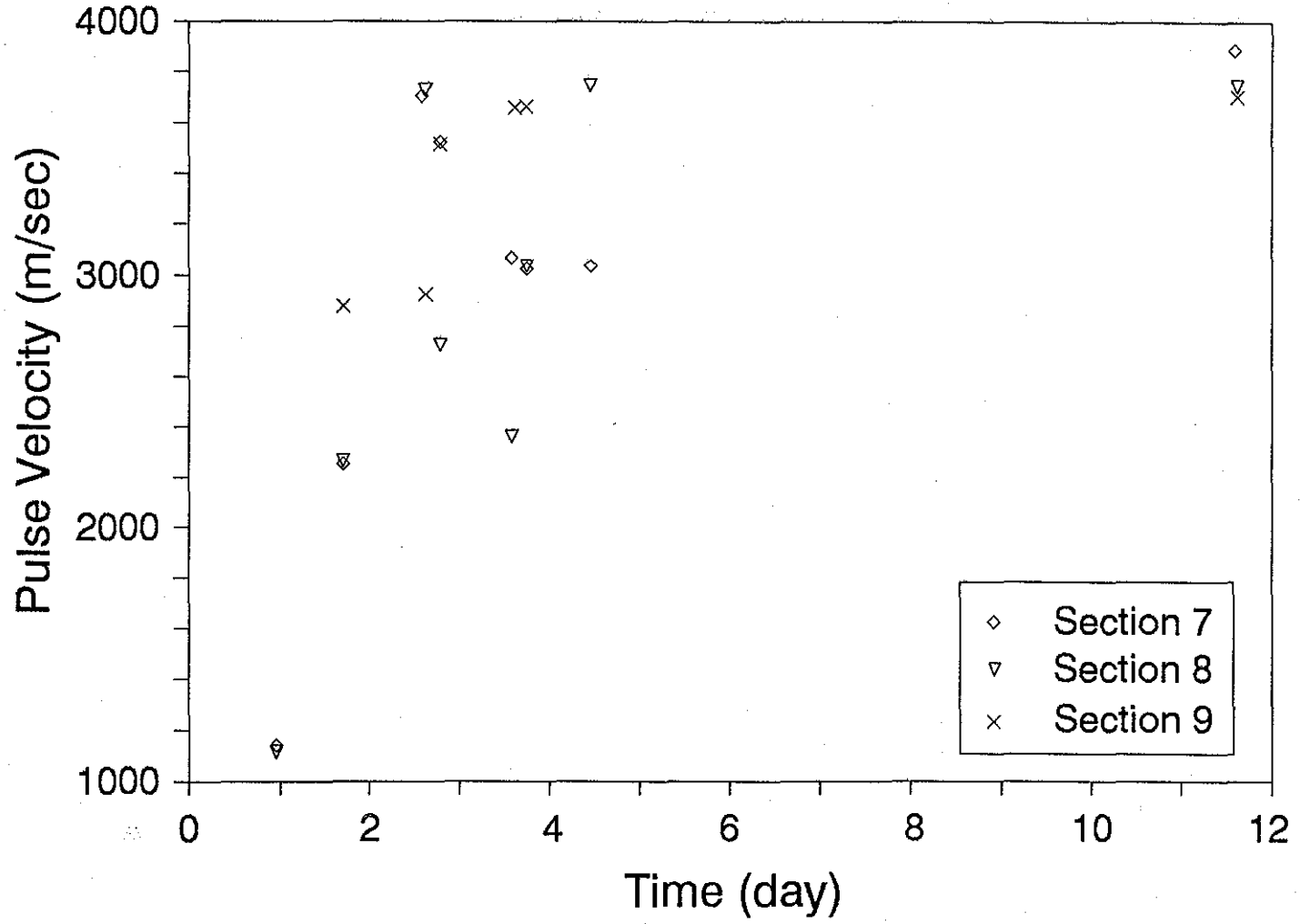

Fig. 2.18. The Pulse Velocity in Sections 7 to 9.

compensation for the pulse travelling distance since the pulse path was not along a straight line.

From the V-meter measuring records on test sections 5 and 6, an increase in pulse velocity with the pavement age can be expressed as with the coefficient of correlation $r^2 = 0.715$ (Fig. 2.19):

$$\left[\frac{PV}{1000}\right] = 7.80\ (Age)^{0.306} \tag{2.1}$$

where PV is the pulse velocity in feet/sec and Age is the pavement age in days.

Since the pulse velocity was not measured as early as the sawcutting started in the test sections, the above equation would be extrapolated to estimate the pulse velocity in the pavement when the sawcutting started. As reported above, the sawcutting started 7 hours after paving for Sub-Section 6. The pulse velocity then is given by Eq. (2.1) as PV = 5350 feet/sec (1630 m/sec). As the Concrete Technology Laboratories, Inc. (CTL) reported, the pulse velocity of the concrete that used 500 lb/yd^3 (2.12 MN/m^3) of cement in the mix design with the rounded gravel as the coarse aggregate was 5800 ft/sec (1800 m/sec) at 9-hour age when curing temperature was 50°F (10°C). This confirms the conclusion drawn by the field test as part of the same research project, Project 1244, on the test sections in Texarkana, Texas. The test sections in Texarkana were jointed concrete pavement, placed in October and November 1991, where the pulse velocity was measured when the joints were sawcut. It was reported that, in Texarkana, no apparent ravelling occurred when the pulse velocity had increased to 3600 ~ 4600 feet/sec (1100 ~ 1400 m/sec). These results suggest that the pulse velocity may be used for determining the proper time for sawcutting.

2.7. Measurement of Compressive Strength of Concrete

Two batches of standard-sized concrete cylinders were cast in the field. The first set was prepared at 1:00 p.m. when Sub-Section 5 was paved. The second set was prepared at 5:00 p.m. when test section 9 was paved. These specimens were tested in compression at concrete ages ranging approximately from 12 hours to seven days. The test data are

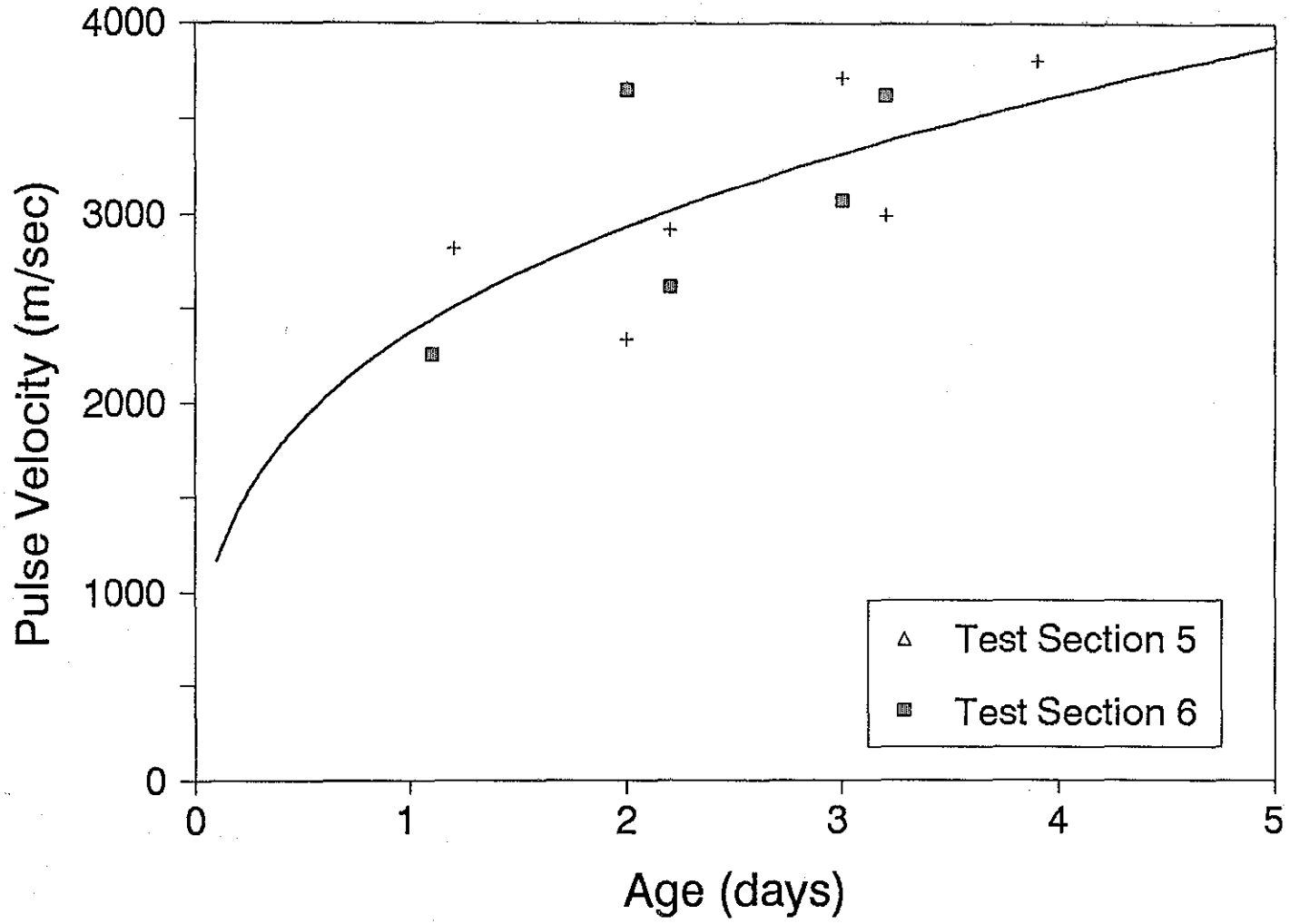

Fig. 2.19. Change in the Pulse Velocity with Pavement Age.

included in Appendix IV and shown in Fig. 2.20, where regression of the data on a semi-logarithmic curve is

$$\text{Age} = 0.534 + 2.613\times10^{-4}\ (f_c') + 1.901\times(10)^{-7}\ (f_c')^2 \qquad (2.2)$$

where f_c' is the compressive strength in psi and *Age* is the concrete age in days. The coefficient of correlation r^2 is 0.956. From this regression and relationship between the pulse velocity and the concrete age, correlation of the pulse velocity with the compressive strength is obtained, which is shown in Fig. 2.21. The regression curve for the correlation is included in the figure as well. The regression equation is as follows:

$$\left[\frac{PV}{1000}\right] = 0.724\ (f_c')^{0.340} \qquad (2.3)$$

where PV is the pulse velocity in feet/sec, and f_c' is the compressive strength in psi. The coefficient of correlation r_2 is 0.694. According to previous work by Construction Technology Laboratories, Inc. (CTL), the relationship between the pulse velocity and the compressive strength can be expressed as:

$$\log f_c' = 0.732 + 0.192\ \frac{PV}{1000} \qquad (2.4)$$

This curve is shown in Fig. 2.21, noted as CTL. From the same value of the pulse velocity, the CTL curve predicts lower compressive strength. It is worthwhile to point out that CTL curve was obtained based on the laboratory specimens while readings taken for the pulse velocity in this study were taken on actual pavements.

2.8 Measurement of Fracture Toughness

Four beam bending specimens were prepared in the field along with the first set of cylinder specimens. These specimens were of the same shape (Fig. 2.22). The depth of

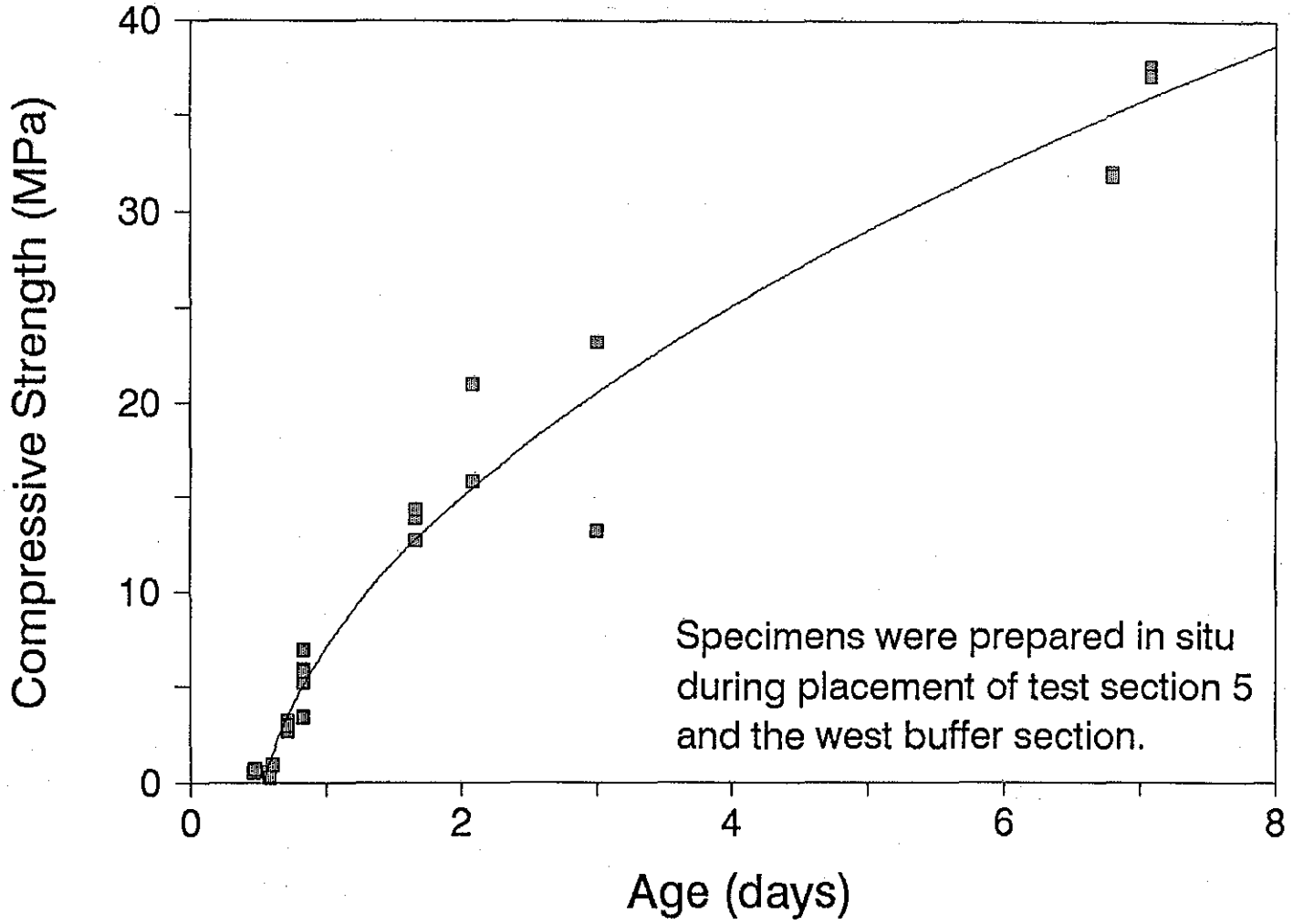

Fig. 2.20. Change in the Compressive Strength with Concrete Age.

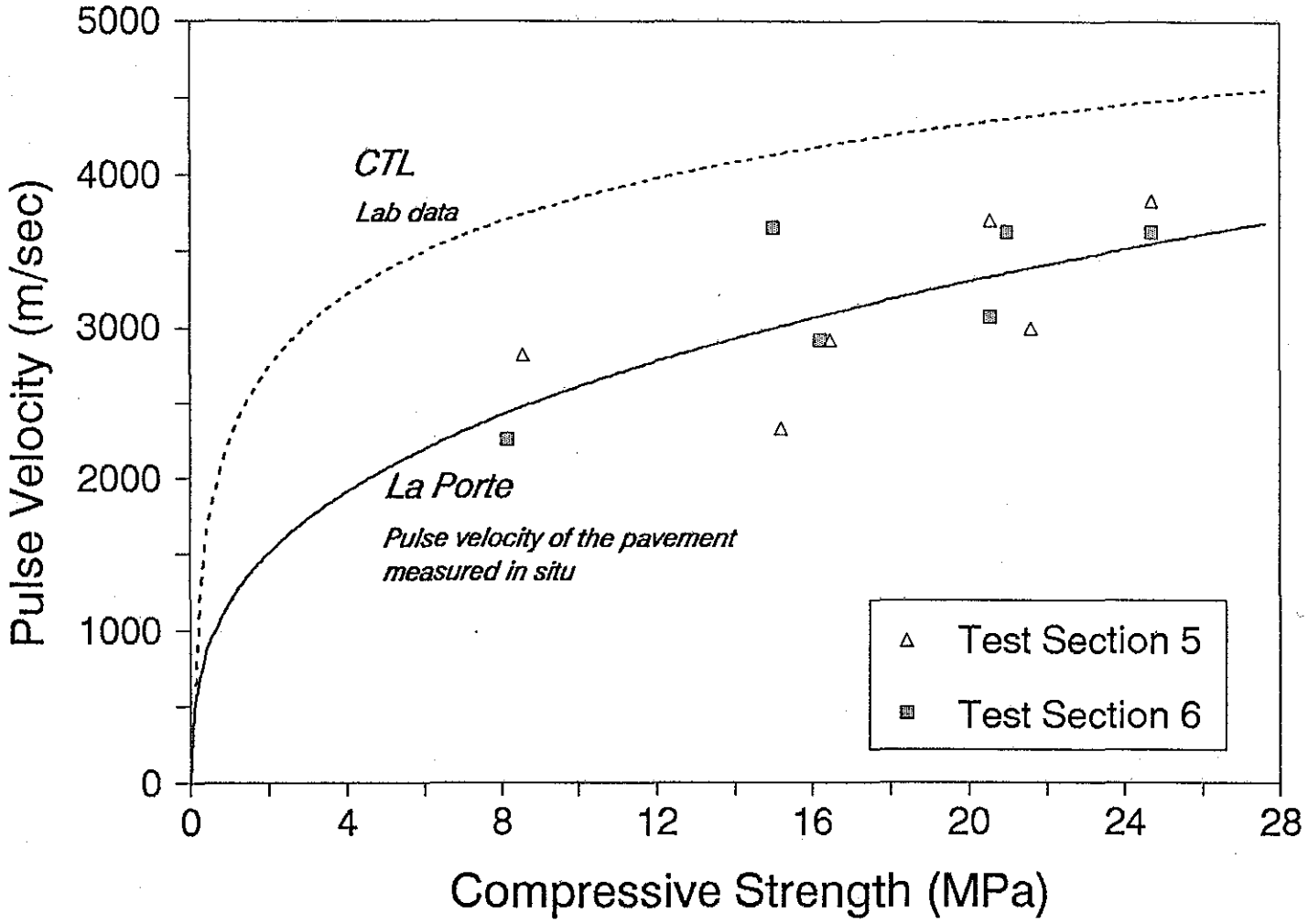

Fig. 2.21. The Pulse Velocity versus the Compressive Strength.

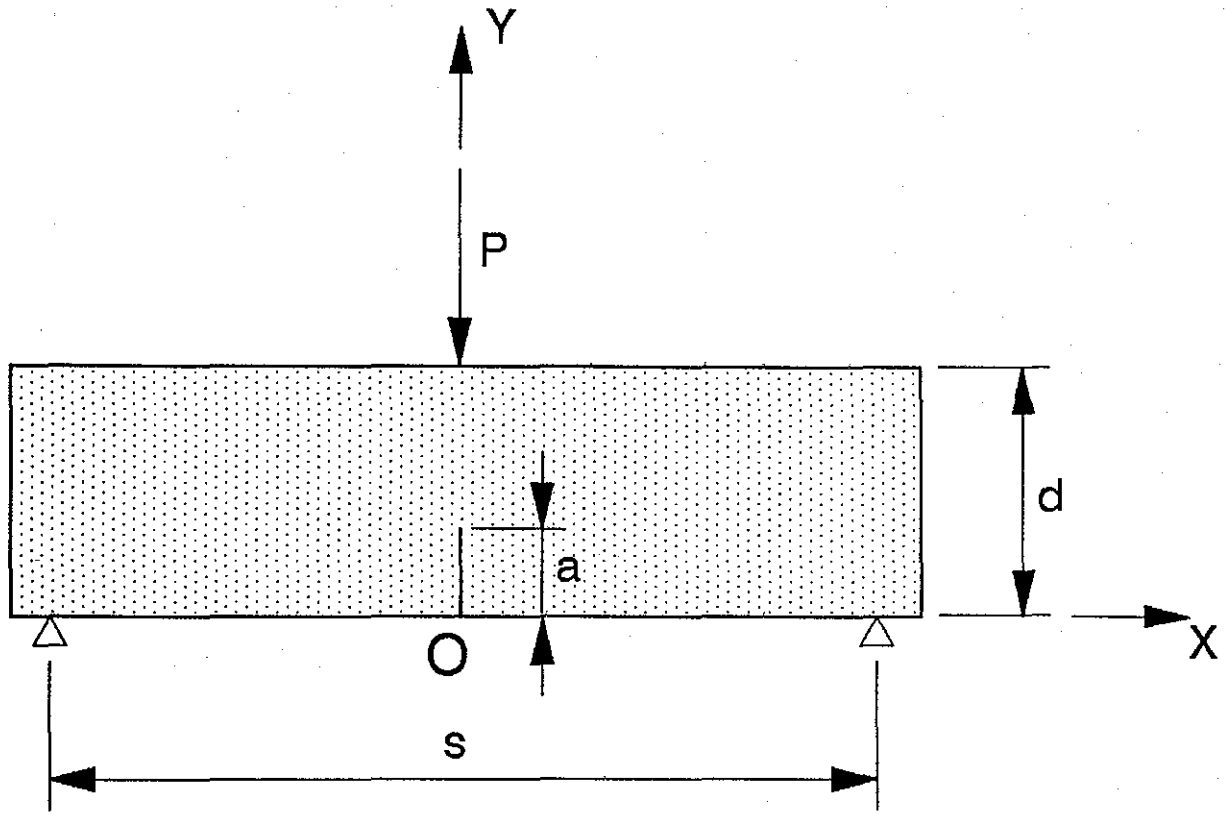

Fig. 2.22. Notched Beam Specimen.

the specimens was 4.5 inches (114 mm), 6 inches 152 mm), 9 inches (229 mm) and 12 inches (305 mm), respectively. The support span of the beam specimen was 2.5 times the depth of the specimen. A notch was cut by a saw before testing. The length of the notch was a quarter of the beam depth. The width of notch was about 1/8 inch (3.2 mm). Three point bending tests were performed on these specimens two days after preparation of the specimens. The load was placed on the other side of the beam specimen rather than the notched side. Two fracture parameters were calculated from the peak loads of the four tests based on the size effect law (SEL). For a brief review of this theory and the test method, see Chapter 4. Fig. 2.23, shows the test data and a regression line. The parameters obtained are:

K_{If} = 987 psi$\sqrt{in}$ = 1.08 MPa$\sqrt{m}$, and c_f = 2.23 inches (56.6 mm),

where K_{If} is the critical stress intensity factor for an infinite specimen and c_f is the effective critical crack increase for an infinite specimen, as defined in the size effect law. These are both material parameters which can serve as indicators of the crack susceptibility of the concrete.

2.9 Correlation of Fracture Toughness with Compressive Strength

From the laboratory fracture tests and compressive tests on concrete using river gravel as the coarse aggregate, K_{If} increases with the age ranging from 12 hours to 28 days following an equation as:

$$\left[\frac{K_{If}}{K_{If}^{28}}\right] = \sqrt[4]{\frac{Age}{28}} \tag{2.5}$$

where K_{If}^{28} is the K_{If} value at the 28-day age (See Chapter 4). This curve does not fit the data for the 12 hour and twenty-eight day ages well, but shows the trend of increase in K_{If} with the age of concrete. By assuming a linear relationship, the following equation is obtained for change in K_{If} during the first day:

$$\frac{K_{If}}{K_{If}^{1}} = 1.333 \left[\frac{Age}{1}\right] - 0.333 \tag{2.6}$$

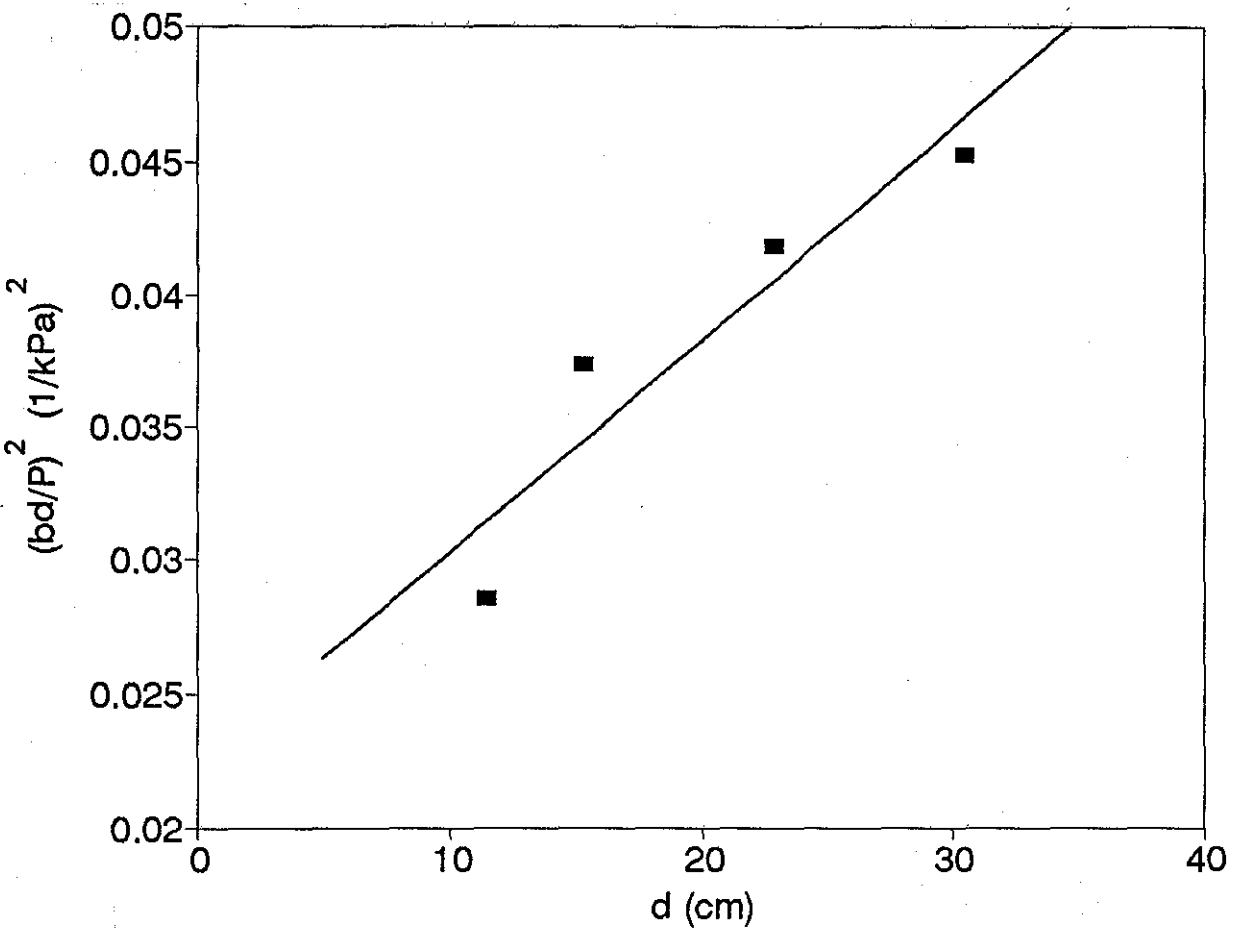

Fig. 2.23. Fracture Test Data and the Regression.

where K_{If}^1 is the K_{If} value at the one-day age (Fig. 24). According to this equation, K_{If} remains zero for a couple of hours after specimen casting. This may be reasonable since the concrete needs some time to take on a set. Also, compressive strength cannot be measured before concrete has taken on a set. By combining Eqs. (2.1) and (2.6), K_{If} increase can be related to the compressive strength. For a more accurate correlation for the age within the first day, change in the compressive strength with time may be obtained:

$$f_c' = 1625 \text{ Age} - 705 \tag{2.7}$$

where f_c' is in unit of psi. Consequently, K_{If} may be expressed in terms of the compressive strength as:

$$\frac{K_{If}}{K_{If}^1} = 0.818 \times 10^{-4} f_c' + 0.244 \tag{2.8}$$

where f_c' is in unit of psi.

2.10. Crack Surveys

Cracks in the pavement of the test sections were surveyed. Sub-Sections 6, which was transversely sawcut after paving, was surveyed on November 14 (3 days after paving), November 15 (4 days after paving), November 19 (8 days after paving), November 22 (11 days after paving), and November 26 (15 days after paving) in 1991. It was surveyed again on March 16, 1992 (125 days after paving). Other sub-sections were surveyed 3, 15 and 125 days after paving. All the sections were opened to traffic on December 12, 1992.

In Sub-Section 6, most of the cracks were initiated from the sawcuts, but in other sections, many cracks were initiated from the steel rebars. Fig. 2.25 is a sketch of the view of the pavement edge. Many of these cracks initiated from the steel rebars finally developed and moved completely through the pavement (Fig. 2.26). Table 2.1 shows the increase in the number of cracks that were through to the pavement top surface (called "surface cracks" for brevity) of each section at the 3-, 15- and 125-day ages of the

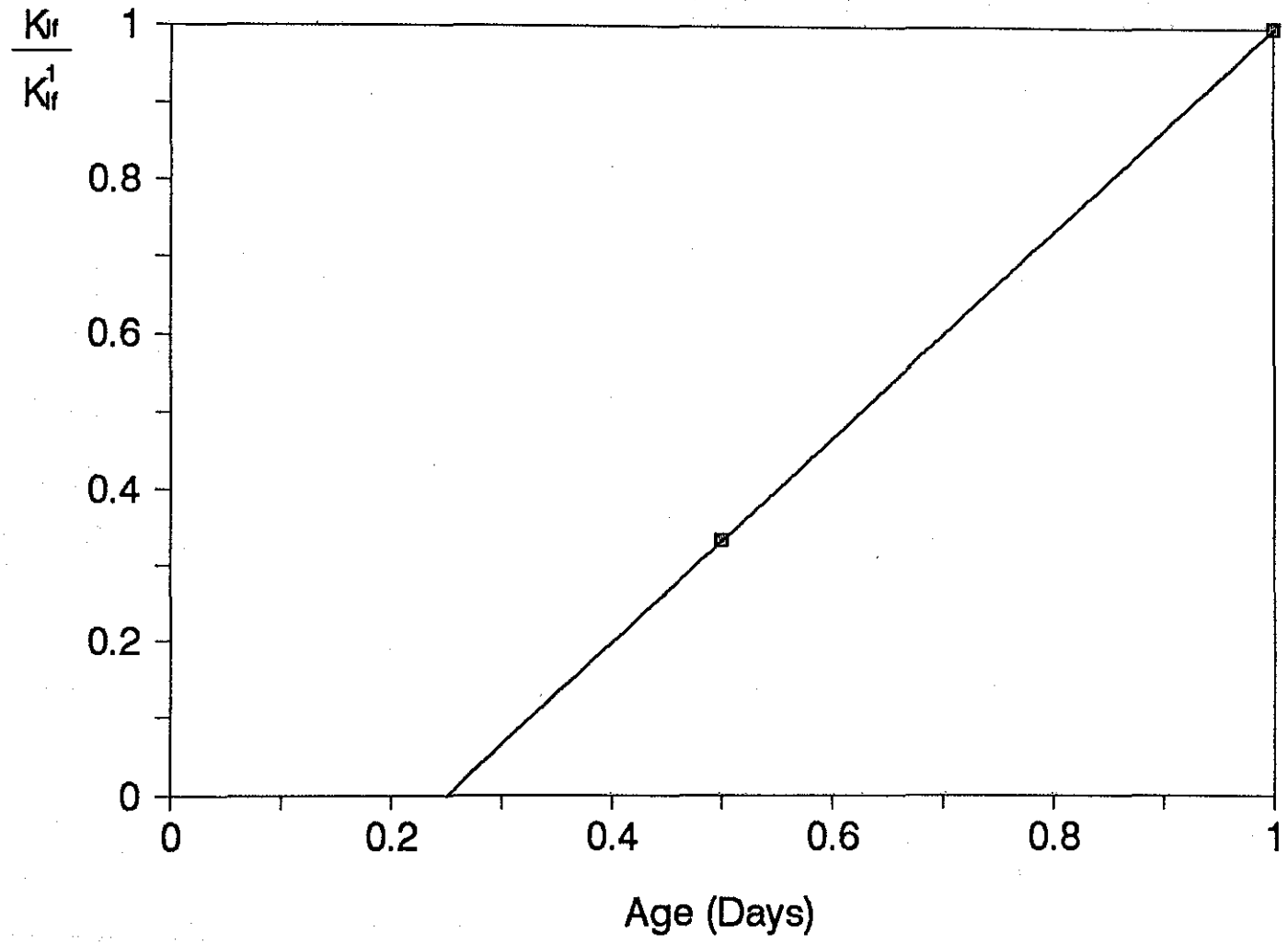

Fig. 2.24. Increase in K_{if} Value with the Concrete Age within One Day.

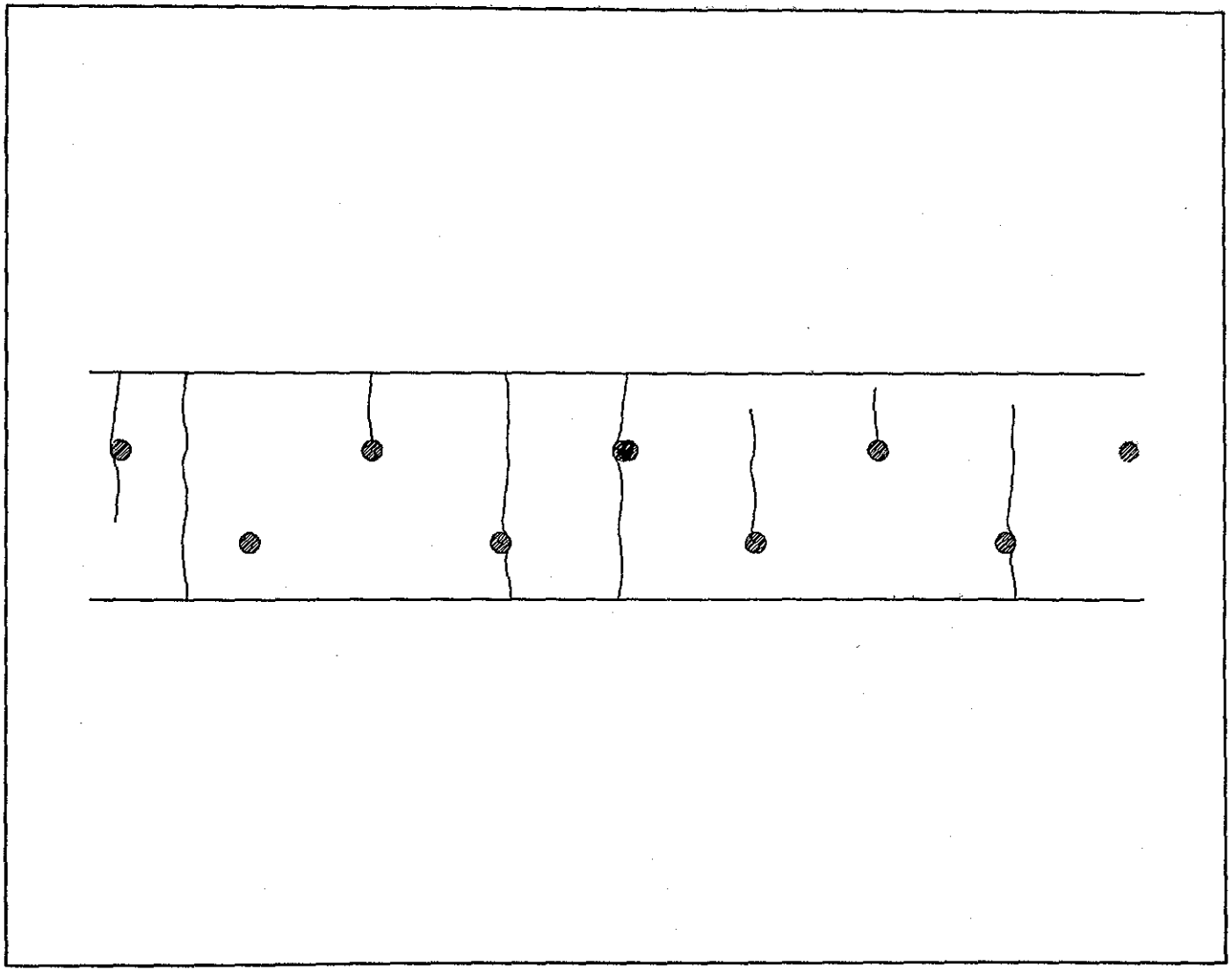

Fig. 2.25. Cracking Patterns on the Pavement Edge.

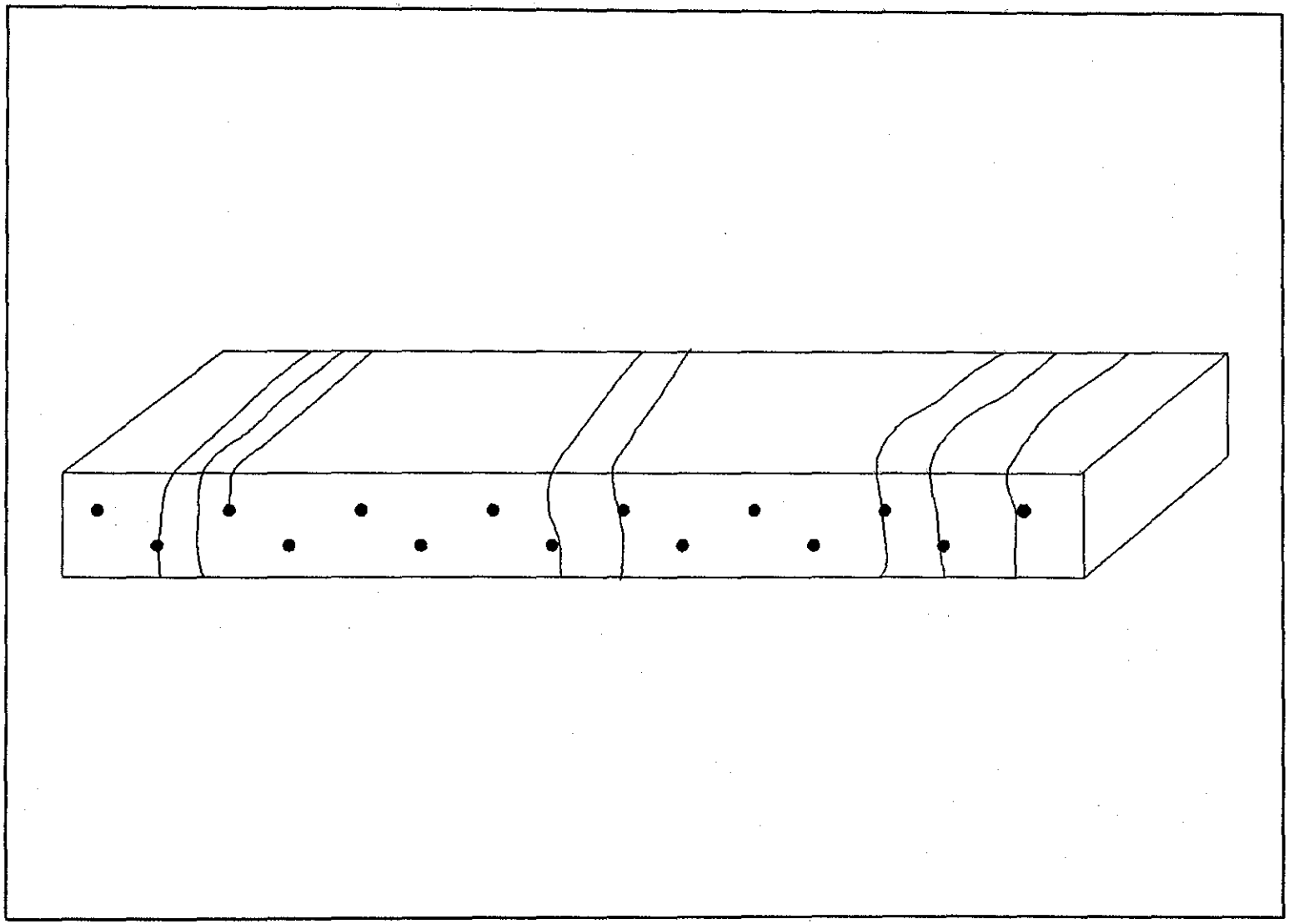

Fig. 2.26. Cracks Initiated from the Transverse Steel Rebars.

pavement, where Section 0 designates the buffer section at the east end, and Section 10, the buffer section at the west end. The first column lists the number of the surface cracks observed on the 3rd day and the second column shows the number of the surface cracks formed between the 3rd day and the 15th day. In the survey of the 15th day, cracks that had been initiated on the pavement edge but had not yet developed as surface cracks were carefully investigated and recorded. It was found in the survey of the 125th day, that some of the surface cracks formed between the 15th day and the 125th day were from these edge cracks observed on the 15th day, and the rest of the surface cracks were "newly" initiated. The numbers of these two categories of cracks, initiated before and after the 15th day, are listed in the table. The last column of the table gives the total number of surface cracks that existed on the 125th day. Since the shoulder had been built up with Sub-Sections 9 and 10 at 15th day, pavement edge of these two sections could not be seen then. The shoulder had been built up along with every section on the 125th day, and therefore, cracks distributed on the pavement edge of all the sections could not be seen on that date.

Table 2.1. Surface Crack Development with Time.

Section No	New Cracks @ Day 3	New Cracks @ Day 15	New Cracks @ Day 141 Initiated Before Day 15	New Cracks @ Day 141 Initiated After Day 15	Total Cracks @ Day 141
0	11	0	10	4	25
1	21	0	17	12	50
2	24	0	11	7	42
3	18	6	13	16	53
4	21	5	26	6	58
5	24	2	5	18	49
6	13	18	0	4	35
7	24	0	0	27	51
8	31	1	1	11	44
9	25	3	3	12	43
10	11	2	1	8	22

To exhibit the increase in the number of the surface cracks, Fig. 2.27 shows a bar chart. Sub-Sections 0 and 10 (the west and east buffer sections) had fewer cracks than other sub-sections (they were shorter). Among Sub-Sections 1 to 9, Sub-Section 6 had the fewest surface cracks at the 3rd day and 15th day, obviously because the sawcuts controlled cracking. The number of surface cracks of Sub-Section 6 at the 125th day was somewhat uncertain since the edge had been covered by the shoulder and surface cracks newly initiated from the sawcuts, if any, were unable to be recognized. From the number of surface cracks, the average surface crack spacing was calculated. Change in the spacing with time is shown in Fig. 2.28 for Sub-Sections 0 to 5, and in Fig. 2.29 for Sub-Sections 7 to 10.

Sub-Section 6 has been surveyed more frequently than other sections. Fig. 2.30 shows the records of numbers of surface cracks in the sawcut part of the section. Although a part of test section 9 was transversely sawcut also, crack development in this part was not investigated in detail because this part was much shorter than the sawcut part of Sub-Section 6. Change in the average surface crack spacing with time for the sawcut part of Sub-Section 6 is shown in Fig. 2.31. Since it is not certain whether any surface cracks from the sawcuts were formed between the 15th day and 125th day, the average spacing at the 125th day is not included in Fig. 2.31. Two new surface cracks were observed at the 125th day, and it was identified that they were both located over transverse steel rebars, though all the rebars could not have been seen since the shoulder had been placed and covered the pavement edge. However, all the surface cracks observed were either from the sawcuts or from the transverse steel rebars. All the surface cracks in this part were initiated from weak points in the pavement, the pavement sawcuts or interfaces between rebars and mortar. In other words, no random surface cracks were observed in the sawcut part of Sub-Section 6. From the change in the average crack spacing for all the sections but Sub-Section 6 (Figs. 2.28 and 2.29), it is seen that the number of the surface cracks increased rapidly within the first three days, and the rate of the increase in number of surface cracks decreased with time. Many sections did not have new surface cracks between the 3rd day and 125th day.

Among the four different curing methods, cotton mat and polyethylene reduced temperature variation in the pavement and slowed down the concrete drying process, as

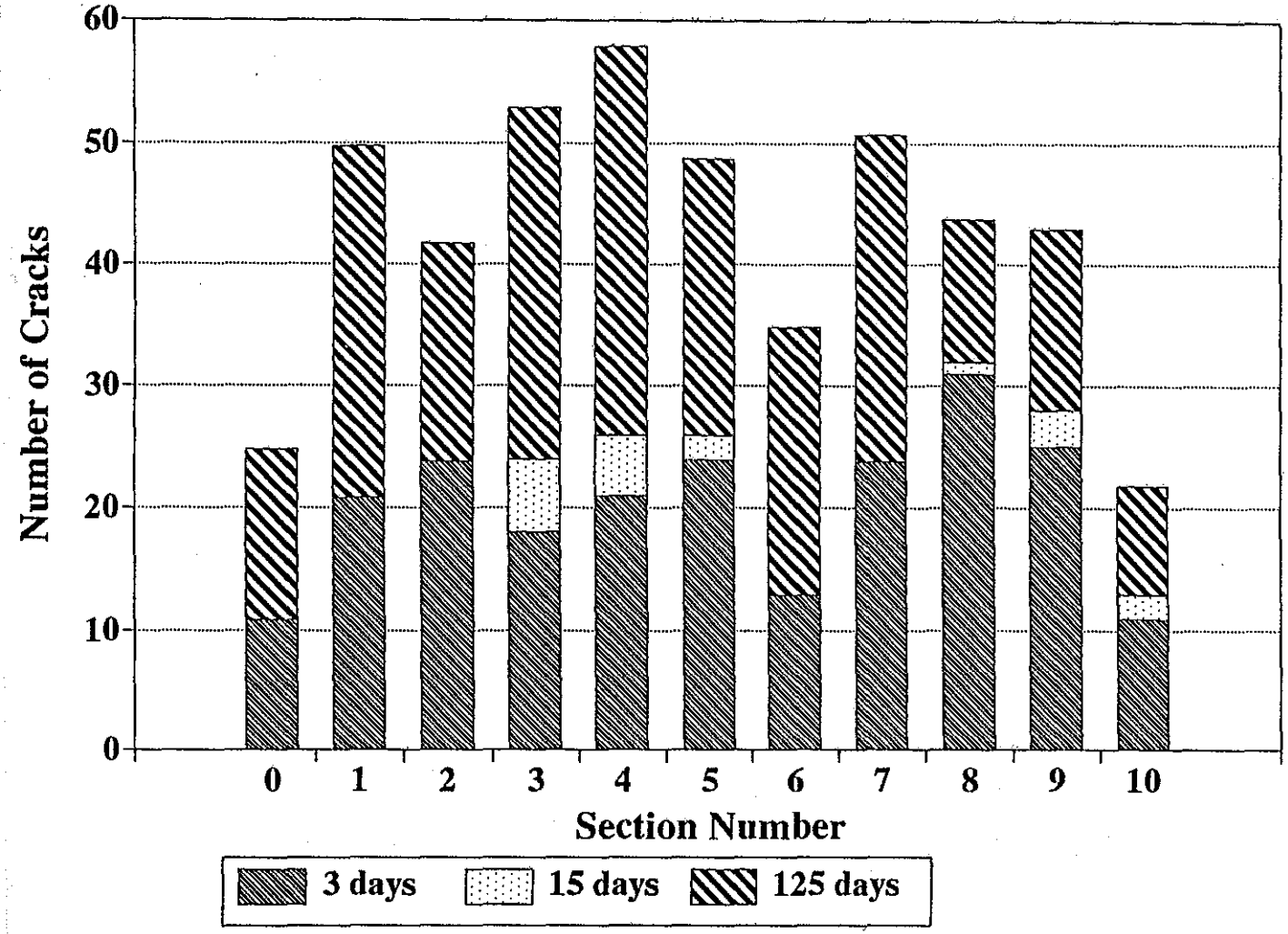

Fig. 2.27. Number of Surface Cracks of Each Section Observed on Different Dates.

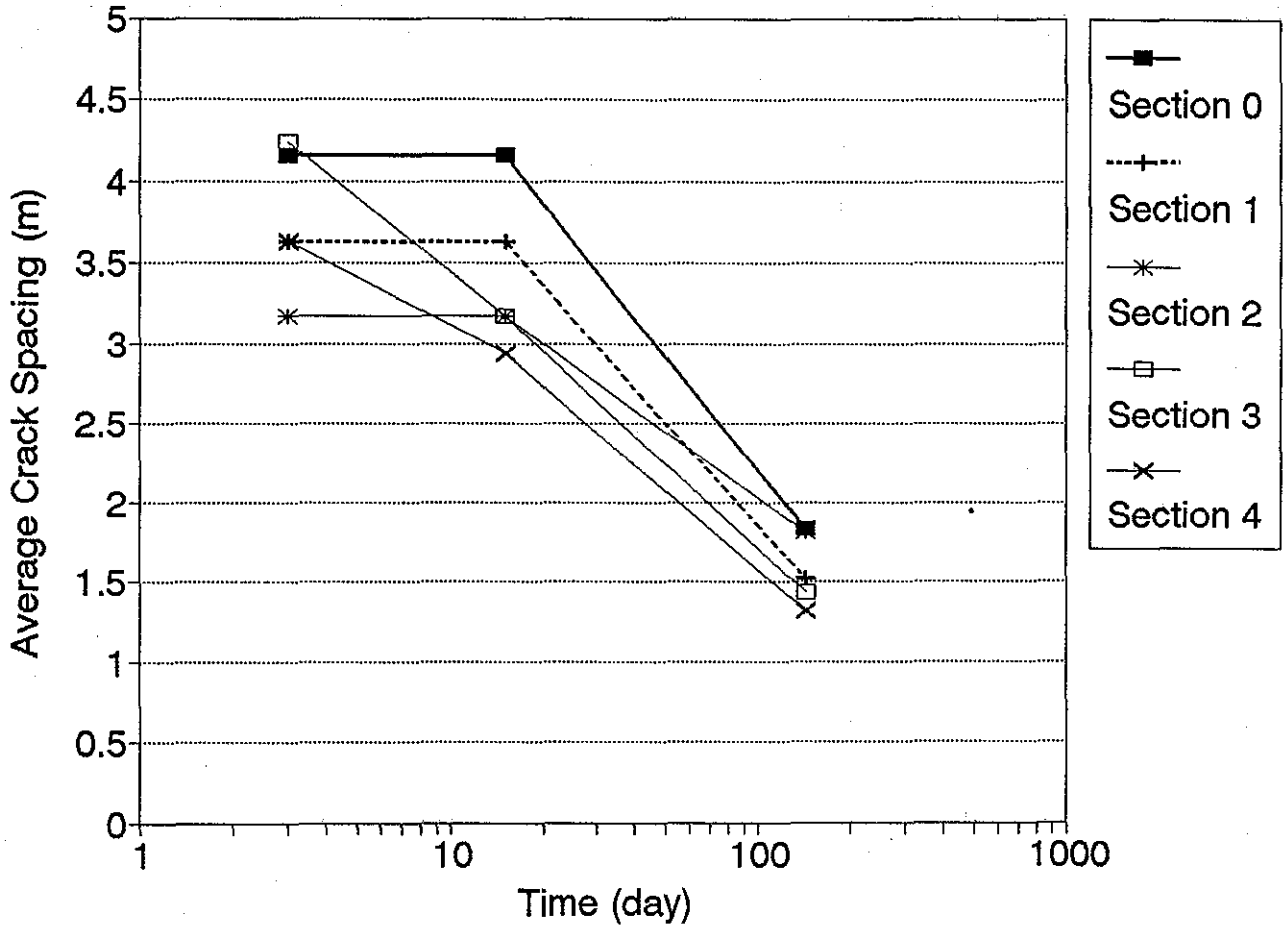

Fig. 2.28. Change in the Average Surface Crack Spacing with Time for Sub-Sections 0 to 4.

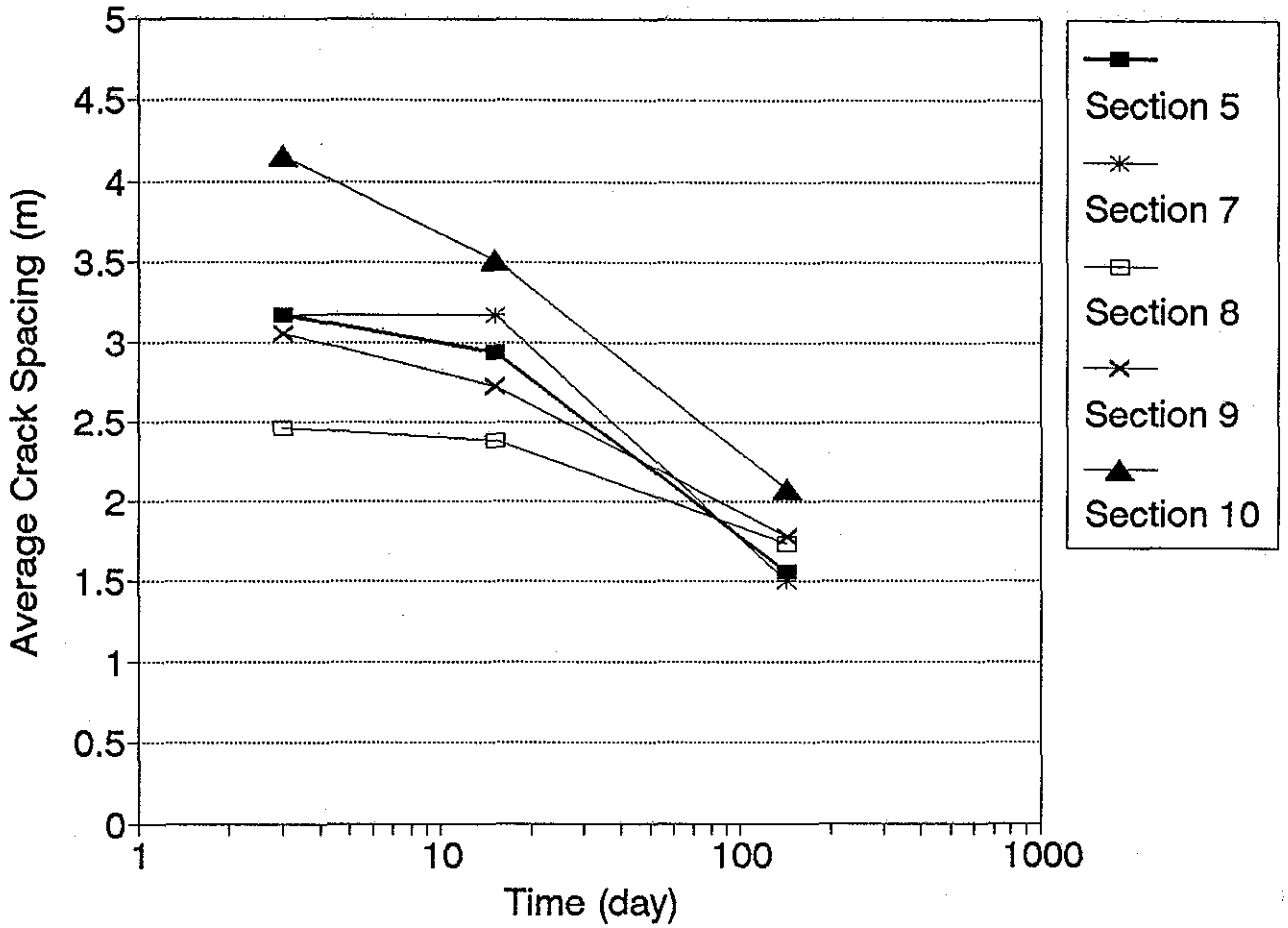

Fig. 2.29. Change in the Average Surface Crack Spacing with Time for Sub-Sections 5 and 7 to 10.

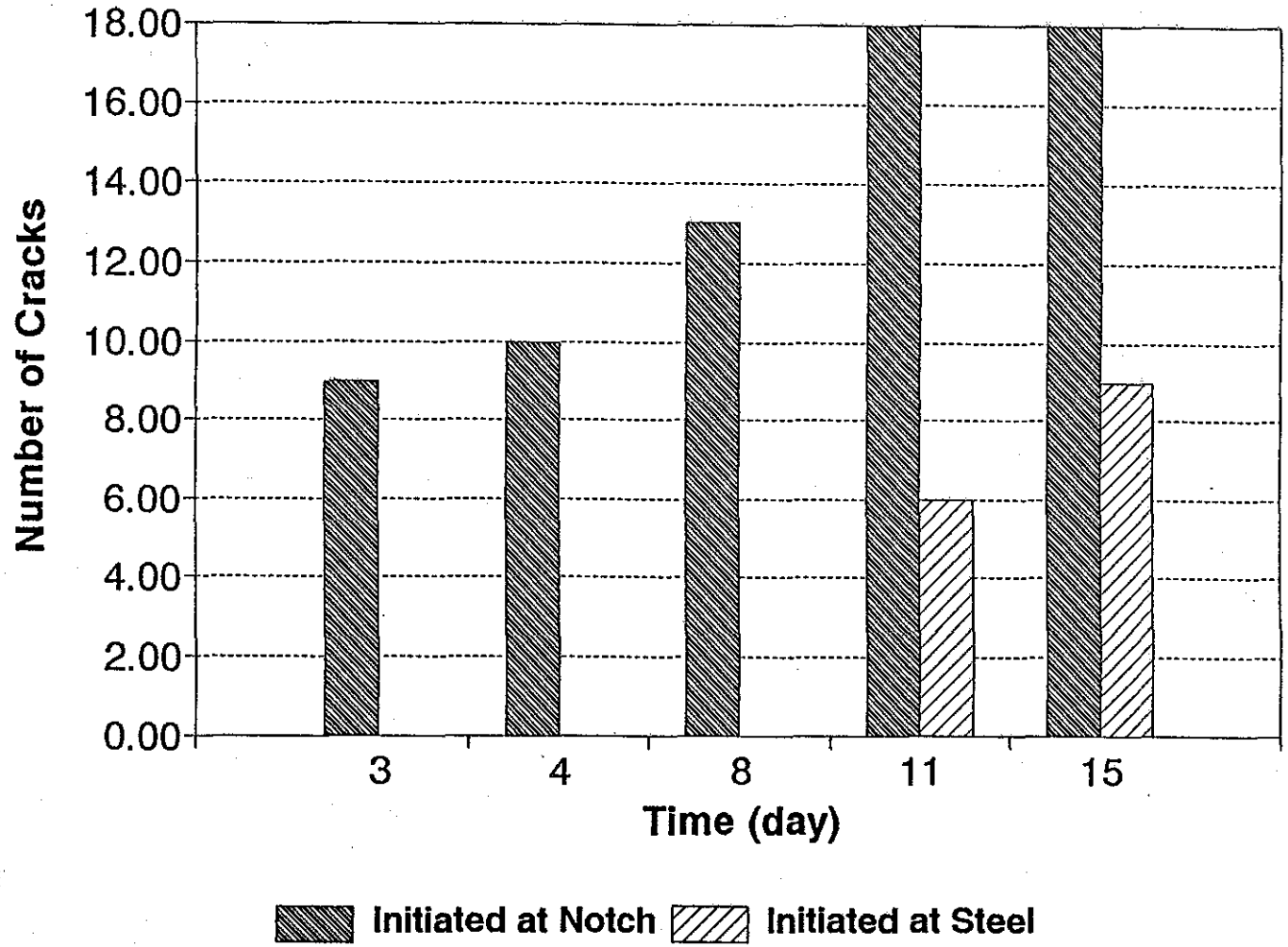

Fig. 2.30. Change in the Number of Surface Cracks with Time for the Sawcut Part of Sub-Section 6.

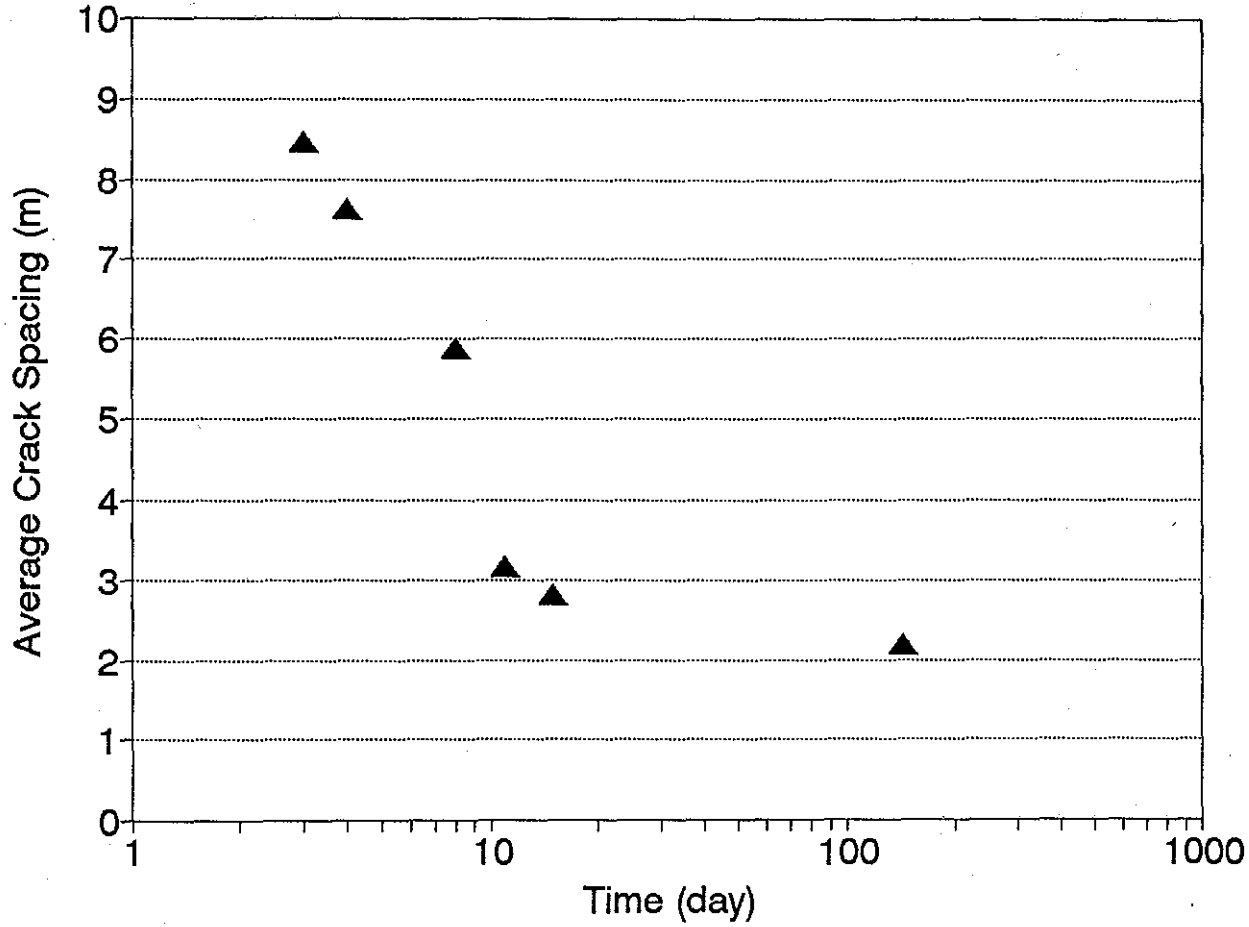

Fig. 2.31. Change in the Average Surface Crack Spacing with Time for the Sawcut Part of Sub-Section 6.

displayed in the section titled "Measurement of Pavement Temperature and Relative Humidity." As a result, increase in the number of surface cracks in Sub-Sections 3, 5 and 8 was suppressed in the first three days, but more surface cracks were formed between the 3rd day and 15th day (Cotton Mat and Polyethylene were removed 7 days after paving). It appears that the formation of these surface cracks were delayed by the effect of these two curing methods.

Data listed in Table 2.2 are the results of the survey conducted on the 15th day, which indicates that cracks were mostly initiated from the interfaces of the steel rebar and mortar or the sawcut tips, because of the stress concentration at these locations, where structure geometry, and/or material properties changed sharply. Fig. 2.32 shows the number of surface cracks at the 15th day for each sub-section and the number of surface cracks that were initiated from the steel rebars. Besides surface cracks, or cracks that went through the top surface of the pavement, there were many cracks observable on the edge surface of the pavement, which would potentially develop to form new surface cracks (Fig. 2.33). These cracks, which were observed on the pavement edge but did not extend to the pavement surface, are called "edge cracks" for brevity. Except for Sub-Section 6 and Sub

Table 2.2. Crack Survey Results on Day 15.

Section Number	0	1	2	3	4	5
No. of Surface Cracks	11	21	24	24	26	26
No. of Surface Cracks Initiated at Steel	7	17	11	18	21	26
No. of Edge Cracks not Developed to Surface Cracks	19	46	18	7	21	3
No. of Edge Cracks Not Developed to Surface Cracks, and Initiated at Steel	16	43	12	2	16	3
Total No. of Surface & Edge Cracks	30	67	42	31	47	29
Percentage of Cracks Initiated at Steel	77	90	55	65	79	100

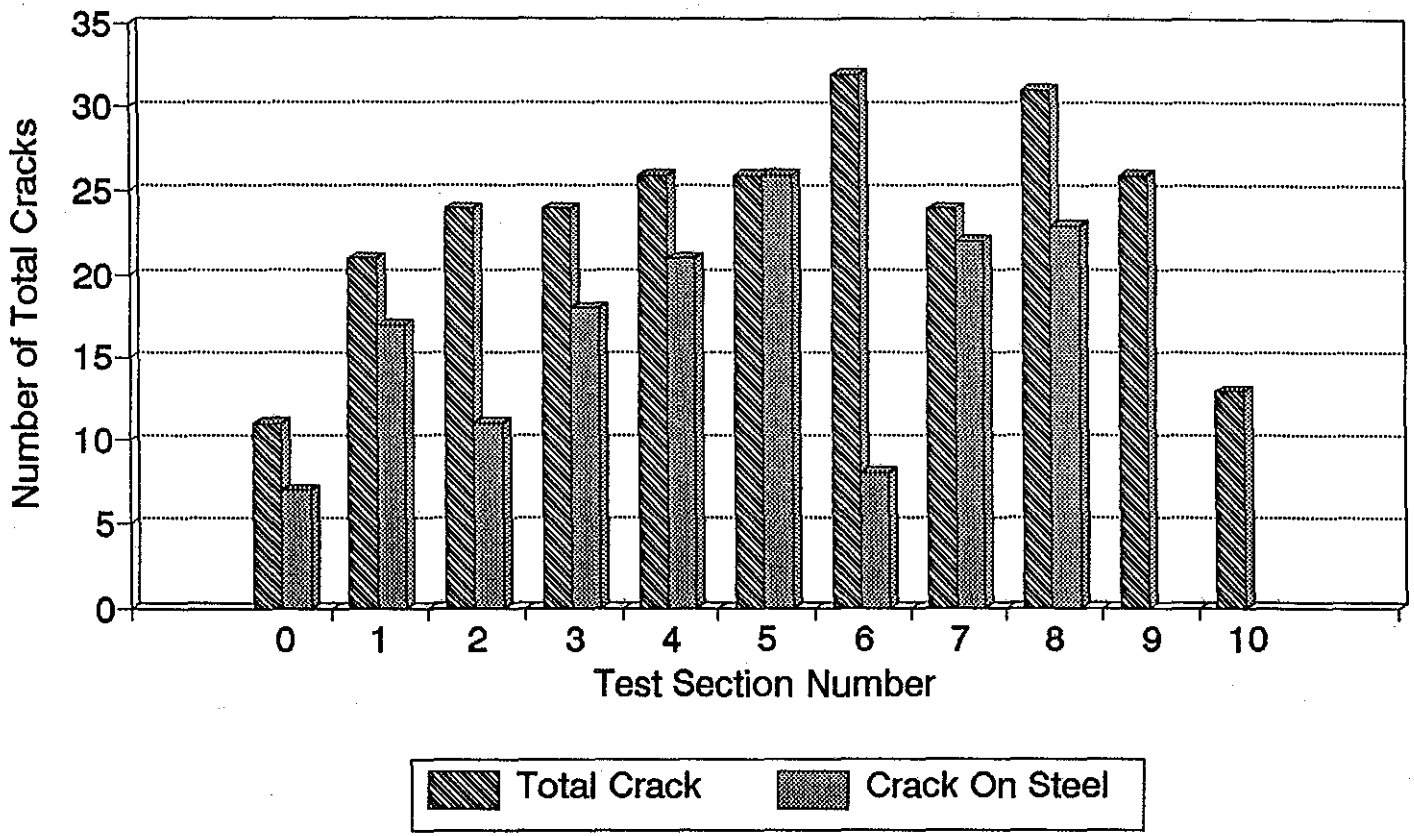

Fig. 2.32. Number of Surface Cracks for Each Section on the 15th Day.

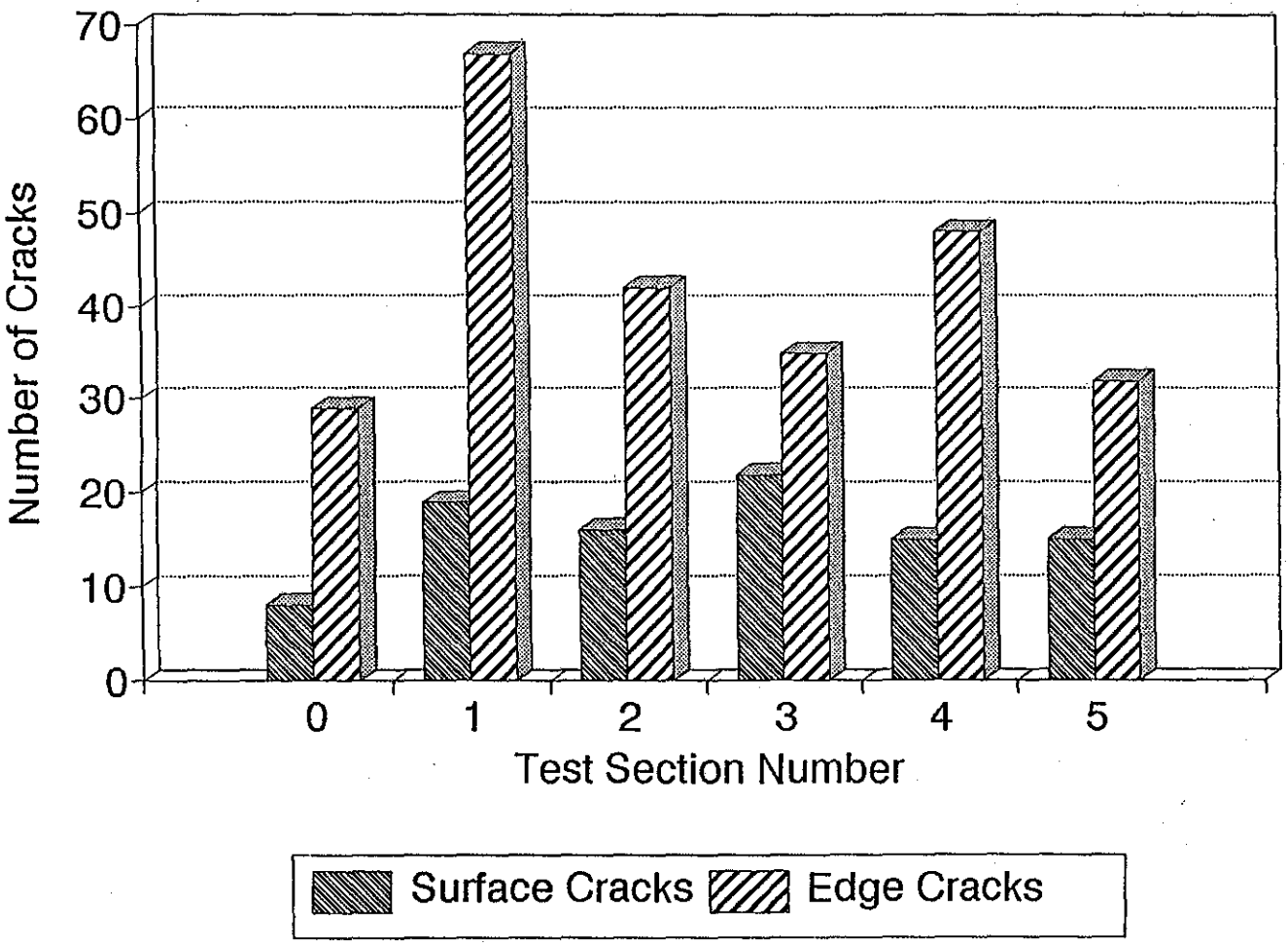

Fig. 2.33. Number of Surface Cracks and Edge Cracks for Sections 0 to 5 on the 15th Day.

Section 2 , most of the cracks, either surface cracks or edge cracks, were initiated from steel rebars (see Fig. 2.34 for the 15th day). Fig. 2.35 shows the percentage of the transverse steel rebars at which cracks had been initiated at the 15th day. In both Figs. 2.34 and 2.35, it is seen that the number of cracks initiated from the rebar in Sub-Section 2 is much less than that in Sub-Sections 0, 1, 3, or 4. This may be because the transverse rebars and Sub-Section 2 were skewed while the maximum tensile stress was in the longitudinal direction of the pavement. Accordingly, the tensile stress in the direction perpendicular to the rebar in Sub-Section 2 was smaller than it would have been if the rebar were perpendicular to the longitudinal direction of the pavement.

Many more cracks were observed on the pavement edge than the pavement top surfaces. All the surface cracks could be traced to cracks observable on the pavement edge, but many cracks observed on the pavement edge did not reach the pavement top surface. It is speculated that cracks were mostly initiated from the pavement edge. Because the edge was exposed to the ambient conditions, the temperature and moisture condition possibly changed more rapidly than at the pavement top surface. This two-dimensional effect deserves further consideration in future test pavements. As shown in Fig. 2.35, different curing methods have effects on the number of cracks initiated from the transverse steel rebars. Cotton mat (Section 3) and Polyethylene (Section 5) made fewer rebars initiate cracks than the two membrane curing methods: Procrete (Section 1) and the white pigments (Section 4).

It would be interesting to note the distribution of the number of surface cracks with respect to the location of the sub-section (Figs. 2.27 and 2.32). The number of surface cracks either at the 15th day or at the 125th day has a shape of the half-sine function (which is not surprising). Formation of cracks results from interaction between stresses, which are induced by temperature variation in the pavement, drying shrinkage, and restraint of the pavement movement. In CRC Pavement, the restraint is caused by the pavement weight, rebar reinforcement, subgrade support forces and friction. Apparently, greater restraint exists in the middle section of the pavement than at the ends of the pavement. Since Sections 0 and 10 are shorter than other sections, it is more reasonable to study the crack distribution

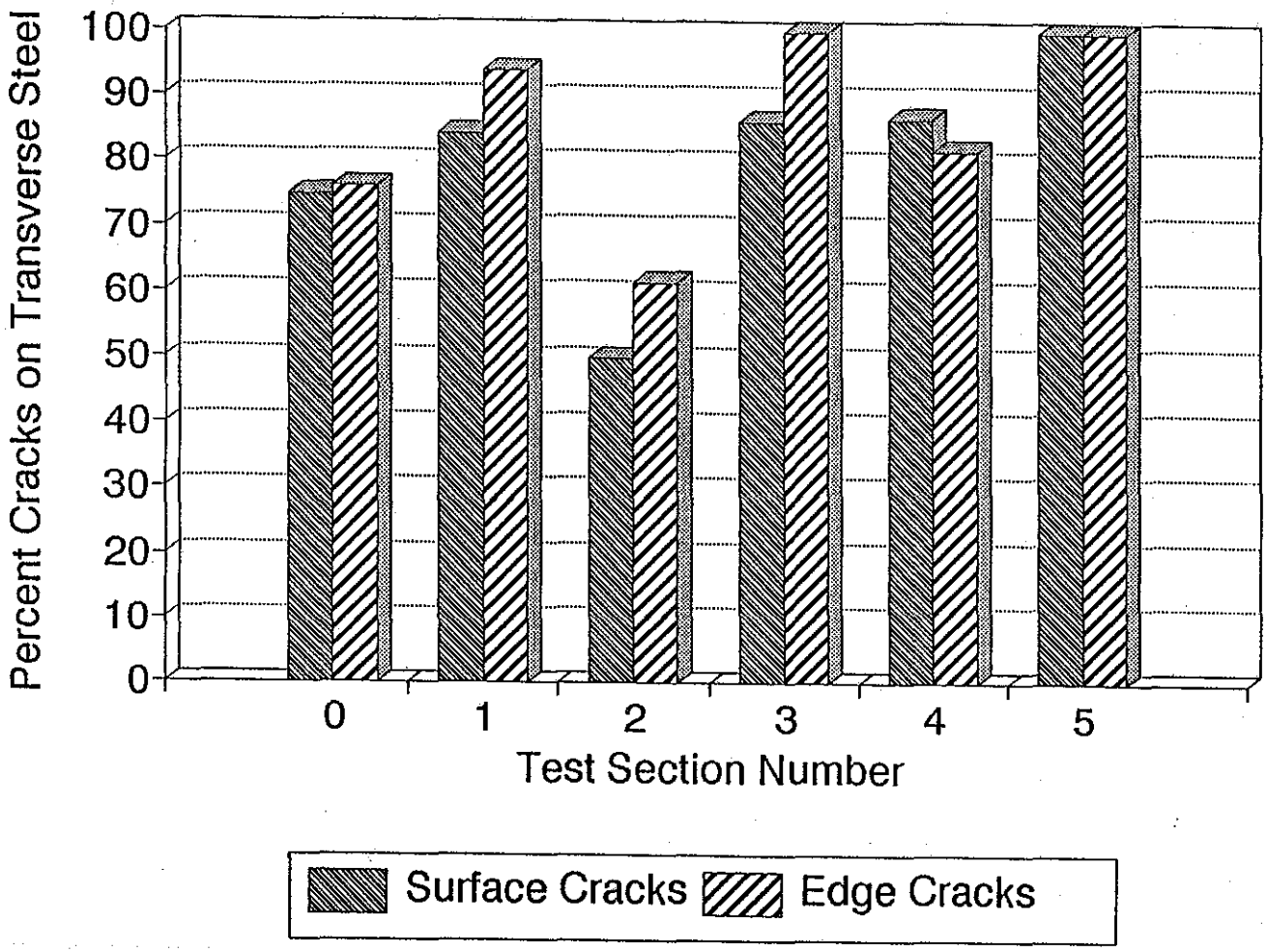

Fig. 2.34. Percentages of Surface Cracks and Edge Cracks that Were Initiated at Transverse Steel Rebars in Sections 0 to 5 on the 15th Day

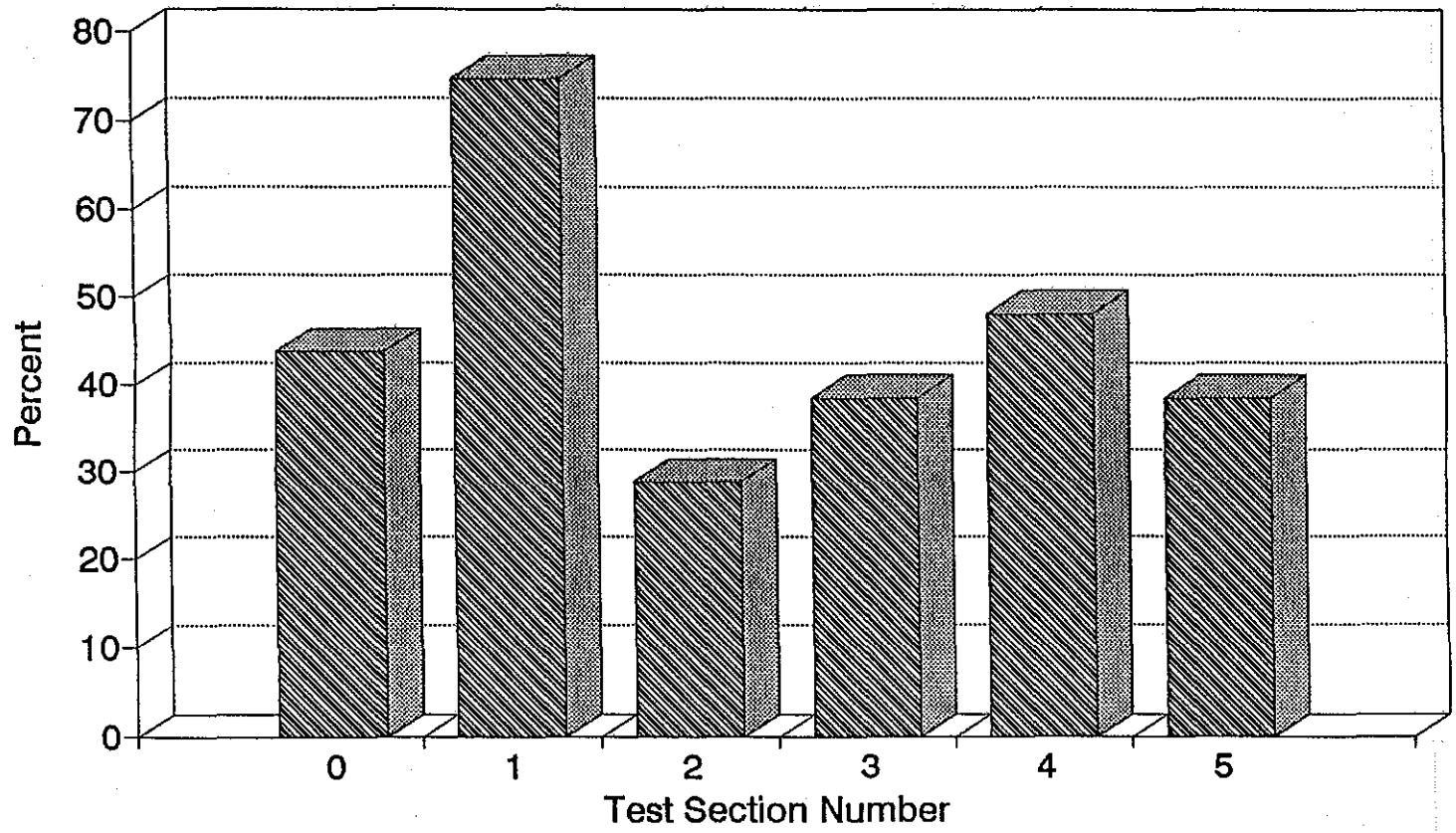

Fig. 2.35. Percentages of Transverse Steel Rebars that Initiated Cracks on the 15th Day.

in terms of number of surface cracks per unit length, which is called "crack density," instead of the number of total cracks for each section. Distribution of the crack density on the 15th day and the 125th day is shown in Figs. 2.36 and 2.37 respectively. A regression on the half-sine function based on the least square method is given in each of the figures. In Fig. 2.36, the regression equation based on the least square method is:

$$\zeta = 0.0599 + 0.511 \sin\pi(\frac{x}{L}) \quad \text{at the 15th day} \tag{2.9}$$

where ζ is the crack density in number of surface cracks per foot and x designates the distance from the west end of the pavement, and L is the total length of the pavement, or 2550 feet (777 m). (This length of pavement was placed in one day) The coefficient of correlation r^2 is 0.827. The regression with the least square method for the 125th-day data is:

$$\zeta = 0.167 + 0.034 \sin\pi(\frac{x}{L}) \quad \text{at the 125th day} \tag{2.10}$$

The coefficient of correlation r^2 is 0.988. Crack densities for Sub-Sections 6, 8 and 9 at the 15th day (Fig. 2.36) are far apart from the regression, which was calculated from the data for Sub-Sections 0, 1, 2, 4, 7 and 10. This may mean that sawcutting and polyethylene curing caused higher crack densities than the other crack control and curing methods. Sub-Section 3 was cured with cotton mat and had fewer cracks than the sub-sections cured by membrane methods at the 3rd day, but its crack density at the 15th day had increased to be close to the regression curve. Sub-Section 5 was cured with polyethylene. Although it did not obtain an increase in the crack density as rapidly as Sub-Section 8, it did obtain a higher crack density from the 3rd day to the 15th day. However, at the 125th day (Fig. 2.37), the crack density for Sub-Section 6, and Sub-Sections 5 and 8 were lower than the regression, which was calculated from the data for Sub-Sections 0, 1, 4, 7, 9 and 10. In other words, these preliminary results indicate that sawcutting developed cracking in early ages but reduced the crack density on a long-term basis. Besides Sub-Sections 5, 6 and 8,

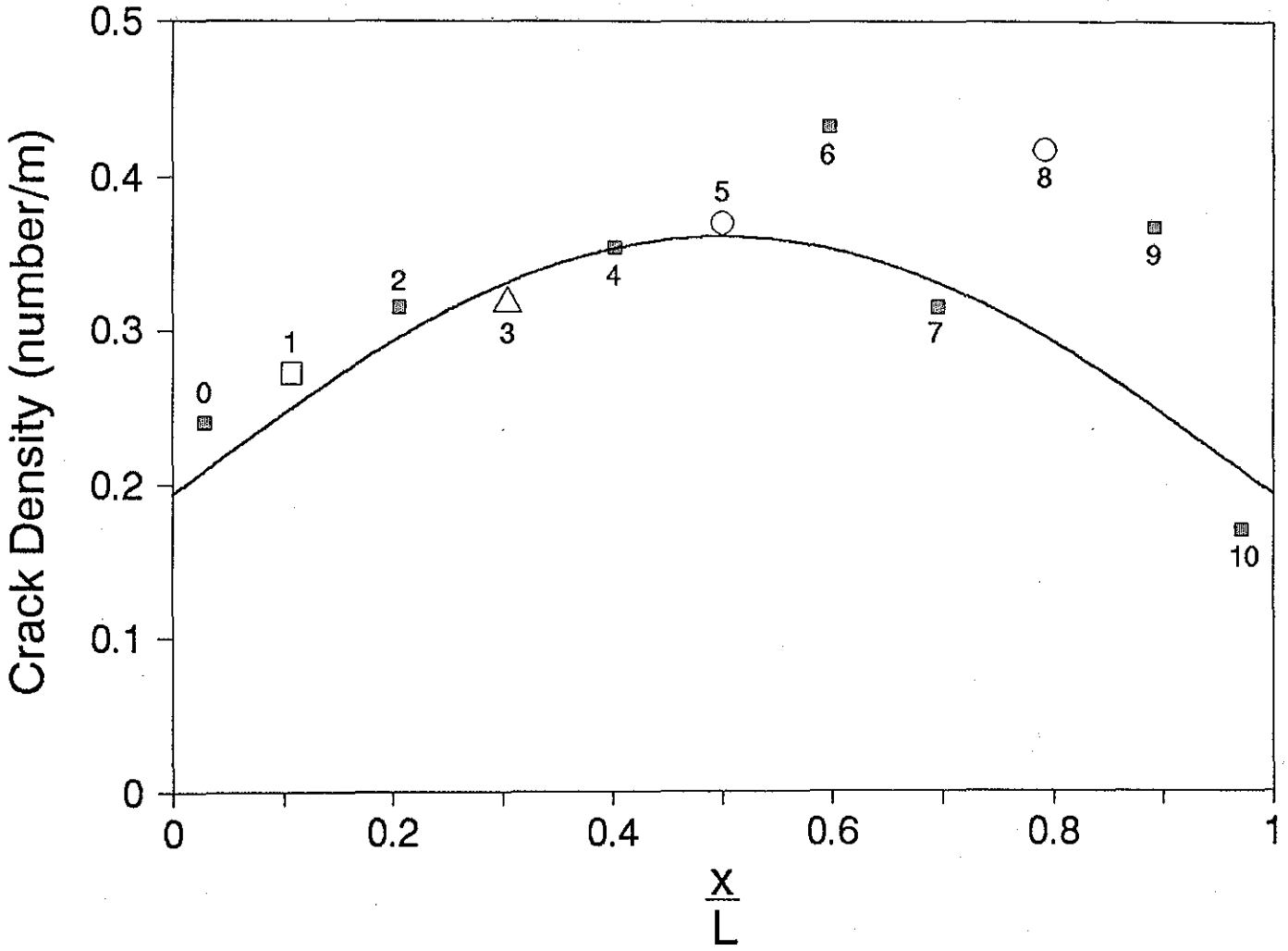

Fig. 2.36. Crack Density Distribution on the 15th Day.

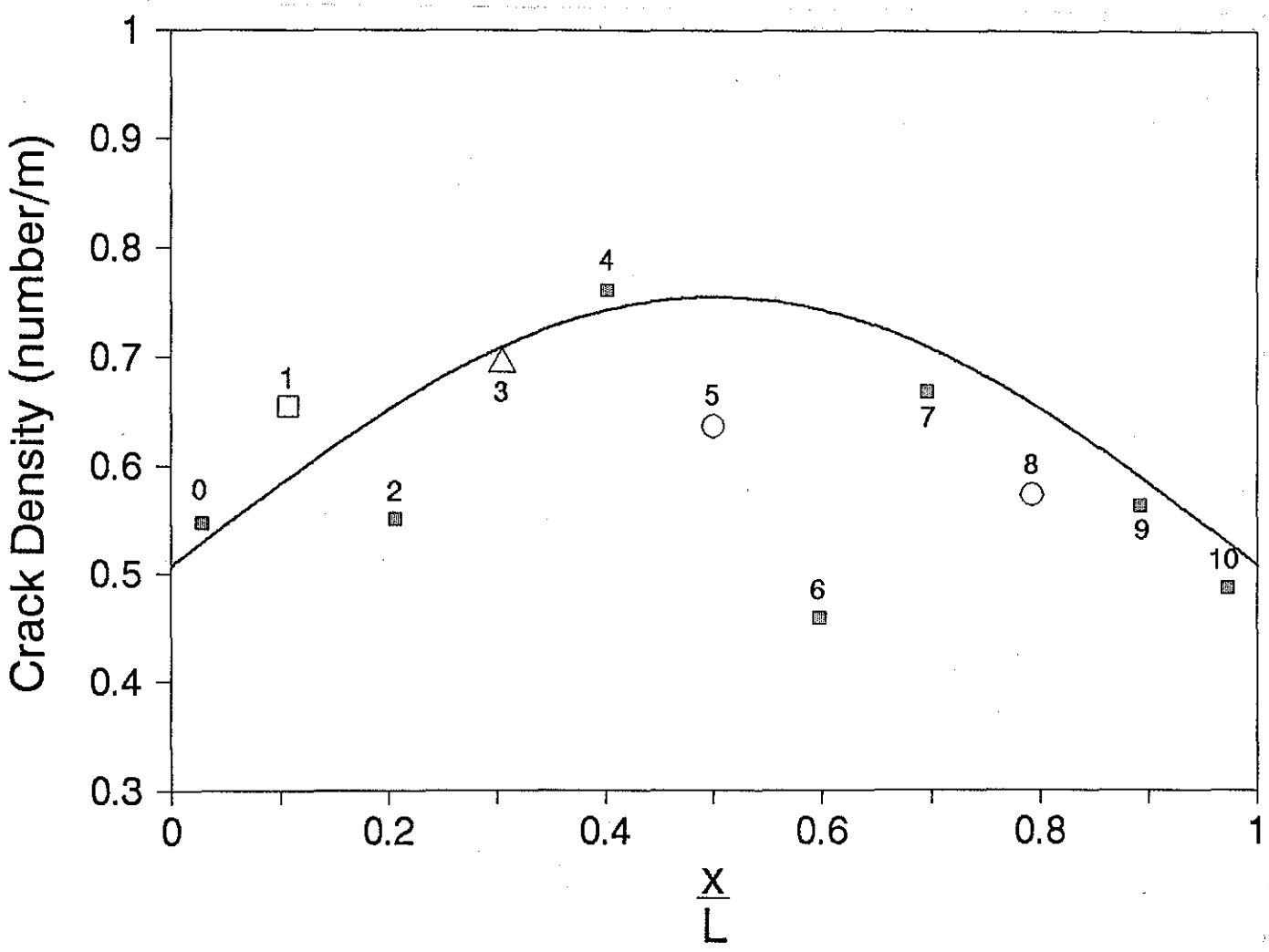

Fig. 2.37. Crack Density Distribution on the 125th Day.

Sub-Section 2 had a low crack density at the 125th day, showing that skewed transverse rebars may cause reduced cracking. Sub-Section 3 (cotton mat cured) did not deviate from the regression curve in the crack density.

Among the points close to the regression curve in both Figs. 2.36 and 2.37 those on the left side of the figure are higher than the curve while those on the right side are lower than the curve. It may indicate that the pavement placed in the morning tended to create more cracks than the pavement placed in the afternoon.

2.11. Analysis of Specimens Cored from the Pavement

Fig. 2.1 indicates the layout of different test sections in the SH-225 eastbound direction in La Porte, Texas. These test sections were located in the 2 outside lanes in the eastbound direction of the 8-lane highway. The main objectives of the coring operation were to see if there were any delaminations being developed in the pavement, and to see if the early sawcutting of the pavement (within a matter of a few hours) achieved the desired effects on the pavement. The concrete pavement was paved on November 11, 1991 and was open for traffic on December 12, 1991. Coring was performed on September 24, 1992. This made the pavement a little over 10 months old and in use for more than 9 months. Our previous investigations of spalling in BW-8 in Houston under this same research project indicated that there were pronounced delaminations and spalling in pavements as early as 3 years after construction. This coring study would let us know if there were any delaminations before a period of one year after construction.

The study indicated that there were delaminations present in the slab. Even though these delaminations were not as pronounced as those we have seen in much older pavements, there was no doubt about their presence. This adds credence to our earlier assertion that the process of delamination starts at a very early age in the pavement, even as early as just after the paving in the afternoon since they experienced different temperature cycles. This may suggest that a different function, such as a Weibull Distribution, may be a more appropriate distribution.

Details of this coring study are summarized in Tables 2.3 and 2.4. Cores were taken both along the longitudinal sawcut as well as at the transverse sawcuts and cracks and at the

Table 2.3. Details of Cores Taken at the Longitudinal Sawcut.

Core ID	Test Section		Distance from preceding section	Remarks
	ID	Description		
L1	2	Standard cure, Skewed rebar	40 ft (12 m)	Crack originated from saw cut, but progressed at an angle of 60° from vertical
L2	5	Polyethylene cure	80 ft (24 m)	No crack originated from sawcut
L3	6	Standard cure, Sawcut	150 ft (46 m)	No crack originated from sawcut

middle of the crack/sawcut. In all cores, transverse cracks were clearly visible down to the level of the bottom rebar layer (4 in. or 102 mm from the bottom). Fig. 2.38 illustrates some typical cores taken at both random transverse cracks as well as at transverse saw cuts.

Important Observations

1. There were delaminations present near random transverse cracks.

2. In the cores taken, there were no indications of delaminations in the sawcut section.

3. The delaminations at random transverse cracks occurred during the first 10 months of the life of the pavement.

4. Slight spalling was observed mostly along wheel paths.

5. In the sawcut section (No. 6), a longitudinal crack runs through at a distance varying from 0 to 3 feet from the longitudinal sawcut. This may be an indication that the crack had already initiated when sawcutting was done.

6. Similarly, where cracks were not observed starting from sawcuts, there were transverse cracks away from sawcuts nearby. This again may be an indication of a delay in sawcutting.

Table 2.4. Summary of Coring Operation Along Transverse Cracks/Sawcuts.

Core #	Test Section		Lane	Distance from preceding section	Does core indicate Delaminations ?	Remarks
	ID	Description				
1	1	Procrete	IL	187 ft (57 m)	N	
2	1	Procrete	OL	187 (57 m)	Y	Delaminations at 2.5 and 6 in (64 and 152 mm) depths (top rebar) on both sides of random crack.
3	2	Standard cure, Skewed rebar	IL	176 (54 m)	Y	Delamination at 1.5 in (38 mm) depth on one side of crack (only 2 inches or 51 mm long).
4	2	Standard cure, Skewed rebar	OL	176 (54 m)	Y	Delaminations at 2.5 and 4.5 in (64 and 114 mm) depths (on opposing sides of crack).
5	3	Cotton mat cure	OL	40 (12 m)	Y	
6	3	Cotton mat cure	OL	40 (12 m)	N	Core taken at crack branching.
7	4	Standard cure	IL	191 (58 m)	Y	Delaminations at 1 in (25 mm) and top rebar depths.
8	5	Polyethylene cure	OL	220 (67 m)	N	
9	6	Standard cure, 3 ft (9 m) sawcuts	IL	20 (6 m)	N	Core taken at sawcut and longitudinal crack. Longitudinal crack is at rebar. No crack from sawcut.
10	6	Standard cure, 3 ft (9 m) sawcuts	OL	20 (6 m)	N	No crack starts from saw cut.
11	6	Standard cure, 5 ft (1.5 m) sawcuts	OL	65 (20 m)	N	No crack at sawcut. Random transverse cracks 6 in and 36 in (252 and 912 mm) away from sawcut. Sawcut only 0.5 in (13 mm) deep (others 1 in or 25 mm).
12	6	Standard cure, 5 ft (1.5 m) sawcuts	IL	120 (37 m)	N	Crack extended from sawcut.
13	6	Standard cure, 5 ft (1.5 m) sawcuts	OL	120 (37 m)	N	Crack extended from sawcut.

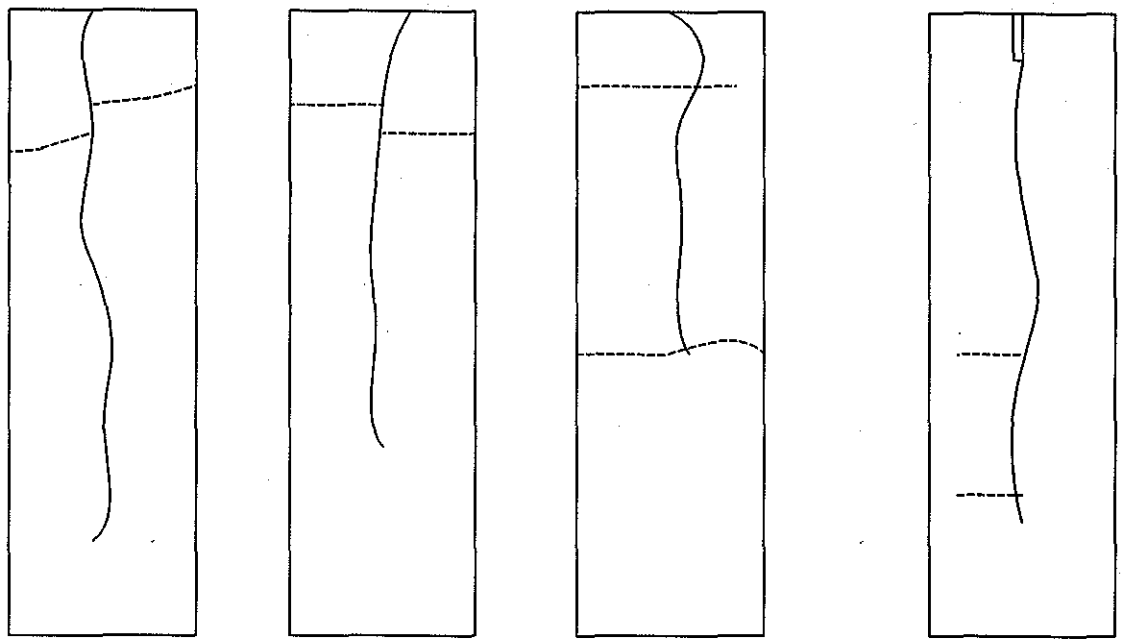

Core # 2 (Random Crack) | Core # 4 (Random Crack) | Core # 7 (Random Crack) | Core # 12 (Saw Cut)

Note: Dashed lines indicate delaminations.
Solid curved lines indicate transverse cracks.

Fig. 2.38. Illustration of Some Representative Core Samples.

2.12 Conclusions and Recommendations

1. A 2550-feet (777 m) long CRC pavement test section was placed in La Porte, Texas for experimental studies in crack control. Different curing methods and crack-control methods were applied to different sections of the pavement to compare their influences on performance of the pavement. Temperature and relative humidity in these sections were monitored. Differences made by these various methods were obvious, which made it clear that such field tests are useful in helping understand the effects of these curing methods and crack-control methods.

2. In comparison with the membrane curing method (using white pigments or Procrete), cotton mat and polyethylene film reduced daily temperature variation and slowed down the drying process in pavement concrete. Accordingly, the number of surface cracks, cracks that went transversely through the top surface of the pavement, in test sections cured with cotton mat or polyethylene film was lower than in test sections cured with membrane in the first three days after paving. After the mat or the film was removed, the number of surface cracks increased in the sections that were initially covered by the mat or film.

3. The crack density (number of surface cracks per unit length of pavement) was affected by the restraints inherent within the pavement system (longitudinal steel rebars, subbase friction, etc.). Its distribution with respect to the distance from the pavement end (over a one-day placement) may be expressed in terms of a half-sine function. Regression was made for the crack-density distribution on the 15th day and on the 125th day. On the 125th day, or four months after paving, crack density in sections cured by polyethylene film was lower than the regression curve based on the data from membrane-cured sections, while crack density in the section cured by cotton mat was very close to the regression curve.

4. A 175-feet (53.3 m) long test section cured by the standard membrane curing method was transversely cut with the early-aged sawcut technique at an interval of 3 ft (0.91 m) and 5 feet (1.5 m). Different from the conventional sawcut method, no water-cooling was used and the depth of the cut was 1 inch, approximately, which is much less than D/4 or D/3 (where D is the pavement thickness), as used for conventional sawcutting of joints in jointed concrete pavement. In the sawcut section, the average crack spacing decreased more

rapidly than any section that was not sawcut. The average crack spacing in the sawcut part was ultimately larger than that in the non-sawcut sections.

The sawcut not only reduced the number of cracks, but it also controlled the location of the crack. In the sawcut portion, most of cracks were initiated from the sawcut and the rest of the cracks were initiated from the transverse steel positions.

5. No significant raveling occurred although the sawcutting operation started relatively early, which indicates an improved sawcut efficiency with this type of approach. Data analysis shows that early-aged sawcutting can occur without ravelling when the pulse velocity reaches 5,000 feet/sec (1520 m/sec), and verifies the same conclusions drawn in the previous field tests performed in Texarkana test sections.

6. A large percentage of the transverse steel rebars initiated cracks, part of which developed as surface cracks. This means that these surface cracks are not random cracks, but actually were initiated from the rebars' transverse positions. Good design practice may suggest that cracking at the rebar interface should be avoided to improve the utility of the reinforcement. It is apparent, however, that the transverse steel can be used to control cracking which occurs randomly between rebars.

7. Some cracks may have been initiated on the lateral edge surface of the pavement from the rebar interface. It may be because temperature varies more often and drying proceeds faster on the edge surface than elsewhere in the pavement. Even in the cotton mat and polyethylene film curing methods, the edge surface was not covered by the mat or film, but exposed to the air. More moisture can evaporate from the surface so that, at the same depth, moisture content could be lower near the edge than at greater distances from the edge. Heat could dissipate faster from the edge surface due to the increased surface area. This two-dimensional effect needs to be investigated in future test sections.

8. The General Eastern digital system, for temperature and relative humidity measurement in pavement, provided significant data to show different effects of different curing methods. This system may serve well for quality control purposes. To detect the two-dimensional effect described previously, distributions of temperature and relative humidity on the edge surface and in the depth from the edge surface should be considered in future tests.

9. Since skewed transverse steel rebars constituted weak bonding not perpendicular to the direction of the maximum tensile stress, the number of surface cracks in the skewed rebar reinforced pavement section was lower than the half-sine regression curve on the 125th day after paving. It may be appropriate to provide guidelines for the implementation of polyethylene film curing method, sawcutting crack-control method and the arrangement of skewed rebars in the construction of concrete pavements.

10. In the first one or two days after placement of the concrete, an increase in the compressive strength of the concrete used to pave the test sections may be expressed in terms of a linear relation with the concrete age. Formulas to correlate the pulse velocity and fracture toughness with the compressive strength were constructed for the concrete used in the test sections. These formulas may be improved to better reflect the relationships among these parameters after more data are accumulated in further research.

11. Continuing cracking surveys on these test sections is required to trace future crack development.

2.13 Appendix I: Test Data of Temperature and Relative Humidity in Pavement

The following five figures (Figs. 2.39 to 2.43) show the readings from the Vaisala digital system for the east buffer section (or section 10). Paving for the section started at 5:30 p.m., November 11, 1991.

Temperature and relative humidity at three different depths, 1 inch (25 mm), 2 inches (51 mm) and 4 inches (102 mm), were measured with three channels of the Vaisala.

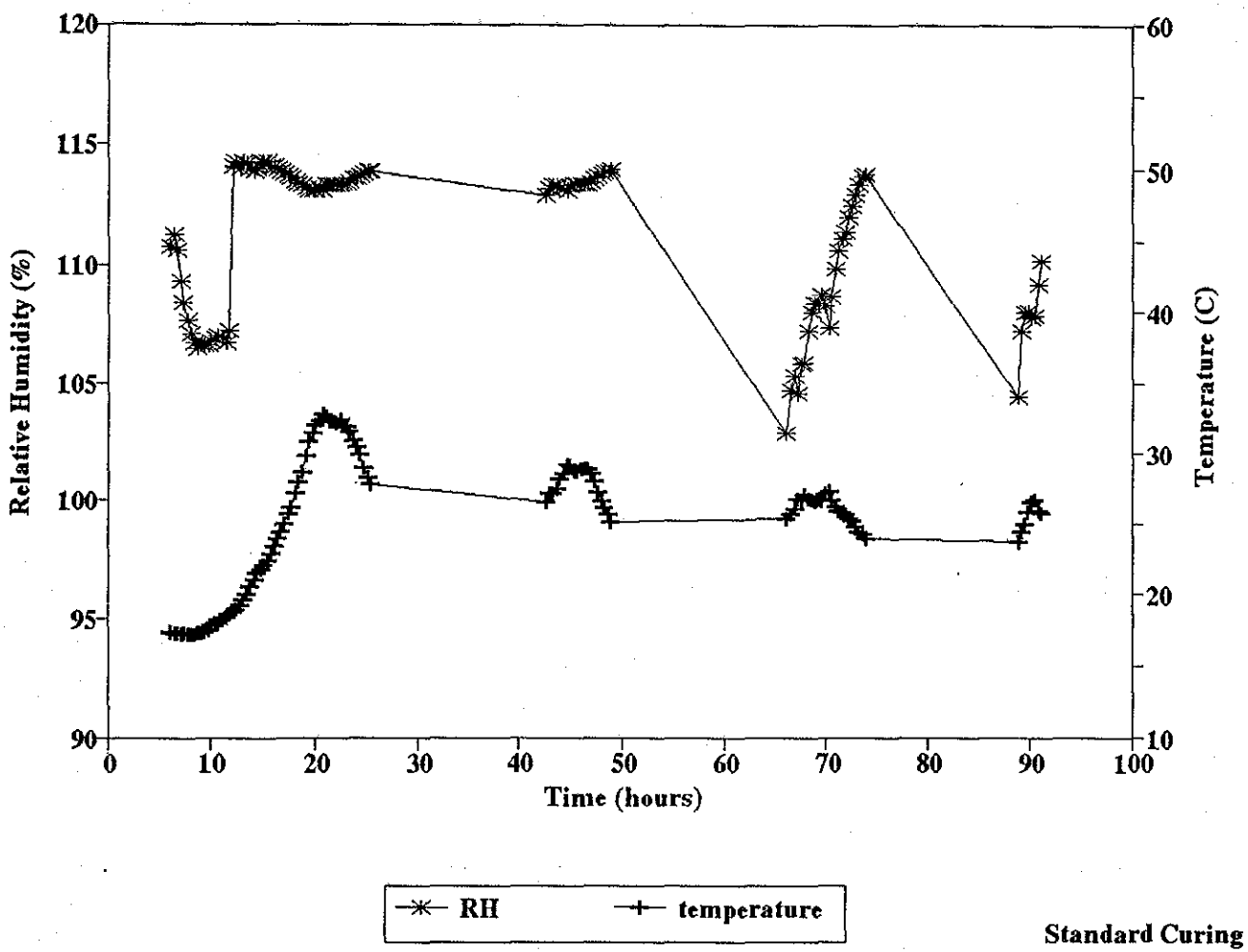

Fig. 2.39. Temperature and Relative Humidity Records at the 1-inch (25 mm) Depth.

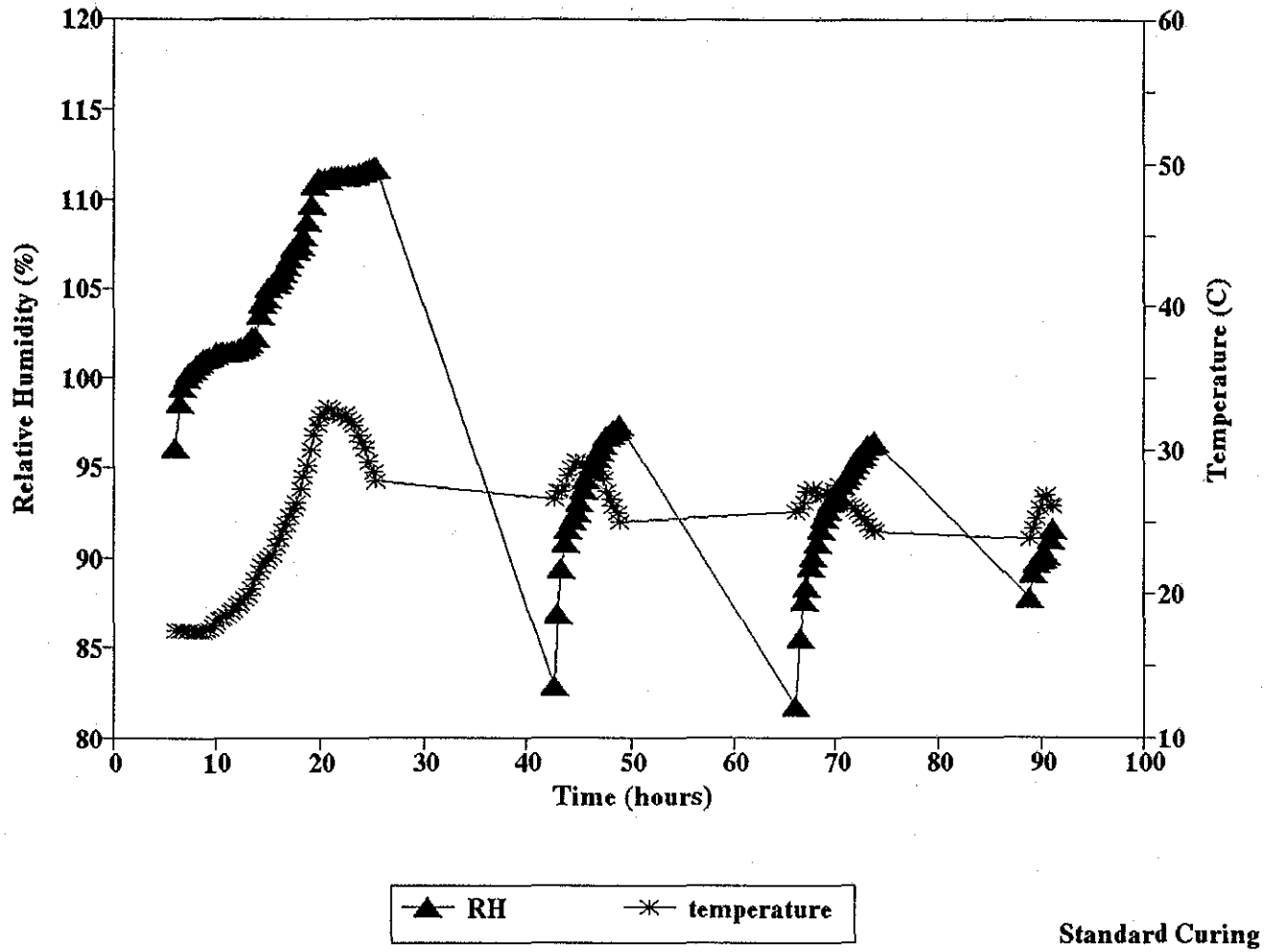

Fig. 2.40. Temperature and Relative Humidity Records at the 2-inch (51 mm) Depth.

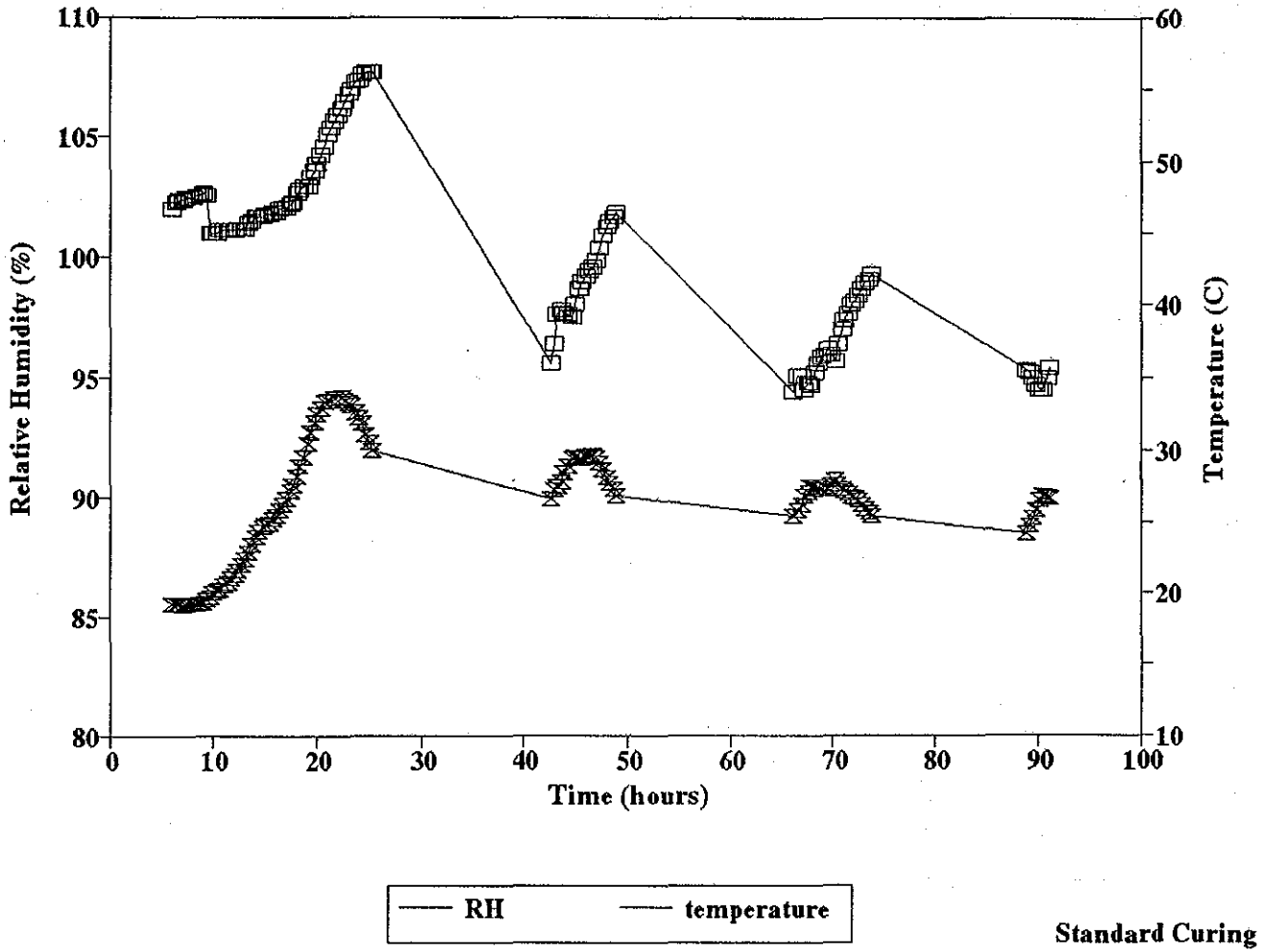

Fig. 2.41. Temperature and Relative Humidity Records at the 4-inch (102 mm) Depth.

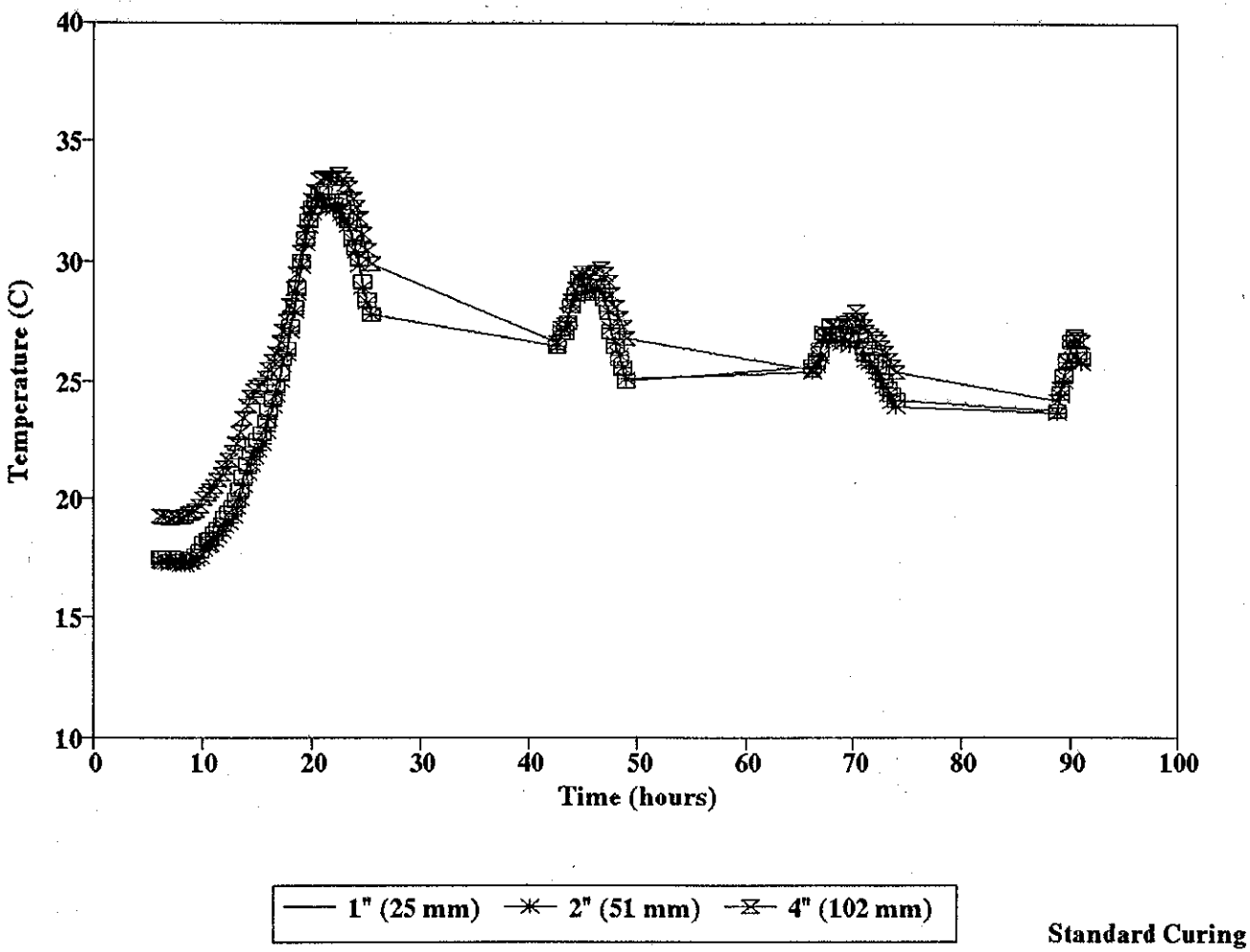

Fig. 2.42. Temperatures at Different Depths.

CHAPTER 3: ANALYSIS OF CONCAVE CURLING IN PAVEMENT [1]

ABSTRACT

A concrete pavement curls to a concave configuration when it is subjected to a negative temperature gradient, which results when the temperature at its bottom surface is higher than at its top surface. A gap may occur between the bottom of the slab and the subgrade if the temperature gradient is large. This chapter offers an analytical approach to the determination of displacement and stress distributions for a semi-infinite slab and for an infinitely long slab of a finite width, which takes into account a gap which may occur under the slab resulting from curling. The elementary plate theory is applied to the slab resting on a Winkler foundation.

The analysis for thermal stresses in a curled pavement slab developed by Westergaard assumes a spring model to represent the subgrade support as a Winkler foundation. The approach adopted by Westergaard is not valid for the case where a gap exists, although it has been widely employed without respect to the effect of the gap on the resulting stress distribution. This chapter examines a critical temperature difference between the bottom and the top slab surfaces at the threshold of gap formation at the slab/subgrade interface in terms of the concrete elastic constants and density, the thermal expansion coefficient of the concrete, thickness of the pavement, and the modulus of the foundation support. If the temperature difference is below the critical value, it is shown that Westergaard's solutions are valid. Based on the solutions presented herein, correction of the coefficients in Bradbury's approximate formula for the maximum stress in a finite pavement are suggested.

3.1. INTRODUCTION

A concrete slab will tend to curl when it is subjected to a temperature gradient extending vertically through the slab thickness. The tendency to curl induces stresses in the

---

[1] Contents of this chapter are published in "Analysis of Concave Curling in Concrete Slabs" By Tianxi Tang, Dan G. Zollinger and Sanjaya Senadheera in Journal of Transportation Engineering, Vol.119, N0.4, Jul./Aug. 1993, pp. 618-633.

pavement as the pavement is restrained by its weight and the support pressures from the subgrade (or foundation). The thermally induced stress caused by such interaction can be a significant factor in contributing to early pavement cracking. This set of circumstances may be critical, particularly within a few hours after placement since concrete is in the early stage of hydration such that the strength may be insufficient to prevent cracking. Research has shown (Emborg, 1991) that temperature rise caused by hydration does not immediately produce thermal stresses because of the process of stress relaxation or creep in the concrete. Thermal stresses arise when the temperature drops after its peak value and the concrete has taken on a set. However, the temperature gradient which causes the slab to curl, as affected by the heat of hydration, could be greater than that caused only by the effect of ambient temperature and solar radiation. Therefore, analysis of thermal strains, as generated from all sources of heat, is especially important for a curled slab at a very early concrete age.

Westergaard's solution (Westergaard, 1926) has been widely used in estimating thermal stresses in curled concrete pavements (e.g., Yoder and Witczak, 1975; and Okamoto et al., 1991). In his solutions, temperature change is assumed to be linear through the thickness of the pavement, the concrete is assumed linear elastic, and a spring model is used to define an elastic subgrade or a Winkler foundation. However, when the temperature difference between the bottom surface and the top surface of the pavement slab exceeds a critical value, the pavement may be so curled that a length of it near the slab edge separates from the subgrade and a gap between the slab bottom and the subgrade results. Although no mutual action exists between the separated portion of the slab and the subgrade, the spring model in Westergaard's solutions is assembled over the entire slab bottom. A modification to the Westergaard analysis is suggested which provides a separation of the spring model from the portion of the slab which is free from the subgrade so as to more appropriately reflect actual slab behavior. The Westergaard analysis provides expressions for displacement and stress distributions for a semi-infinite slab and an infinitely-long slab of a finite width. For a slab of finite dimensions, Bradbury (1938) suggested an approximate formula to estimate the maximum stress, where two coefficients were given based on the Westergaard analysis. Consequently, modifications of the Westergaard analysis can be encompassed within modifications for curled slabs which all account for slab lift off at the slab edge.

3.2. BASIC EQUATIONS

Solutions of this study are, in a general sense, solutions to thermal stress and displacement distributions in an elastic plate resting on a Winkler foundation, and consequently, are applicable to concrete pavements.

The subgrade reaction of a Winkler foundation is expressed as (Scott, 1981):

$$q = -kw. \tag{3.1}$$

where q is the subgrade stress on a unit area, w is the displacement of the slab, and constant k is called the Foundation Modulus. The minus sign in Equation (1.1) indicates that the reaction occurs in the opposite direction of displacement w. When the temperature in a pavement slab is uniformly distributed, the slab theoretically remains planar, that is, accompanied with a uniform vertical subgrade displacement. By denoting ρ and h as the density and thickness of the concrete slab, respectively, one obtains the vertical displacement due to the weight of the slab as:

$$w_o = \frac{\rho h}{k} . \tag{3.2}$$

If the pavement slab is subjected to a negative temperature gradient through its thickness (where the temperature of the slab bottom is higher than the temperature of the slab surface), the slab tends to deform with its edges in an upward position, which contributes an additional component of deflection. Thus, the total displacement of the slab in the downward direction can be decomposed into two parts: w_o and w, that is, $w_{total}=w_o+w$, where w can be determined by the following equations of the elementary plate theory and appropriate boundary conditions for a weightless slab with a uniform temperature gradient (Westergaard, 1926):

$$-\frac{\partial^2 w}{\partial x^2} = \frac{12}{Eh^3}\left(M_x - \nu M_y\right) + \frac{\alpha \Delta t}{h} \tag{3.3}$$

$$-\frac{\partial^2 w}{\partial y^2} = \frac{12}{Eh^3}\left(M_y - \nu M_x\right) + \frac{\alpha \Delta t}{h} \tag{3.4}$$

and $$-\frac{\partial^2 w}{\partial x \partial y} = \frac{12\ (1 + \nu)}{E\ h^3} M_{xy}\ . \tag{3.5}$$

The displacement w is in the z direction (Fig. 3.1), and E, ν and α are respectively Young's modulus, Poisson's ratio and the thermal expansion coefficient of the slab. The moments in Eqs. (3.3) to (3.5) and shear forces are denoted as positive when their directions are the same as shown in Fig. 3.2. The temperature difference Δt is assumed to vary linearly between the slab bottom surface and the slab top surface with no temperature change at the mid-plane of the slab. When the temperature at the top surface is lower than at the bottom surface, Δt is denoted as positive.

3.3. STRESSES IN AN INFINITE PAVEMENT

When the pavement slab is considered to be of infinite extent with respect to the width and length of the slab, the tendency to curl is fully restrained or $w \equiv 0$ such as

$$M_x = M_y = -\frac{Eh^2 \alpha \Delta t}{12\ (1 - \nu)}, \quad M_{xy} = 0 \tag{3.6}$$

With a positive Δt, the maximum tensile stress is at the top surface of the slab either in x or y direction, whose value is:

$$\sigma_o = \frac{E\alpha \Delta t}{2\ (1 - \nu)}. \tag{3.7}$$

If $E = 3 \times 10^6$ psi (2070 MPa) , $\nu = 0.15$, $\alpha = 6 \times 10^{-6}$/°F, $k = 100$ lb/in^3 (27.1 MN/m^3), and $\Delta t = 22.2$°C (40°F), then $\sigma_o = 424$ psi (2.92 MPa) according to Eq. (3.7). These parameters will be employed in other examples in this chapter without further

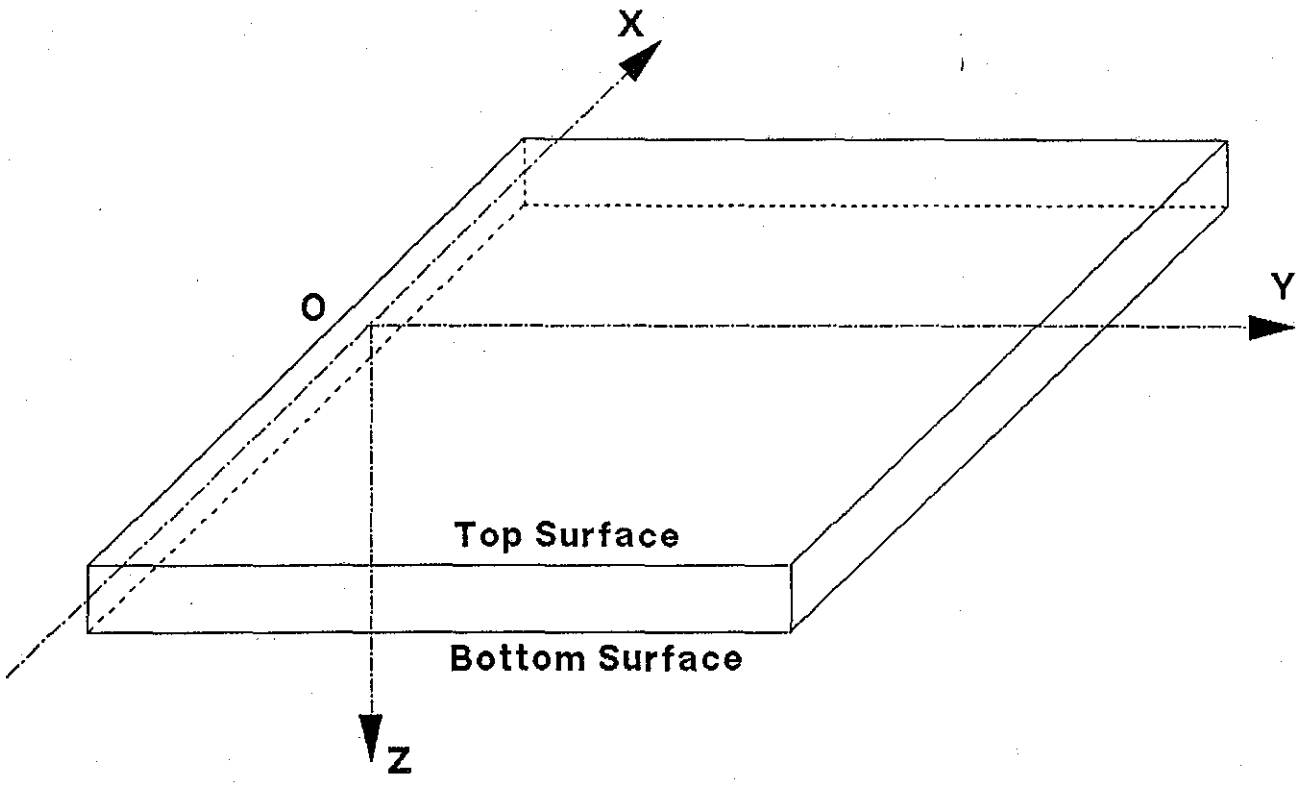

Fig. 3.1. A Pavement Slab with the Coordinate System.

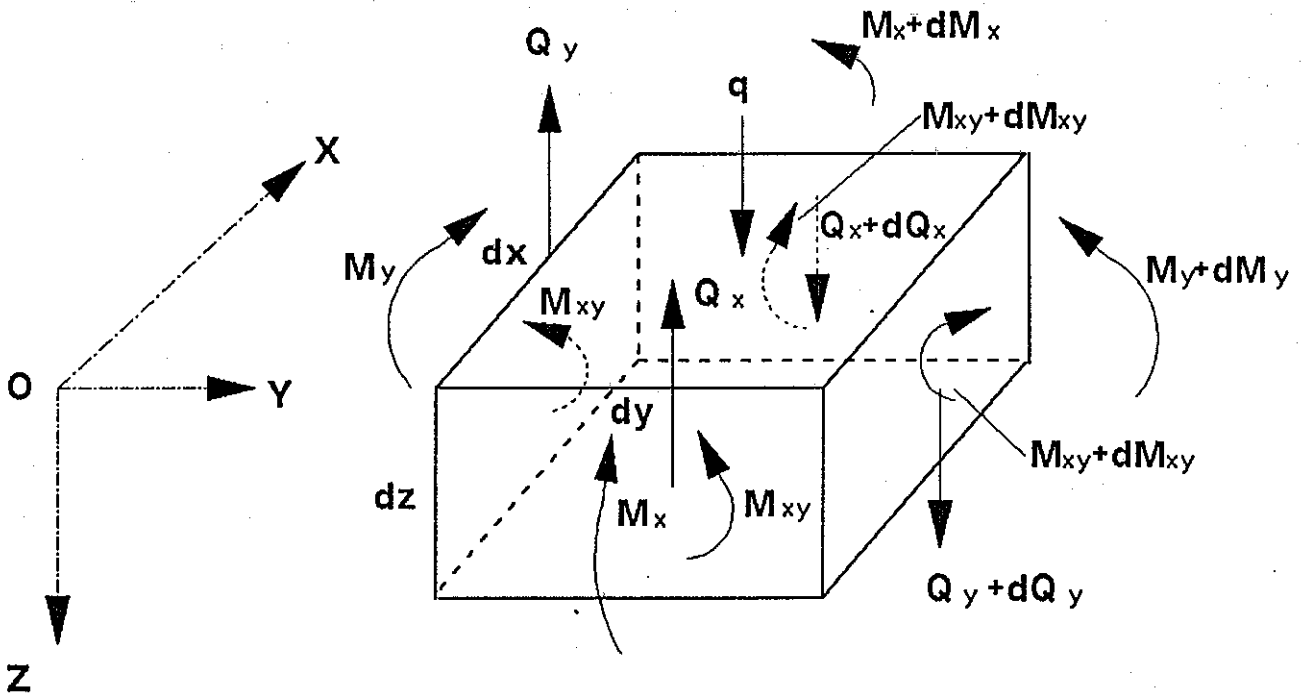

Fig. 3.2. Stress Resultants Acting on Plate Element.

comment unless otherwise indicated. Infinite slab behavior can be considered to apply to the area that is far enough from the slab edges.

3.4. STRESSES IN A SEMI-INFINITE PAVEMENT

A pavement slab with an edge at $y = 0$ that is assumed to be infinite in the positive y direction and in the positive and negative x directions is shown in Fig. 3.1. The slab behavior in this instance is independent of x. Combining Eqs. (3.3) and (3.4), one obtains (Westergaard, 1926):

$$M_y = \frac{Eh^3}{12(1 - \nu^2)} \left[- \frac{d^2w}{dy^2} - \frac{(1 + \nu)\ \alpha\Delta t}{h} \right]. \tag{3.8}$$

Static equilibrium requires:

$$\frac{\partial^2 M}{\partial y^2} = kw \tag{3.9}$$

for a slab element that is in contact with the subgrade. For the portion of the pavement which is in contact with the subgrade, the following equation, from Eqs. (3.8) and (3.9), holds:

$$\frac{Eh^3}{12(1 - \nu^2)} \frac{d^4w}{dy^4} + kw = 0 \tag{3.10}$$

or $$\ell^4 \frac{d^4w}{dy^4} + w = 0, \qquad \ell = \sqrt[4]{\frac{Eh^3}{12\ (1 - \nu^2)k}} \tag{3.11}$$

where ℓ is called the radius of relative stiffness. The general solution to Eq. (3.11) which satisfies, the condition $w = 0$ at $y = \infty$ is:

$$w = \left[A_1 \cos \frac{y}{\sqrt{2}\,\ell} + A_2 \sin \frac{y}{\sqrt{2}\,\ell} \right] e^{-\frac{y}{\sqrt{2}\,\ell}}. \tag{3.12}$$

With the boundary conditions moment $M_y = 0$, shear force $Q_y = 0$ at the edge $y = 0$, one obtains:

$$A_1 = -A_2 = -\frac{\ell^2 (1 + \nu)\, \alpha \Delta t}{h} = -w_{so}, \tag{3.13}$$

which the associated displacement is (Westergaard 1926):

$$w = -w_{so} \sqrt{2} \cos \left(\frac{y}{\sqrt{2}\,\ell} + \frac{\pi}{4} \right) e^{-\frac{y}{\sqrt{2}\,\ell}}, \qquad w_{so} = \frac{\ell^2 (1 + \nu) \alpha \Delta t}{h} \tag{3.14}$$

where w_{so} is the magnitude of the displacement at the edge $y = 0$. The stress in y direction at the top surface is (Westergaard 1926):

$$\sigma_y = \sigma_o \left[1 - \sqrt{2} \sin \left(\frac{y}{\sqrt{2}\,\ell} + \frac{\pi}{4} \right) \right] e^{-\frac{y}{\sqrt{2}\,\ell}}, \tag{3.15}$$

which is the maximum tensile stress within the cross-section of the slab parallel to the x axis. The stress in x direction at the top surface can be calculated by using the following relationship (Westergarrd 1926):

$$\sigma_x = \sigma_o + \nu \left(\sigma_y - \sigma_o \right). \tag{3.16}$$

These solutions are valid for a slab which remains in contact with the subgrade whether the slab is subjected to a negative or positive temperature gradient. Nevertheless, when $\Delta t > 0$ (the temperature at the top surface is lower than at the bottom surface) the pavement is

curled such that the displacement at the edge w (y=0) = $-w_{so}$. Therefore, the necessary and sufficient condition for Eq. (3.9) to be valid is:

$$w_{so} \leq w_o \tag{3.17}$$

or

$$\Delta t \leq (\Delta t)_{sc} = \left[\frac{h}{\sqrt{2}\,\ell}\right]^2 \frac{2\rho}{k(1+\nu)\alpha} \tag{3.18}$$

where $(\Delta t)_{sc}$ is the critical temperature difference for the semi-finite pavement, since it is the maximum temperature difference correlating to impending slab lift off.

When the temperature difference is larger than $(\Delta t)_{sc}$, the length of slab lift off, s, is assumed to separate from the subgrade surface (Fig. 3.3). When the x=0 is positioned at the end of the length s rather than the edge of the slab as shown in Fig. 3.3, the governing equations for the part $-s \leq y \leq 0$ are provided by Eq. (3.8) and the following equation:

$$\frac{\partial^2 M}{\partial y^2} = -\rho h \,. \tag{3.19}$$

Combination of Eqs. (3.8) and (3.19) yields

$$\frac{Eh^3}{12(1-\nu^2)} \frac{d^4 w}{dy^4} - \rho h = 0 \,. \tag{3.20}$$

The boundary condition for this portion is $M_y = 0$ and $Q_y = 0$ at $y = -s$. The general solution for the displacement w, Eq. (3.12), is still applicable for the slab portion between the limits $0 \leq y \leq +\infty$, but the coefficients A_1 and A_2 and another unknown s should be determined to comply with the boundary condition at $y = 0$: $w = -w_o$, and w and its derivatives with respect to y are continuous. In terms of loads, the boundary condition at $y = 0$ can be summarized as (Fig. 3.4):

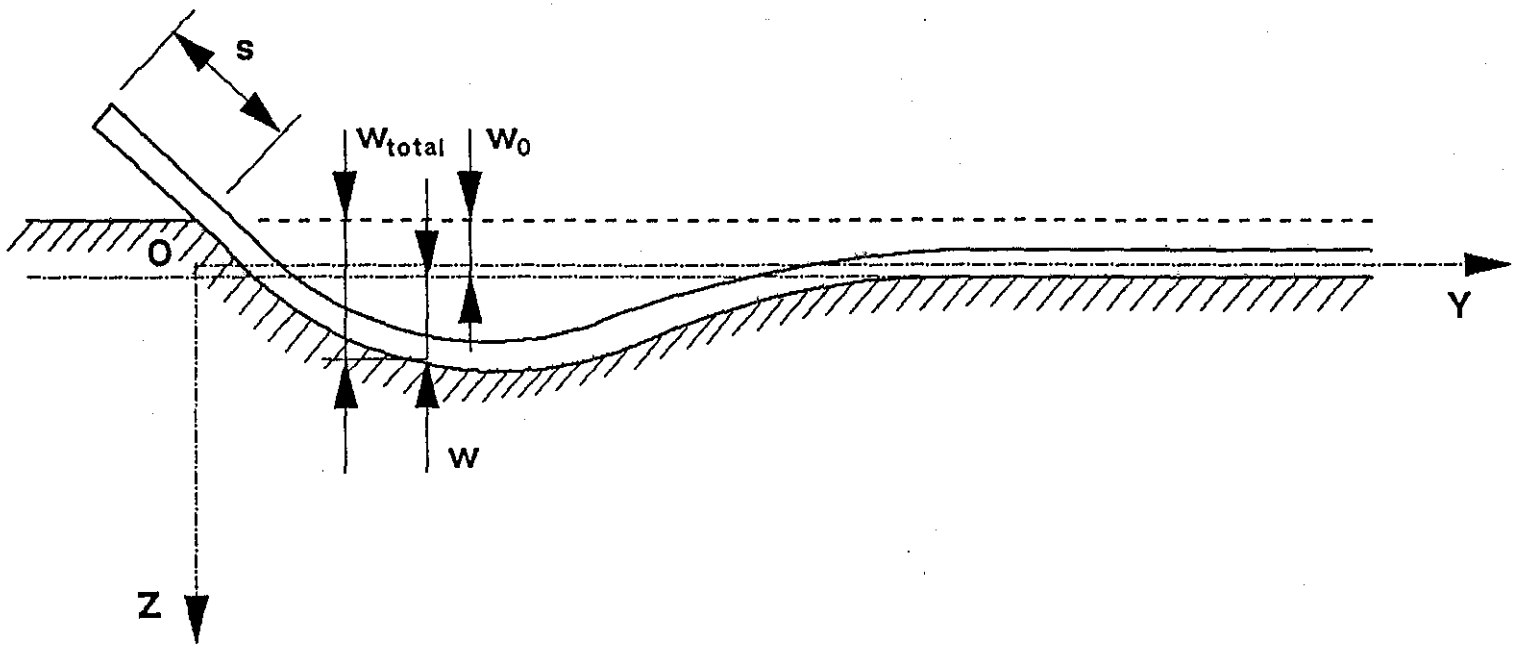

Fig. 3.3 Sketch of an Up-Curled Semi-Infinite Pavement Slab

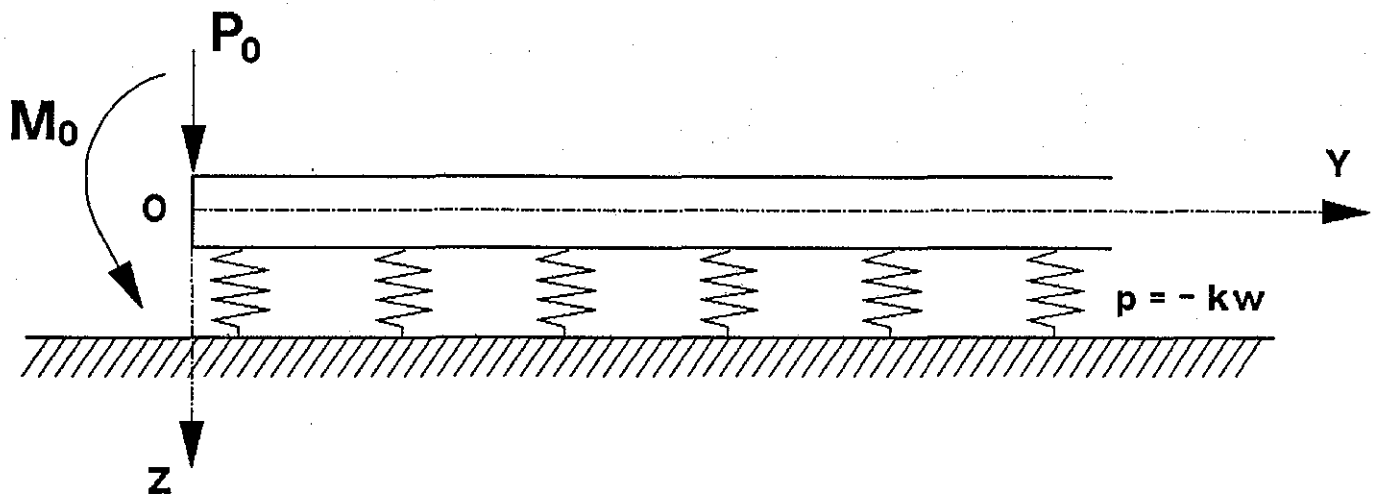

Fig. 3.4 Mathematical Model for the Up-Curled Semi-Infinite Slab

$$\left.\begin{aligned} M_y &= -M_o = -\frac{1}{2}\rho h s^2 \\ Q_y &= -P_o = -\rho h s \\ w &= -w_o \end{aligned}\right\} \qquad at\ y = 0. \tag{3.21}$$

The results are:

$$A_1 = -w_o, \tag{3.22}$$

$$A_2 = -w_o(1+2\gamma), \tag{3.23}$$

and $$\frac{s}{\sqrt{2}\ell} = \gamma - 1, \tag{3.24}$$

where $$\gamma = \sqrt{\frac{w_{so}}{w_o}}\ . \tag{3.25}$$

Therefore,

$$w = -\frac{w_o}{\cos\varphi}\cos\left[\frac{y}{\sqrt{2}\ell} + \varphi\right] e^{-\frac{y}{\sqrt{2}\ell}}, \tag{3.26}$$

and

$$\sigma_y = \sigma_o\left[1 - \frac{w_o}{w_{so}\cos\varphi}\sin\left[\frac{y}{\sqrt{2}\ell} + \varphi\right] e^{-\frac{y}{\sqrt{2}\ell}}\right], \tag{3.27}$$

where

$$\cos \varphi = \frac{1}{\sqrt{2(2\gamma^2-2\gamma+1)}}. \tag{3.28}$$

Note that solutions (3.26) and (3.27) are for temperature differences $\Delta t \geq (\Delta t)_{sc}$. In the extreme case, where $\Delta t = (\Delta t)_{sc}$ or $w_{so} = w_o$, and hence $s = 0$, and $\varphi = \pi/4$, Eqs. (3.26) and (3.27) become identical with Eqs. (3.14) and (3.15). Differentiating the right side of Eq. (3.27) and equating it to zero, one concludes that σ_y reaches its maximum value at

$$y = \sqrt{2}\ \ell(\ 5\pi\ /4\ -\ \varphi).$$

With the parameters used in the previous example and $\rho = 0.087$ lb/in^3 (2.4 g/cm^3) and $h = 8$ in (2.03 cm), the following is calculated:

$\ell = 33.8$ in (85.9 cm),

$\Delta t = 40°$F (22.2°C) $> (\Delta t)_{sc} = 14.13°$F (7.85°C) or

$w_{so} = 0.0394$ inch (1.001 mm) $> w_o = 0.00696$ inch (0.177 mm).

Eqs. (3.14) and (3.15) are not valid in this instance. From Eqs. (3.24), (3.26), and (3.27), one obtains:

$s = 1.37\ell = 5.46$ ft (166 cm), and

$\varphi = 75.1°$.

Displacement and stress distributions with these parameters calculated with Eqs. (3.26) and (3.27) are shown in Figs. 3.5 and 3.6, where abscissa 0 represents the edge of the slab and $s/\sqrt{2}\ell$ represents the location of the x axis shown in Figs. 3.3 and 3.4. As seen in the figures, Westergaard's solutions without consideration of the gap effects overestimate σ_y for the range $0 < (y/\sqrt{2}\ell) < 3.7$. As illustrated, stress σ_y approaches σ_o when $(y/\sqrt{2}\ell)$ is approximately 6. For $y > 6\sqrt{2}\ell$, the slab behavior can be considered to be infinite.

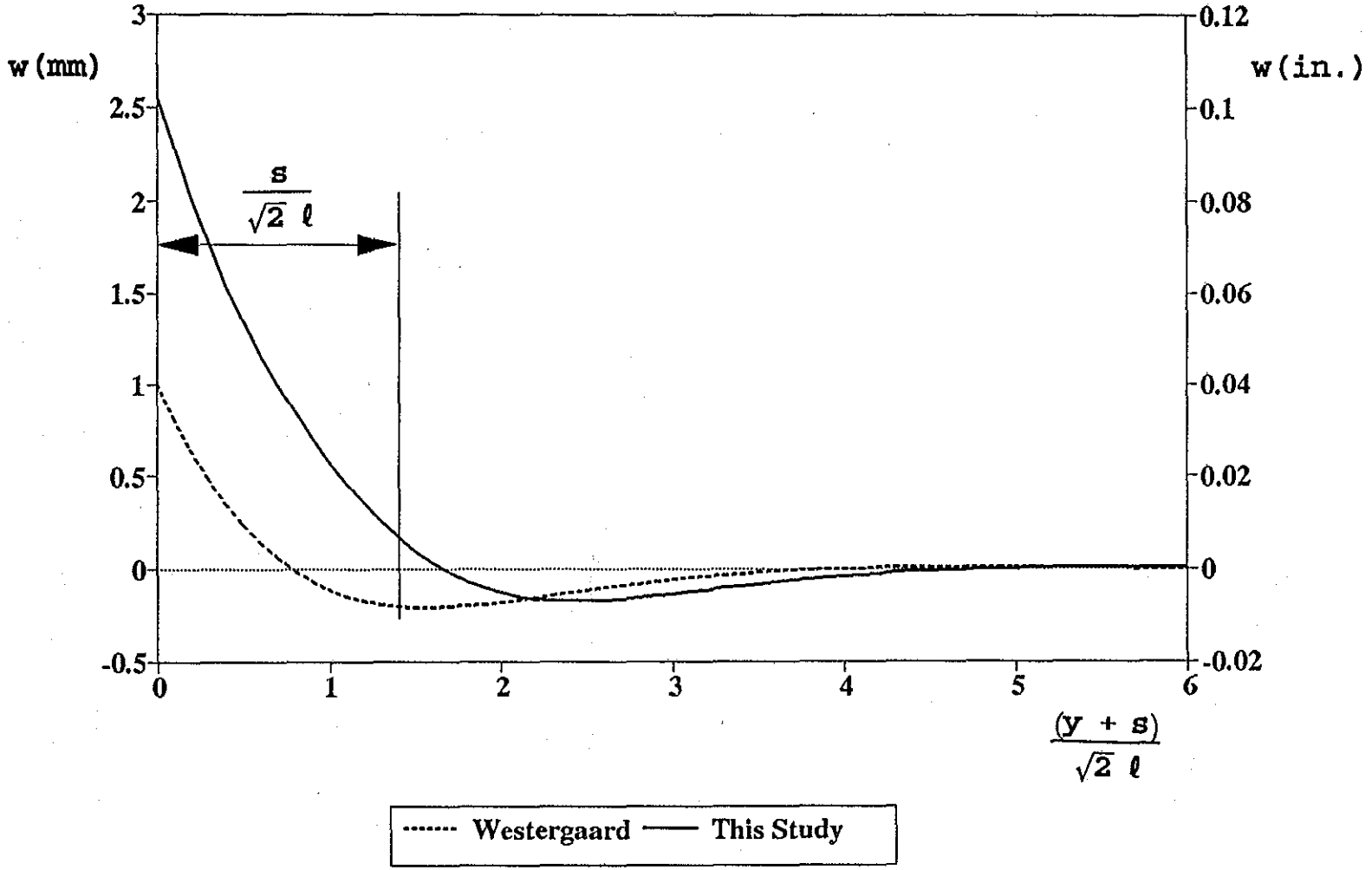

Fig. 3.5. Stress Distribution for an Up-Curled Semi-Infinite Slab.

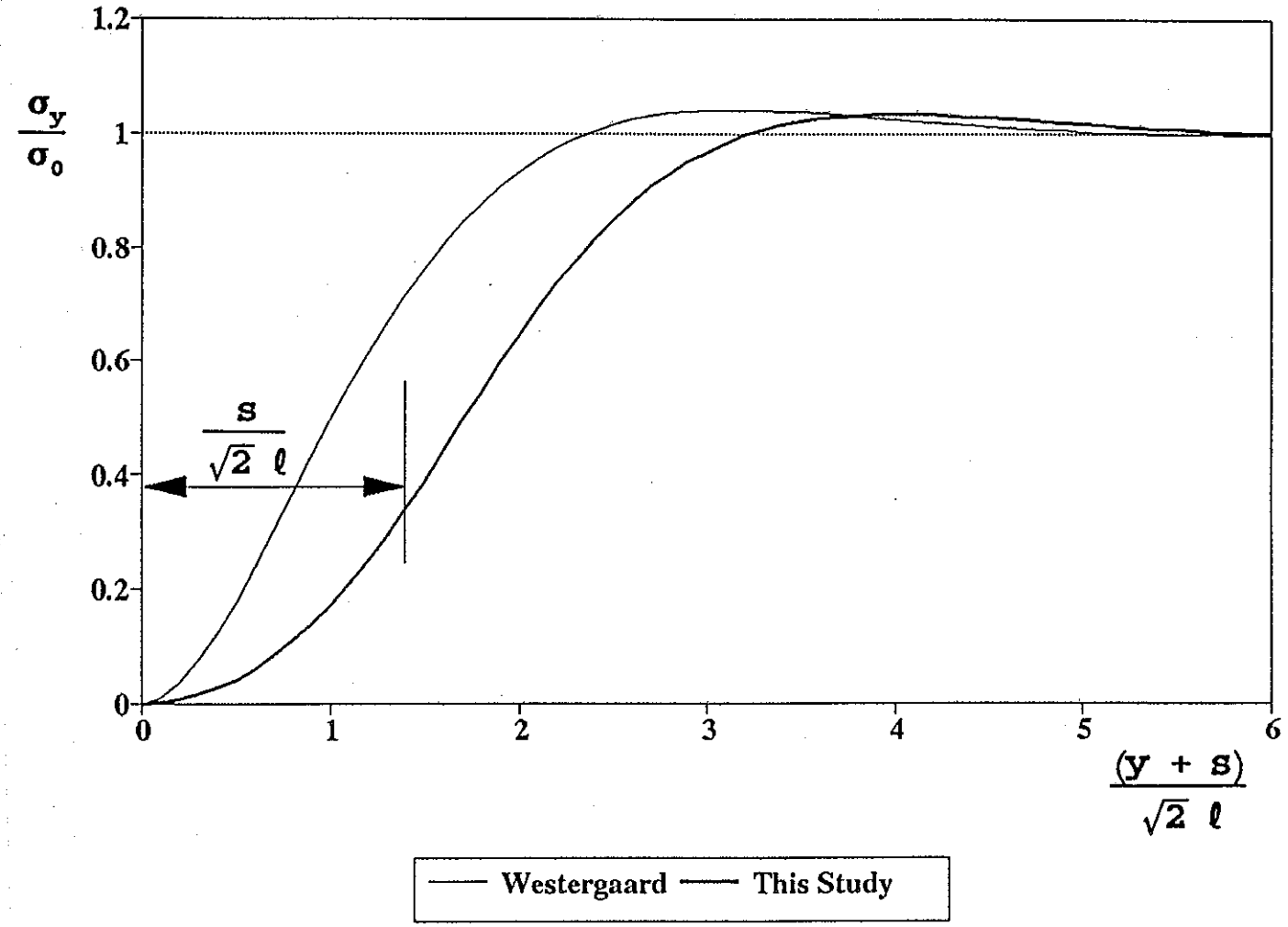

Fig. 3.6. Displacement for an Up-Curled Semi-Infinite Slab.

3.5. STRESSES IN AN INFINITELY LONG PAVEMENT OF A FINITE WIDTH

For the condition where the pavement slab is infinite in both the positive and negative x directions with a finite width of b in the y direction ($-b/2 \leq y \leq b/2$), the problem is symmetric with respect to the x axis. The general solution to Eq. (3.10) becomes:

$$w = B_1 \cos\frac{y}{\sqrt{2}\ell} \cosh\frac{y}{\sqrt{2}\ell} + B_2 \sin\frac{y}{\sqrt{2}\ell} \sinh\frac{y}{\sqrt{2}\ell} \tag{3.29}$$

Then the corresponding σ_y is:

$$\sigma_y = \sigma_o - \frac{E}{2(1-\nu^2)} \frac{h}{\sqrt{2}\ell} \left[\frac{B_1}{\sqrt{2}\ell} \sin\frac{y}{\sqrt{2}\ell} \sinh\frac{y}{\sqrt{2}\ell} - \frac{B_2}{\sqrt{2}\ell} \cos\frac{y}{\sqrt{2}\ell} \cosh\frac{y}{\sqrt{2}\ell} \right] \tag{3.30}$$

For a slab in full contact with the subgrade, Eqs. (3.29) and (3.30) must satisfy the boundary condition:

$$\left.\begin{aligned} M_y &= 0 \\ Q_y &= 0 \end{aligned}\right\} \qquad at\ y = \frac{b}{2} \tag{3.31}$$

such that

$$B_1 = w_{so} \frac{2(\tan m - \tanh m)\cos m \cosh m}{\sin 2m + \sinh 2m}, \tag{3.32}$$

$$B_2 = -w_{so} \frac{2(\tan m + \tanh m)\cos m \cosh m}{\sin 2m + \sinh 2m}, \tag{3.33}$$

and then

$$w = -w_{bo}\frac{2\cos m\,\cosh m}{-\sin 2m + \sinh 2m}\left[(-\tan m + \tanh m)\cos\frac{y}{\sqrt{2}\,\ell}\cosh\frac{y}{\sqrt{2}\,\ell} + (\tan m + \tanh m)\sin\frac{y}{\sqrt{2}\,\ell}\sinh\frac{y}{\sqrt{2}\,\ell}\right] \tag{3.34}$$

and

$$\sigma_y = \sigma_o\left[1 - \frac{2(\tan m - \tanh m)\,\cos m\,\cosh m}{\sin 2m + \sinh 2m}\sin\frac{y}{\sqrt{2}\,\ell}\,\sinh\frac{y}{\sqrt{2}\,\ell} - \frac{2\,(\tan m + \tanh m)\,\cos m\,\cosh m}{\sin 2m + \sinh 2m}\cos\frac{y}{\sqrt{2}\,\ell}\,\cosh\frac{y}{\sqrt{2}\,\ell}\right], \tag{3.35}$$

where $m = b/(2\sqrt{2}\ell)$, $-w_{bo}$ is the displacement at $y = \pm b/2$, and

$$w_{bo} = w_{so}\,\frac{-\sin 2m + \sinh 2m}{\sin 2m + \sinh 2m}. \tag{3.36}$$

Solutions (3.34) and (3.35) were given by Westergaard. Similar to the semi-infinite case, when $\Delta t > 0$, σ_y is the maximum tensile stress in the y direction within the cross-section parallel to the x axis, located at the top surface. The stress in the x direction at the top surface is determined by Eq. (3.16).

Displacement and stress distributions shown in Eqs. (3.34) to (3.35) are valid only when:

$$w_{bo} \le w_o \tag{3.37}$$

or

$$\Delta t \le (\Delta t)_{bc} = \left[\frac{h}{\sqrt{2}\,\ell}\right]^2 \frac{2\rho}{k\,(1+\nu)\alpha}\left[\frac{\sin 2m + \sinh 2m}{-\sin 2m + \sinh 2m}\right], \tag{3.38}$$

where $(\Delta t)_{bc} = (\Delta t)_{sc}\,(w_{so}/w_{bo})$ is the critical temperature at which slab lift-off occurs for the infinitely long pavement of a finite width.

When $\Delta t > (\Delta t)_{bc}$, the slab lift-off occurs at each edge of the slab. By assuming that the width of the pavement slab, b', is $b+2s$ (s previously defined), Eq. (3.29) is still applicable for w within $0 \le y \le b/2$, but it must satisfy the following boundary condition:

$$\left.\begin{aligned} M_y &= -\frac{1}{2}\rho h s^2 \\ Q_y &= \rho h s \end{aligned}\right\} \qquad at\ y = \frac{b}{2}. \tag{3.39}$$

The constants B_1, B_2 and s have a dimension of length. The following dimensionless expressions are given for determining the three constants:

$$\left[\frac{s}{\sqrt{2}\,\ell}\right]^2 + \frac{4\,(\sin^2 m \sinh^2 m + \cos^2 m \cosh^2 m)}{-\sin 2m + \sinh 2m}\left[\frac{s}{\sqrt{2}\,\ell}\right] + \left[\frac{w_{so}}{w_{bo}} - \frac{w_{so}}{w_o}\right] = 0, \tag{3.40}$$

$$\left[\frac{B_1}{\sqrt{2}\,\ell}\right] = \frac{1}{\sinh m \cosh m + \sin m \cos m}\left[-(\sin m \cosh m - \cos m \sinh m)\left[\frac{w_o}{\sqrt{2}\,\ell}\right]\left[\frac{s}{\sqrt{2}\,\ell}\right]^2 + 2\cos m \cosh m\left[\frac{w_o}{\sqrt{2}\,\ell}\right]\left[\frac{s}{\sqrt{2}\,\ell}\right] + (\sin m \cosh m - \cos m \sinh m)\left[\frac{w_{so}}{\sqrt{2}\,\ell}\right]\right], \tag{3.41}$$

and

$$\left[\frac{B_2}{\sqrt{2}\,\ell}\right] = \frac{1}{\sinh m \cosh m + \sin m \cos m}\left[(\sin m \cosh m + \cos m \sinh m)\left[\frac{w_o}{\sqrt{2}\,\ell}\right]\left[\frac{s}{\sqrt{2}\,\ell}\right]^2 + 2\sin m \sinh m\left[\frac{w_o}{\sqrt{2}\,\ell}\right]\left[\frac{s}{\sqrt{2}\,\ell}\right] - (\sin m \cosh m + \cos m \sinh m)\left[\frac{w_{so}}{\sqrt{2}\,\ell}\right]\right]. \tag{3.42}$$

By substituting the above results, Eqs. (3.40) to (3.42), into Eqs. (3.29) and (3.30), one obtains the displacement and stress distributions for $-b/2 \le y \le b/2$.

Eq. (3.40) can be rewritten as follows:

$$\left[\frac{s}{\sqrt{2}\,\ell}\right]^2 + \frac{2}{\eta}\left[\frac{s}{\sqrt{2}\,\ell}\right] + \frac{w_{so}}{w_{bo}} = \frac{w_{so}}{w_o} \tag{3.43}$$

where $\eta = (-\sin 2m + \sinh 2m)/2(\sin^2 m \sinh^2 m + \cos^2 m \cosh^2 m)$ and $m = b/(2\sqrt{2}\ell) = (b' - 2s)/(2\sqrt{2}\ell)$. Eq. (3.43) for b or s is nonlinear for a specified b' since η and (w_{bo}/w_{so}) are not constant, but can be determined by iteratively solving the results using the quadratic formula. The relations for the dimensionless quantities η and (w_{bo}/w_{so}) versus the normalized length m, respectively, are shown in Fig. 3.7. These two curves provide an initial estimate of b or s value in the iterative process. When the slab is wide enough, both η and (w_{bo}/w_{so}) approach unity, and then Eq. (3.43) can be simplified as:

$$\left[\frac{s}{\sqrt{2}\,\ell}\right]^2 + 2\left[\frac{s}{\sqrt{2}\,\ell}\right] + 1 = \frac{w_{so}}{w_o} \tag{3.44}$$

or

$$\frac{s}{\sqrt{2\ell}} = \sqrt{\frac{w_{so}}{w_o}} - 1 \tag{3.45}$$

which is identical to Eq. (3.24) for a semi-infinite slab. Eq. (3.45) may be taken as an approximation for determining s when m is not too small. Judging the expressions for η, w_{bo} and w_{so}, one finds that both η and (w_{bo}/w_{so}) approach unity as $\sinh 2m >> 1$ or $m >> 1$. If an s value obtained from Eq. (3.45) results in $m >> 1$ for a specified b', behavior of slab of corresponding width can be approximately considered to be a semi-infinite slab.

If the width of the slab is assumed as $b' = 24$ ft (7.3 m) as in a highway pavement before the longitudinal joint is formed, the lengths b and s can be determined with Eq. (3.43). First, an s value is solved from Eq. (3.44) as the initial value of s for iteration, which is $s = 5.52$ ft (168 cm) or $s/\sqrt{2}\ell = 1.38$. By substituting this s value in η in Eq. (3.43), the second value of s is obtained. After four runs of iteration, an accurate s

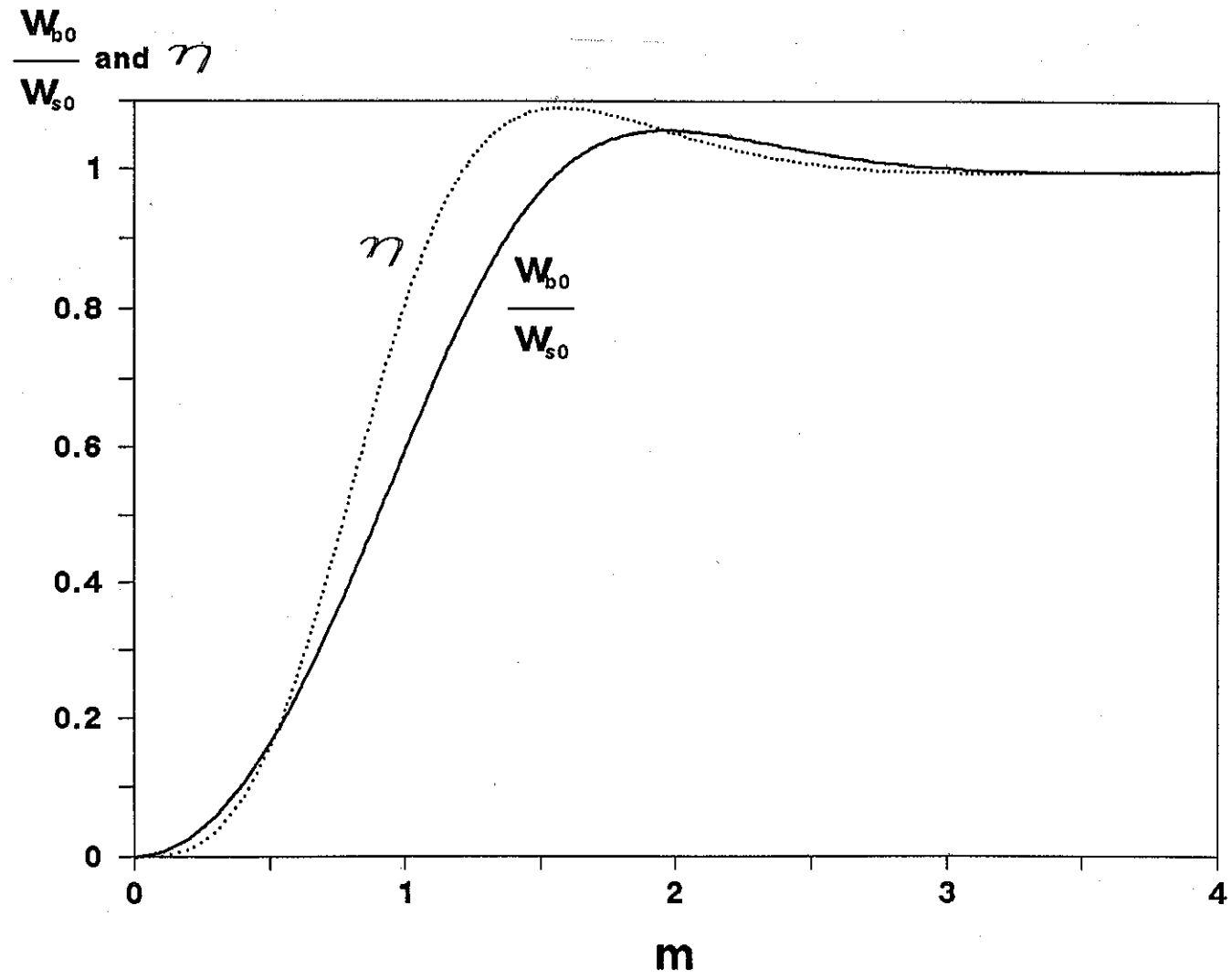

Fig. 3.7. Stress Distribution for an Up-Curled Infinitely Long Slab of a Finite Width.

value appears, which is s = 5.72 ft (174 cm) or $s/\sqrt{2\ell}=1.43$. The displacement and stress distributions calculated from this value are shown in Figs. 3.8 and 3.9. Since the strength of concrete at early ages can be rather lower than that when concrete is mature, analysis of thermal stresses in concrete pavement slab before the longitudinal joint is formed is significant.

Location and the magnitude of the maximum σ_y in an infinitely long pavement of a finite width can be acquired by maximizing σ_y in Eq. (3.30). When m is not too small, the slab behavior along the slab edge may be assumed to be semi-infinite. Accordingly, the maximum σ_y may be obtained by simply substituting $y = \sqrt{2\ell}(5\pi/4 - \varphi)$ to Eq. (3.27).

3.6. MAXIMUM STRESS IN A FINITE PAVEMENT

When a slab with a finite length L_x and a finite width L_y on a Winkler foundation is curled in a concave configuration as subjected to a negative temperature gradient, displacement and stress distributions can also be found analytically, where the governing equations are not ordinary differential equations but partial differential equations. For estimating the maximum σ_y in a finite slab, Bradbury (1938) proposed an approximate formula as follows:

$$\sigma = \frac{E\ \alpha\ \Delta\ t}{2} \left[\frac{C_1 + \nu C_2}{1 - \nu^2} \right] \tag{3.46}$$

where the coefficients C_1 and C_2 for the appropriate slab dimensions were given based on Westergaard's stress solution Eq. (3.35) for an infinitely long slab of a finite width in terms of the ratio of the maximum σ_y / σ_o . In the cases where the temperature difference exceeds the critical temperature difference $(\Delta t)_{bc}$, the Bradbury coefficients should be corrected. By combining Eq. (3.35) and Eqs. (3.40) to (3.42), the ratio of the maximum σ_y to σ_o, C_1 or C_2, is obtained for values of m. Fig. 3.10 shows an example of application for Δt = 40°F (22.2°C), where the relation of C (C_1 or C_2) in terms of the ratio of d (= L_x or L_y) to ℓ, rather than m, is given. It should be noted that the curve determined by this study is dependent on the temperature difference, because the length s is dependent on the

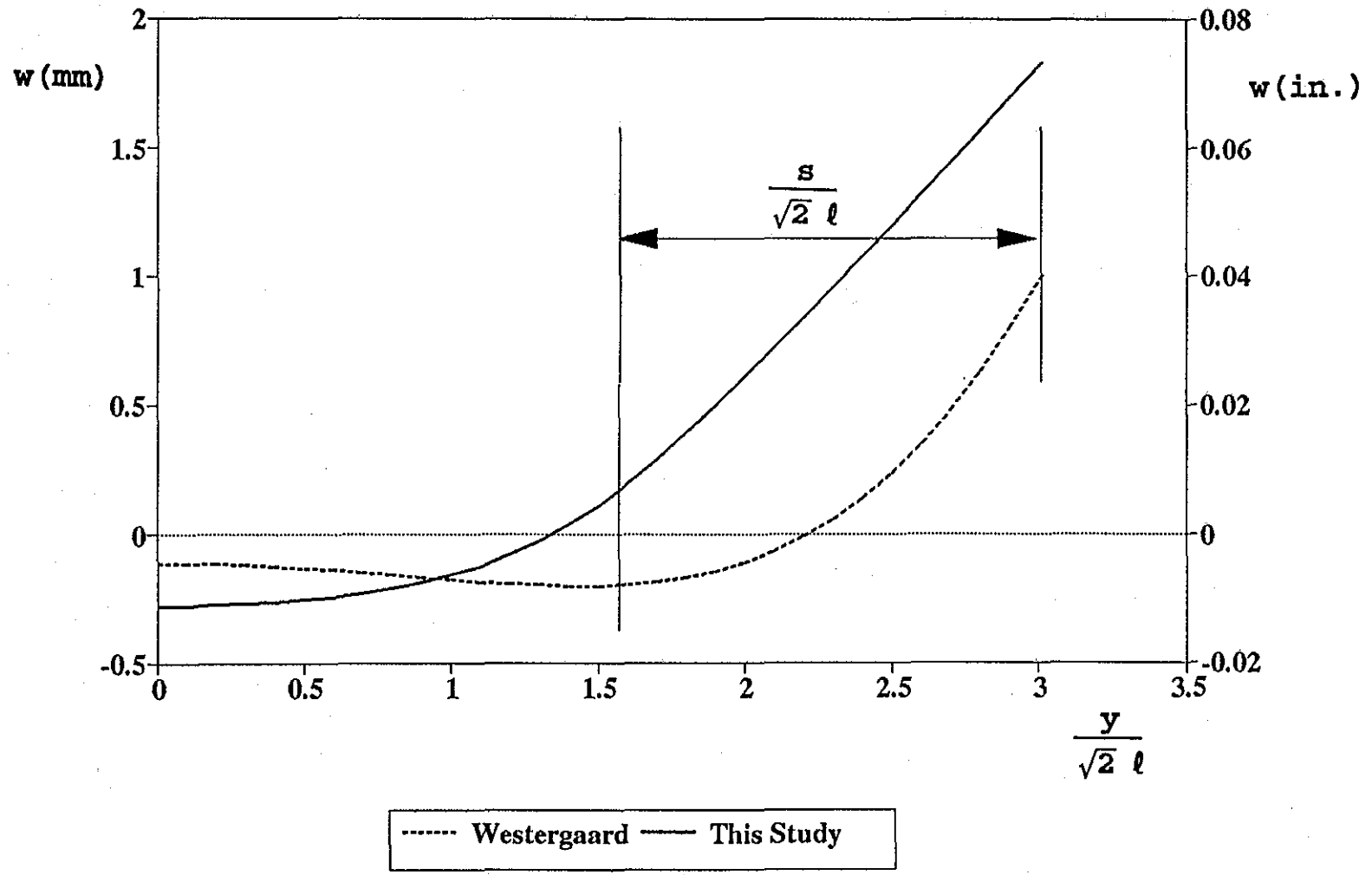

Fig. 3.8. Displacement Distribution for an Up-Curled Infinitely Long Pavement of a Finite Width.

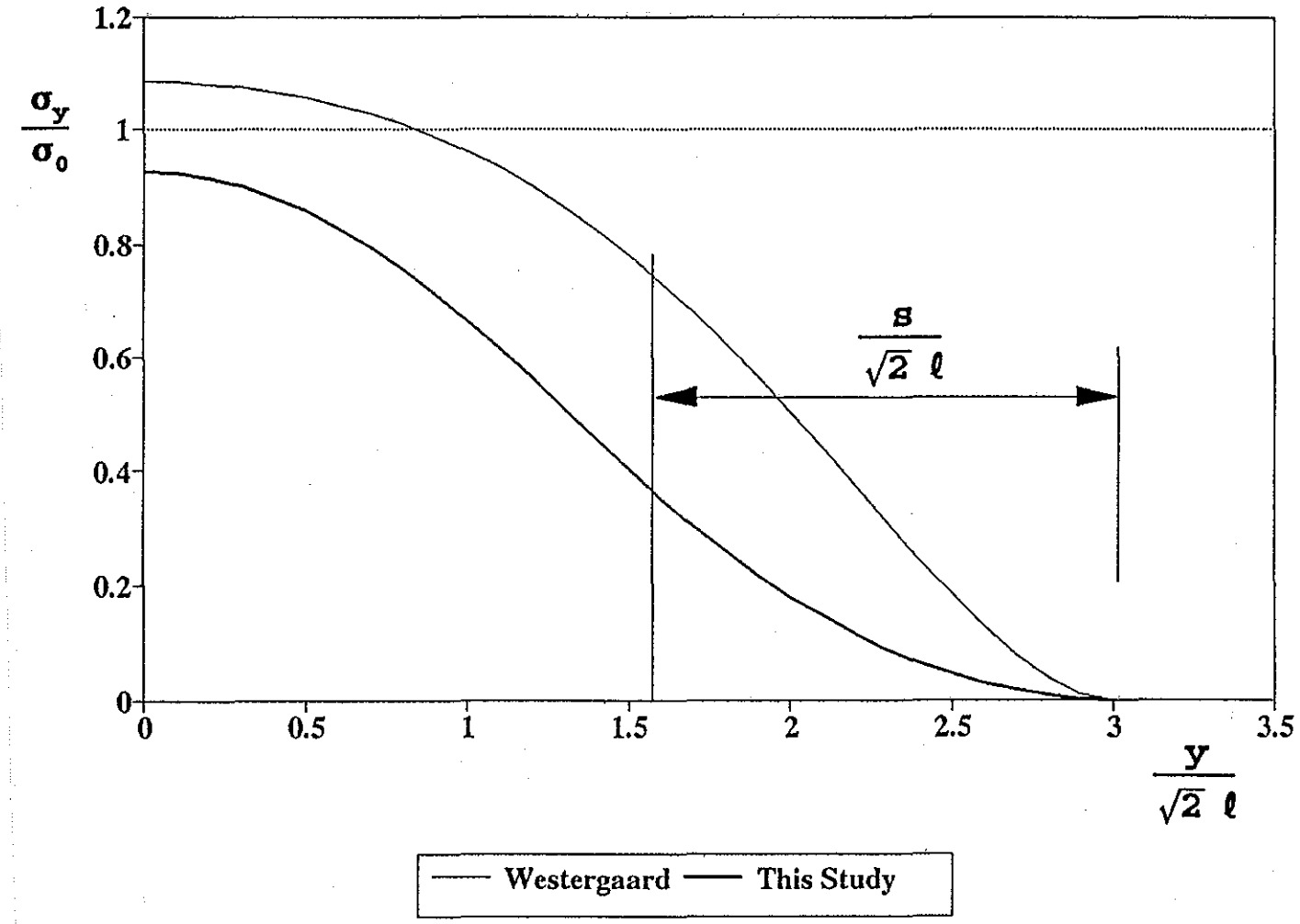

Fig. 3.9. Coefficients in Equation (3.43).

temperature difference for a specified slab. However, there appears to be no significant differences between the curves shown in Fig. 3.10. This analysis provides improved values for coefficients C_1 and C_2, and confirms that Westergaard's solution is applicable in estimating the maximum stress (not the stress distribution) in the slab without significant errors in a wide range of temperature differences. When the temperature difference between the bottom surface and top surface of the slab is large enough, modification of C_1 and C_2 based on the solutions of this study is appropriate.

The above analysis is applicable to slabs with free boundary conditions. For the case where the slab edge is restrained, displacement and stress solutions are provided in the following section.

3.7. STRESSES IN A CURLED SLAB WITH ITS EDGE RESTRAINED

When a slab with its edge restrained is curled as subjected to a negative temperature difference, displacement and stress distributions still can be found. Generally, the restrained edge may be assumed to be connected to the subgrade or a neighboring structure through two springs: K_h for the translational stiffness and K_r for the rotational stiffness. For example, a U-shaped drain structure connecting two concrete slabs may be simplified as a rotational spring.

As an example, a semi-infinite slab on a Winkler foundation with its edge restrained by a rotational spring K_r is analyzed. When the temperature difference Δt is not very large, all the slab is in contact with the foundation. Eqs. (3.8) to (3.12) are valid in the case, but the boundary condition (Fig. 3.4) is $M_y = -M_o = K_r\theta_0$ and $Q_y = 0$ at $y = 0$, where θ_0 is the rotation of the end surface $y = 0$. Thus, the displacement and stress solutions are obtained as follows:

$$w = -\left[w_{so} - \frac{M_o}{k\ell^2}\right]\sqrt{2}\cos\left[\frac{y}{\sqrt{2}\,\ell} + \frac{\pi}{4}\right]e^{-\frac{y}{\sqrt{2}\,\ell}}, \tag{3.47}$$

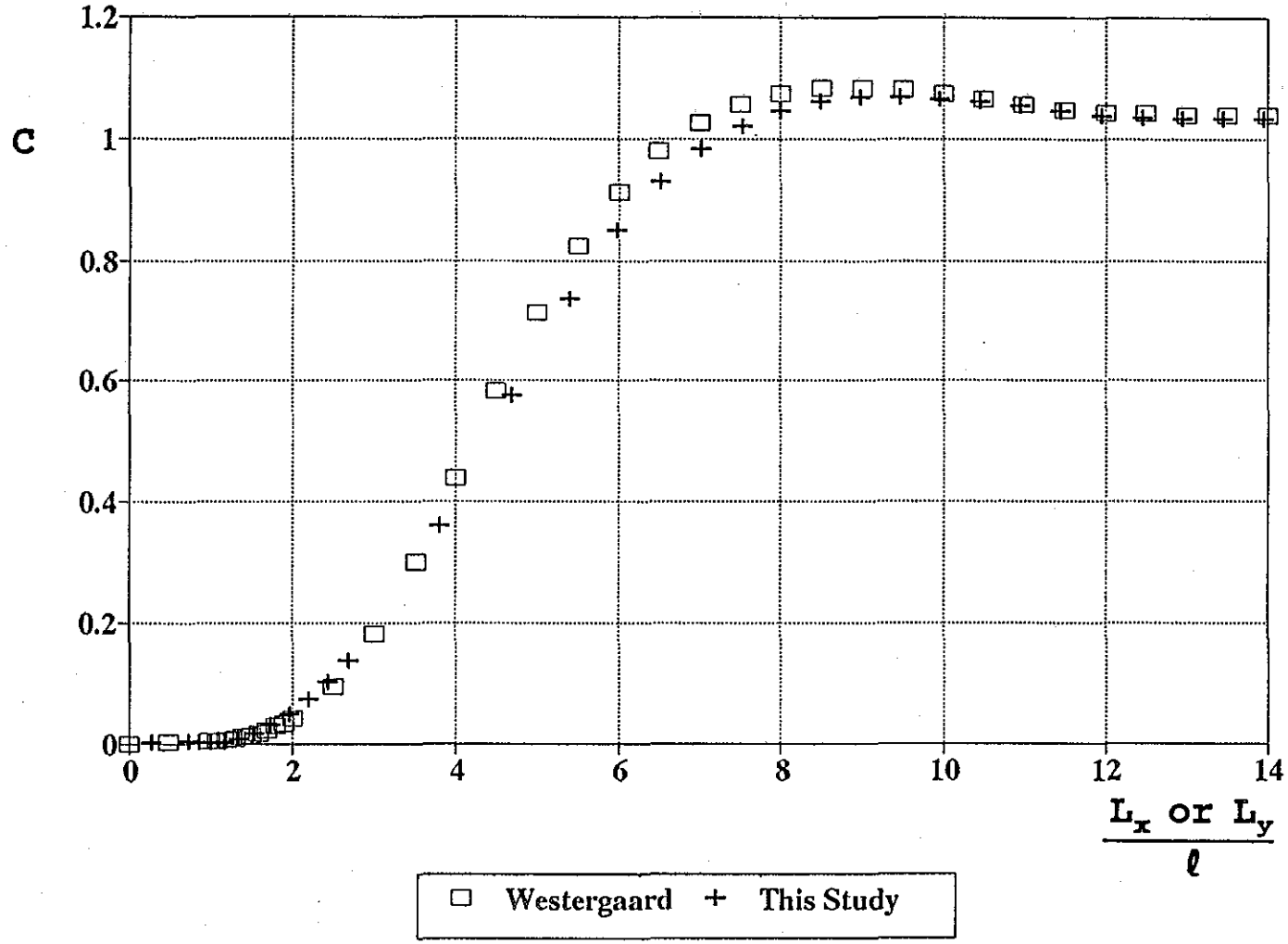

Fig. 3.10. Coefficients for the Maximum Stress in a Finite Pavement Slab Curled Up Due to Temperature Gradient.

$$\sigma_y = \sigma_o \left[1 - \left(1 - \frac{6M_o}{\sigma_o h^2} \right) \sqrt{2} \sin \left(\frac{y}{\sqrt{2}\,\ell} + \frac{\pi}{4} \right) e^{-\frac{y}{\sqrt{2}\,\ell}} \right] , \tag{3.48}$$

and

$$M_o = \theta_o K_r = \frac{w_{so} K_r}{\frac{\ell}{\sqrt{2}} + \frac{K_r}{k\ell^2}} . \tag{3.49}$$

These solutions are valid under the following condition:

$$w_{so} - \frac{M_o}{k\ell^2} \leq w_o \tag{3.50}$$

or

$$\Delta t \leq (\Delta t)_{sc} \left(1 + \frac{\sqrt{2} K_r}{k\ell^3} \right) = (\Delta t)_{sc}(1+\zeta) , \tag{3.51}$$

where $\zeta = (\sqrt{2}K_r)/(k\ell^3)$. As seen in Eq. (3.51), the critical temperature difference is raised because of the existence of the spring support at the slab edge. When the temperature difference Δt is so large that Eq. (3.51) is not satisfied, there would be a portion of the slab separated from the subgrade.

Similar to the case shown in Fig. 3.3, the part of the slab ($-s \leq y \leq 0$) is free from the subgrade and governed by Eq. (3.20), but its edge $y = -s$ is restrained by a rotational spring K_r, while the rest of the slab ($y \geq 0$) is governed by Eqs. (3.8) and (3.9). In this case the boundary condition is $M_y = -M_o = -K_r\theta_s$ and $Q_y = 0$ at $y = -s$, where θ_s is the rotation of the end surface $y = -s$, and $w = w_o$ at $y = 0$. Certainly w, θ ($= dw/dy$) and the third and fourth derivatives of w with respect to y are all continuous at $y = 0$. The displacement and stress distributions are dependent on the length s:

$$w = -\frac{w_o}{\cos\varphi} \cos\left[\frac{y}{\sqrt{2}\,\ell} + \varphi\right] e^{-\frac{y}{\sqrt{2}\,\ell}}, \tag{3.52}$$

and

$$\sigma_y = \sigma_o \left[1 - \frac{w_o}{w_{so}\cos\varphi} \sin\left[\frac{y}{\sqrt{2}\,\ell} + \varphi\right] e^{-\frac{y}{\sqrt{2}\,\ell}}\right], \tag{3.53}$$

where

$$\cos\varphi = \frac{1}{\sqrt{1 + \left[1 + \frac{2s}{\sqrt{2}\,\ell}\right]^2}}. \tag{3.54}$$

The length s is determined by the following equation:

$$\frac{2}{3}\zeta\left[\frac{s}{\sqrt{2}\,\ell}\right]^3 + (1+2\zeta)\left[\frac{s}{\sqrt{2}\,\ell}\right]^2 + (2+2\zeta-\gamma^2\zeta)\left[\frac{s}{\sqrt{2}\,\ell}\right] + (1+\zeta-\gamma^2) = 0. \tag{3.55}$$

where $\gamma = \sqrt{(w_{so}/w_o)}$ and $\zeta = (\sqrt{2}K_r)/(k\ell^3)$ as noted before. Eq. (3.55) is reduced to Eq. (3.24) when there is no restraint at the slab edge, that is, $K_r = 0$.

3.8. CONCLUSIONS

Displacement and stress distributions are provided for a semi-infinite and an infinitely long slab of a finite width on a Winkler foundation as the slab is subjected to a negative temperature gradient that takes into account that a gap can form between the slab edge and the subgrade. A critical temperature difference for each of the cases is noted such that when the temperature difference is greater than the critical value, the gap occurs and solutions of this study apply.

When an infinitely long strip of pavement is wide enough, it can be considered as a semi-infinite pavement for determining stress and displacement distributions. This chapter gives a procedure to judge if the width of the slab is "wide enough."

For a finite slab curled in a concave configuration due to the negative temperature gradient, the maximum stress in either direction with sufficient accuracy may be approximately estimated with Bradbury's formula. The coefficients in the formula can be determined with the stress solution for the infinitely long strip of pavement.

3.9. APPENDIX I: REFERENCES

Bradbury, R. D., *Reinforced Concrete Pavement*, Wire Reinforcement Institute, Washington, D.C., 1838, pp. 34-41.

Emborg, M., "Thermal Stress in Concrete at Early Ages," *Analysis of Concrete Structures by Fracture Mechanics*. L. Elfgren and S. P. Shah, eds., Chapman and Hall, New York, 1991, pp. 69-87.

Okamoto, P. A., Nussbaum, P. J., Smith, K. D., Darter, M. I., Wilson, T. P., Wu, C. L., and Tayabji, S. D., *Guidelines for Timing Contraction Joint Sawing and Earlier Loading for Concrete Pavements*, Report No. FHWA-RD-91-070, Federal Highway Administration, McLean, Virginia, 1991.

Scott, R. F., *Foundation Analysis*. Prentice-Hall, Eaglewood Cliffs, New Jersey, 1981, pp. 119-201.

Yoder, E. J. and Witczak, M. W., *Principles of Pavement Design*. 2nd Edition, John Wiley & Sons, New York, 1975, pp. 85-86.

Westergaard, H. M., "Analysis of Stress in Concrete Pavements due to Variations of Temperature," *Proceedings of Sixth Annual Meeting*, Highway Research Board, 1926, pp. 201-205.

3.10. APPENDIX II: NOTATION

The following symbols are used in this pages:

E = Young's modulus;

h = pavement depth;

k = foundation modulus;

K_h = translational stiffness;

K_r = rotational stiffness;

ℓ = radius of the relative stiffness;

M = moment on the cross-section of the pavement;

q = reaction by the foundation;

Q = shear force on the cross-section of the pavement;

w = displacement in the z direction;

α = thermal expansion coefficient;

Δt = temperature difference between the bottom surface and the top surface of the pavement;

ν = Poisson's ratio;

σ = maximum tensile stress in the y direction;

σ_x = stress in the x direction at the top surface of the pavement; and

σ_y = stress in the y direction at the top surface of pavement.

CHAPTER 4: FRACTURE TOUGHNESS OF CONCRETE AT EARLY AGES [1]

ABSTRACT

This chapter reports the experimental results involving the application of the size effect law to early-age concrete for determining the material fracture parameters K_{If} and c_f. These parameters were determined for concrete with several different coarse aggregates at 1-day age, showing that this test method is applicable both in the laboratory and at the construction work site. Tests for concrete at different ages from 1/2 day to 28 days showed that early-age concrete is more brittle than mature concrete. Increases in K_{If} and c_f with concrete age are observed. The K_{If} and c_f values at early ages may be used as a criterion to evaluate concrete quality.

4.1. INTRODUCTION

Since linear elastic fracture mechanics (LEFM) was applied to concrete by Kaplan in 1961[1], several investigations have measured apparent values of the critical stress intensity factor K_{IC} for cement paste, mortar and concrete specimens at their early ages. For example, Naus and Lott[2] showed, by testing notched 4 × 4 × 12 inch (10.2 X 10.2 X 30.5 cm) and 4 × 4 × 14 inch (10.2 X 10.2 X 35.6 cm) concrete beam specimens, that the apparent value of the critical stress intensity factor K_{IC} increased as the curing time was increased from 3 to 28 days. Test results indicated that the corresponding increase for concrete using a river gravel coarse aggregate was 54.2% and for concrete using a crushed limestone as its coarse aggregate, K_{IC} increased 23.0%. It was also noted in this study that as the length of moist cure was increased from 28 days to 90 days, the increase in K_{IC} was 7% for the concrete containing river gravel while there was no apparent change in K_{IC} for the concrete with the crushed limestone. Ojdrovic, et al.[3]

---

[1] Contents of this chapter are published in "Fracture Toughness of Concrete at Early Ages" by Dan G. Zollinger, Tianxi Tang and Rae H. Yoo in the ACI Material Journal, V.90, No.5, September-October 1993, pp. 463-471.

tested notched split-tension cylinders of concrete with the maximum aggregate size of 9.5 mm, in which the coarse aggregate type and the specimen size were not reported. Their tests showed that K_{IC} increased with the concrete age from 1-day to 28-day age. The value of K_{IC} at 1-day age was approximately 45% of the K_{IC} at 28-day age. Although these observations indicated the trend of rapid increase in the apparent value of K_{IC} with concrete age within 28 days, they also provided a great deal of evidence for dependence of K_{IC} on the concrete specimen geometry and size. In other words, the critical stress intensity factor K_{IC} based on LEFM and brittle fracture concepts does not constitute a material constant for concrete.

With the development of the nonlinear fracture mechanics of concrete, which takes into account the effect of the process zone at the crack tip, RILEM has tentatively recommended two effective (or equivalent elastic) crack models, Jenq and Shah's two-parameter fracture model[4] (TPFM) and Bažant's size effect law[5] (SEL), for determining the fracture parameters of concrete which are material constants, and independent of specimen geometry and size. These models characterize the fracture process zone by an effective crack length that can be determined from an additional instability condition. Recently, Wong and Miller[6] measured the two material fracture parameters defined in TPFM, the critical stress intensity factor K_{IC}^{s} and the critical crack tip opening displacement $CTOD_C$, for concrete at 1-day, 3-day and 5-day ages, and concluded that K_{IC}^{s} increased with concrete age and that early age concrete was more brittle than mature concrete. Our work tends to confirm the findings of the earlier studies by Shah, et al.[7] This chapter presents the results of an experimental investigation on concrete at early ages based on SEL. Fourteen batches of concrete beams using different coarse aggregates with the maximum size of 19 mm or 38 mm were produced and tested one day after casting in laboratories or at work sites to obtain K_{If}, the critical stress intensity factor (or fracture toughness) in the infinite specimen, and c_f, the effective critical crack length (or the process zone size) in the infinite specimen, as defined in SEL. The value of c_f can be used to evaluate the brittleness of concrete structures as SEL suggests. Also, concrete beams were tested at the ages of 1/2 day, 1 day, 7 days, 21 days and 28 days to show increases in K_{If} and c_f with concrete age.

4.2. RESEARCH SIGNIFICANCE

Failure of concrete is a process of crack formation and growth. With fracture parameters defined in SEL, resistance of concrete material against fracturing can be appropriately and correctly evaluated. Through this study, it is shown that the size effect law originally proposed for mature concrete can also be applied to early-age concrete. Since many cracks in concrete structures are initiated due to temperature and shrinkage stresses at early ages, the understanding and determination of fracture toughness and effective critical crack length of early-age concrete are crucial for crack control.

4.3. SIZE EFFECT LAW

According to LEFM and brittle fracture concepts, material fractures failure occurs when K_I reaches a critical value K_{IC}. However, it has been long observed that a steady crack growth takes place in concrete before the peak load. In addition, many microscopic-scale investigations have indicated that a process zone exists around the concrete crack tip[8]. Microcracking in the process zone consumes energy, and therefore, toughens the material and causes nonlinear fracture behavior, which, in turn, results in the size effect on the nominal strength of the concrete structure. The size effect law proposed in 1984 by Bažant[5] gives a formula to describe the size effect for the geometrically similar structures (or specimens) as follows:

$$Maximum\ \sigma_N = \frac{Bf_u}{\sqrt{1+\frac{d}{d_o}}}, \tag{4.1}$$

where f_u is the tensile strength of the concrete, d is a specimen dimension, B and d_o depend on material, structure geometry and load type. A modification of the size effect law proposed in 1990 by Bažant and Kazemi[9] attributes the nonlinearity of concrete fracture in an infinite specimen to two material constants: the critical stress intensity factor in an infinite specimen K_{If}, and the critical effective crack length or the process

zone size in an infinite specimen c_f, from which B and d_o for any geometry and load type can be derived through LEFM. (For expressions of B and d_o in terms of K_{If}, and c_f, and geometry, and load type and related LEFM formulas, see Appendix I.) Inversely, K_{If} and c_f can be obtained by a series of tests on the geometrically similar specimens of different sizes. The three-point bending beam test has been suggested for this purpose[10]. By using linear regression techniques, test data can be analyzed as follows:

$$Y^* = A^* X^* + C^* \quad , \tag{4.2}$$

where, for the three-point bending beam test, $Y^* = (bd/P)^2$, $X^* = d$, P = the peak load, b = thickness and d = depth of the beam, and A^* and C^* are regression constants. (See Appendix I for the general expression for any geometry and load type.) It has been shown[11] that, in the three-point bending test, the contact width of the load does not have a significant influence on the stress distribution or the value of K_I. Therefore, the load in this test can be reasonably simplified to a concentrated point-load in analysis. An advantage of the three-point bending beam test is that it is convenient to conduct and a reasonable degree of accuracy is assured in the analysis of the test results. Based on the regression constants A^* and C^*, K_{If} and c_f can be calculated with:

$$K_{If} = \sqrt{\frac{g(\omega_o)}{A^*}} \quad , \tag{4.3}$$

and

$$c_f = \frac{C^* K_{If}^2}{g'(\omega_0)} = \frac{C*}{A*} \frac{g(\omega_0)}{g'(\omega_0)} \quad , \tag{4.4}$$

where $g'(\omega)$ denotes the derivative of a function $g(\omega)$ with respect to ω, and ω is the ratio of the crack length a to the specimen dimension d, $g(\omega_o)$ and $g'(\omega_o)$ are values of functions $g(\omega)$ and $g'(\omega)$ at $\omega = a_o/d$ respectively, and a_o is the notch (initial crack) length. It should be pointed out that function $g(\omega)$ is dependent on the specimen

geometry. (For the definition of $g(\omega)$ and its form for the three-point bending beam specimen used in this study, see Appendix I.

To characterize the brittleness of structural response, a number of so-called brittleness numbers have been proposed[12, 13, 9] and are summarized by Gettu et al[14]. The brittleness number is defined as $\beta = d/d_o$ by SEL and it can be calculated as

$$\beta = \frac{d}{d_o} = \frac{g(\omega_0)}{g'(\omega_0)} \frac{d}{c_f} = \frac{D}{c_f}, \tag{4.5}$$

where $D = [g(\omega_0)/g'(\omega_0)]d$ is called the effective structural dimension. After the structure dimension is thus accounted for, β is independent of the geometrical shape[15].

4.4. EXPERIMENTAL PROGRAM

Materials and specimens

The coarse aggregates used in this study were obtained from stockpiles prepared for concrete pavement construction projects. The coarse aggregate was of maximum size of 3/4 inch (19 mm) or 1-1/2 inch (38 mm). Due to the effect of the coarse aggregate, the sizes of the beam specimens in this study were larger, in general, than those which have been reported in many references. Fig. 4.1 shows the geometry of the beam specimen. The thickness of each specimen was 5 inches (12.7 cm). For concretes with aggregate size of 3/4 inch (1.9 cm), depths of the specimens for each batch were 3 inches (7.6 cm), 4.5 inches (11.4 cm), 6 inches (15.2 cm), 9 inches (22.9 cm) and 12 inches (30.8 cm). For concrete with maximum aggregate size of 1-1/2 inches (3.8 cm), the depth of 3 inches (7.6 cm) is less than three times the maximum aggregate size so that only the four largest specimen sizes were used. The ratio of the support span of the beam (s) to the beam depth (d) was 2.5 for each specimen, and the ratio of the notch length (a_o) to the beam depth was 0.25 for each specimen. The total length of the beam specimen was 1.2 times as long as the support span. Therefore, all the beam specimens were geometrically similar. The ratio of s/d for these specimens was 2.5 in comparison to the ratio of s/d = 4 or 8 which is more frequently used in bending tests. This ratio

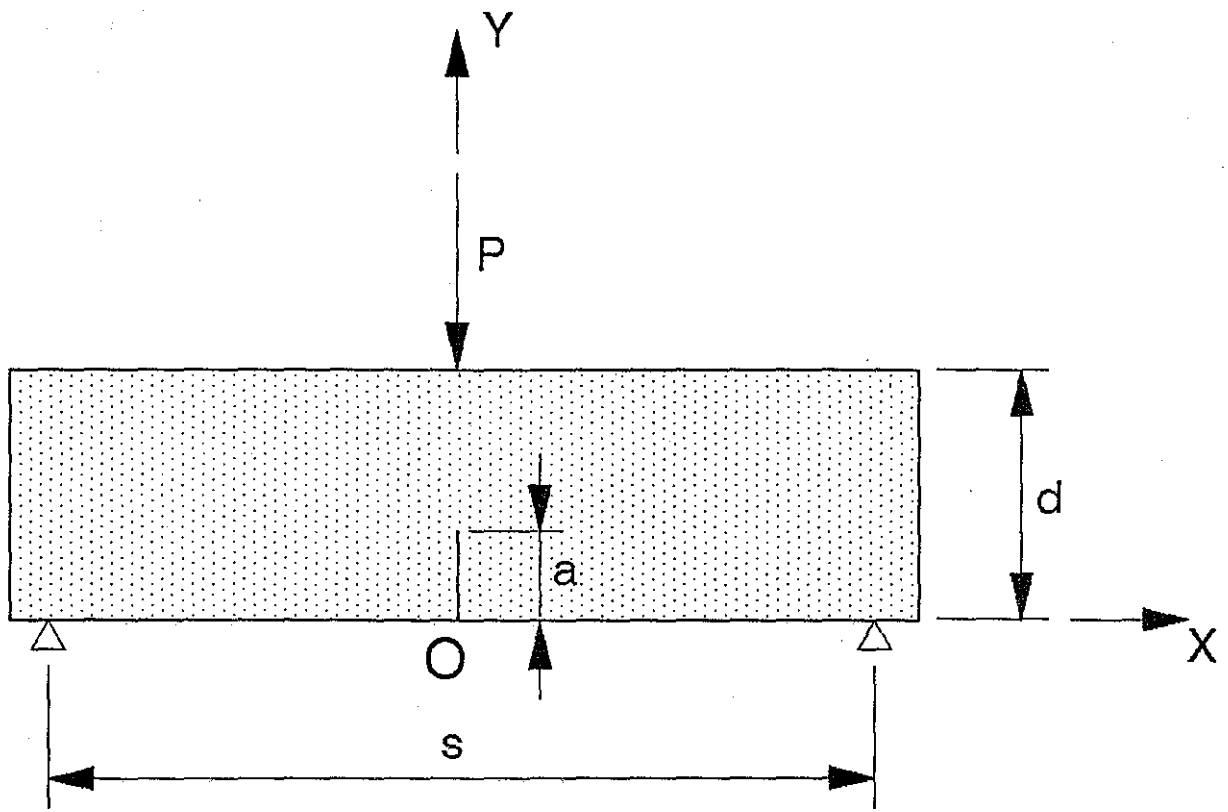

Fig. 4.1. Geometry of the Three-Point Bend Beam Specimen.

was chosen since the support span was restricted by the dimension of the work table and the allowable stroke of the testing machine. It is conceivable that the depth of 12 inches (30.8 cm) may be close to the limit for most industry and research laboratories.

When the specimen is very thin, it can be simplified as a plane stress problem; when the specimen is very thick, it can be simplified as a plane strain problem. Since Poisson's ratio of concrete is small, the two extreme simplifications do not make significant differences in stress distribution in the specimen, which allows the specimens of different sizes to be of the same thickness. In this study, all the beam specimens were 5 in (12.7 cm) thick, which is larger than three times the maximum aggregate size of 1-1/2 inches (3.8 cm).

Fourteen different concrete batch designs were prepared and tested in this study. Eleven of them were prepared in the laboratory and the remaining four were prepared on site of concrete pavement construction projects.

Each of the ten batches prepared in the laboratory contained Type I cement and Class C fly ash provided by the same manufacturer. Siliceous river gravel, crushed sand stone, and crushed limestone from different sources in Texas were used as coarse aggregates. Physical properties and gradations of these aggregates were examined by following test standards: ASTM Designation C 127 and C 128[16], Test Method Tex-403-A, Test Method-405-A and Test Method-401-A[17]. The results are listed in Tables 4.1 to 4.3. Table 4.4 gives the mix proportions based on one-sack of cement (43 kg or 94 lb). These mix designs were based on designs which were used in concrete pavements constructed in Texas, using slip-formed paving techniques which range in slump from 1 to 2 inches (2.5 to 5.1 cm).

A series of concrete batches using a siliceous river gravel, designated as G2 in Table 4.4, were prepared. Two batches of specimens were cast indoors at the room temperature of approximately 73 F (22.8 C) and another batch of specimens was cast outdoor under ambient conditions at temperatures near 95 F (35 C). One set of specimens cured under indoor conditions contained an unwashed coarse aggregate while another set that was cured indoors contained an coarse aggregate that was thoroughly

Table 4.1. Physical Properties of the Aggregates.

Aggregate I.D.	SSD Specific Gravity	Bulk Specific Gravity	Absorption Capacity (%)	Percent Solid (%)
SRG G1	2.467	2.411	2.27	57.81
SRG G2	2.646	2.604	1.59	60.70
SRG G3	2.588	2.580	0.33	58.73
SRG G4	2.796	2.783	0.46	54.28
CSS	2.499	2.405	3.76	55.31
CL L1	2.600	2.566	1.31	56.25
CL L2	2.566	2.517	1.91	55.78
CL L3	2.688	2.676	0.46	53.21
Dolomite	2.757	2.730	0.99	54.10
Sand	2.441	2.331	5.31	69.13

Note: SRG - Siliceous River Gravel,
CSS - Crushed Sandstone,
CL - Crushed Limestone,
DM - Dolomite

cleaned. All other specimens were cured indoors at the room temperature of 73 F (22.8 C).

A series of specimens that were cast using mix design G1 consisted of five batches which were tested at 1/2-day, 1-day, 7-day, 21-day and 28-dayages (one batch per age). Fracture tests were performed only at a concrete age of one day for all other specimens.

The concrete beam specimens were cast in steel molds. The specimens were demolded just before testing if they were tested at the 1/2-day and 1-day ages. Otherwise, they were demolded one day after casting and then cured at 73 F (22.8 C) until testing.

Table 4.2, Gradations of the Coarse Aggregates.

Aggregate I.D.	Percent Retained (%)					
	1 1/2" (38 mm)	3/4" (19 mm)	5/8" (15.9 mm)	1/2" (12.7 mm)	3/8" (9.5 mm)	Pan
SRG G1	0	2.86	6.96	22.32	30.35	37.52
SRG G2	0	23.50	12.45	23.35	18.01	22.69
CL L1	0	44.28	10.96	13.33	19.29	12.15
Aggregate I.D.	Percent Retained (%)					
	1 1/2" (38 mm)	3/4" (19 mm)	1/2" (12.7 mm)	3/8" (9.5 mm)"	No. 4	Pan
SRG G3	1.26	52.46	23.87	10.17	9.33	2.91
SRG G4	28.54	26.79	25.42	13.03		5.01
CL L2	10.95	19.94	23.58	19.08	24.94	1.51
CL L3	33.72	33.10	18.03	14.61		0.54
CSS	0	21.89	63.07	12.49		2.55
DM	6.42	19.77	44.66	16.75	12.06	0.35

Note: SRG - Siliceous River Gravel,
CSS - Crushed Sandstone,
CL - Crushed Limestone,
DM - Dolomite.

Table 4.3. Gradation of the Siliceous Sand.

Percent Retained (%)						
No. 4	No. 8	No. 16	No. 30	No. 100	No. 200	Pan
0.48	10.08	16.83	20.01	52.36	0.18	0.05

Table 4.4. Mix Designs of Concretes Tested in the Laboratory Batch (using one sack of cement).

Mix	Coarse Aggregate		Fine Aggregate	Cement	Fly Ash	Water	W/c Ratio
	I.D.	Weight					
G1	G1	500 lb (227 kg)	240 lb (109 kg)	94 lb (42.6 kg)	0	50 lb (22.7 kg)	0.53
G2	G2	500 lb (227 kg)	240 lb (109 kg)	94 lb (42.6 kg)	0	50 lb (22.7 kg)	0.53
G3	G3	333 lb (151 kg)	205 lb (93 kg)	73.4 lb (33.3 kg)	20.5 lb (9.3 kg)	47.8 lb (21.7 kg)	0.51
G4	G4	348 lb (158 kg)	201 lb (91 kg)	70 lb (31.7 kg)	23.4 lb (10.9 kg)	38.6 lb (17.5 kg)	0.41
GS1	G1	298 lb (135 kg)	267 lb (121 kg)	94 lb (42.6 kg)	0	57 lb (25.9 kg)	0.60
	CSS	161 lb (73 kg)					
GS2	G2	298 lb (135 kg)	267 lb (121 kg)	94 lb (42.6 kg)	0	57 lb (25.9 kg)	0.60
	CSS	161 lb (73 kg)					
L1	L1	333 lb (151 kg)	214 lb (97 kg)	74 lb (33.6 kg)	19.8 lb (9.0 kg)	39 lb (17.7 kg)	0.42
L2	L2	377 lb (171 lb)	225 lb (102 kg)	73.4 lb (33.3 kg)	20.5 lb (9.3 kg)	41.5 lb (18.8 kg)	0.44
L3	L3	315 lb (143 kg)	238 lb (108 kg)	74 lb (33.6 kg)	19.8 lb (9.0 kg)	43.7 lb (19.8 kg)	0.46
DM	DM	311 lb (141 kg)	234 lb (106 kg)	74 lb (33.6 kg)	19.8 lb (9.0 kg)	43.7 lb (19.8 kg)	0.46

Four series of specimens were similarly prepared and cured at concrete pavement construction sites located in north and south Texas (Texarkana and La Porte). (See Chapters 1 and 2 for the field tests). Three of the series of specimens contained river gravel as the coarse aggregate, and the remaining one contained crushed limestone as the coarse aggregate. The specimens prepared in Texarkana consisted of three different concrete batches which were tested at a 1-day age. Their mix designs are provided in Table 4.5. The specimens prepared in La Porte (with river gravel as the coarse aggregate) were tested at a 2-day age. (The mix design is not given.) These tests were performed in laboratories near the construction sections.

Notches in the beam specimen were cut by a diamond saw prior to conducting the fracture tests. The width of the notch was about 3 mm (1/8 inch). Each bending test was performed immediately after the notch was made.

For some batches of concrete, cylinders of 6-inch diameter (15.2 mm) and 12 inch length (30.5 mm) were prepared for determining the compressive strength. They were cast in PVC molds and cured under the same conditions as the beam specimens.

Test procedure and data treatment

One of the advantages of employing SEL, among the existing nonlinear fracture models for determining toughness of concrete against fracturing, is that only peak loads need to be recorded in testing. Consequently, this feature allows this test method to be extended to remote construction sites where testing equipment that can record deflection or strain may be unavailable. In this study, tests were performed with a Tinius-Olsen testing machine with a displacement rate of 0.05 in/minute.

Each batch of beam specimens made in the laboratory consisted of specimens of four or five different sizes. Each batch made in the field had four specimens, which were 4.5 inches (11.4 cm), 6 inches (15.2 cm), 9 inches (22.9 cm) and 12 inches (30.8 cm) in depth. The test data, taken from one batch of specimens, was fit by a linear regression using the least squares method. Fig. 4.2 illustrates regression results for 1-day old test data for concrete batch G1. Figs. 4.3 and 4.4 illustrate similar analysis for the tests on concrete batch L1. For the specimens cast at the concrete pavement

Table 4.5 Mix Designs of Concretes Used in Pavement Test Section in Texarkana, Texas (for 1 cubic yard, or 0.765 m^3, of concrete).

Mix	Coarse Aggregate		Intermediate Aggregate		Fine Aggregate	Type-1 Cement	Type-C Fly Ash	Water	w/c Ratio	Slump
	Type	Weight	Type	Weight	Type and Weight					
#3	1" (25 mm) SRG	1618 lb or 734 kg	BS	408 lb or 185 kg	CS 734 lb (333 kg) Sand 399 lb (181 kg)	379 lb or 172 kg	141 lb or 64 kg	205 lb or 93 kg	0.39	1.5" or 3.8 cm
#4	3/4" (19 mm) SRG	1560 lb or 707 kg	BS	400 lb or 182 kg	CS 780 lb (354 kg) Sand 430 lb (195 kg)	379 lb or 172 kg	141 lb or 64 kg	205 lb or 93 kg	0.39	1.5" or 3.8 cm
#5	CL	1710 lb or 776 kg	BS	380 lb or 173 kg	CS 743 lb (337 kg) Sand 406 lb (184 kg)	379 lb or 172kg	141 lb or 64 kg	205 lb or 93 kg	0.39	1.5" or 3.8 cm

Note: SRG - Siliceous River Gravel
CL - Crushed Limestone
BS - Buckshot
CS - Crushed Sand

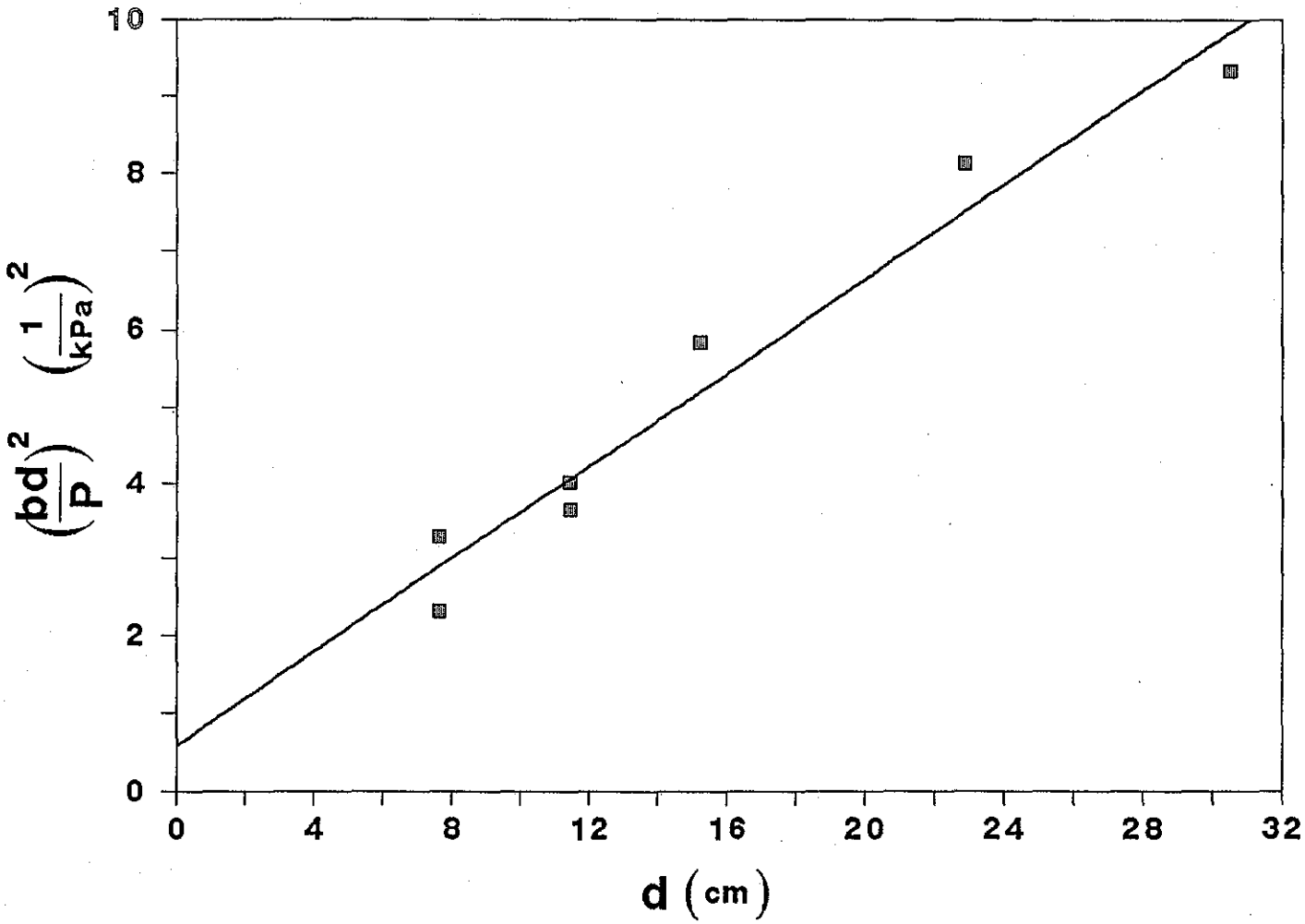

Fig. 4.2. Test Data and the Regression for Concrete G1 at the 1-Day Age ($R^2 = 0.960$).

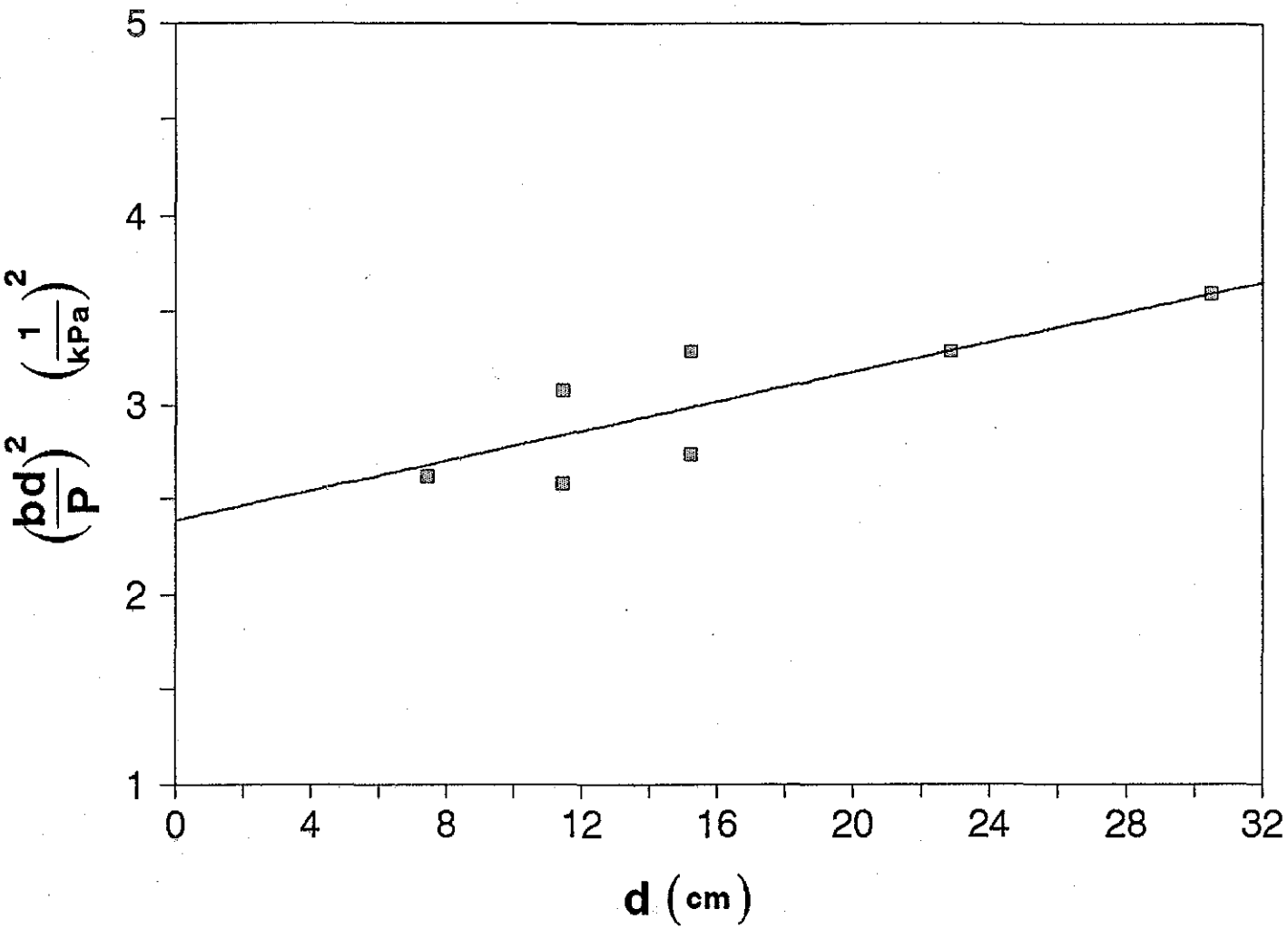

Fig. 4.3. Test Data and the Regression for Concrete L1 at the 1-Day Age ($R^2 = 0.682$).

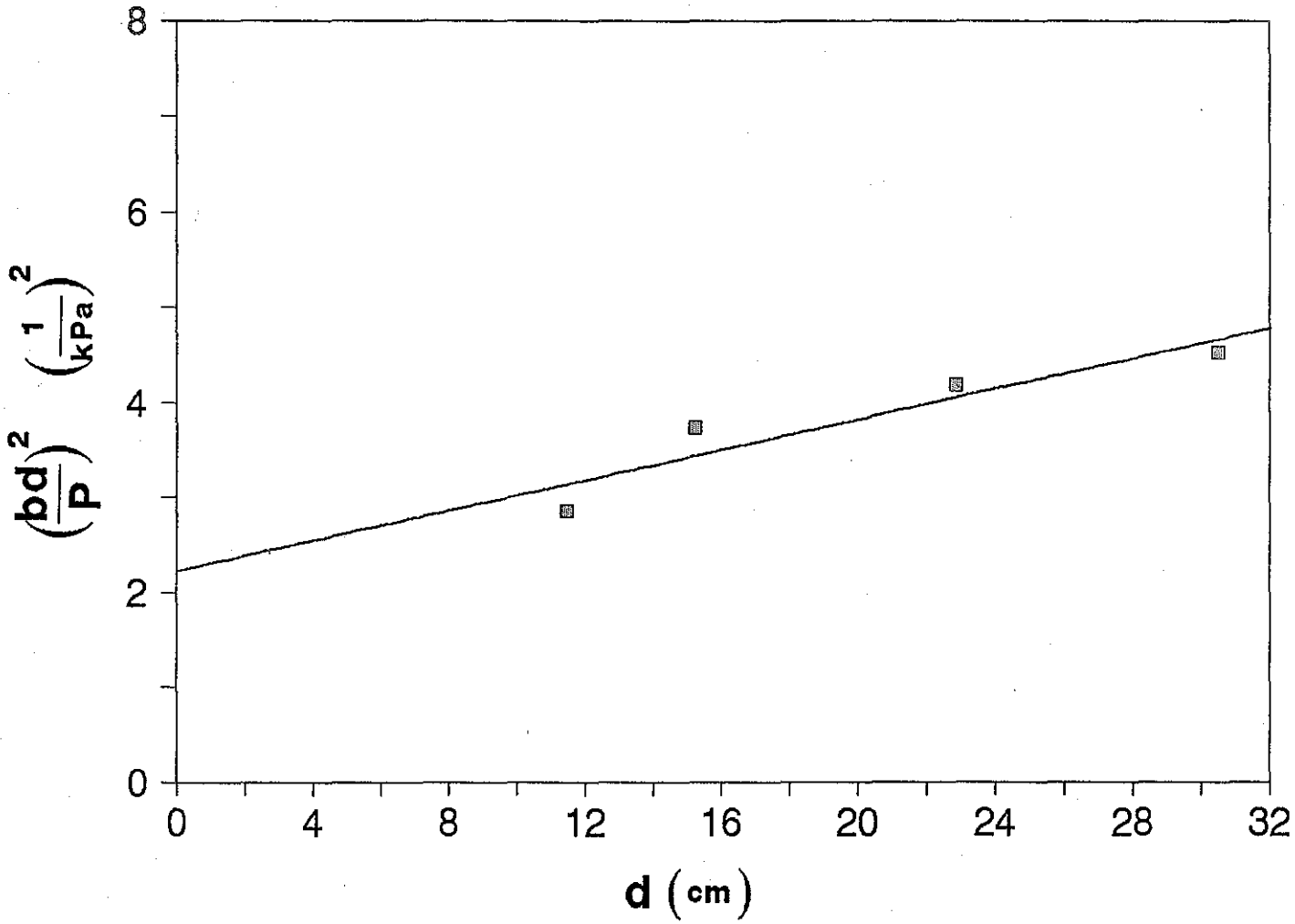

Fig. 4.4. Test Data and the Regression for Concrete of a Pavement Test Section in South Texas at the 2-Day Concrete Age ($R^2 = 0.871$).

sites, the regression analysis vertical intercept of the line is the constant A^* in Eq. (4.2) and the slope of the line is the constant C^*. From these two constants, K_{If} and c_f were calculated with Eqs. (4.3) and (4.4). The square of the coefficient of correlation, (R^2), for these regressions is 0.96 and 0.68, respectively. Conventional compression tests using cylindrical specimens were performed according to ASTM Designation C 39.

4.5. RESULTS AND DISCUSSIONS

For concrete batch G1 (river gravel coarse aggregate), batches of beam specimens and compression cylinders were cast and tested at different ages. The results are shown in Table 4.6 and Fig. 4.5. It is seen that the fracture toughness K_{If} increases faster

Table 4.6. Fracture Parameters and Compressive Strength of Concrete G1 at Different Ages.

Age	K_{if}		C_f		f'_c	
day	MPa$\sqrt{m}$	psi$\sqrt{in}$	cm	in	MPa	ksi
1/2	0.157	173	0.09	0.04	1.65	0.24
1	0.556	506	0.40	0.16	4.90	0.71
7	0.636	579	0.53	0.21	14.3	2.07
21	0.844	768	1.07	0.42	21.2	3.07
28	0.928	844	1.63	0.64	21.4	3.10

than the compressive strength f'_c within the first day, where K_{If}^{28} = 844 psi$\sqrt{in}$ (0.928 MPa$\sqrt{m}$) is the fracture toughness of concrete at the 28-day age and $f_c'^{28}$ = 3.10 ksi (21.4 MPa) is the compressive strength of concrete at the 28-day age. When both the fracture toughness and the concrete age are normalized, the following curve can be used to approximately fit the test data (Fig. 4.6):

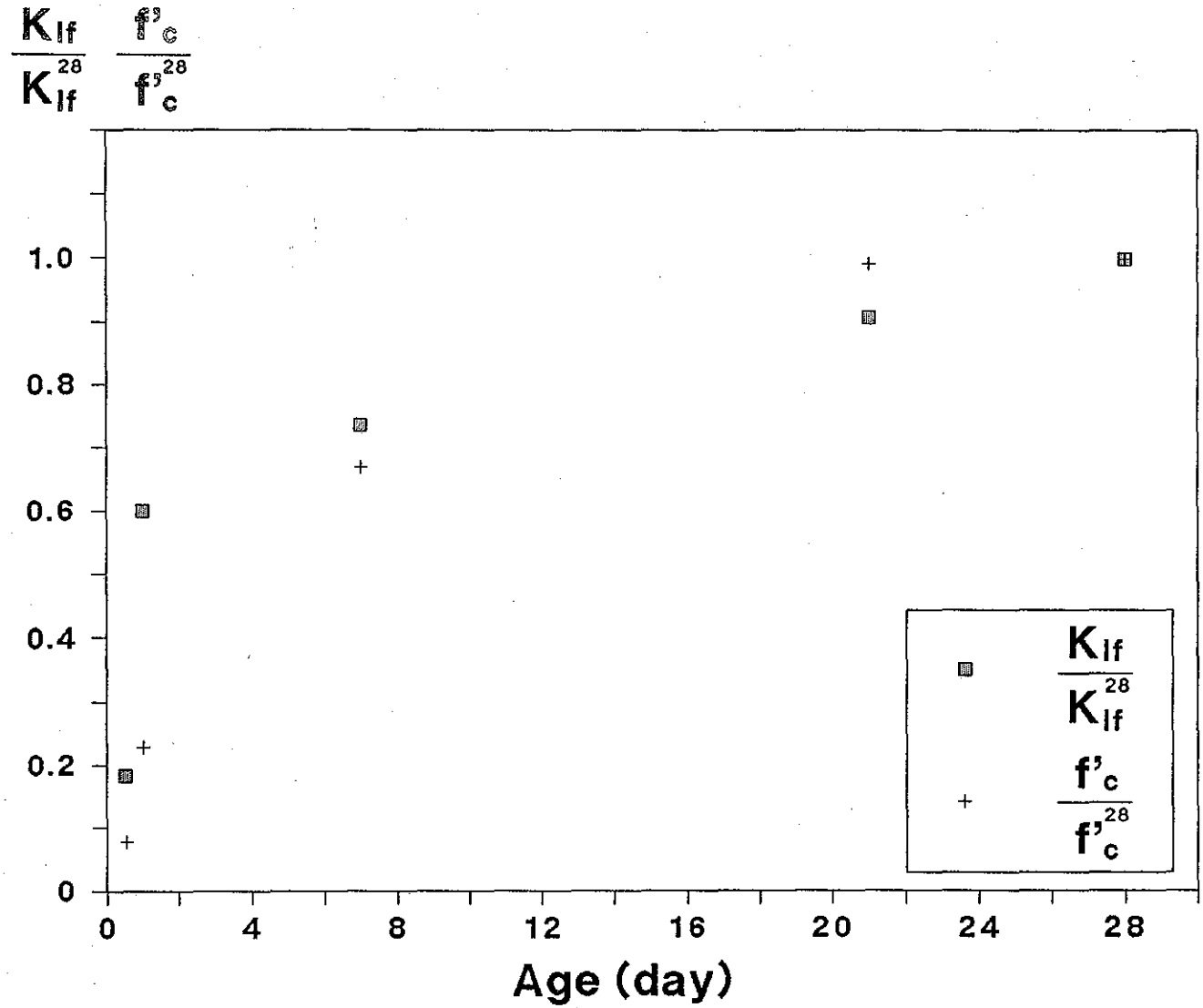

Fig. 4.5. Fracture Toughness K_{If} and the Compressive Strength f'_c versus Concrete Age.

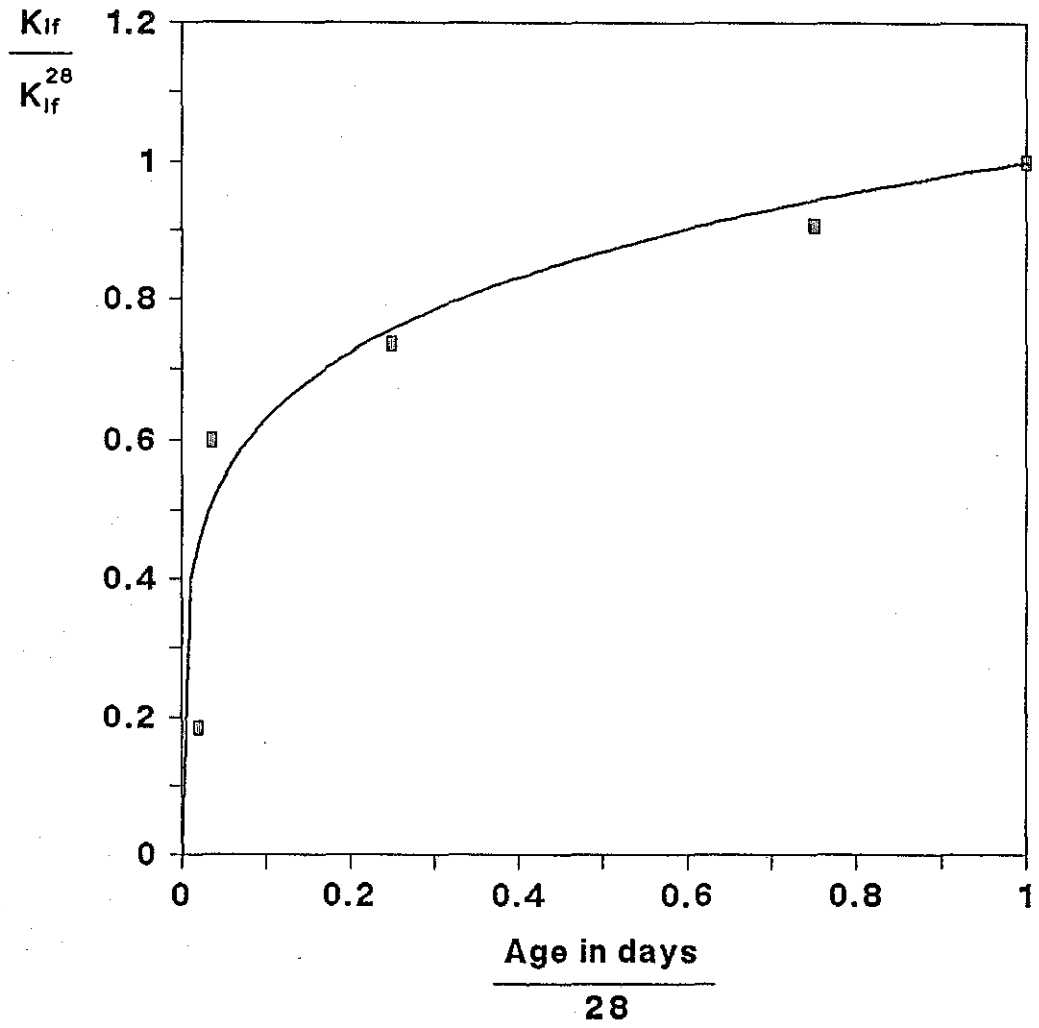

Fig. 4.6. Increase in K_{If} Values with Concrete Age.

$$\frac{K_{If}}{K_{If}^{28}} = \left(\frac{t}{28}\right)^{\frac{1}{4}} , \tag{4.6}$$

where t is the concrete age in days. Increase in K_{If} and c_f with concrete age indicates that early aged concrete is more brittle. Wong and Miller[6] reached a similar conclusion by measuring the fracture parameters defined by TPFM. The development of K_{If} and c_f with concrete age is significant in the timing of sawcutting operations in jointed concrete pavement systems and in determining or assessing the appropriate depth of the sawcut. For mix G1, c_f is of particular interest since it is small in comparison to other 1-day old concrete batches (Table 4.7). With little change within the first seven days (Table 4.6), a small c_f value causes a large brittleness number β according to Eq. (4.5). The β value exceeds 10 at the 7-day age for a beam of the same geometry as those tested, when the depth of the beam is greater than 10 in (25.4 cm). As Bazant and Kazemi[9] suggested, the failure can be analyzed according to LEFM when $\beta > 10$. With a small notch depth, β becomes even greater, in which case LEFM is applicable. The same conclusion can be reached if apparent K_{IC} values from the beam tests are analyzed. Fig. 4.7 shows these values calculated based on the assumption that no subcritical crack growth occurs. No obvious trends in K_{IC} with respect to the specimen size can be observed, which means that the size effect is approximately governed by LEFM. Accordingly, the average of these K_{IC} values from specimens of different sizes at the same age of concrete is close to the corresponding K_{If} value. For example, at half-a-day age, the average K_{IC} is 0.159 MPa$\sqrt{m}$ and K_{If} is 0.157 MPa$\sqrt{m}$. This may be a significant conclusion in terms of the application of fracture analysis to concrete pavement at the early ages. Additional tests are required on specimens exhibiting greater strengths, such as those using limestone as the coarse aggregate at ages less than 1 day old.

Table 4.7 shows 1-day-old test results of K_{If} and c_f for the eleven laboratory concrete batches prepared with thoroughly washed aggregates. The data indicates that limestone concretes have higher K_{If} and c_f values than river gravel concretes at the

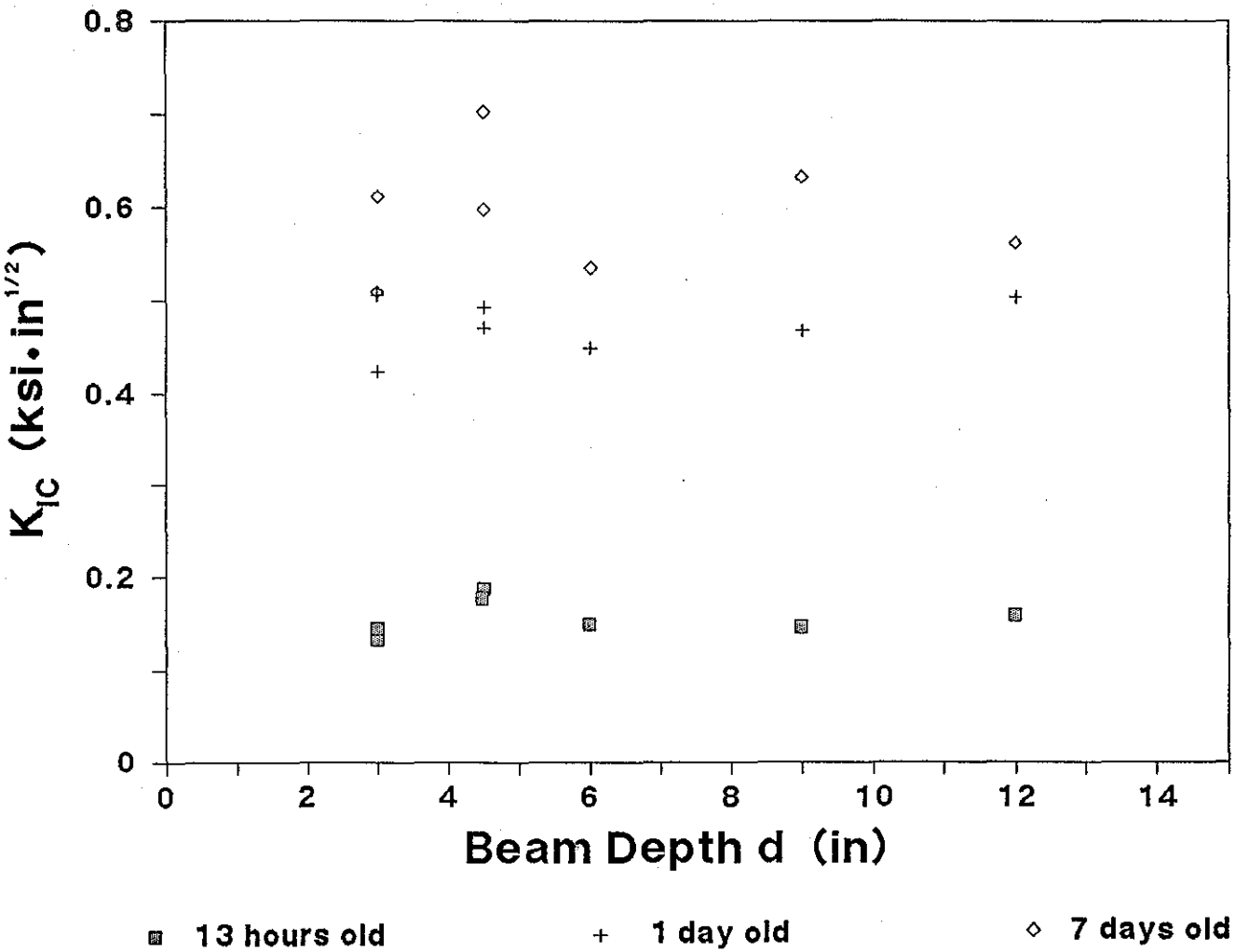

Fig. 4.7. Apparent K_{Ic} Values of Concrete G1 from Specimens of Different Sizes.

Table 4.7 Fracture Parameters of Different Concretes at the One-Day Age.

Concrete I.D.	K_{If}		c_f	
	MPa $\sqrt{m}$	psi $\sqrt{in}$	cm	in
G1	0.556	506	0.41	0.16
G2	0.757	689	3.58	1.41
G3	0.761	693	3.84	1.51
G4	1.08	981	8.51	3.35
GS1	0.670	610	0.91	0.36
GS2	0.806	733	4.95	1.98
L1	1.56	1390	12.1	4.76
L2	1.84	1670	22.9	9.02
L3	1.03	933	9.07	3.57
DM	0.950	864	5.64	2.22

Note: All the aggregates were washed thoroughly before mixing. Specimens were prepared at temperature of 73 F (22.8 C).

age of one day. The fracture surface of the specimens of limestone concretes passed through nearly all the limestone coarse aggregates in the path of the fracture surface. However, only very few river gravel aggregates were broken in similar fracture tests. Fig. 4.8 shows a close-up view of fracture surfaces specimens. The behavioral characteristics of crushed limestone and river gravel in concrete fracturing described above have been observed and reported by Petersson[18], except that limestone was identified as a "weak" aggregate which produced a lower value of the fracture energy G_c (note that the definition of G_c is different from G_f as defined in SEL.) It was also pointed out that gravel is a "strong" aggregate because large fracture surfaces form since the crack surfaces move around the aggregate particles. Naus and Lott[2] obtained nearly equal K_{IC} strengths at the 28-day age for limestone and river gravel concrete mixes. However, the 28-day age, the K_{IC} value of the limestone concrete was much higher than that of the river gravel concrete at the 3-day age. In other words, K_{IC} of the limestone concrete increased more rapidly with age than the river gravel concrete within the first

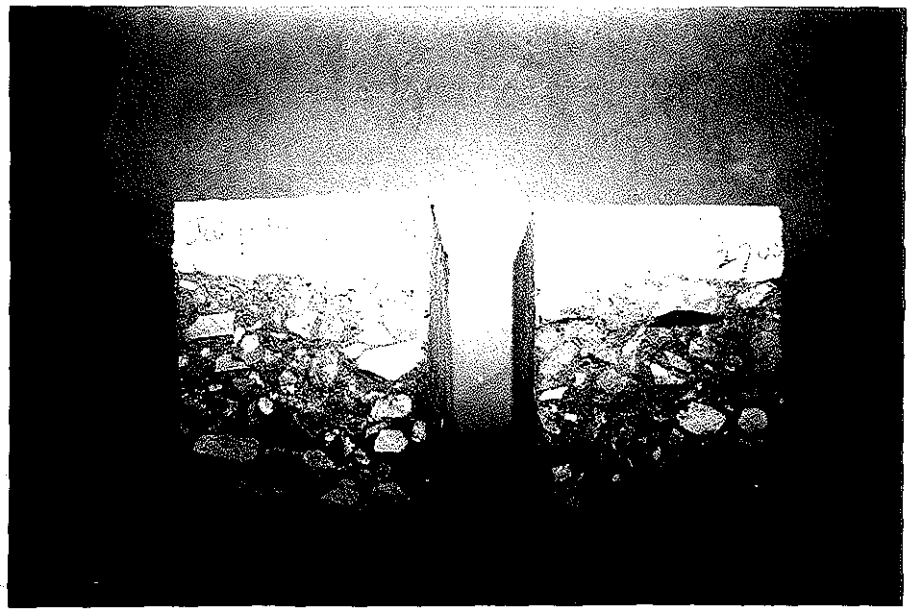

(a) Fracture Surfaces of Two Specimens of Limestone Concrete L1;

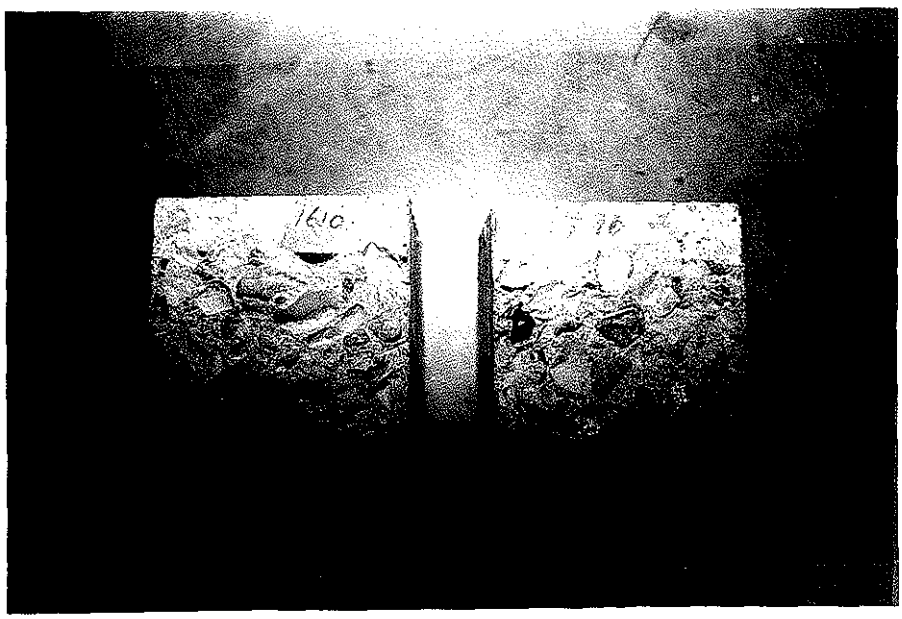

(b) Fracture Surfaces of Two Specimens of River Gravel Concrete G4

Fig. 4.8. Fracture Surfaces of Notched Concrete Beam Specimens.

days. According to their tests, fracturing of the limestone aggregates did not make concrete "weaker," at least in the first days. Zaitsev[19] compared the critical stress intensity factors for the matrix, aggregate and the bond interface to examine the mechanism associated with the compressive strength of normal concrete, high-strength concrete and lightweight concrete. He indicated that, in the case of high-strength concrete, fracturing of the aggregates enhanced the strength. In a study of spalling distress in Texas concrete pavements, it was noted the concrete pavements containing river gravel coarse aggregates tended to develop a "shrinkage " delamination below the pavement surface which was found to initiate at the early concrete ages[20]. However, very few of these types of distress were noted in concrete pavements with limestone as the coarse aggregate. Perhaps the higher fracture toughness and critical effective length at the early ages may explain why this type of distress has not been as frequent in pavement made of limestone concrete.

Among the four river gravel concretes, the K_{If} value of concrete G4 is 36% higher than the average of the other three. Concrete G4 had lower water/cement ratio and a larger maximum coarse aggregate size. However, it is not clear, from the test data of this study, how the aggregate size affects the K_{If} value. By replacing an amount of river gravel with sandstone and keeping other component percentages unchanged in the mix designs for concretes G1 and G2, respectively, the mix designs for concretes GS1 and GS2 were created. This change in mix design caused the K_{If} and c_f values to increase by a factor of 21% and 25%, respectively, for concrete GS1, and by a factor of 6% and 40%, respectively, for concrete GS2. Among all the concretes listed in Table 4.7, G1 has the lowest K_{If} and c_f values. An interesting fact is that extensive spalling has been observed in concrete pavements made of concrete G1 (Fig. 4.9) while, in contrast, little spalling has been seen in the highway pavement made of concrete GS1. It indicates that, in order to reduce distresses related to early-age cracks in concrete structures, the two fracture parameters, K_{If} and c_f, may be used as criteria for quality control.

The test results for three batches of beam specimens using mix G3 are given in Table 4.8. One of these batches was prepared using unwashed coarse aggregate while the

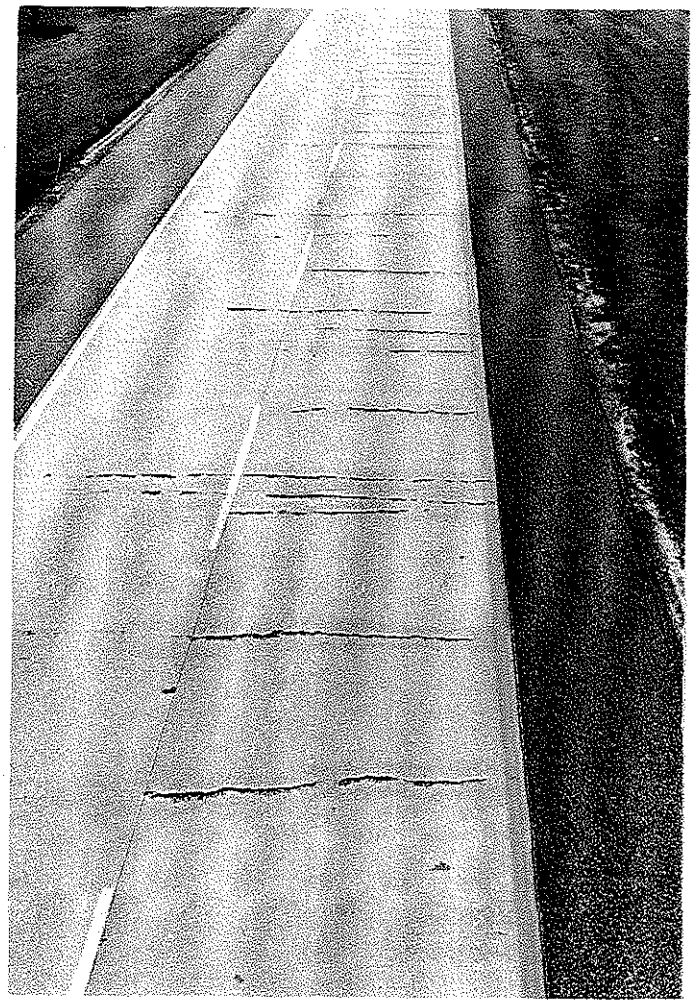

Fig. 4.9. Spalling of the Highway Pavement Made of River Gravel Concrete G1.

Table 4.8. Fracture Pavements of Concrete G2 Prepared Under Different Conditions.

Casting Conditions	K_{If}		c_f	
	MPa $\sqrt{m}$	psi $\sqrt{in}$	cm	in
* +	0.761	693	3.84	1.51
** +	0.689	627	2.97	1.17
** ++	0.787	716	5.21	2.05

Note: * Coarse Aggregate Cleaned,
** Coarse Aggregate Unwashed,
+ Prepared at Temperature of 73 F (22.8 C),
++ Prepared at Temperature near 95 F (35 C).

Table 4.9. Fracture Parameters and Compressive Strength of Concrete Prepared at the Pavement Work Sites.

Work Site Location	Mix Design I.D.	Concrete Age	K_{If}		c_f	
			MPa $\sqrt{m}$	psi $\sqrt{in}$	cm	in
Texarkana, Texas	#3	1 day	0.788	717	5.03	1.98
	#4	1 day	0.755	687	1.42	0.56
	#5	1 day	0.909	827	3.33	1.31
La Porte, Texas		2 day	1.08	987	5.67	2.23

remaining two were prepared using washed aggregates. The data from these mixes are provided in Table 4.8 for comparison. Though washing may have lowered the aggregate temperature and therefore slowed down the hydration of the concrete, the K_{If} and c_f values of the concrete using washed coarse aggregates are higher than those of the concrete using uncleaned coarse aggregate (Fine aggregates in both the concretes were washed.) Table 4.9 shows the K_{If} and c_f values for the specimens prepared at the highway pavement construction sites which consisted of different mix designs.

4.6. CONCLUSIONS

1. The method based on the size effect law has been used for determining the fracture parameters K_{If} and c_f of early-age concrete. Fourteen kinds of concretes of different coarse aggregates have been tested at early ages, showing that this test method is applicable both in the laboratory and at the construction work site.

2. The values of K_{If} and c_f increase with concrete age from half a day to twenty-eight days. Very early-age concrete is more brittle than 28-day concrete. It confirms the previous studies based on other models. When concrete is very young, it may behave as a brittle material to which linear elastic fracture mechanics applies.

3. At 1-day age, concrete using limestone as the coarse aggregate is tougher than the concrete using the river gravel as the coarse aggregate. It was observed that limestone coarse aggregates were ruptured in 1-day aged concrete while only the interfaces between river gravel and mortar fractured in the concrete using river gravel as the coarse aggregate.

4. The K_{If} and c_f values at early ages of concrete can be used as criteria to evaluate concrete quality, especially when cracks at the concrete early ages are to be controlled. More tests are needed to identify factors such as aggregate size, water/cement ratio, etc., that affect these two parameters.

4.7. APPENDIX I: RELATED FORMULAS

Formulas in LEFM

According to LEFM solutions to the plane stress and plane strain problems, the stress intensity factor[21] for the opening-mode fracture can be expressed as

$$K_I = \sigma_N \sqrt{\pi a}\, N(\omega) \ , \tag{4.7}$$

where a is the crack length, $N(\omega)$ is a function of geometry and the ratio of the crack length to a specimen dimension (ω = a/d), and ω_N is the nominal stress. For the beam specimen, the beam depth is taken as d (Fig. 4.1), and the nominal stress is defined as

$$\sigma_N = \frac{P}{bd} , \tag{4.8}$$

where P is the concentrated load, and b is the specimen thickness.

For a short beam[10] where s/d = 2.5,

$$N(\omega) = \frac{1.0-2.5\omega+4.49\omega^2-3.98\omega^3+1.33\omega^4}{(1-\omega)^{\frac{3}{2}}} , \tag{4.9}$$

By substituting Eq. (4.8), Eq. (4.7) becomes

$$K_I = \frac{P}{b\sqrt{d}} f(\omega) , \tag{4.10}$$

where $f(\omega) = \sqrt{(\pi\omega)}N(\omega)$. In LEFM, the elastic energy release rate G_I is related to K_I as

$$G_I = \frac{K_I^2}{E'} , \tag{4.11}$$

where E' = E for plane strain,

E' = $E/(1-\nu^2)$ for plane stress, and

E is Young's modulus and ν is Poisson's ratio. Eq. (4.11) can be rewritten as

$$G_I = \frac{\sigma_N^2 \pi a}{E'} N^2(\omega) , \tag{4.12}$$

or

$$G_I = \frac{P^2}{E'd} g(\omega) , \tag{4.13}$$

where

$$g(\omega) = f^2(\omega) = \pi\omega N^2(\omega) . \tag{4.14}$$

Formulas of SEL

The size effect of the nominal strength of concrete specimen is expressed as follows[5]:

$$Maximum\,\sigma_N = \frac{Bf_u}{\sqrt{1+\frac{d}{d_o}}}, \tag{4.15}$$

where Bf_u and d_o are related to the material fracture parameters K_{If} and c_f[9]:

$$d_o = \frac{g'(\omega_0)}{g(\omega_0)} c_f, \tag{4.16}$$

$$Bf_u = \sqrt{\frac{E' G_f}{c_f g'(\omega_0)}}, \tag{4.17}$$

and similar to (11), $$G_f = \frac{K_{If}^2}{E}, \tag{4.18}$$

therefore, the size effect can be expressed in terms of G_f and c_f as:

$$\sigma_N = \sqrt{\frac{E' G_f}{g'(\omega_0) c_f + g(\omega_0) d}}, \tag{4.19}$$

or $$Y^* = A^* X^* + C^*, \tag{4.20}$$

where $Y^* = (1/\sigma_N)^2$, $X^* = d$, $A^* = g(\omega_0)/(E'G_f)$, and G_f is the elastic energy release rate in an infinite specimen. When K_{If} instead of G_f is required, the value of E' is not needed.

4.8. APPENDIX II: REFERENCES

1. Kaplan, M. F., "Crack Propagation and the Fracture of Concrete," *Journal of the American Concrete Institute*, V. 58, No. 11, November 1961, pp. 591-610.

2. Naus, D. J.; and Lott, J. L., "Fracture Toughness of Portland Cement Concretes," *ACI Journal*, V. 66, No. 6, June 1969, pp. 481-489.

3. Ojdrovic, R. P.; Stojimirovic; and Petroski, H. J., "Effect of Age on Splitting Tensile Strength and Fracture Resistance of Concrete," *Cement and Concrete Research*, V. 17, No. 1, January 1987, pp. 70-76.

4. Jenq, Y. S.; and Shah, S. P., "A Two Parameter Fracture Model for Concrete," *Journal of Engineering Mechanics*, V. 111, No. 4, October 1985, pp. 1227-1241.

5. Bažant, Z. P., "Size Effect in Blunt Fracture: Concrete, Rock, Metal," *Journal of Engineering Mechanics*, V. 110, No. 4, April 1984, pp. 518-535.

6. Wong, W.; and Miller, R. A., "Mixed Mode Fracture at Early Ages," *Micromechanics of Failure of Quasi-Brittle Materials*, eds., S. P. Shah, S. E. Swartz, and M. L. Wang, Elsevier, New York, 1990, pp. 166-175.

7. Shah, S. P.; Miller, R. A.; and Virding, T. E., "Early-Age Shear Strength of Reinforced Concrete Beams," *Properties of Concrete at Early Ages*, ACI SP-95, ed., J. F. Young, the American Concrete Institute, Detroit, MI, 1986, pp. 71-82.

8. Ziegeldorf, S., "Phenomenological Aspects of the Fracture of Concrete," *Fracture Mechanics of Concrete*, ed., F. W. Wittmann, Elsevier, New York, 1983, pp. 31-41.

9. Bažant, Z. P.; Kazemi, M. T., "Determination of Fracture Energy, Process Zone Length and Brittleness Number from Size Effect, With Application to Rock and Concrete," *International Journal of Fracture*, V. 44, July 1990, pp. 111-131.

10. RILEM Committee on Fracture Mechanics of Concrete - Test Methods, "Size-Effect Method for Determining Fracture Energy and Process Zone Size of Concrete," *Materials and Structures*, V. 23, No. 138, November 1990, pp. 461-465.

11. Tang, T.; Shah, S. P.; and Ouyang, C., "Fracture Mechanics and Size Effect of Concrete in Tension," *Journal of Structural Engineering*, Vol. 118, No. 11, November 1992, pp. 3169-3185.

12. Hillerborg, H., "The Theoretical Basis of a Method to Determine the Fracture Energy G_F of Concrete," *Materials and Structures*, V. 18, No. 106, March 1985, pp. 291-296.

13. Carpinteri, A., "Notch Sensitivity in Fracture Testing of Aggregative Materials," *Engineering Fracture Mechanics*, V. 16, No. 4, April 1982, pp. 467-481.

14. Gettu, R.; Prat, P. C.; and Kazemi, M. T., "Material Brittleness from Nonlinear Fracture Mechanics," to appear in *Fracture Mechanics of Concrete Structures*, ed. Z. P. Bažant, Elsevier, London, 1992.

15. Bažant, Z. P.; and Pfeiffer, P. A., "Determination of Fracture Energy from Size Effect and Brittleness Number," *ACI Material Journal*, V. 84, No. 6, June 1987, pp. 463-480.

16. *Annual Book of ASTM Standards,* Vol. 04.02, American Society for Testing and Materials, Philadelphia, 1991.

17. *Manual of Testing Procedures*, Texas State Department of Highways and Public Transportation, Austin, Texas, 1990.

18. Petersson, P. E., "Fracture Energy of Concrete: Practical Performance and Experimental Results," *Cement and Concrete Research*, V. 10, No. 1, January 1980, pp. 91-101.

19. Zaitsev, Y., "Crack Propagation in a Composite Material," *Fracture Mechanics of Concrete*, ed., F. H. Wittmann, Elsevier, New York, 1983, pp. 251-300.

20. Senadheera, S.; Zollinger, D. G.; and Tang, T., "Spalling of Continuously Reinforced Concrete Pavements," *Journal of Transportation Engineering*, ASCE, 120(3), May/June 1994.

21. Broek, D., *Elementary Engineering Fracture Mechanics*, Martinus Nijhoff Publishers, Boston, 1982.

CHAPTER 5: SAWCUT DEPTH CONSIDERATIONS FOR JOINTED CONCRETE PAVEMENTS BASED ON FRACTURE MECHANICS ANALYSIS

ABSTRACT

The efficient control of slab cracking that develops in concrete pavements is important to pavement performance. From the viewpoint of engineering analysis and design of pavements, it is desirable to control pavement cracking to joint locations at desirable intervals to decrease the possibility of uncontrolled cracking. The purpose of this paper is to suggest an approach to estimate appropriate sawcut depths and placement timing using fracture mechanics for jointed concrete systems. Early-aged sawcutting, as one form of crack induction, has been applied to concrete pavement surfaces at specific contraction joint locations. This paper presents a mechanics-based approach to the determination of sawcut depth and spacing requirements using fracture mechanics analysis. The stress field in a concrete slab induced by thermal and shrinkage gradients is based upon curling and warping analysis, which also leads to sawcut spacing criteria. Fracture parameters K_{If} and C_f defined by the size effect law are obtained from laboratory notched beam fracture tests for specific coarse aggregate types. Modified linear elastic fracture mechanics is applied to determine a sufficient notch or sawcut depth to insure controlled cracking. Preliminary field results show that early-aged sawcutting with appropriately determined joint spacing and depth can be utilized for the positive control of cracking in jointed plain concrete pavements. The theoretical sawcut depth, as determined by fracture analysis which can be used in pavement construction practice, is significantly less than the conventional d/3 or d/4, where d is the slab thickness. Recent pavement surveys have verified this conclusion.

5.1. INTRODUCTION

In newly-paved concrete pavements, the temperature rise caused by the hydration process can be considerable. If unrestrained, the concrete pavement can expand and

contract during the heating and subsequent cooling process without stresses being induced. Similar displacements may result due to shrinkage as the pavement dries and expansion when it is wetted. However, actual pavements in the field, are nearly always restrained to some degree either by external restraint such as friction, the slab weight, tied adjoining lanes, or a combination of these. Interaction of the induced temperature and drying shrinkage gradients and the slab restraint can induce tensile stresses, that lead to slab cracking.

Field experiments have indicated that, typically, many sawcut joints break in the concrete pavement within the first few days after placement under hot weather concreting conditions. It is evident that an understanding of the mechanism related to early-age cracking in concrete pavements should provide a basis for improvement in current pavement sawcutting practice with respect to an appropriate combination of sawcut timing and sawcut depths. The sawcut should be deep enough such that a crack initiated at a sawcut-surface notch will propagate in an unstable manner from the sawcut tip to the slab bottom under stresses caused by temperature and shrinkage gradients or variations. Since this cracking consumes elastic energy which developed within the concrete slab, stress and the incidence of cracking elsewhere is reduced in the slab. The controlled cracks reduce the restraint in the concrete pavement slab, and therefore, lowers the maximum tensile stress. One-third of the pavement thickness (d/3) has been accepted and assumed to be the necessary depth of cut since the early 1950's. However, literature reviews reveal little technical justification for this assumption, other than field experience in isolated instances of uncontrolled cracking in which engineers may have assumed that deeper sawcuts would solve the problems they were experiencing with random cracking. It will be shown later that little benefit is to be gained from deeper sawcuts, and that the most significant factor in the effective control of random cracking is the time of sawcut placement. In this sense, a sawcut depth of d/3 or d/4 without respect to aggregate type, concrete properties, or pavement thickness characteristics is technically unjustified. The conventional analysis of crack development in sawcut concrete pavement typically assumes a flawless beam or plate, although crack formation and development is of primary interest. In this paper, fracture mechanics is applied to determine sawcut depth

requirements based on stresses which develop during the first few days after placement. Since the use of fracture mechanics to analyze sawcut depth criteria in jointed concrete systems constitutes a new approach to the analysis of crack development (and, basically, is the only rational approach to accurately account for the factors pointed out above), sufficient mathematical derivation will be provided to adequately document and justify the approach.

5.2. THEORETICAL APPROACH: CLIMATIC STRESSES

Environmental stresses in concrete pavements may be attributed to both temperature and drying shrinkage effects, and are particularly important at an early age. Stresses causes by both of these effects are discussed subsequently.

Thermal Stresses

The growth of early-age thermal stresses in a concrete structure may be illustrated in the consideration of a fully-restrained concrete element in which the stress state is uniaxial (Fig. 5.1) during a heating and cooling cycle. Laboratory tests [1] have indicated that during the first few hours after placement, while the concrete is fully plastic, no measurable stress build-up occurs. After this plastic stage, the strength of the concrete can increase rapidly where continued rise in temperature induces compressive stresses. However, due to the high creep of early-aged concrete, the compressive stresses may be substantially relaxed. In the referenced study, laboratory results indicated that a temperature maximum occurred at about 26 hours after casting of concrete, but relaxation within the concrete occurred leading to a possible zero stress condition. (Due to varying temperature conditions, this process may proceed at varying rates under field conditions.) As cooling proceeds, tensile stresses gradually develop and increase until, finally, a tensile failure occurs. Thus, tensile stresses and thermal cracking in the structure result from temperature and shrinkage effects during the early stages of hydration while the concrete is developing increasing stiffness.

Due to exposure to ambient conditions, a concrete pavement may cool to a minimum temperature after cycling through a maximum temperature such that tensile stresses can be induced in the slab. The tensile stress distribution through the pavement

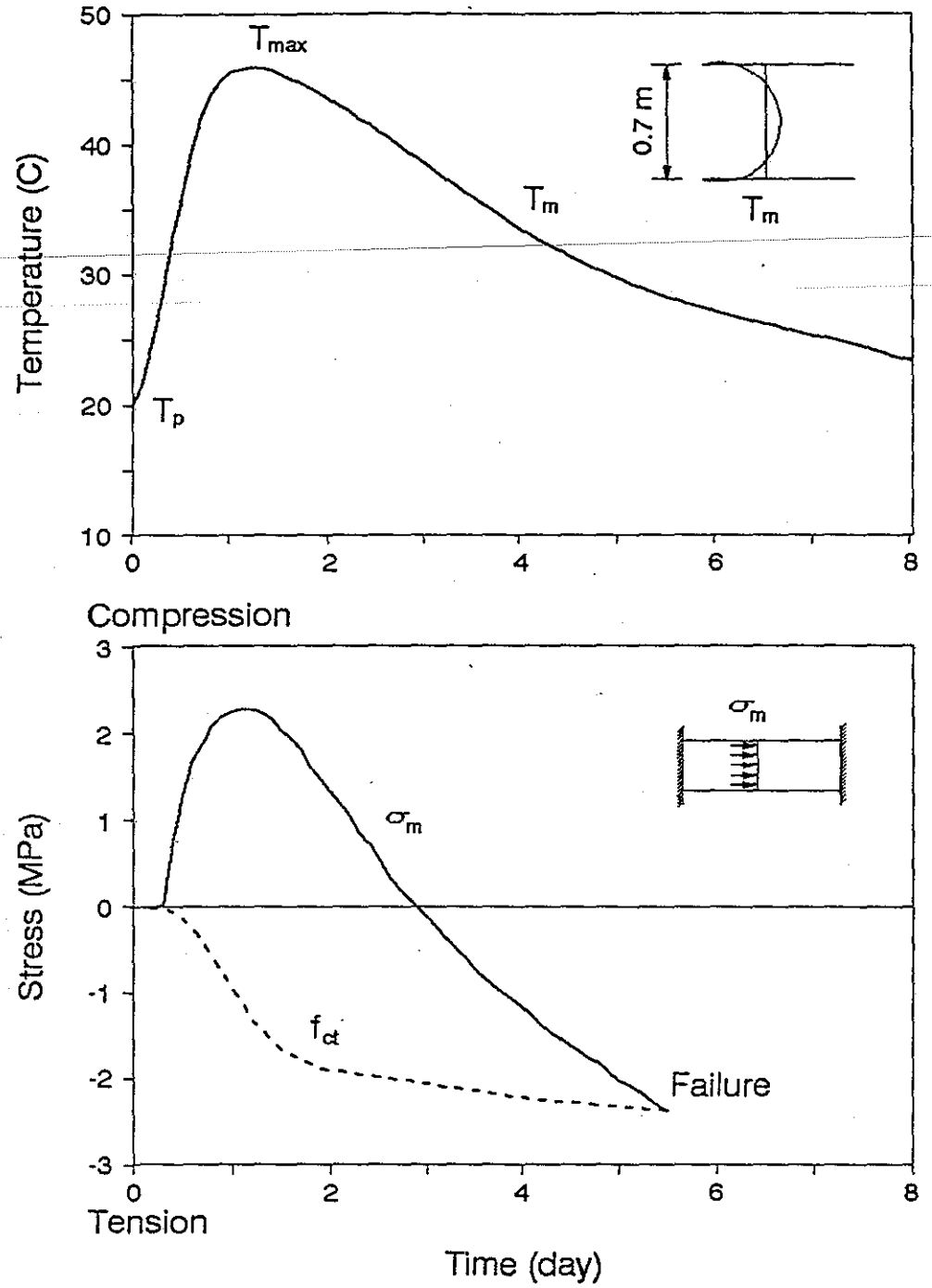

Fig. 5.1. Mean temperature curve in a newly cast concrete specimen and induced thermal stresses at full restraint. Stress time curve is based on laboratory tests.
Concrete: Standard Portland cement Type II (Degerhamn), Cement content = 400 kg/m^3, w/c = 0.41, f_{cc}^{28} = 63.2 MPa (150 mm cubes) (From [1]).

thickness can be assumed to be linear for the sake of simplicity, but others [2] have indicated that the distribution may be decomposed into three parts: axial stress, curling stress and nonlinear stress. Not only is the stress distribution caused by a temperature effect, as referenced above, but it may also be caused by moisture effects which were not included in the above referenced study. Therefore, a complete analysis of early-aged stresses will include curling, warping, and frictional stresses where the axial stress component may be primarily due to subbase/subgrade frictional effects. Stress development may become significant very soon after placement, perhaps even before the concrete has attained a certain degree of stiffness (which may not occur until 18 to 24 hours after placement). Crack development in concrete pavements has been noted to be sensitive to diurnal temperature effects. The tendency to curl is restrained by the slab weight in which the resulting level of stress development is a function of the stiffness of the subbase layer as reflected in the radius of relative stiffness (ℓ). When the slab curls in an upward configuration, tensile stresses are induced in the upper part of the slab while compressive stresses are induced in the lower part. Analysis of stress induced by a linear temperature gradient in rigid pavements was developed by Westergaard [3] and others [4].

The Westergaard solution for slab stresses under temperature gradients will not be elaborated on here. However, a similar approach will be presented later for slab stresses caused by moisture gradients. Westergaard presented solutions which considered curling stresses in a slab of infinite and semi-infinite dimensions based on the following governing equations:

$$\ell^4 \frac{d^4w}{dy^4} + kw = 0 \qquad (5.1)$$

where $\ell = \left[\frac{Eh^3}{12(1-\nu^2)k} \right]^{1/4}$ as pointed out previously is called the radius of relative stiffness and:

E = Young's modulus (psi)

ν = Poisson's ratio

k = Foundation modulus (psi/in)

h = Slab thickness (in)

w = Slab deflection (in).

Eq. (5.1) encompasses a spring model that was proposed for the base reaction with the k value as the spring modulus. Though the slab weight restrains the curling, the weight is not included in the equation. However, the displacement (w) caused by curling can be considered only part of the slab displacement [5]. In addition to w, the slab weight causes a uniform subsidence w_s. The total displacement w_t is the sum of w_s and w. So long as $w_t = w_s + w \geq 0$, the spring model is valid even if $w < 0$.

The solution to Eq. (5.1) indicates a negative w or upward displacement at and near the slab edge in concave curling, which should not be interpreted that the slab is pulled down by the base. Wherever $w < 0$, part of the slab weight is supported by the base while the rest of it is supported by the slab itself which contributes to the stresses in the slab. The total displacement w_t must be positive, otherwise Eq. (5.1) is not valid. Further explanation is provided elsewhere [5].

Nonetheless, the maximum curling stress (σ_o) from Westergaard's analysis taken far away from the slab edge is:

$$\sigma_o = \sigma^t = \frac{E_c \, \alpha \, t}{2(1-\nu)} = \frac{E_c}{2(1-\nu)} \, \epsilon^t \tag{5.2}$$

where

α = Thermal coefficient of expansion (/°F)

t = Temperature change or drop

$\epsilon^t = \alpha t$

Bradbury [4] developed coefficients based on the Westergaard solution as applied to slabs of practical dimensions. The coefficients are shown in Fig. 5.2 and are used in the following equations:

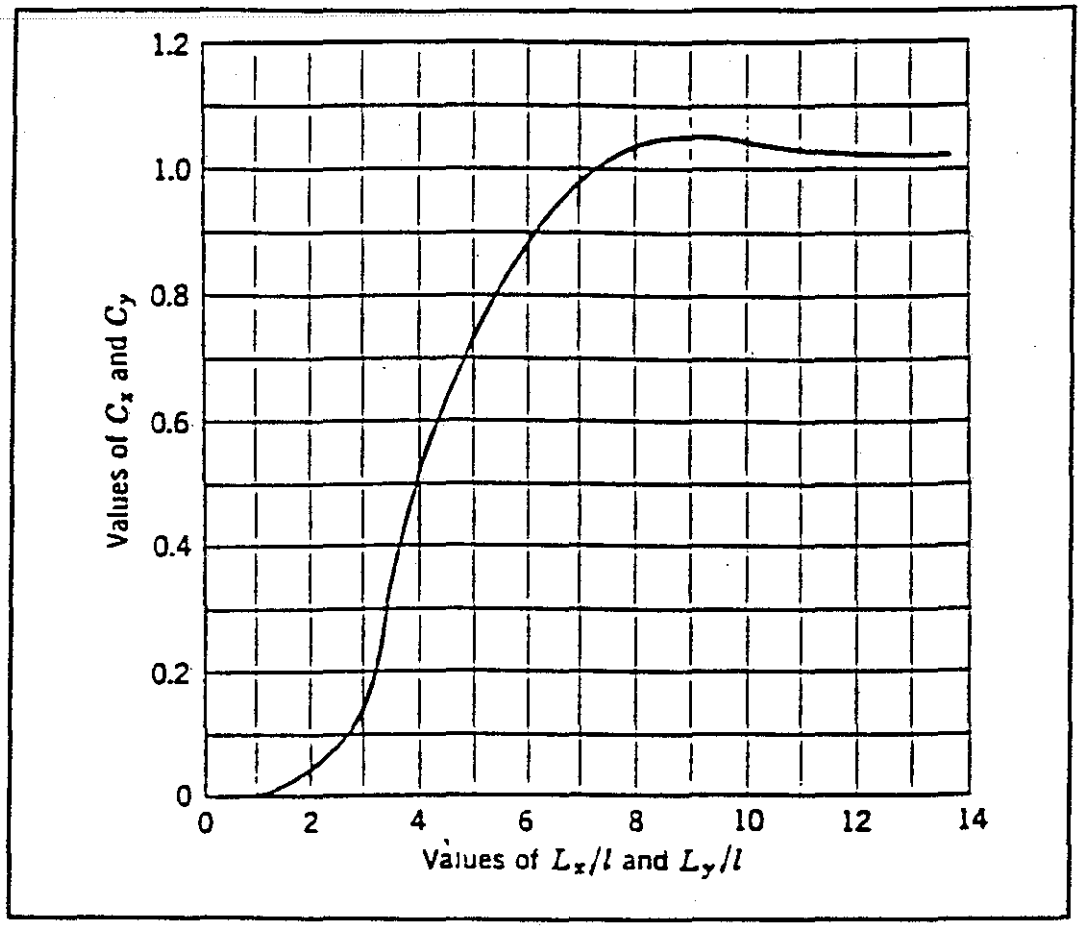

Fig. 5.2. Curling Stress Coefficients (From [4]).

Edge stress:

$$\sigma = \frac{CE_c\alpha t}{2} = C(1-\nu)\ \sigma^t \tag{5.3}$$

Interior stress:

$$\sigma = \frac{E_c\alpha t}{2}\left[\frac{C_1 + \upsilon C_2}{1 - \nu^2}\right] = \left[\frac{C_1 + \upsilon\ C_2}{1-\nu^2}\right]\ \sigma^t(1-\nu) \tag{5.4}$$

$$= \sigma^t\ (\frac{C_1 + \nu C_2}{1 + \nu})$$

If $C_1 = C_2 = C$, then $\sigma = C\sigma^t$. The coefficient C_1 is the desired direction, whereas C_2 is for the direction perpendicular to this direction. L_x and L_y are the free length and width, respectively.

Shrinkage Stresses

Similarly, the interaction of drying shrinkage (ϵ^{sh}) of concrete and pavement restraint can induce stresses in a concrete slab. According to Bažant and Wu [6], the shrinkage of concrete can be described by the following function of humidity:

$$\epsilon^{sh} = \epsilon^{sh\infty}\ \left(1 - h^3\right)\ \text{(microstrain)} \tag{5.5}$$

where h (or rh to avoid confusion with slab thickness) in this and following expressions is the relative humidity, and $\epsilon^{sh\infty}$ is a material parameter, which is the ultimate concrete shrinkage at the reference rh = 50%. A formula from Bažant and Panula's model [7] for calculating $\epsilon^{sh\infty}$ is applied here:

$$\epsilon^{sh\infty} = 1330 - 970y \tag{5.6}$$

$$y = (390z^{-4} + 1)^{-1} \tag{5.7}$$

$$z = 0.381\sqrt{f_{28}} \left[1.25 \left[\frac{a}{c}\right]^{1/2} + 0.5 \left[\frac{g}{s}\right]^{2} \right] \left[\frac{1 + \frac{s}{c}}{\frac{w}{c}} \right]^{1/3} - 12 \tag{5.8}$$

where

$\frac{a}{c}$ = Total aggregate/cement ratio

$\frac{g}{s}$ = Coarse aggregate/fine aggregate ratio

$\frac{s}{c}$ = Fine aggregate/cement ratio

$\frac{w}{c}$ = Water/cement ratio

f'_{28} = 28-day cylinder compressive strength (psi).

In the infinitely large concrete slab, $\frac{\partial^2 w}{\partial x^2} = \frac{\partial^2 w}{\partial y^2} = 0$, the shrinkage is totally restrained. The shrinkage-induced stresses (σ^{sh}) are:

$$\sigma_x = \sigma_y = \frac{E_c}{1 - \nu} \epsilon^{sh} \tag{5.9}$$

Moisture measurements in actual field slabs, using instrumentation described by others [8], have indicated that the process tends to go through to the bottom of the concrete slab. These measurements have also indicated the non-linearity of the humidity profile vertically through a pavement slab during wetting and drying cycles. One would expect that such variations will result in similar profiles or distributions of moisture-induced warping stresses. The representation of these distributions numerically in analysis may well require sophisticated methods, such as the finite element or finite difference approaches. However, for the purpose of introducing an approach to the analysis of moisture-induced warping, the moisture-induced stress distribution in a concrete slab is simplified (as was done for temperature-gradient related stresses) to vary linearly along the thickness with the maximum tensile stress σ^{sh} at the top surface as shown in Fig. 5.3. It is assumed that the shrinkage stress distributes linearly through the thickness of the slab, varying from σ^{sh} at the top to zero at the bottom. The solutions provided by Westergaard [3] and Bradbury [4] can be implemented by only replacing ϵ^t in all the equations (e.g. Eqs. [5.2] to [5.4]) with ϵ^{sh}. Another simplification results in no shrinkage related stresses within $-H/2 < z < h/2$ ($0 < H < h$ - as defined in Fig. 5.3) and that the shrinkage-induced normal stress σ^{sh} linearly decreases from z - -h/2 to 0 at $z = -H/2$. Work is currently underway at the Texas Transportation Institute to model and verify the non-linear temperature and moisture stress distributions in jointed concrete pavement using numerical analysis techniques.

The following mathematical expressions are provided to lend adequate explanation of the inclusion of moisture-induced stresses in curling and warping analysis, since analysis of this nature has received little attention in published literature. The moment caused by the shrinkage-induced, linearly distributed stress when the slab is fully restrained is calculated as follows:

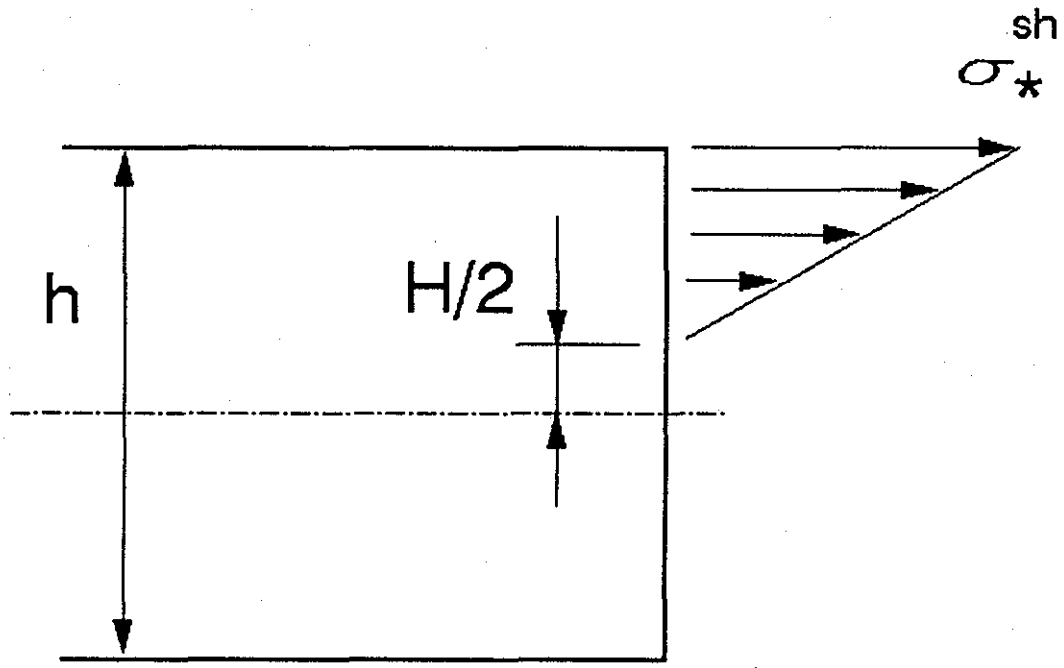

Fig. 5.3. Shrinkage-Induced Stresses.

$$M_y^{sh} = -\int_{-\frac{h}{2}}^{-\frac{H}{2}} \frac{\sigma^{sh}}{\frac{h - H}{2}} \left[z + \frac{H}{2}\right] z\,dz$$

$$= -\frac{\sigma^{sh}}{24(h - H)} \left[2h^3 - 3Hh^2 + \frac{1}{24} H^3\right] \tag{5.10}$$

$$\sigma^{sh} = \frac{E}{1 - \nu} \epsilon^{sh} \tag{5.11}$$

where ϵ^{sh} is the free shrinkage at the top surface of the pavement, which may be estimated with Eqs. (5.6) to (5.8).

For the warping due to shrinkage, the following equations (in addition to Eq. [5.1]) yield results corresponding to Westergaard's analysis for the thermal curling case.

$$M_y = D\left[-\frac{d^2w}{dy^2} - \frac{(1 + \nu)(2h^3 - 3Hh + H^3)\epsilon^{sh}}{2(h - H)h^3}\right] \tag{5.12}$$

$$\frac{d^2M_y}{dy^2} = -kw \tag{5.13}$$

Therefore, for a slab which has an edge along the axis of x and extends infinitely far in the positive y-direction and positive and negative x-directions the tensile stress at the top of the slab is:

$$\sigma_y = \sigma^{sh}\left[1 - \frac{\sqrt{2}}{4} \frac{(2h^3 - 3Hh^2 + H^3)}{(h - H)h^2} \sin\left[\frac{y}{\ell\sqrt{2}} + \frac{\pi}{4}\right] e^{-\frac{y}{\ell\sqrt{2}}}\right] \tag{5.14}$$

$$\sigma_x = \sigma^{sh} + \nu\left(\sigma_y - \sigma^{sh}\right) \tag{5.15}$$

For an infinitely long strip of slab of finite width b with two edges y = ± b/2:

$$\sigma_y = \sigma^{sh}\left[1 - \frac{1}{2}\,\frac{(2h^3 - 3Hh^2 + H^3)}{(h - H)h^2}\,\frac{\cos\lambda\cosh\lambda}{\sin 2\lambda + \sinh 2\lambda}\right.$$
$$\left.\left((\tan\lambda + \tanh\lambda)\cos\frac{y}{\ell\sqrt{2}}\cosh\frac{y}{\ell\sqrt{2}} + (\tan\lambda - \tanh\lambda)\sin\frac{y}{\ell\sqrt{2}}\sinh\frac{y}{\ell\sqrt{2}}\right)\right] \tag{5.16}$$

and σ_x is found from Eq. (5.15) given above.

As seen, the difference between Westergaard's solution and Eq. (5.14) is a factor of the second term in the brackets. The numerical solution listed in Tables IV and V in Westergaard's paper can be easily modified for Eq. (14). For example, $\sigma_c/\sigma_0 = 1.084$ for $\lambda = b/\ell\sqrt{8} = 3$ in Table V, but for the shrinkage case with H = 0:

$$\sigma_y = \sigma^{sh}\left[1 - \frac{\cos\lambda\cosh\lambda}{\sin 2\lambda + \sinh 2\lambda}(\tan\lambda + \tanh\lambda)\right.$$
$$\left.\cos\frac{y}{\ell\sqrt{2}}\,\frac{\cosh y}{\ell\sqrt{2}} + (\tan\lambda - \tanh\lambda)\,\sin\frac{y}{\ell\sqrt{2}}\sinh\frac{y}{\ell\sqrt{2}}\right] \tag{5.17}$$

Comparing (5.17) with Westergaard's solution, one gets:

$$\frac{\sigma_y}{\sigma^{sh}} = 1 + \frac{(1.084 - 1)}{2} = 1.042$$

Maximum frictional stresses (σ_f) at the mid-slab area of a concrete pavement may be calculated from the traditional expressions elaborated by Yoder and Witzak [10]. If the unit weight of concrete is taken as lbs/CF then:

$$\sigma_f = \frac{L}{2}\,\mu \tag{5.18}$$

where μ is the coefficient of subbase friction, and L is the length of the slab. Eq. (5.18) suggests that σ_f will increase directly with L (for a given value of μ); however, a practical limit does exist for σ_f when it equals the maximum frictional stress (σ_m) that results from complete restraint at the bottom of the slab of the climatic induced strains:

$$\sigma_m = E\left(\epsilon^t + \epsilon^{sh}\right)$$

Therefore:

$$\frac{L}{2} = L' \leq \frac{1}{M} E\left(\epsilon^t + \epsilon^{sh}\right)$$

where L' represents the length of pavement (from a construction joint) where:

$$\sigma_f = \sigma_m$$

Note in Eq. (5.19) that as the friction coefficient increases, the distance to where $\sigma_f = \sigma_m$ decreases.

Friction coefficients depend upon the type of subbase, and typical coefficients are listed below in Table 5.1. The variation in frictional stress along the slab length as it approaches the maximum frictional stress (σ_f) was found to vary non-linearly by numerical analysis, as suggested by McCullough [11] and Palmer, et al. [12]. Accordingly, the frictional stress at any point (x) from a construction joint (up to L') of a newly placed pavement may only be linearly approximated by Eq. (5.19) if x is substituted for L' in Eq. (5.19).

Creep Analysis

Creep can generally be defined as a time-dependent deformation of a material subjected to a sustained stress. When deformation is kept constant, the creep reduces the

Table 5.1 Typical Friction Coefficients for Subbases [11]

Subbase Type	Peak	Slab Thickness
Unbound Granular	3.0, 3.4 psi (21, 23 kPa)	4, 8 in (100, 200 mm)
AC - Stabilized	1.6, 2.2 psi (11, 15 kPa)	3.5, 7 in (89, 178 mm)
Cement Stabilized	15.4 psi (106 kPa)	3.5 in (89 mm)
Lime-treated Clay	1.6, 1.7 psi (11, 11.7 kPa)	3.5, 7 in (89, 178 mm)
Untreated Clay	0.6, 1.1 psi (4.1, 7.6 kPa)	3.5, 7 in (89, 178 mm)

stress. This process is defined as relaxation. As suggested by Grzybowski [13], stresses that result from the relaxation under varying strain such as restrained thermal expansion and shrinkage can be calculated with the rate of Flow Method [14]. In this method, the stress increment $\Delta\sigma_i = \sigma_{i+1} - \sigma_i$ due to the strain increment $\Delta\epsilon_i = \epsilon_{i+1} - \epsilon_i$ can be obtained as follows:

$$\Delta\sigma_i = \frac{E(t_i)}{1 + \varphi(t_{i+1}, t_i)} \Delta\epsilon(t_i) = R(t_{i+1}, t_i)\Delta\epsilon(t_i) \tag{5.20}$$

where t is time, $R(t_{i+1}, t_i)$ is the relaxation function, and $\varphi(t_{i+1},t_i)$ is the creep coefficient. From Eq. (5.20), the stress increment $\Delta\sigma_i = \sigma_{i+1} - \sigma_i$ due to the strain increment $\Delta\epsilon_j = \epsilon_{j+1} - \epsilon_j$, which is imposed at time j before time i can be calculated as

$$\Delta\sigma = \frac{E(t_j)}{\varphi(t_{i+1}, t_i) - \varphi(t_i, t_j)} \Delta\epsilon(t_j) \tag{5.21}$$

The total stress increment that occurs during the i^{th} time interval is the sum of the stress increments: $\Delta\sigma_i$ due to every strain increment $\Delta\epsilon_j (j \leq i)$, and the stress increment due to the strain increment $\Delta\epsilon_i$:

$$\Delta\sigma_{i,tot} = \sum_{j=1}^{i=1} [R(t_{i+1}, t_j) - R(t_i, t_j)] \Delta\epsilon(t_j) + R(t_{i+1}, t_i) \Delta\epsilon(t_i) \quad (5.22)$$

Thus, the stress at the end of the i^{th} time interval can be written as:

$$\sigma(t_{i+1}) = \sigma(t_i) + \Delta\sigma_{i,tot} \quad (5.23)$$

A creep coefficient of the two time instants, t and t_0 is suggested by ACI Document 209R as:

$$\phi(t,t_0) = \frac{(t - t_0)^{0.6}}{10 + (t - t_0)^{0.6}} \phi\infty(t_0) \quad (5.24)$$

where

t - the actual age of concrete.

t_0 - the age of concrete at which the strain increment is imposed.

$\phi_\infty(t_0)$ - an ultimate creep coefficient, depending on the load age, $(t\text{-}t_0)$, concrete properties and environmental conditions.

In absence of specific creep and shrinkage data for the aggregates and conditions, ACI 209R suggests

$$\phi_\infty(t_0) = 2.35\ \gamma_c \quad (5.25)$$

where

γ_c is the correction factor, which is the product of correction factors for the load age, ambient relative humidity, the average thickness of the concrete structure, cement content, fine aggregate content, and air content in the concrete.

Calculation of Climatic Stresses

The calculation of climatic stresses in a pavement slab at an early age will require the determination of Young's Modulus and Poisson's Ratio for the concrete. Oluokum,

et al. [15] examined the existing formula for Young's modulus of concrete at an early age proposed by ACI 318. Their investigation showed that the ACI 318 relation for Young's modulus evaluation is essentially valid at concrete ages 12 hours and greater:

$$E = 57000 \sqrt{f_c'} \quad \text{(psi)} \tag{5.26}$$

where f'_c is compressive strength of concrete in psi.

Klimk [16], and Higginson, et al. [17] observed that Poisson's ratio of concrete varied little at different ages and curing conditions. According to their observations, Poisson's ratio is insensitive to the mixture content as well as age, and it may be taken as 0.15.

For illustration purposes, climatic stresses in a 13-inch concrete slab constructed in a closely monitored test section in Texarkana, Texas, placed directly on subgrade are calculated. It is assumed that the test pavement, during the period of crack development, meets the boundary conditions for an infinitely long slab of finite width b (assuming a 24-foot-wide (7.3 m), two-lane pavement). The frictional subbase stresses (σ_f) are calculated according to Eq. (5.18) on the portion of the pavement segment where curling and warping stresses are at a maximum. This was shown by Westergaard to be 4.44ℓ from a free edge (the construction joint for new pavements or greater). The computation of frictional stresses are based upon the temperature and moisture changes which occur at the bottom of the slab and the appropriate coefficient of friction for an untreated clay subgrade ($\mu = 1.5$).

Information from one of the concrete mix designs (Fig. 5.17) used in experimental pavement sections referred to previously is utilized in demonstrating the development of early-aged stresses in jointed concrete pavements. Table 5.2 contains mix design ratios relevant to Eq. (5.6). For this mix design, the correction factor relevant to the equation for relaxation analysis is the product of all the correction factors listed in Table 5.3.

Table 5.2 Tabulated Concrete Mix Ratios

Aggregate Type			
a/c	w/c	g/s	s/c
7.36	0.51	1.36	2.80

Table 5.3 Correction Factors for the Ultimate Creep Coefficient

variable	load age $(t-t_o)$	ambient R.H.=75%	pavement thickness h=12 in (305 mm)	Slump s=1.5 in (38 mm)	Cement Content c=521 lb/yard^3 (309 kg/m^3)	air content α=5%	fine aggregate percentage ψ=35.9%
Correction factor	$1.25(t-t_o)^{-0.118}$	0.768	0.864	0.92	0.938	1	0.966

Fig. 5.4 illustrates the temperature record at the top of the pavement within five days after placement and the calculated maximum thermal stress history when under full friction restraint conditions. Fig. 5.5 illustrates the relative humidity at the top of the pavement, and the calculated maximum stress caused by shrinkage with full friction restraint. Maximum curling (σ^t) and warping (σ^{sh}) stresses over the first few days of construction require the determination of time-dependent properties of the concrete which vary during hardening and a period of time after hardening. These properties may be illustrated in the variation of the concrete compressive strength (f_c'), modulus of elasticity (E_c), and the ℓ-value shown in Figs. 5.6, 5.7, and 5.8. Noting how these parameters vary with time, it is no surprise to see variation in the maximum σ^t and σ^{sh} values (as determined at the surface in the longitudinal direction shown in Figs. 5.4 and 5.5. Since the pavement under consideration was placed directly on subgrade, the subgrade k - value

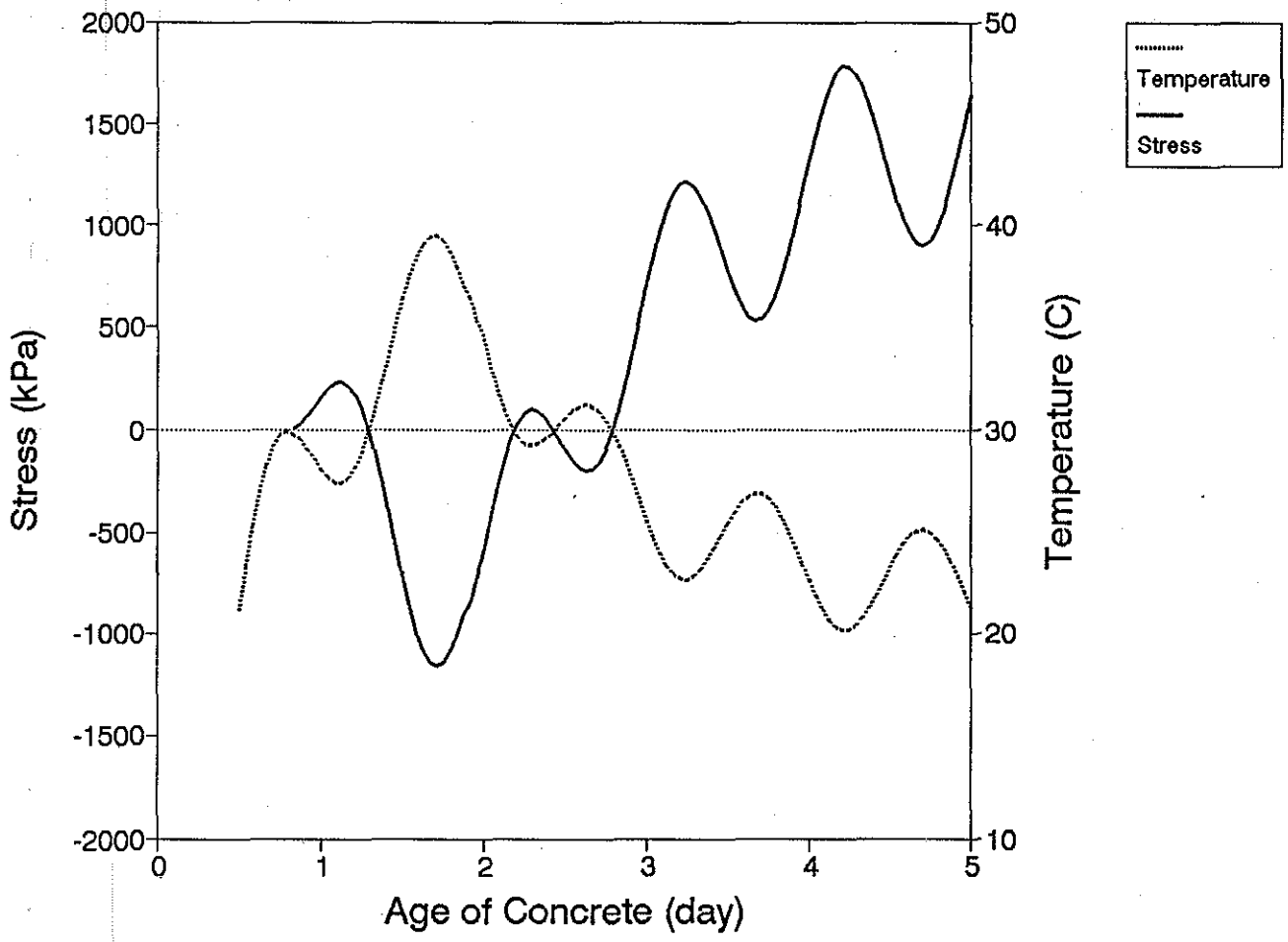

Fig. 5.4. Record of Temperature of Concrete at the Top of the Pavement and Calculated Stresses.

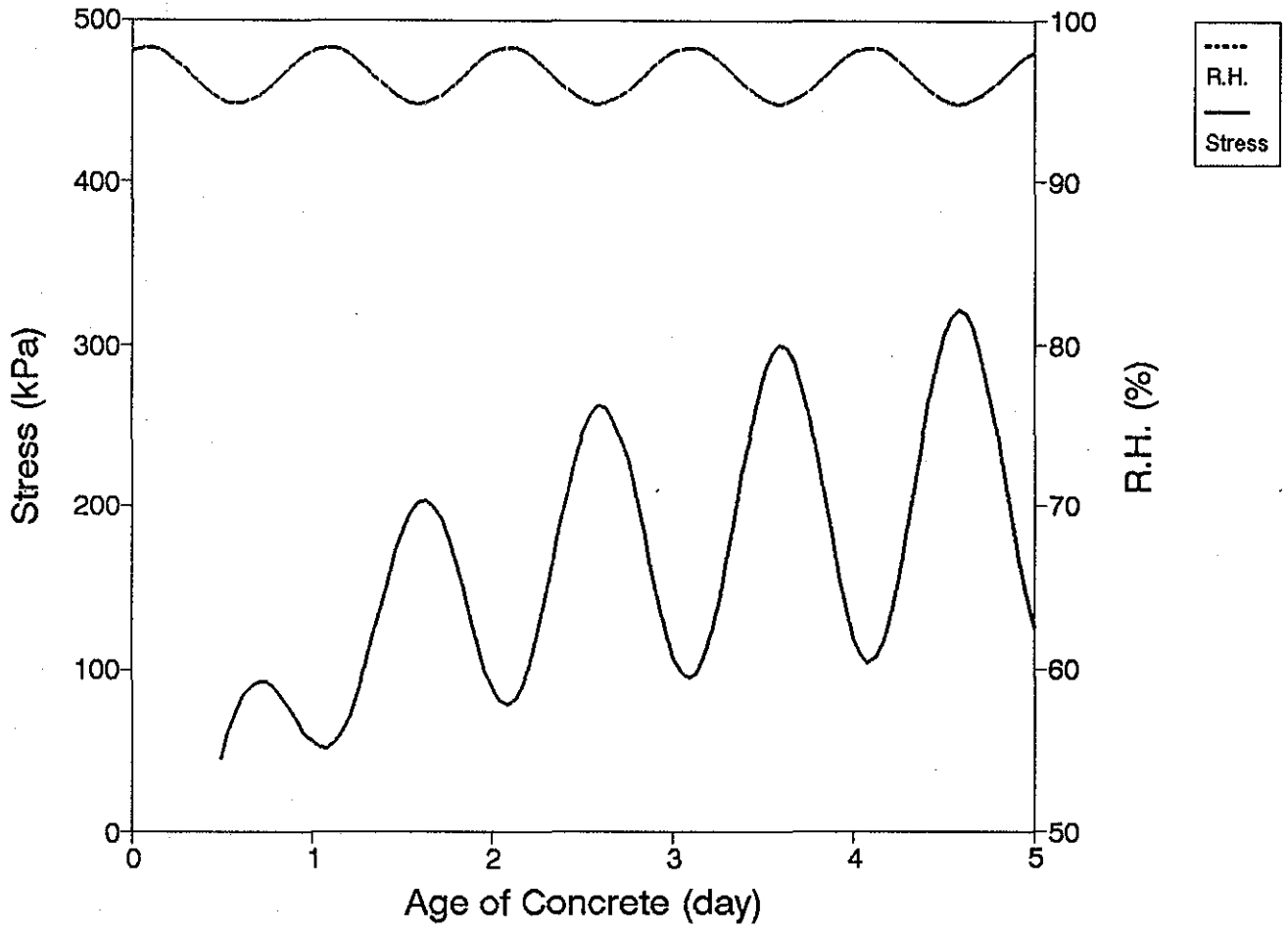

Fig. 5.5. Record of Relative Humidity in Concrete at the Top of the Pavement and Calculated Stresses.

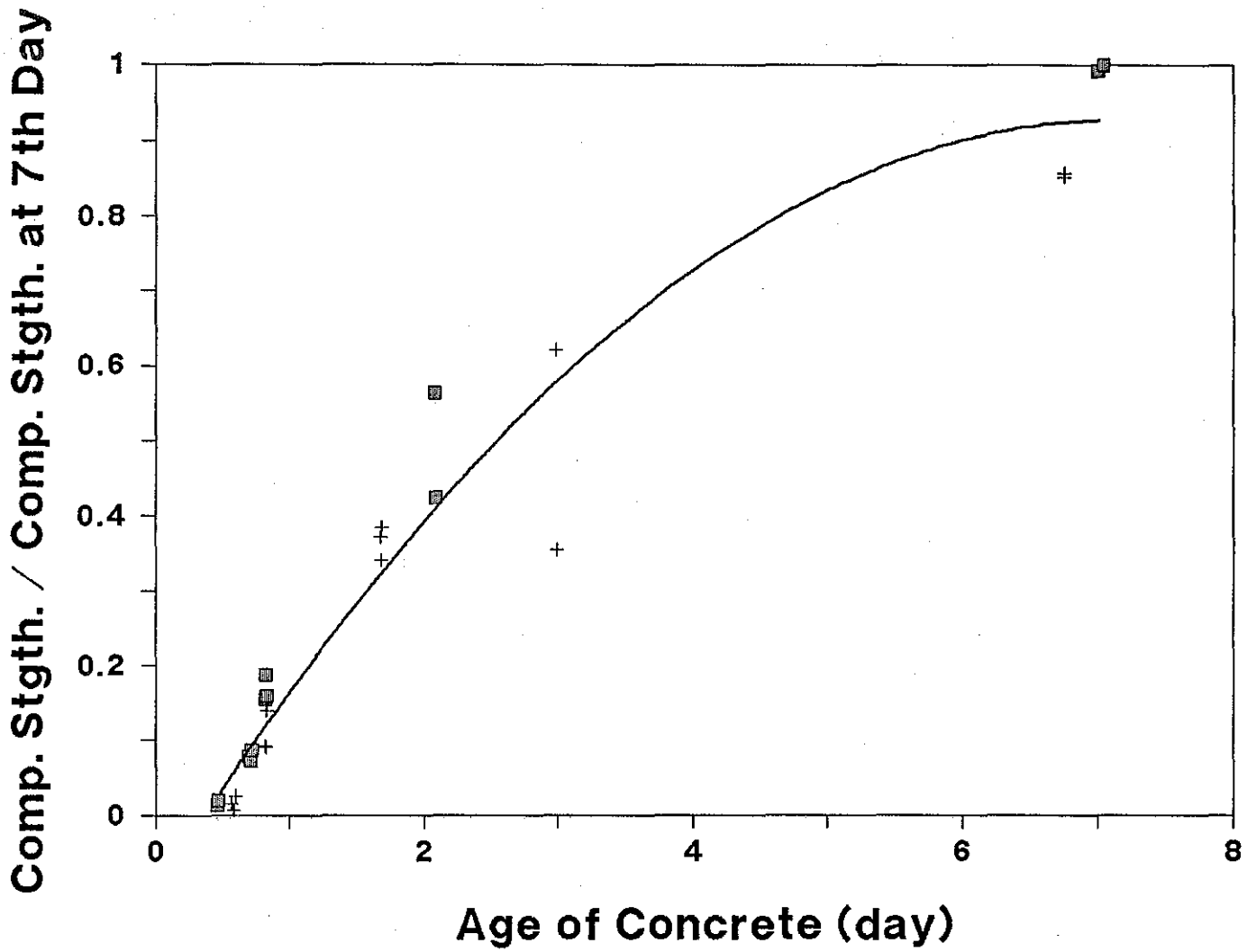

Fig. 5.6. Variation of Compressive Strength of Early-Aged Concrete.

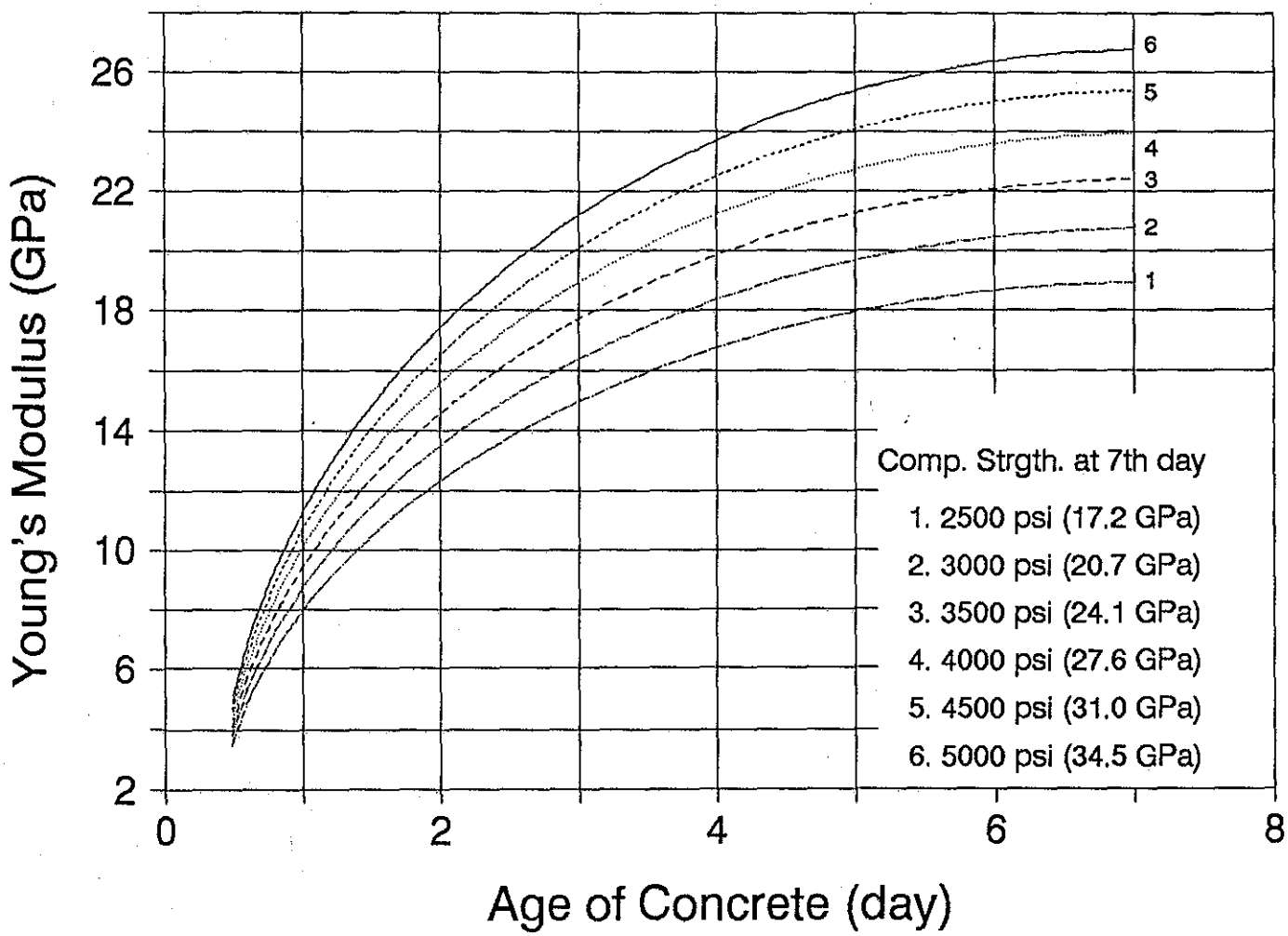

Fig. 5.7. Variation of Young's Modulus of Early-Aged Concrete.

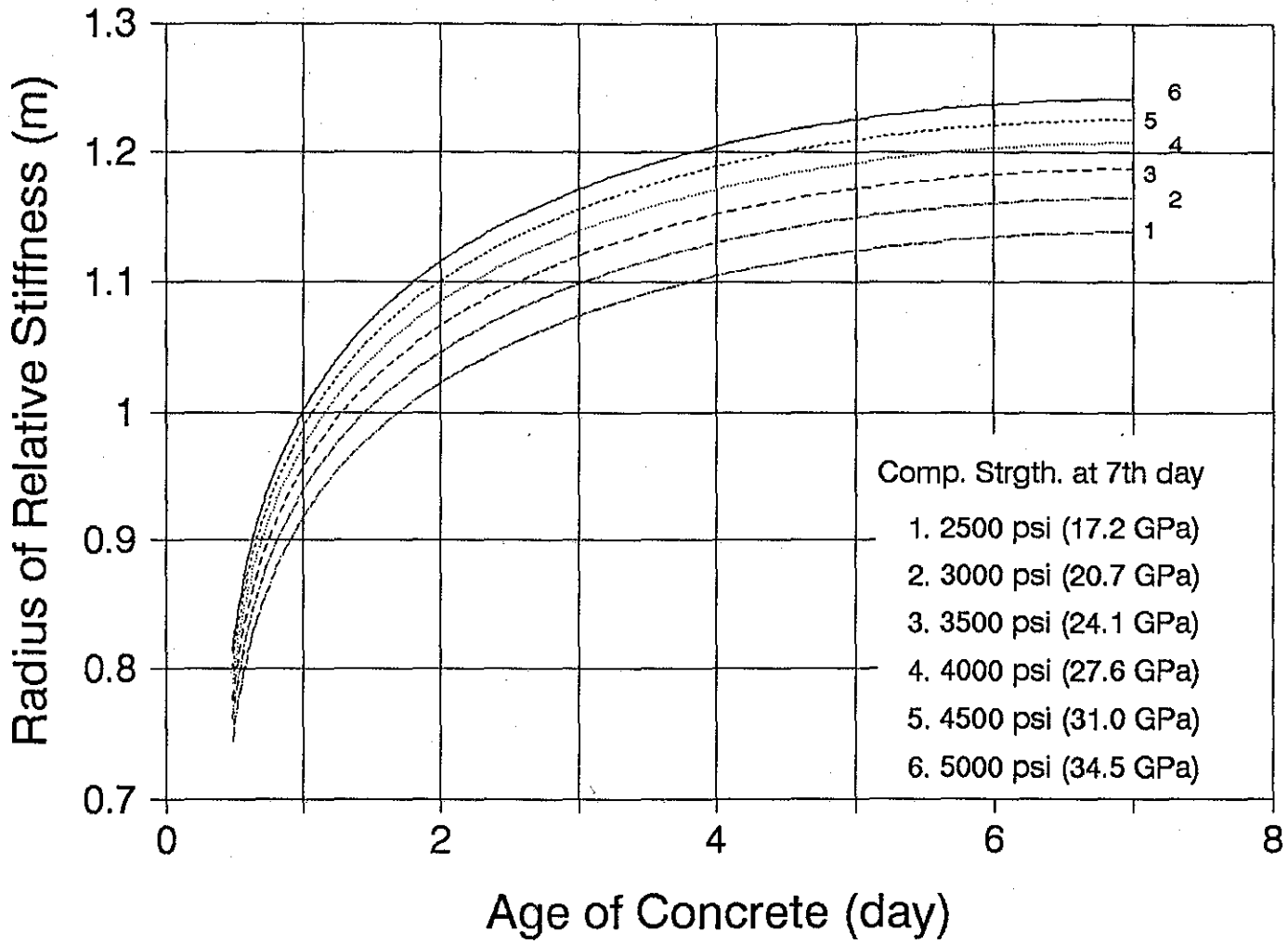

Fig. 5.8. Variation of the Radius of Relative Stiffness of the Pavement at the First Seven Days.

was taken as 100 psi/in (17.5 N/mm). Frictional stresses are calculated, as pointed out previously, based upon the temperature and moisture changes at the slab bottom. Depending on the magnitude and direction of change, the total stresses may be tensile or compressive. The shrinkage stresses were calculated using Eqs. (5.6) to (5.8) and the ratios tabulated in Table 5.2. Eq. (5.16) yields the warping stresses in the longitudinal direction. Eq. (5.2) yields the warping stresses in the longitudinal direction, where shrinkage-caused strain is assumed to exist from the top to the bottom of the pavement; however, these are not shown in Fig. 5.5. The Bradbury expressions (Eqs. [5.3] and [5.4]) are used to find similar thermal stresses. The combination or total of the stresses discussed above is also illustrated in Fig. 5.9 at a distance of 90 feet (27.4 m) from the pavement free edge. The stresses were found at this distance since this is approximately where maximum restraint occurred in the paved segment, which approaches the center of the paving segment. The sum of the combination of curling, warping and friction will vary along the longitudinal axis of the paving segment. The maximum combination of these stresses, which occurs near the center of any paving segment, may be dominated by the frictional component. However, curling and warping stresses may dominate near the free edge of the paving segment. A combination of the longitudinal curling and warping stresses at the top of the pavement is shown with a solid line in Fig. 5.9. By considering the process of relaxation, the result of these two stress components is calculated by using Eqs. (5.20) to (5.25) and indicated with a dotted line in the figure. The maximum friction-caused stress at 90 feet (27.4 m) from the pavement free edge (see Fig. 5.17, where a first crack was found near the center of the paved segment) is 141 psi for a pavement thickness of 12 inches (30 cm), a specific weight of the concrete is 0.087 lb/in^3 (0.0236 MN/m^3), and a friction coefficient of 1.5. The total longitudinal stress at the top of the pavement is the sum of the curling, warping and friction-caused stresses at that position. Fig. 5.10 shows superimposition of these three stresses at 90 feet (27.4 m) from the pavement free edge. The dashed line includes only the combination of the curling and warping stresses. When the contribution due to curling and warping is less than 141 psi the subbase friction dominates the restraint to slab movement and causes tresses that are equal to the value of the combination or exceeds them. The bold solid

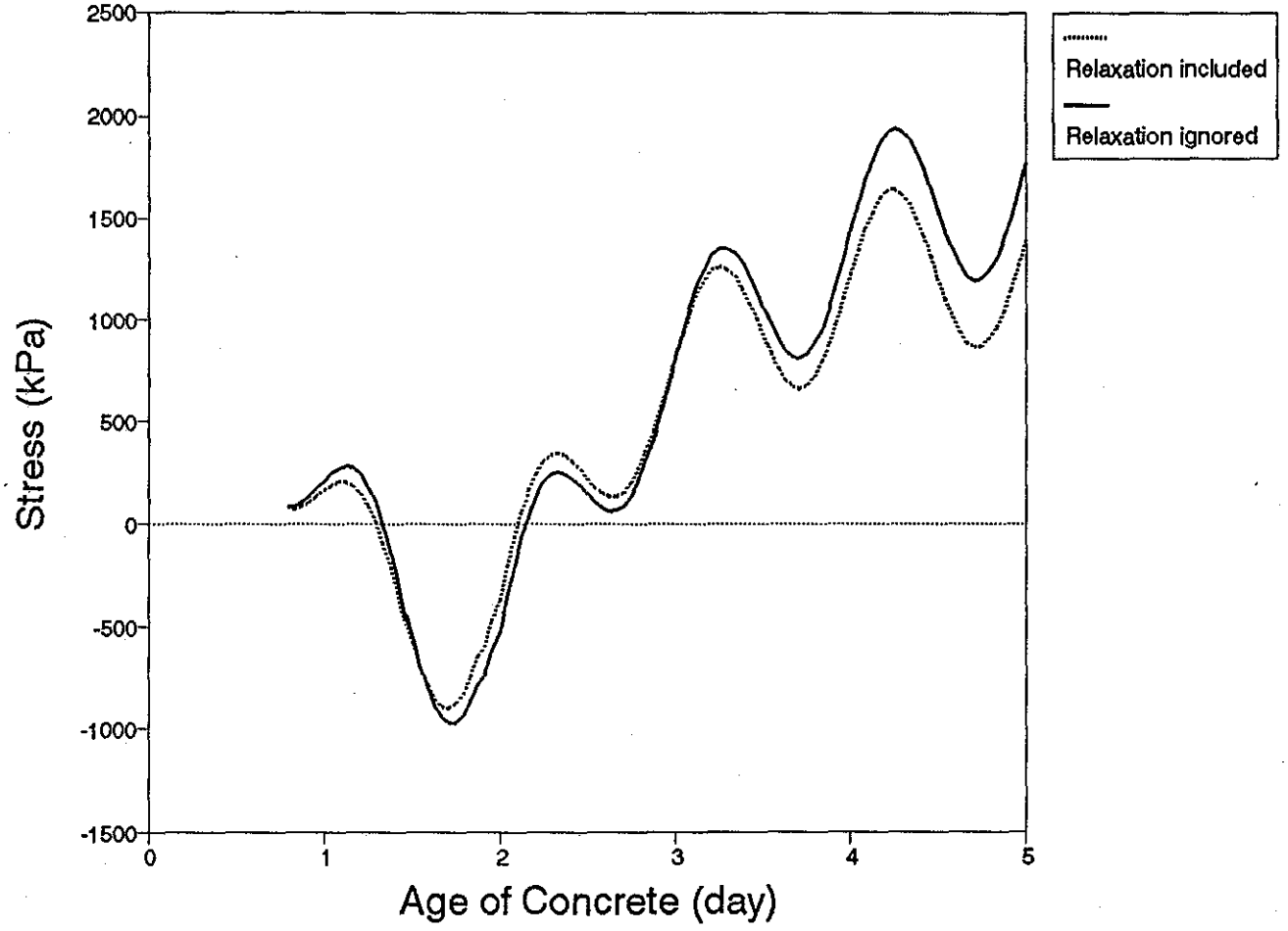

Fig. 5.9. Combination of the Curling and Warping Stresses at the Top of the Pavement.

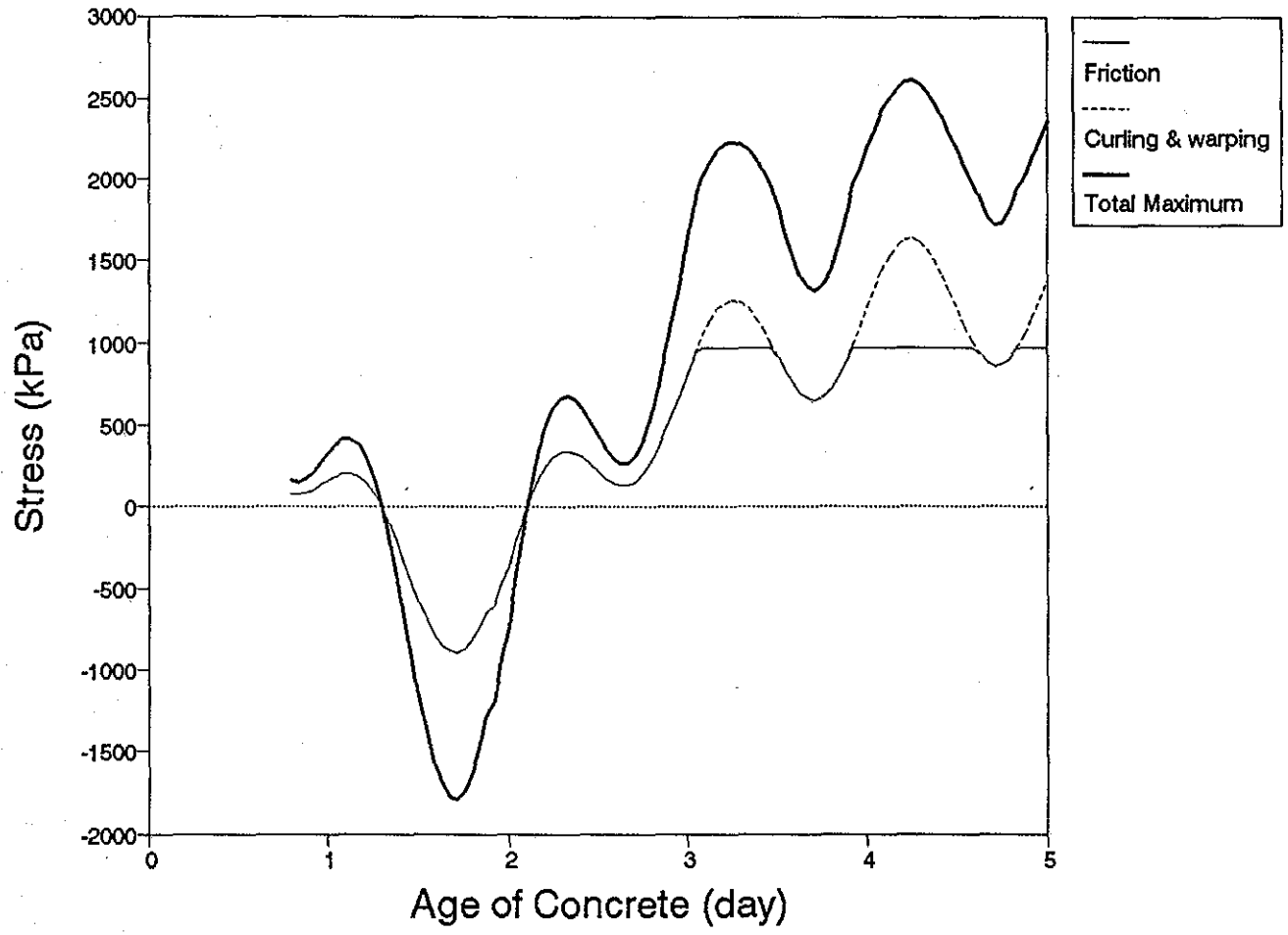

Fig. 5.10. Superimposition of the Curling, Warping and Friction-Caused Stresses.

line in the figure is the result of thesuperimposition, the total longitudinal stress at the top of the pavement (which includes creep). Cracking appears to occur initially from the portion of the paved segment of maximum restraint, and then proceeds from this point at intervals of 4.44ℓ.

5.3 SAWCUT SPACING DEPTH REQUIREMENTS

To determine the spacing of the transverse joint locations or sawcuts for a newly placed concrete pavement, the assumption applies that a newly paved pavement in the encroached condition is infinitely long. Therefore, the maximum total climatic stress (as described above) is calculated at approximate intervals of 4.44ℓ as predicted by Westergaard analysis. The position of maximum stress may vary for early-aged concrete since ℓ changes during this period of time. As the concrete ages, maximum stress locations typically stabilize at 13 to 16 foot intervals, depending on the subbase type, which provides some guidance as to the recommended joint spacing for design and construction purposes.

The same analysis may apply to the spacing of the longitudinal sawcut locations; however, the focus in this instance is normally to examine the suitability of standard joint locations which often serve as lane dividers. In a two-lane pavement, the longitudinal tensile stress at the pavement top is calculated at the longitudinal joint location (such as along the center line where the pavement is divided to two 12-ft-wide strips). The total tensile stress σ_x is reduced by a factor of 50% according to Eq. (16) which, in this case, is below the tensile strength of concrete.

5.4. THEORY AND APPLICATION OF FRACTURE MECHANICS

The analysis of notched concrete pavement slab based on fracture mechanics incorporates the stresses generated by temperature and shrinkage effects which are applied as loads. Important material parameters as identified by the Size Effect Law [18] are determined based on notched beam tests. The notch depth is great enough such that the crack will develop quickly and extend to the slab bottom under the applied stress. Through fracture tests, fracture parameters K_{If} and C_f at early ages of concrete have been

obtained for concretes of different coarse aggregates [19]. The K_{If} is the critical stress intensity factor for a specimen of infinite dimension (in depth), in which linear elastic fracture mechanics (LEFM) applies to the analysis thereof. With respect to the application of K_{If} to a concrete slab, LEFM still can be applied to determine a sufficient notch depth, even though a concrete slab is not infinitely large. This is because the nominal strength of an infinite specimen is lower than the nominal strength which is predicted for the finite specimen with LEFM based on K_{If} as the failure criterion (see Fig. 5.11).

As in linear mechanics, the superposition principle can be used for the stress intensity when a specimen or structure is subjected to more than one load. The stress intensity factor due to any load can always be expressed as follows:

$$K_I = \sigma \sqrt{\pi a}\ N(\omega) \tag{5.27}$$

where σ is defined as the nominal stress, a is the crack length, and $N(\omega)$ is a non-dimensional function of the ratio, ω, of the crack length (a) to the specimen dimension, d. $N(\omega)$ is called nominal stress intensity factor. The beam depth (pavement thickness h) is usually taken as the dimension d. The nominal stress intensity factor is dependent on the specimen geometry, but independent of the specimen size. The nominal stress intensity factor $N(\omega)$ for the simple tension [20] is:

$$N(\omega) = 1.122 - 0.231\omega + 10.550\omega^2 - 21.710\omega^3 + 30.382\omega^4 \tag{5.28}$$

where ω = a/h (Fig. 5.12(a)) and the nominal stress σ is the load intensity. For the pure bending [20]:

$$N(\omega) = 1.122 - 1.40\omega + 7.33\omega^2 - 13.08\omega^3 + 14.0\omega^4 \tag{5.29}$$

where ω = a/h (Fig. 5.12(b)) and the nominal stress σ is the maximum in the distributed load. Note that these two formulas are for the geometry with top and bottom surfaces free from external forces. Fig. 5.13 shows the tendencies of curling and warping due to the temperature gradient and shrinkage, where Eq. (5.29) is

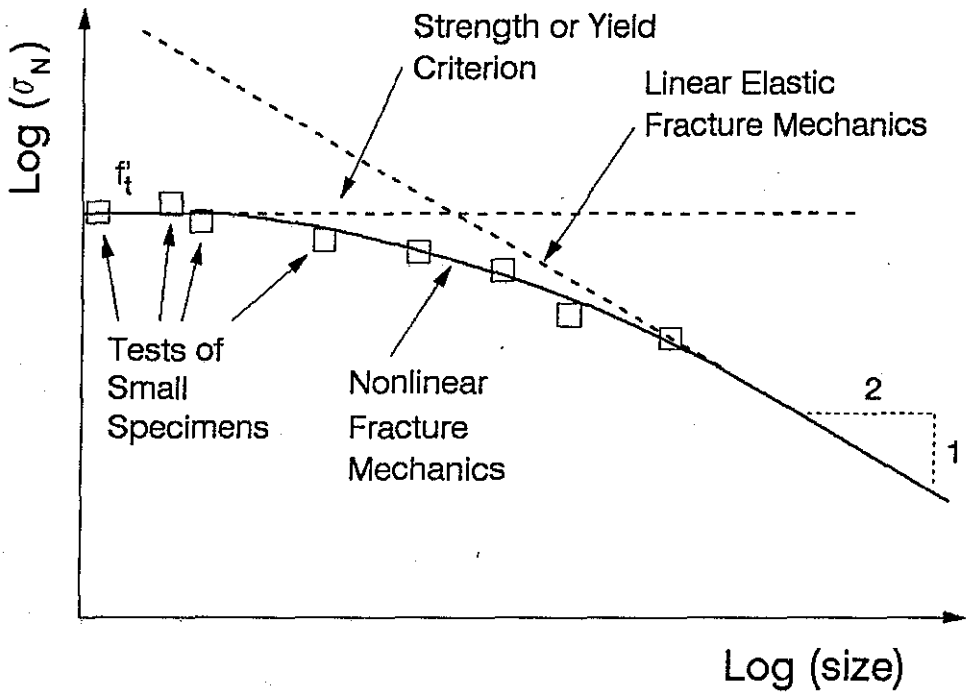

Fig. 5.11. Size Effect of the Nominal Strength of the Concrete Structure.

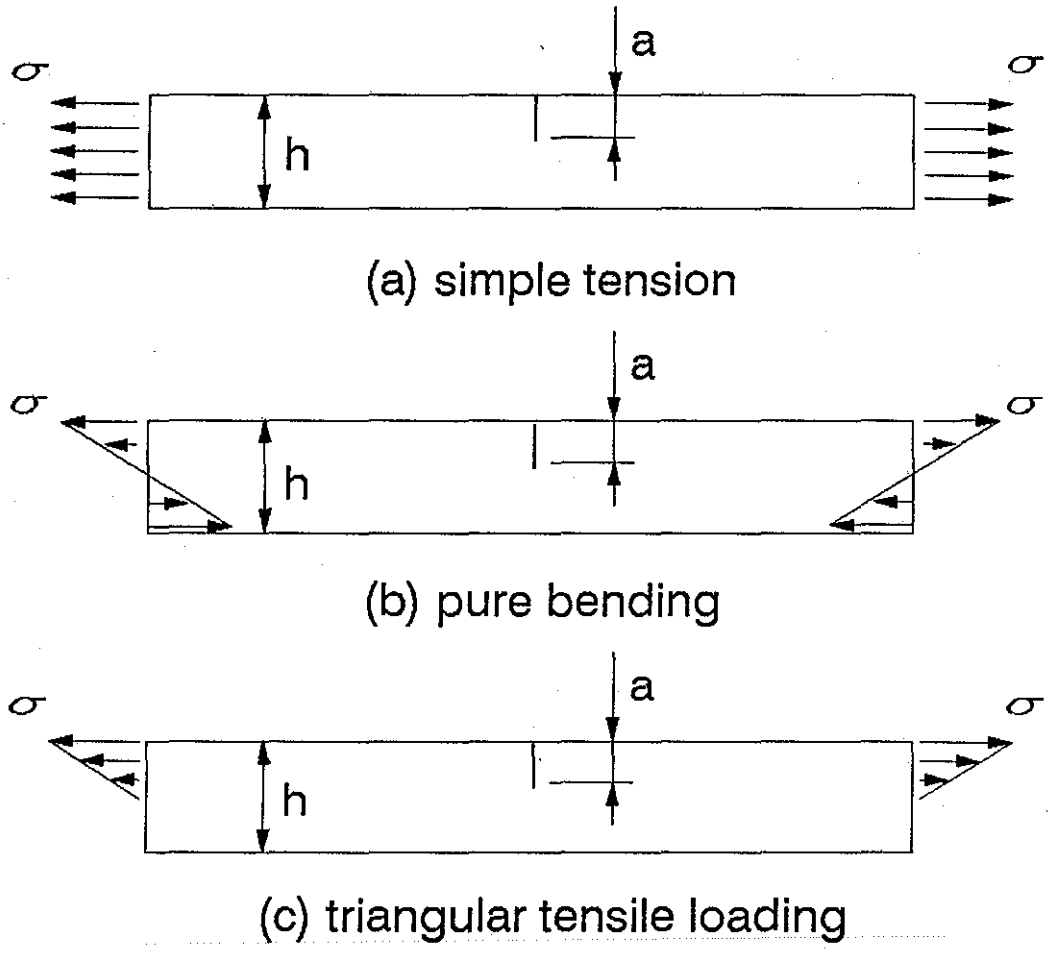

Fig. 5.12. Notched Specimens Under Loading.

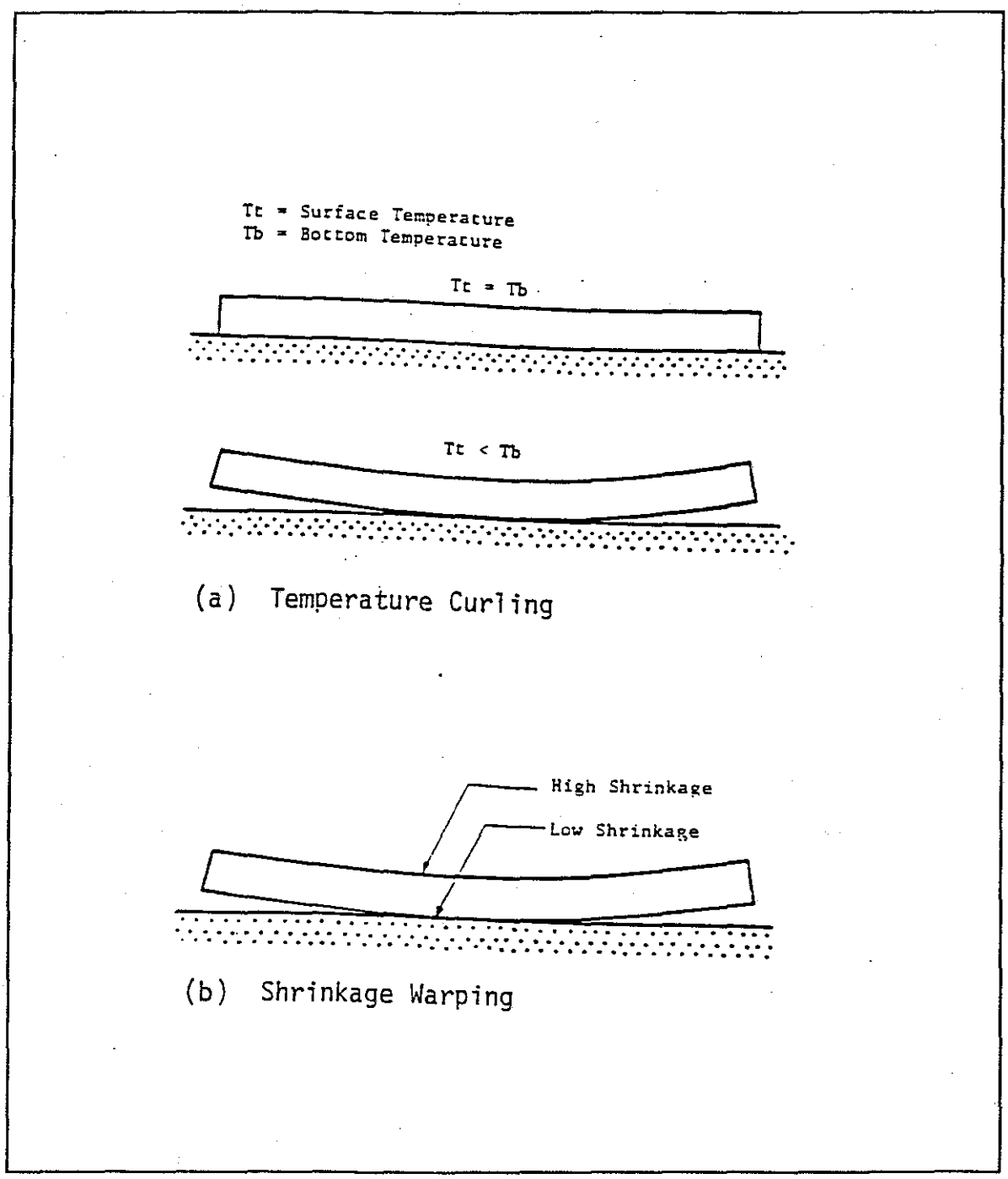

Fig. 5.13. Curling and Warping of Concrete Pavement.

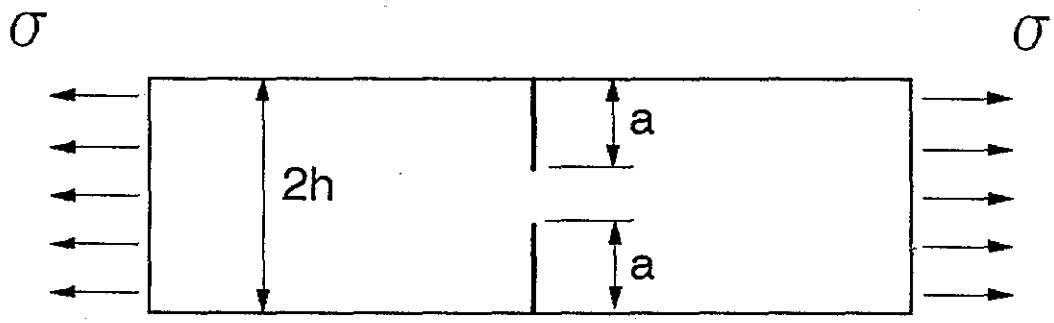

Fig. 5.14. Doubled Edge Notched Specimens in Tension.

approximately valid. The double edge notched test specimen (Fig. 5.14) can be used to develop the fracture analysis as this specimen is somewhat representative of a slab configuration since the centerline in this symmetrical specimen does not move in the vertical direction. The following equation is valid for $\omega = (a/h) < 0.7$:

$$N(\omega) = 1.12 + 0.203\,\omega - 1.197\,\omega^2 + 1.930\,\omega^3 \quad (5.30)$$

where the nominal stress σ is the load intensity. Eqs. (5.22) and (5.23) are useful in applying the stress field induced by climatic effects to the determination of the stress intensity given in Eq. (5.27) by dividing the stress field into components of tensile forces and bending moments. The finite element analysis in this study has shown that replacement of the distributed load on a specimen in simple tension by its resultant--a concentrated load acting along the specimen centerline--does not yield significant change in the K_I value, particularly where the specimen length is four times the thickness. Eq. (5.29) can be applied to pure bending loads other than that shown in Fig. 5.12(b) by substituting $\sigma = 6M/h^2$. Accordingly, the shrinkage-induced stresses (Fig. 5.3) are transformed to a tensile force and a bending moment. For instance, if $H = h/2$, the resultant tensile force is $h\,\sigma^{sh}/8$ then Eq. (5.30) can be used in Eq. (5.27) by substituting $\sigma = \sigma^{sh}/8$ (the resultant force). The bending moment, $M = (5/96)\,\sigma^{sh}\,h^2$, yields $\sigma = (5/16)\,\sigma^{sh}$ in which Eq. (5.29) can be used for K_I Eq. (5.28) with σ due to the bending moment.

Determination of the stress intensity, as given in Eq. (5.27), can be accomplished for a given set of climatic conditions at anticipated sawcut locations to generate sawcut depth guidelines (Fig. 5.15). The K_I values with different notch (sawcut) depths under temperature and shrinkage stresses are determined with Eqs. (5.29) and (5.30). Fig. 5.16 also gives the K_I values for the temperature difference t of 10 F (5.6 C), 20 F (11 C), 30 F (17 C), 40 F (22 C), and 50 F (28 C) between the pavement top and bottom, with the same shrinkage-induced stresses.

The type of coarse aggregate is also important. When the critical stress intensity factor K_{If} equals or exceeds the fracture toughness, $K_{If} = 500$ psi·in$^{1/2}$ = 0.550 MPa·m$^{1/2}$ (typical for river gravel concrete at an age of 12 hours), a sawcut depth of 1 inch (2.5) cm is enough if temperature difference is not less than 20 F (11 C).

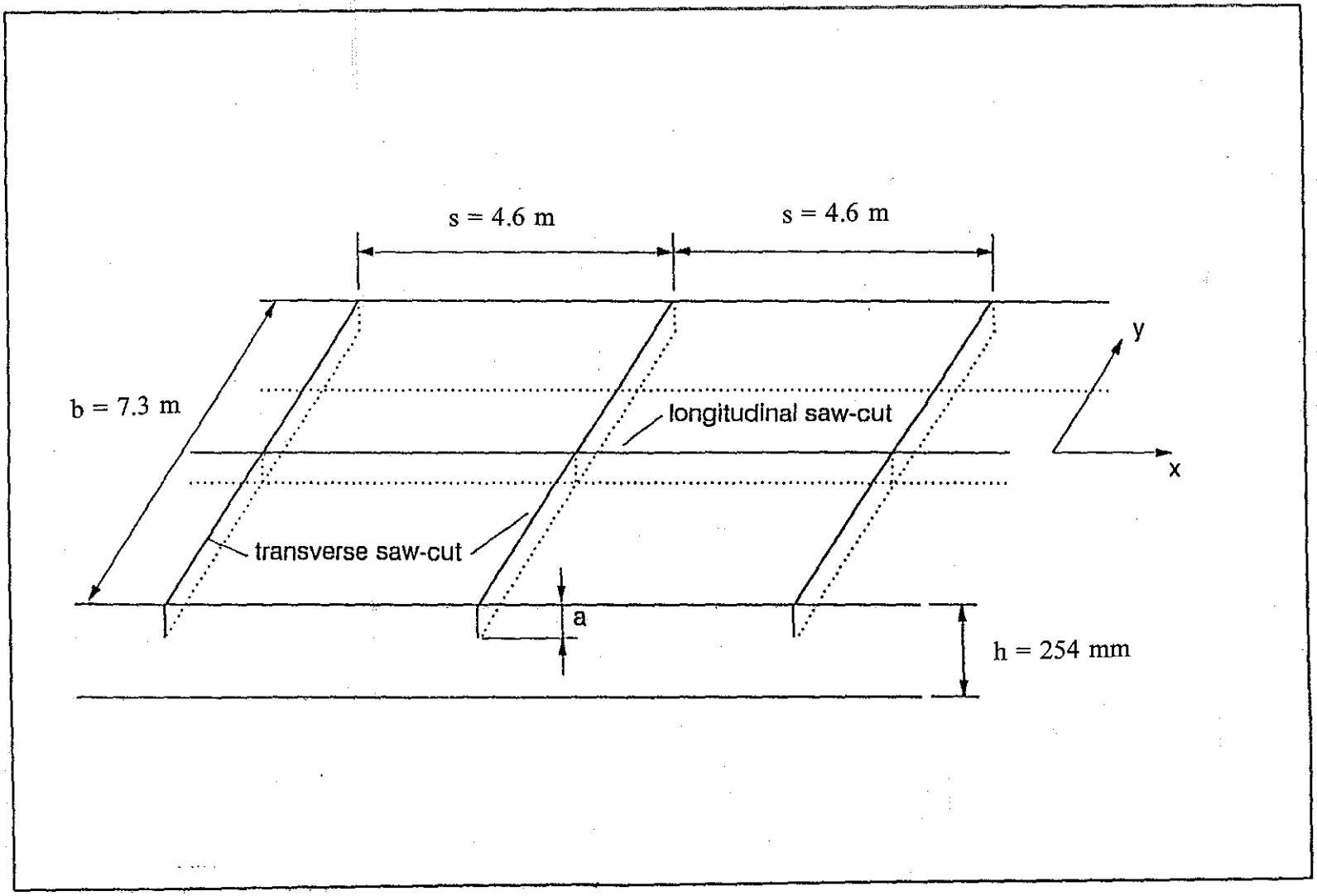

Fig. 5.15. A Two-Lane Sawcut Pavement.

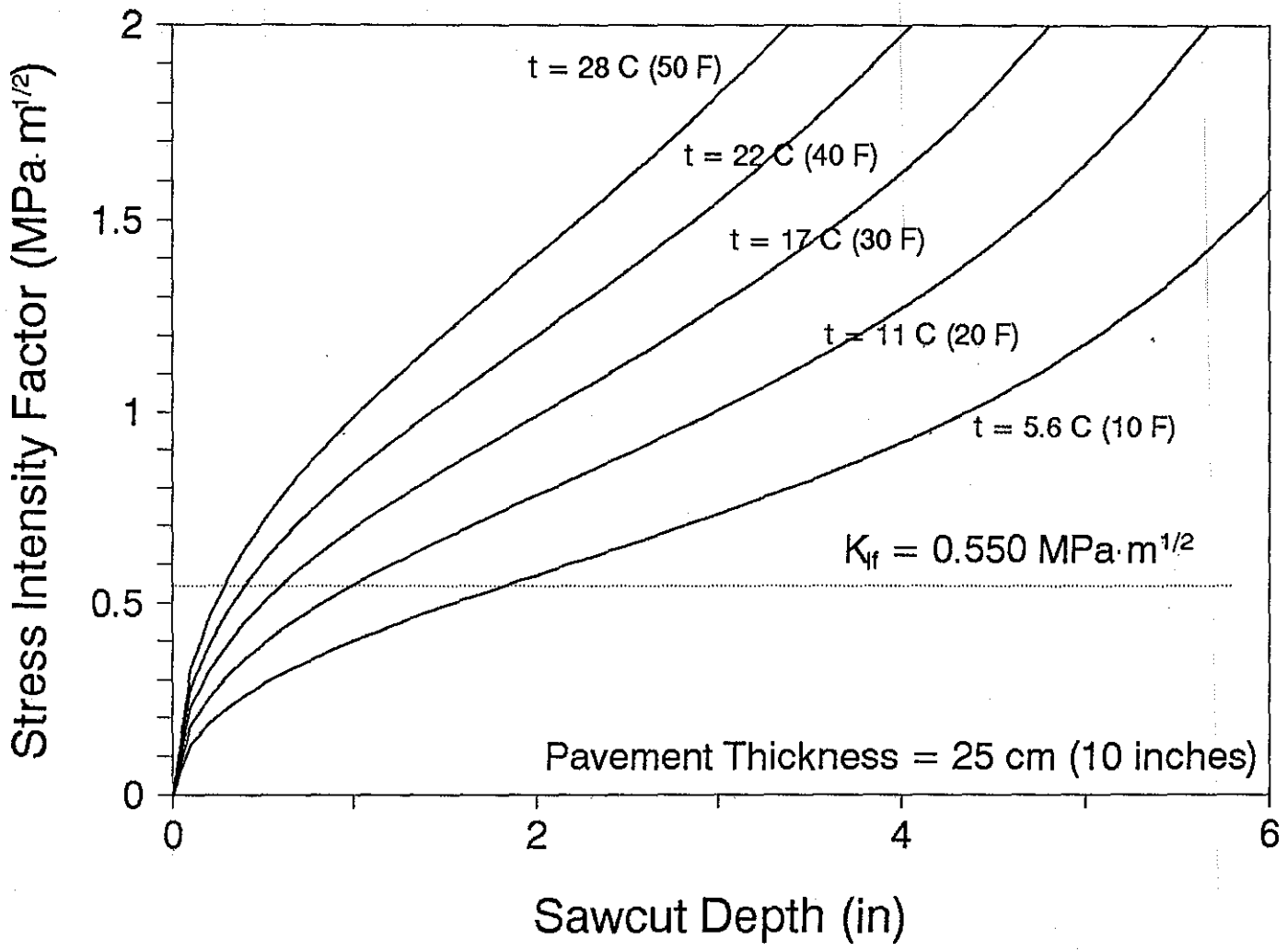

Fig. 5.16. Determination of Sawcut Depths.

When $K_{If} = 800$ psi·in$^{1/2}$ = 0.879 MPa·m$^{1/2}$ (typical for limestone concrete at an age of 12 hours), a sawcut depth of 1.7 inches (4.3 cm) is enough if the temperature difference is not less than 30 F (17 C). Noting the change in stress intensity in comparison to fracture toughness, for the given climatic conditions, one can develop a sense for appropriate sawcut timing to control cracking at the sawcut notches.

5.5. FIELD INVESTIGATION OF CRACK CONTROL

As pointed out previously, the factors that affect the behavior of concrete pavement as they relate to joint formation and crack control, were monitored in a field study undertaken at test sections in Texarkana, Texas, for a 12-inch (20 cm) jointed plain concrete pavement, placed directly on subgrade soils. Several factors were considered in these test sections such as different types of coarse aggregate, different curing methods, and different sawcut techniques and are elaborated on further elsewhere [9]. The type of concrete mixes placed are shown in Table 5.4. These mixes consisted of different coarse

Table 5.4. Aggregates Used in Different Mix Designs.

Mix Design	Coarse Aggregate	Intermediate Aggregate	Fine Aggregate
1 Control Mix	1 1/2 (38 mm) SRG (100%) Item 360.1 (3)	None	Little River Sand (100%) Item 360.1 (4)
2	1 1/2" (38 mm) L.S.(50%) 3/4" (19 mm) SRG (50%) Item 360.1 (3)	Buckshot	Little River Sand (35%) Crushed Sand (65%) Item 360.1 (4)
3	1 1/2" (38 mm) SRG (100%) Item 360.1 (3)	Same as above	Same as above
4	3/4" (19 mm) SRG (100%) Item 421.2	Same as above	Same as above
5	1 1/2" (38 mm) L.S. (100%) Item 360.1 (3)	Same as above	Same as above

aggregate types and blends. However, some results of the crack survey for observation of formation of joints and cracks are provided here which coincide with calculations previously shown. Ambient and pavement temperatures and relative humidities were measured as indicated previously. The development of K_I and K_{If} are calculated and shown in Fig. 5.17. This analysis suggests that cracking initiated 4 to 5 days after placement. The joints in the test section pavement in Texarkana were sawcut by two different techniques at 15 foot (4.6 m) intervals (Fig. 5.18). One method consisted of conventional sawcut techniques using water to cool the saw blade. With this technique, pavement was cut 3-inches (76 mm) deep (d/4). The other method consisted of early-aged sawcut techniques. With this technique, a light and portable sawcutting machine was used so that pavement surface notch could be placed early in the pavement life (typically less than two to three hours after placement). Recent improvements have resulted in a self-propelled saw shown in Fig. 5.19. This was achieved without noticeable joint raveling. Typical sawcut depths were 1 inch (2.5 cm) in which no cooling water was used in the process. Crack surveys conducted from October 1991 to July 1992 (Fig. 5.20) indicated that of all the transverse cracks which developed, only two occurred in between the sawcut joints. These two uncontrolled cracks were initiated from the corners of blockouts (i.e., inlet drainage structures), where stress concentration would have existed. It is speculated that these stress-concentrations at the sharp corners could be avoided by placing joint locations to coincide with sharp corners to guide cracking so that uncontrolled transverse cracks would not occur.

Although the pavement test section in Texarkana was paved on November 8, 1991, (Fig. 5.20) no visible cracks were found until November 26. Cracks at the sawcut tip were observed through the bottom of the pavement slab in later surveys. Earlier cracks occurred at a distance from the pavement construction joint since sufficient stresses needed to develop due to pavement restraint. It should be noted that on June 4, 1992, more joints had been formed at the early-aged sawcuts than at the conventional sawcuts. One month later, three more cracks were found at the conventional sawcuts. A significant amount of cracking developed after the pavement was subjected to a greater range in temperature cycle. Since the concrete strength increased prior to the increase in

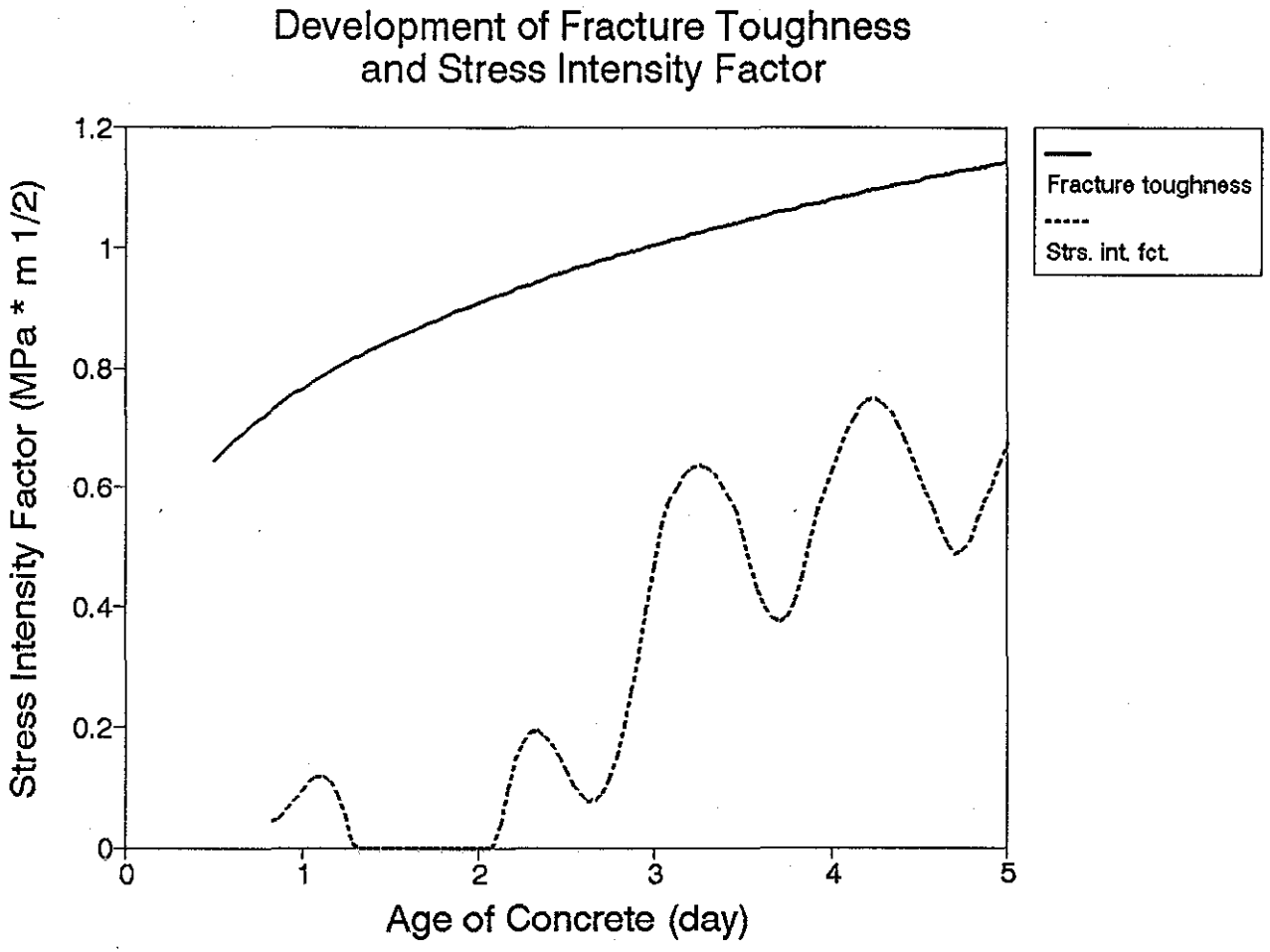

Fig, 5.17. Development of Fracture Toughness and Stress Intensity Factor of the Sawcut.

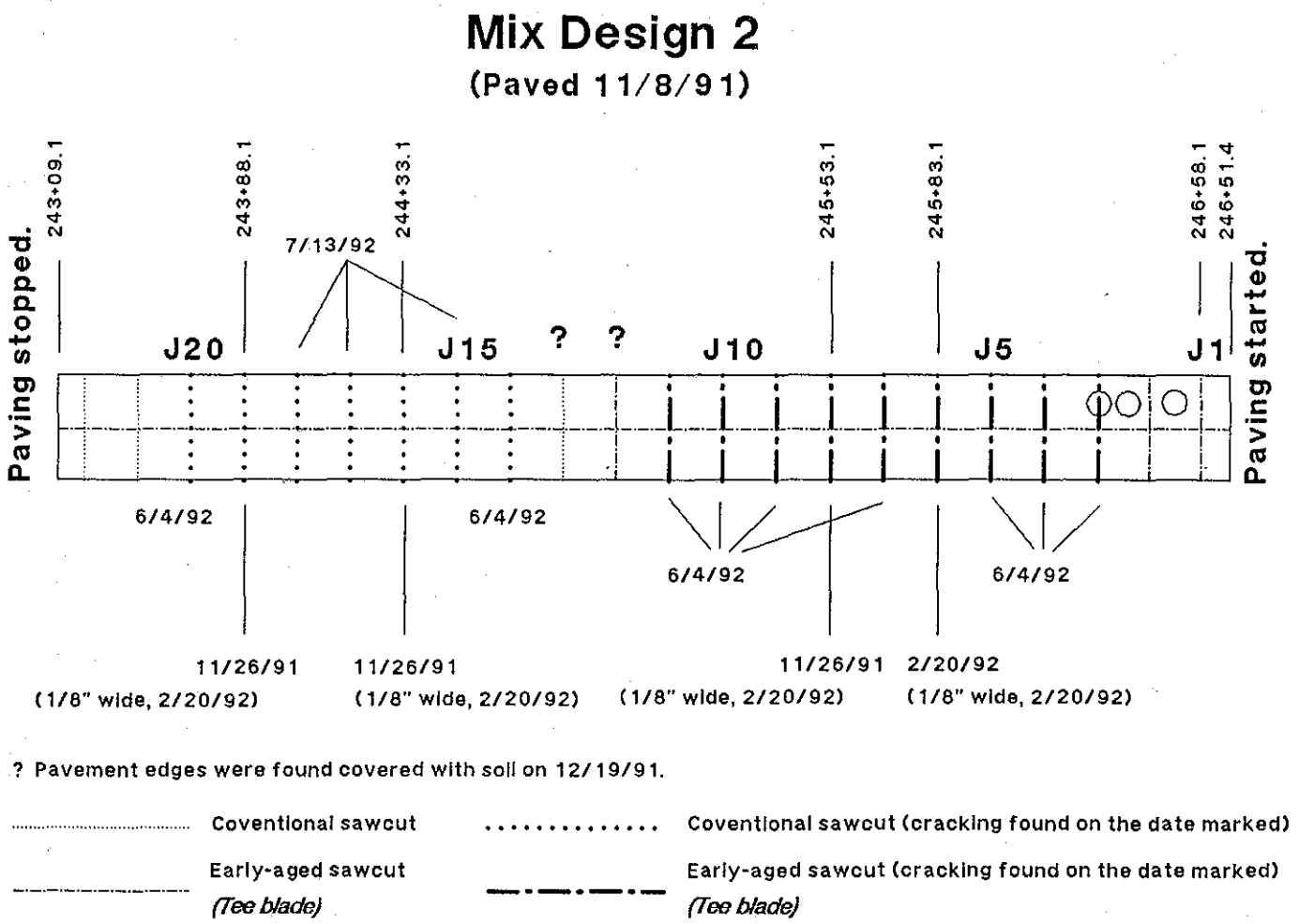

Fig. 5.18. Layout of a Test Section.

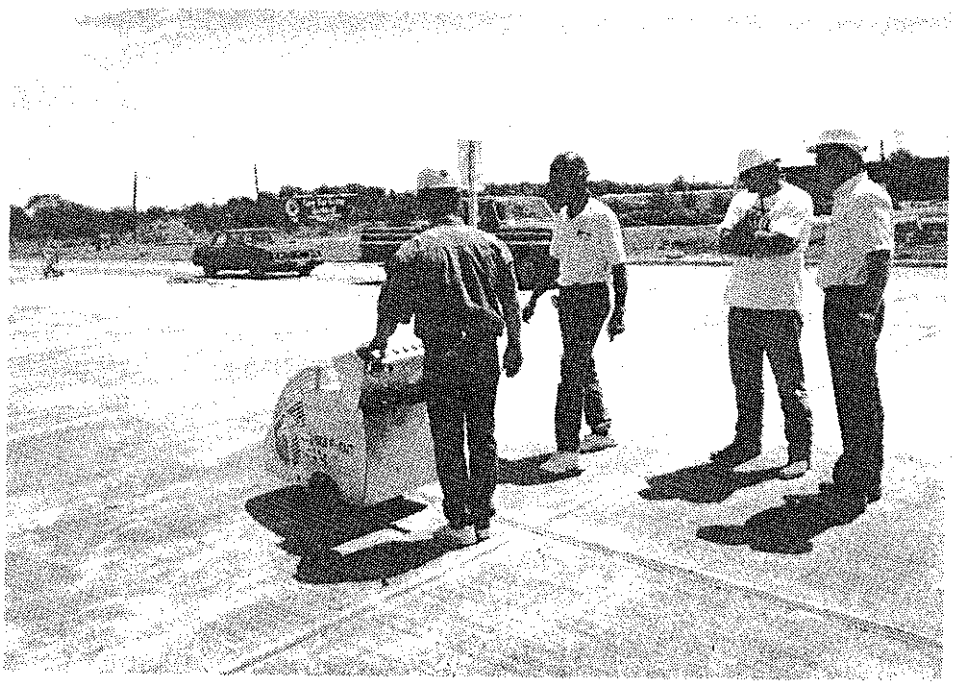

Fig. 5.19. Soft-Cut Early Sawcutting Machine.

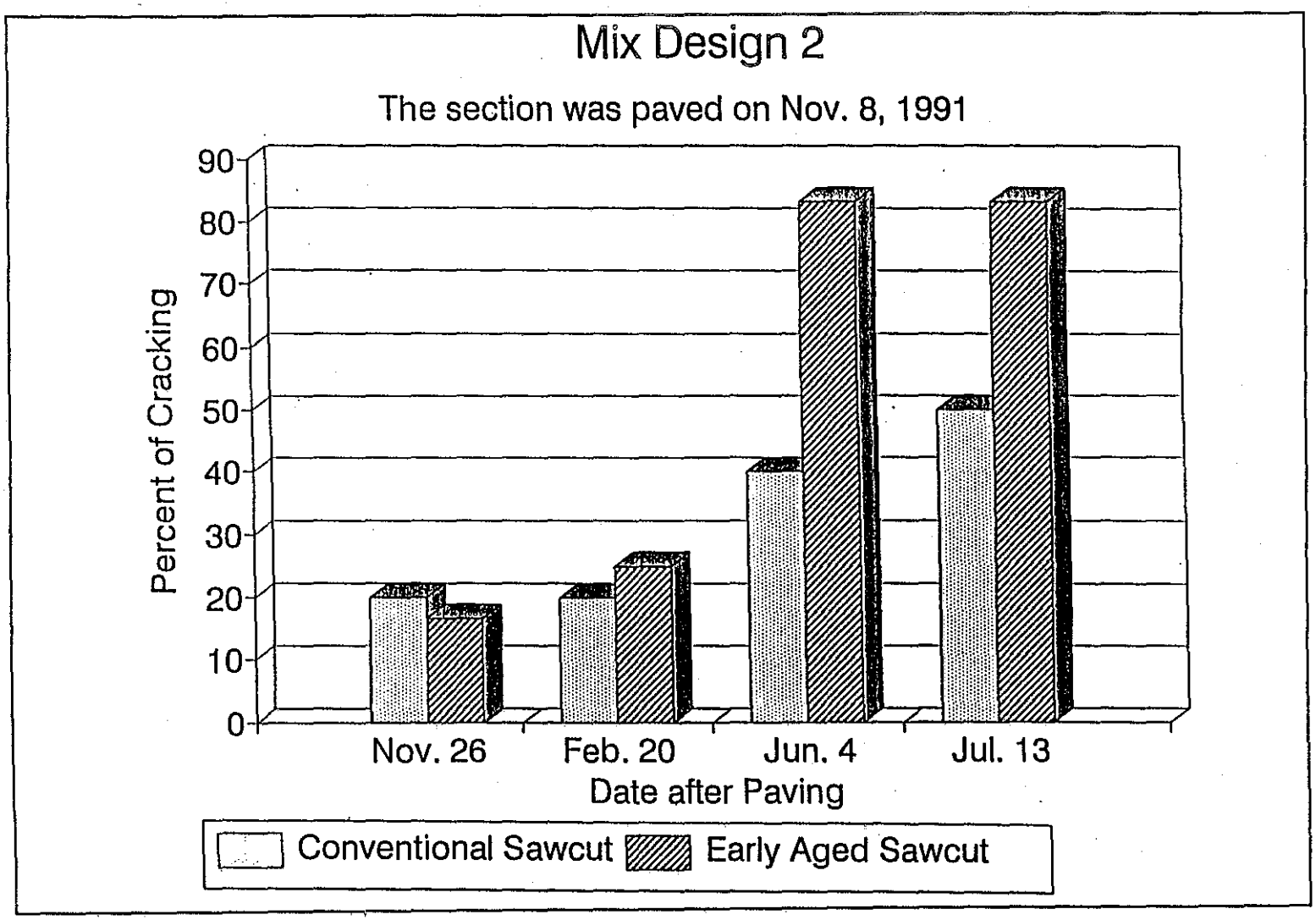

Fig. 5.20. Cracking Development.

cracking, it is speculated that cracking at the sawcuts, although observed much later after construction, initiated early in the life of the pavement which may be indicative that a certain level of damage is necessary to insure that cracking will occur at the sawcut joint. A closer look at the evolution of cracking can be taken by examining the results shown in Fig. 5.8. The initial crack interval was on the order of 90 feet (27.4 m) or more. Apparently, it is intervals of this magnitude where the combination of curl, warping, and frictional stresses was enough to initiate cracking (Fig. 5.17). The frictional stress may have been the significant contribution to crack development given the climatic conditions under which the paving was accomplished although a much improved crack pattern developed the following summer. The disadvantage of a crack pattern developing in this manner is that some joints open wider than designed, which may damage the joint sealant material. It should be pointed out that this characteristic was prevalent whether conventional or early-aged cutting techniques were used. This condition may be minimized by using a jointed reinforced concrete pavement type.

It is interesting to note that different types of aggregate affect the fracture properties and crack development of concrete pavement as shown in Fig. 5.21. Cracking at the sawcut tip occurred more frequently where the concrete coarse aggregate type was river gravel rather than crushed limestone concrete. This was also the case in the subsection paved with the concrete that used a blend of crushed limestone and river gravel as the coarse aggregate in comparison to that paved with the concrete that used crushed limestone only as the coarse aggregate. Lab tests showed that concrete of crushed limestone had higher flexural and compressive strengths than concrete of river gravel at early ages [11, 19]. These field results tend to confirm the validity of using early-aged sawcutting techniques. Although not expressly addressed in this paper, it appears that sawcut timing is much more significant than sawcut depth. A shallow notch placed early in the pavement surface can take advantage of the greater change in temperature and moisture in the vicinity of the pavement surface (in comparison with the changes occuring at a greater depth) which results in a greater amount of crack damage and subsequent incidence of cracking at the notches.

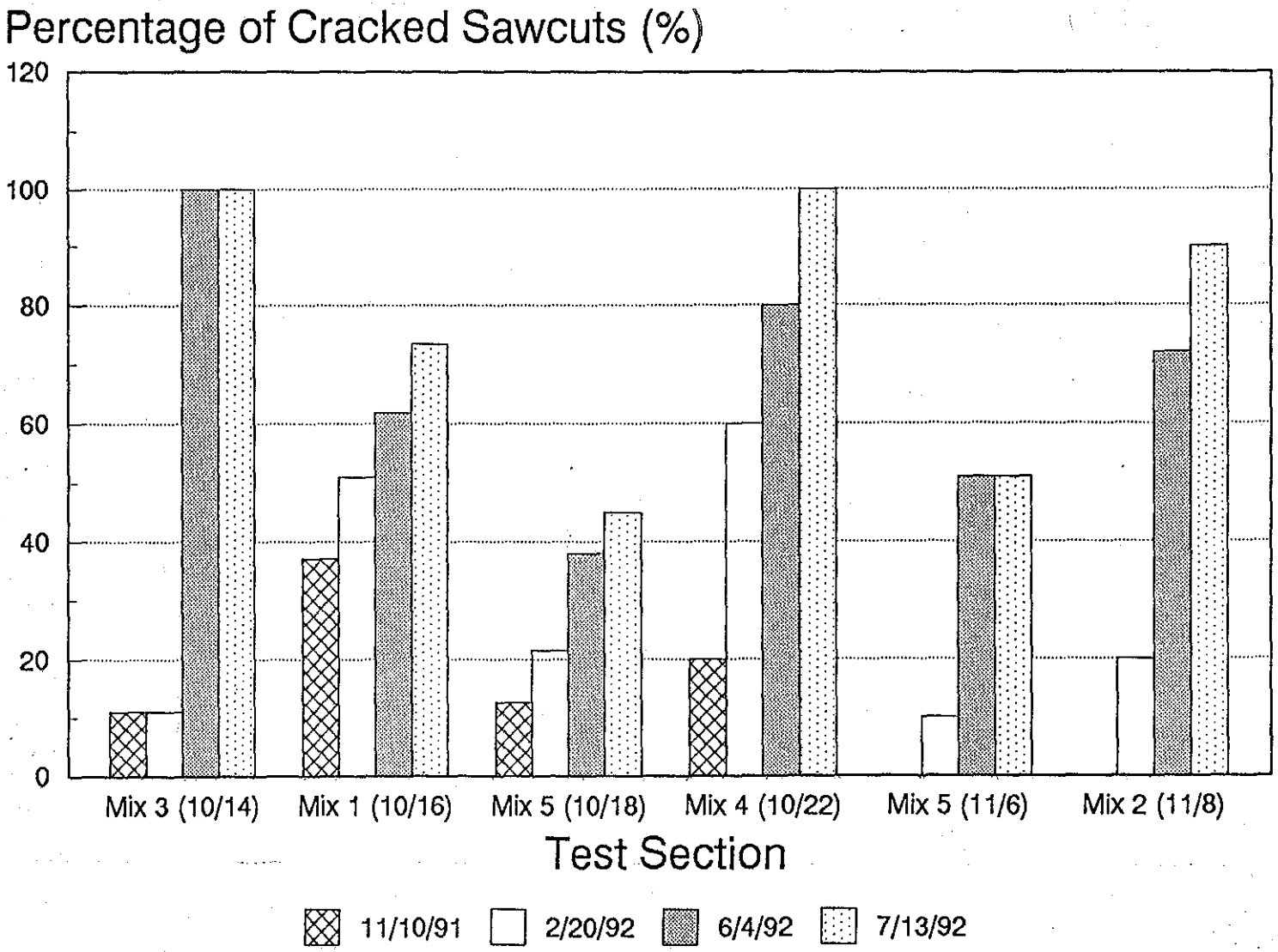

Fig. 5.21. Percentage of the Sawcuts Having Cracked Observed at Different Dates in Test Sections Paved at Different Dates (Dates in Parentheses) with Different Concrete Mix Designs.

5.6. CONCLUSIONS

Modified linear fracture mechanics is applicable in determining sawcut depth for early cracks. The sawcut depth is dependent on the spacing of the transverse sawcut, the material fracture parameters K_{If} and C_f, and the stress level in the concrete slab with given geometrical conditions. The material fracture parameters vary with time, especially at early ages of concrete. Field observation has found that late cracks are also initiated by the sawcutting notches. However, the propagation of these cracks may be caused by long-term fluctuating thermal and moisture loads, for which further research is needed.

The reduction of sawcut depth (less than d/3 or d/4) at concrete joints by early-aged sawcut or placement techniques will take advantage of the greater change in moisture and temperature in the concrete at the pavement surface (in comparison to the change at d/3 or d/4) to initiate cracking at the notches at a greater incidence than otherwise. Therefore, the control of concrete pavement cracking should be improved. Field surveys indicate that under some circumstances (such as cool weather paving conditions) transverse cracks at the sawcut notches may initiate much later after placement. On a preliminary basis, this study indicates that it is reasonable to use notch depths on the order of 1 inch (2.5 cm), to initiate cracking at the pavement surface, which is significantly less than the traditional d/4 or d/3.

5.7. APPENDIX: REFERENCES

1. Emborg, M., "Thermal Stresses in Concrete Structures at Early Ages," Doctoral Thesis, Luleå University of Technology, Luleå, Germany, 1989.
2. Richardson, J. M., and Armaghani, J. M., "Stress Caused by Temperature Gradient in Portland Cement Concrete Pavements," Transportation Research Record 1121, 1987, pp. 7-13. Transportation Research Board, Washington, D. C., 1987.
3. Westergaard, H. M., "Analysis of Stresses in Concrete Pavements Due to Variations of Temperature," Proceedings of the Sixth Annual Meeting, Highway Research Board, 1927, pp. 201-205.
4. Bradbury, R. D., "Reinforced Concrete Pavements," Wire Reinforcement Institute, Washington, D. C., 1938, pp. 34-41.

5. Tang, T., and Zollinger, D.G., and Senadheera, S, "Analysis of Concrete Curling in Concrete Slabs," Journal of Transportation Engineering, V. 119, No. 4, July/August 1993, pp. 618-633.
6. Bažant, Z. P., and Wu, S. T., "Creep and Shrinkage Law for Concrete at Variable Humidity," Journal of the Engineering Mechanics Division, Vol. 100, No. 1974, pp. 1183-1209.
7. Bažant, Z. P., and Panula, L., "Practical Prediction of Time-Dependent Deformation of Concrete. Part 3: Drying Creep. Part 4: Temperature Effect on Basic Creep," Matériaux et Constructions, Vol. 11, No. 66, 1978, pp. 415-424.
8. Buch, Neeraj and Zollinger, D.G., "Preliminary Investigation on the Effect of Moisture on Concrete Pavement Strength and Behavior," A paper prepared for the 72nd Annual Meeting of the Transportation Research Board, 1993.
9. Tang, T., Zollinger, D.G., and McCullough, Frank, "Texarkana Test Sections," Technical Memorandum, Research Project 1244, February 1993.
10. Yoder, E.J. and Witczak, M.W., (1975), Principles of Pavement Design, 2nd Edition, John Wiley and Sons.
11. McCullough, B. Frank, "Mechanistic Analysis of Continuously Reinforced Concrete Pavements Considering Material Characteristics, Variability, and Fatigue," Research Report 1169-2, Center for Transportation Research, the University of Texas at Austin, April 1990.
12. Palmer, R.P., Olsen, M., and Lytton, R.L., "TTICRCP - A Mechanistic model for the Prediction of Stresses, Strains,and Displacements in Continuously Reinforced Concrete Pavements," Research Report 371-2F, Texas Transportation Institute, Texas A&M University, August 1987.
13. Grzybowski, M., "Determination of Crack Arresting Properties of Fiber Reinforced Cementitious Composites," Royal Institute of Technology, Stockholm, Sweden, 1989.
14. England, G. L., and Illston, J. M., "Methods of Computing Stress in Concrete from a History of Measured Strain," Civil Engineering and Public Works Review, Vol. 60, 1965: April - pp. 513-717; May - pp. 692-694; and June - pp. 846-847.